UNIVERSIDADE FEDERAL DO RIO GRANDE DO SUL
INSTITUTO DE GEOCIÊNCIAS
PROGRAMA DE PÓS-GRADUAÇÃO EM GEOCIÊNCIAS

MINERALOGIA E GEOQUÍMICA DO DEPÓSITO DE NIÓBIO DE MORRO DOS SEIS LAGOS: ROCHA PRIMÁRIA, LATERITAS E MINERALIZAÇÃO ASSOCIADA DE ELEMENTOS TERRAS RARAS.

ARTHUR LEMOS GIOVANNINI

ORIENTADOR – Prof. Dr. Artur Cezar Bastos Neto
COORIENTADOR – Prof. Dr. Vitor Paulo Pereira

Volume I
Porto Alegre - 2017

UNIVERSIDADE FEDERAL DO RIO GRANDE DO SUL
INSTITUTO DE GEOCIÊNCIAS
PROGRAMA DE PÓS-GRADUAÇÃO EM GEOCIÊNCIAS

MINERALOGIA E GEOQUÍMICA DO DEPÓSITO DE NIÓBIO DE MORRO DOS SEIS LAGOS: ROCHA PRIMÁRIA, LATERITAS E MINERALIZAÇÃO ASSOCIADA DE ELEMENTOS TERRAS RARAS.

ARTHUR LEMOS GIOVANNINI

ORIENTADOR – Prof. Dr. Artur Cezar Bastos Neto
COORIENTADOR – Prof. Dr. Vitor Paulo Pereira

BANCA EXAMINADORA:

Prof. Dr. José Carlos Frantz, Universidade Federal do Rio Grande do Sul
Prof. Dr. Nilson Francisquini Botelho, Universidade Federal de Brasília
Prof. Dr. Jorge Silva Bettencourt, Universidade Federal de São Paulo

Tese de Doutorado apresentado como requisito parcial para a obtenção do Título de Doutor em Ciências.

Porto Alegre - 2017

CIP - Catalogação na Publicação

Giovannini, Arthur Lemos
Mineralogia e geoquímica do depósito de nióbio de Morro dos Seis Lagos: rocha primária, laterita e mineralização associada de elementos terras raras / Arthur Lemos Giovannini. -- 2017.
228 f.
Orientador: Artur Cezar Bastos Neto.

Coorientador: Vitor Paulo Pereira.

Tese (Doutorado) -- Universidade Federal do Rio Grande do Sul, Instituto de Geociências, Programa de Pós-Graduação em Geociências, Porto Alegre, BR-RS, 2017.

1. Carbonatitos. 2. Morro dos Seis Lagos. 3. Geoquímica. I. Bastos Neto, Artur Cezar, orient. II. Pereira, Vitor Paulo, coorient. III. Título.

Elaborada pelo Sistema de Geração Automática de Ficha Catalográfica da UFRGS com os dados fornecidos pelo(a) autor(a).

AGRADECIMENTOS

Agradeço a todos que de uma forma ou de outra contribuíram para a realização desta Tese de Doutorado.

Agradeço à Universidade Federal do Rio Grande do Sul, ao Instituto de Geociências e ao Programa de Pós Graduação (PPGGEO).

Agradeço ao meu orientador Artur Cezar Bastos Neto por toda a ajuda na realização deste trabalho, agradeço também ao meu co-orintador Vitor Paulo Pereira, pela ajuda na aquisição dos dados. Agradeço também aos meu colegas de bolsa.

RESUMO

O depósito laterítico de Nb (ETR, Ti) Morro dos Seis Lagos (MSL) é derivado de siderita carbonatito (SC). O gnaisse encaixante foi afetado por fenitização potássica (flogopita e ortoclásio + monazita, fluorapatita e bastnäsita). Há três tipos de SC: o de núcleo (siderita e hematita + acessórios Ce-Ba-pirocloro, Nb-brookita, Ti-maghemita e thorbastnäsita; uma variedade do de núcleo rica em ETR-P (siderita e hematita + Ce-Ba-pirocloro, monazita e bastnäsita; e o de borda (siderita e barita + gorceixita, rabdofano e Pb-Ba-pirocloro). Dados de inclusões fluidas e isótopos de C e O indicam que o SC de núcleo é tardi-magmático a hidrotermal e o de borda é hidrotermal. O SC de núcleo é o carbonatito mais rico em Fe e o mais pobre em Ca jamais descrito, é rico em Mn, Ba, Th, Pb, ETRL e Nb. A alta razão Nb/Ta indica líquidos residuais derivados por cristalização fracionada. Dados isotópicos (Sr e Nd) sugerem origem mantélica praticamente sem contaminação crustal. O complexo carbonatítico MSL representa a parte apical de sistema carbonatítico magmático diferenciado e o SC é relacionado a processos tardi-magmáticos a carbo-hidrotermais. O depósito de Nb é associado a lateritas de 6 tipos (do topo para a base): pisolítica, fragmentada, mosqueada, roxa, manganesífera e marrom. Todas são compostas por goethita (predominante nas partes inferior e superior) e hematita (predominante na porção intermediária). As lateritas superiores foram retrabalhadas. Na laterita manganesífera, os óxidos de Mn (hollandita e pirolusita) ocorrem em veios relacionados a evento tardio na formação das lateritas. O principal mineral de Nb é Nb-rutilo presente em todo o perfil, formado juntamente com Ce-pirocloro, Nb-goethita e cerianita. Nb-brookita formada a partir do Nb-rutilo ocorre como esférulas com estrutura Liesegang. Nb-rutilo e Nb-brookita incorporam Nb pela substituição [Fe^{3+} + (Nb, Ta) = 2Ti]. As lateritas têm teor médio de Nb_2O_5 de 2,91% e 5,00% de TiO_2. A mineralização associada de ETR é de 3 tipos: primária, supergênica e clástica-autigênica (em bacias cársticas). O SC de núcleo tem concentração média de 0,70% de ETR_2O_3 (thorbastnäsita) e uma zona mais rica (1,48% de ETR_2O_3) com monazita e bastnasita. Nas lateritas inferiores (1,02% de Ce_2O_3) a cerianita-(Ce) intercalada na goethita foi formada pela decomposição do Ce-pirocloro; na laterita manganesífera (1,41% de Ce_2O_3) ocorre cerianita-(Ce) intercrescida com hollandita; nas lateritas superiores ocorre florencita-(Ce). Na bacia Esperança (233 m de espessura) a mineralização de ETR nas brechas do pacote inferior, ricas em fragmentos de SC, e nos ritmitos lacustres do pacote intermediário (com clastos de materiais ferruginosos relacionados aos estágios iniciais da alteração do siderita carbonatito) é principalmente clástica (monazita e florencita). No pacote superior (0 – 73 m, com 1,72 wt% de ETR_2O_3), formado por argila carbonosa rica em matéria orgânica, que marca a inversão do relevo, a florencita-(Ce) é autigênica, formada principalmente por dissolução de minerais da laterita retrabalhada, transporte e deposição em ambiente alcalino rico em Al e P. A evolução mineralógica e geoquímica dos ETR nesses três domínios são integrados em um modelo compreensível para o comportamento ETR no MSLD.

ABSTRACT

The Morro dos Seis Lagos Nb (REE, Ti) lateritic deposit is derived from a primary siderite carbonatite (SC). The country rock gneiss was affected by potassic fenitization (phlogopite and orthoclase + monazite, fluorapatite and bastnäsite). Three types of SC are recognized: core SC (siderite and hematite + Ce-Ba-pirocloro; Nb-brookita; Ti-maghemita; and thorbastnäsite; a REE-P-rich variety of CSC (siderite and hematite, + Ce-Ba-pyrochlore, monazite and bastnäsite; a border SC (BSC) (siderite and barite + gorceixite, rabdophane and Pb-Ba-pyrochlore). Fluid inclusion and C and O isotopic data indicate that the CSC is late-magmatic to hydrothermal and the BSC is hydrothermal. The CSC is the richest in Fe and the poorest in Ca siderite carbonatite yet recognized, has high Mn, Ba, Th, Pb, LREE and Nb contents. The high Nb/Ta ratio indicates residual liquids from fractional crystallization. Isotopic data (Sr and Nd) suggest the carbonatite has a mantle origin with essentially no crustal contamination. The Morro dos Seis Lagos Carbonatite Complex represent the upper-most parts of a differentiated carbonatite magmatic system, and the SC is related to late-magmatic-to- carbo-hydrothermal processes. The Nb deposit is associated to 6 laterite types (from top to bottom): pisolitic, fragmented, mottled, purple, manganiferous, brown. All are composed of goethite (in the lower and upper laterites) and hematite (in the intermediate types). The upper laterites were reworked. In the manganiferous laterite Mn-oxides (hollandite and pyrolusite) occur as veins formed in a late event during the development of the laterite. The main Nb ore mineral is Nb-rich rutile, which occurs in all laterites and is formed together with Ce-pyrochlore, Nb-rich goethite and cerianite. Nb-rich brookite formed from Nb-rich rutile occurs as broken spherules with Liesegang ring structure. Nb-rich rutile and Nb-rich brookite incorporate Nb following the [Fe^{3+} + (Nb, Ta) for 2Ti] substitution. The laterites have an average 2.91 wt.% of Nb_2O_5 and an average 5.00 wt.% of TiO_2. The associated REE mineralization is of 3 types: primary, supergene and clastic-authigenic (karstic basins). The CSC has an average 0.70 wt% of REE_2O_3 (thorbastnäsite) and a rich zone 1.48wt.% of REE_2O_3 (monazite and bastnäsite). In the lower laterites (1.02 wt% Ce_2O_3) cerianite-(Ce) occurs as bands intercalated with goethite formed by pyrochlore breakdown; at the manganiferous laterite (1,41 wt.% Ce_2O_3) cerianite-(Ce) occurs intergrown with hollandite; florencite-(Ce) occurs in the reworked laterites. At the Esperança Basin (233m thick) the REE mineralization in breccia in lower package, rich in CSC fragments, and in rythmites in the intermediary package rich ferruginous materials related to the early stages of siderite carbonatite alteration, is clastic (monazite and florencite). In the upper package (0 – 73 m, 1,72 wt% of ETR_2O_3), formed by carbonaceous clay rich in organic matter, which marks the relief inversion, occurs an authigenic florencite-(Ce), fomed by dissolution of minerals from the reworked laterites, transportation and deposition in a alkaline environment rich in Al and P. The mineralogical and geochemical evolution of the REE is these three domains are integrated into a comprehensible model for the REE behavior at the MSLD.

SUMÁRIO

1. INTRODUÇÃO

1.1 Considerações Iniciais

O Distrito de Seis Lagos é constituído por três chaminés vulcânicas e está localizado a 64 km a nordeste de São Gabriel da Cachoeira, no alto rio Negro, Amazonas. Este distrito foi descoberto no final dos anos 60 pelos pesquisadores do projeto RADAM-BRASIL. No levantamento da Folha NA.19-Z-D, os geólogos tiveram sua atenção voltada para três estruturas ocorrentes na bacia do rio Cauaburi e que apresentaram anomalias radiométricas com intensidade de até 15.000 cintilações por segundo (cps). Na época, por sua morfologia peculiar, a maior destas estruturas foi denominada Morro dos Seis Lagos, onde foi identificada uma espessa crosta laterítica ferruginosa, com teores anômalos de nióbio e ETR. Issler (1980) e Bonow & Issler (1980) interpretaram que a rocha original deveria ser um carbonatito e apresentaram as primeiras informações sobre o potencial mineral da área para ETR e ferro-ligas.

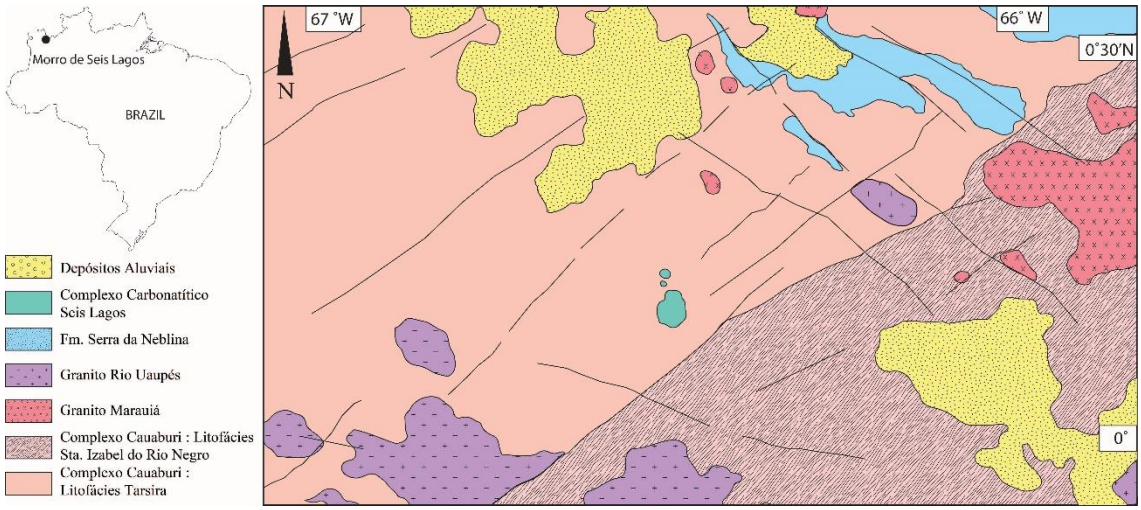

Figura 1. Localização do Morro de Seis Lagos – AM. (Modificado de CPRM 2006)

O Complexo Carbonatítico Seis Lagos (CCSL) é formado por 3 corpos circulares (Fig. 1). O maior corpo circular, denominado Morro dos Seis Lagos, é coberto por uma crosta de ferro que corresponde ao Morro dos Seis Lagos Depósito (DMSL). O CCSL é inserido na parte sudeste da Província do Rio Negro. As rochas do embasamento são representadas pelo Complexo de Cauaburi (Fig. 1), que agrupa metagranitóides porfiríticos, tonalitos, ortognaisses monzoniíticos, augen gnaisses, anfibolitos e migmatitos localizadas, foliadas na direção NE-SW (Almeida et al., 2002 e 2007) Com uma idade de aproximadamente 1,8 Ga

(Santos et al. 2000, 2003; CPRM 2006). A rocha encaixante do corpo de carbonatite de Morro dos Seis Lagos é um augen gnaisse monzogranitico. O CCSL está localizado no cinturão de K'Mudku, que é interpretado por Santos et al. (2006) como um efeito intracratônico distante relacionado à colisão continental Sunsás-Greenvillian (1,3 a 0,98 Ga).

As estruturas regionais que determinam esta intrusão têm orientação NW-SW e NE-SW. O Distrito de Seis Lagos também é descrito com Complexo Carbonatítico de Seis Lagos e correlacionado ao período Juro-Cretáceo, com uma idade de cerca de 160 Ma. A datação U-Pb de zircões do carbonatito forneceu idades entre 1,3 Ga e 1,8 Ga. O estudo químico e mineralógico de zircões mais jovens sugere que parte deles é do carbonatito. Portanto a idade máxima para a carbonatito é de 1,3 Ga. (Rossoni et. al, 2017).

A CPRM, que detém os direitos minerários da área, realizou, numa primeira fase, levantamentos geofísicos e geoquímicos, além de quatro sondagens rotativas (Fig. 2), cujos resultados constam no Projeto Seis Lagos (Viegas Filho & Bonow, 1976). Posteriormente, foram realizados 4 furos de sondagem, com profundidades da ordem de 60m, sendo todos interrompidos dentro da crosta laterítica. O Furo 1 cortou 255m de laterita mineralizada e foi interrompido ainda dentro deste material, sem atingir o saprólito ou a rocha sã. O Furo 2, cortou 34m de laterita não mineralizada e, em seguida, perfurou a rocha encaixante, sendo interrompido a poucos metros após penetrar um material descrito como rocha com carbonatos (beforsito ?), a 230m de profundidade. O Furo 3 cortou 9m de laterita mineralizada, 40m de crosta argilosa e, em seguida, perfurou o gnaisse encaixante, sendo interrompido a 110m de profundidade. O Furo 4, localizado sobre a Bacia Esperança (bacia cárstica sobre o carbonatito), cortou 73m de sedimentos finos carbonosos, dos 73m aos 233 cortou intercalações de argilas com óxidos de ferro e fragmentos de carbonatito e aos 233m de profundidade chegou no carbonatito. Esta brecha carbonática foi interpretada por Issler & Silva (1980) e Bonow & Issler (1980) como sendo alteração do próprio carbonatito e, posteriormente, como sendo de origem sedimentar.

Com base nos dados destes furos de sonda, Justo & Souza (1984, 1986) calcularam as reservas do morro de Seis Lagos como tendo 2,898 bilhões de toneladas de minério com teor de 2,81% de Nb_2O_5 (valor 14 vezes maior do que a reserva mundial então conhecida). Os dados geoquímicos apresentados por estes autores consistem apenas das concentrações médias de Nb e Ce.

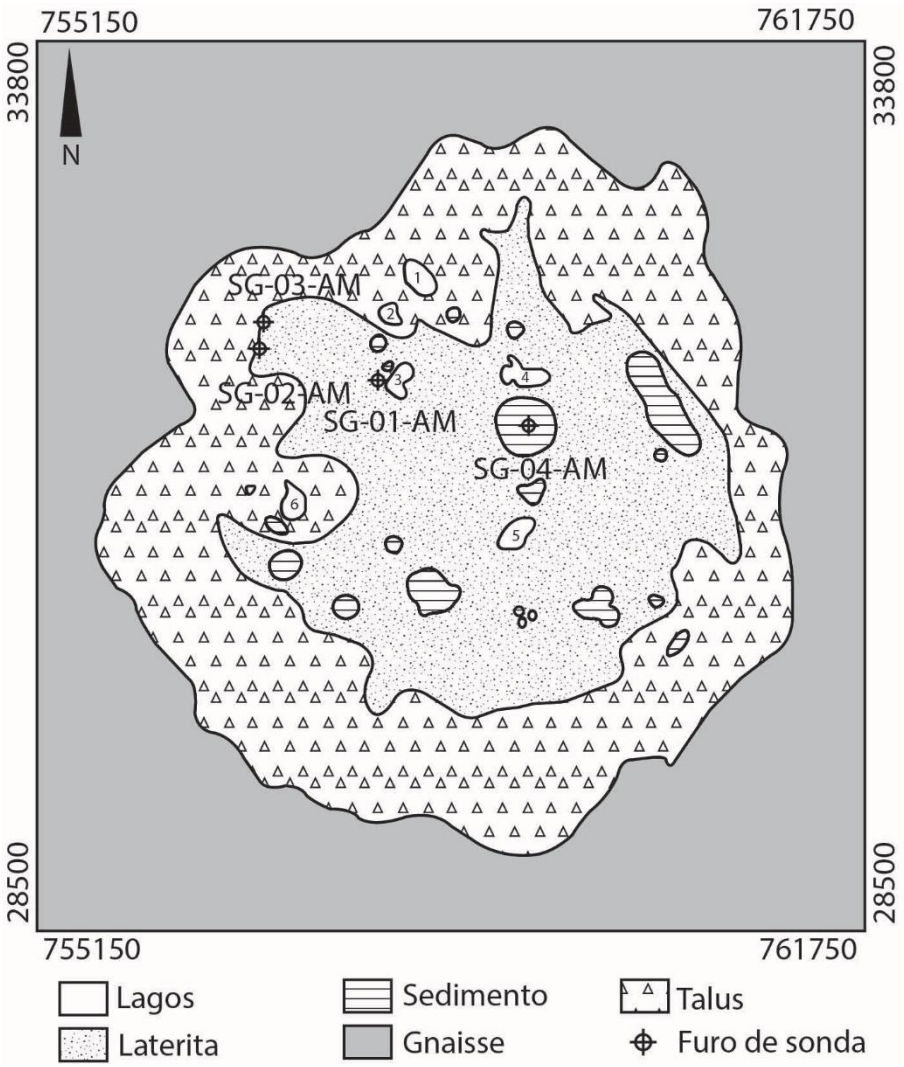

Figura 2. Localização dos furos de sonda no Morro de Seis Lagos - AM. (Modificado de Viegas & Bonow 1976)

Corrêa (1996) e Corrêa & Costa (1997) realizaram os primeiros estudos científicos em Seis Lagos. Por motivos não esclarecidos, estes pesquisadores não tiveram, aparentemente, acesso aos testemunhos das sondagens. Para realizar o estudo, dispuzeram de um grande número de amostras superficiais coletadas nos perfis de geoquímica de solo realizados pela CPRM. Entretanto, dos furos de sonda, receberam apenas as alíquotas das amostras analisadas por esta companhia e somente dos Furos 1, 2 e 4 da primeira fase de sondagem. Mesmo sem poder identificar, caracterizar e interpretar as texturas do minério, os referidos autores produziram importantes dados mineralógicos e geoquímicos (incluindo os de isótopos de O e C, especialmente da brecha carbonática do furo 4). Estes pesquisadores também identificaram e analisaram diversos minerais presentes no perfil laterítico do morro de Seis Lagos, caracterizando este como constituído essencialmente por minerais de ferro (hematita, goethita) com alguns minerais acessórios importantes, como, hollandita, romanechita,

pirolusita, lithioforita, florencita, cerianita, gibbsita, ilmeno-rutilo, brookita niobífera e rutilo niobífero, além de monazita, zircão e quartzo. Estes últimos foram considerados indicativos de que o substrato do morro dos Seis Lagos seria constituído por carbonatito. Os dados químicos da laterita foram comparados com dados químicos dos carbonatitos de outras localidades e considerados típicos de alteração deste tipo de rocha. Um dos enfoques do trabalho destes autores foi a formação/evolução da bacia Esperança e as relações entre a sedimentação e os processos de alteração e erosão ocorridos na sua margem. Com base principalmente nos dados isotópicos, que teriam uma variabilidade muito grande para um carbonatito, os autores concluíram que a brecha carbonática da base do Furo 4 seria sedimento lacustre e não carbonatito alterado. Observa-se que os trabalhos de Corrêa (1996) e Corrêa e Costa (1997) foram os últimos realizados na área em estudo.

Destaca-se que existe uma grande carência de dados sobre as rochas do Complexo de Seis Lagos, especialmente das porções situadas abaixo da crosta laterítica ferruginosa. Estas rochas abaixo de crosta ferruginosa formam uma brecha carbonática, e suas variações fazem parte do intervalo considerado no cálculo das reservas de Nb de Seis Lagos, mas as informações sobre as mesmas restringem-se às análises de Nb e Ce de testemunhos (dados da CPRM) e aos dados de Corrêa (1995) e Corrêa e Costa (1997), que foram obtidos em amostras de calha. Portanto, conclui-se que existe a necessidade de realizar um estudo mais completo, com ênfase a caracterização química e mineralógica das amostras dos testemunhos e de todos os quatro furos de sondagem lá realizados.

O estudo do carbonatito e da crosta laterítica de Seis Lagos, tem grande interesse científico e econômico, por serem portadores de minério de Nb, ETR e fostato. Por isso, é importante tentar delimitar as porções de rocha (fácies) decorrentes da superposição de diferentes processos e, se possível, caracterizar os processos formadores da brecha carbonática.

1.2 Objetivos

Os objetivos gerais com o projeto são (1) construir um modelo genético de formação e posicionamento do carbonatito de Seis Lagos; (2) compreender os processos de alteração que ocorreram na área e possibilitaram a formação dessa espessa crosta laterítica mineralizada e da bacia associada e (3) contribuir para definir o potencial econômico da área.

Para atingir este objetivo, as seguintes metas deverão ser alcançadas:

- caracterizar os minerais primários do carbonatito e da brecha carbonatica;

- caracterizar a crosta laterítica e as suas variações texturais e composicionais;

- caracterizar os minerais de minério com ênfase aos minerais de minério de Nb (Pirocloro, Rutilo e Brookita) e de ETR (Cerianita, Monazita, Rhabdofano e Florencita) e assim como identificar os processos envolvidos na sua formação e alteração.

- reconhecer os diferentes tipos de alteração hidrotermal e sua cronologia relativa;

- caracterizar os minerais presentes nas paragêneses de cada tipo de alteração;

- caracterizar os fluidos envolvidos nos diferentes processos identificados;

1.3 Estrutura da Tese

No capítulo 1 (Introdução) são apresentadas as considerações inciais sobre o Morro dos Seis Lagos, como localização e a geologia local.

No capítulo 2 (Carbonatitos) é feita uma revisão bibliográfica sobre essas rochas, o protólito do depósito.

No capítulo 3 (Crosta laterítica) é feita uma revisão sobre essa rocha e o processo que forma a mesma, processo que concentrou os minérios do depósito.

O capítulo 4 (Resultados) é composto por 3 artigos submetidos e/ou publicados em periódicos internacionais:

- *Mineralogy and geochemistry of the Morro dos Seis Lagos siderite carbonatite, Amazonas, Brazil.* - Este artigo discorre sobre o carbonatito, sua mineralogia e geoquímica, bem como sua gênese.

- *Mineralogy and geochemistry of laterites from Morro dos Seis Lagos Nb (Ti,REE) deposit (Amazonas, Brazil)* – este artigo discorre sobre as características e a formação de laterita formada sobre o siderita carbonatito, a qual concentrou os elementos econômicamente importantes do depósito.

- *REE mineralization (primary, supergene and sedimentary) associated to the Morro dos Seis Lagos Nb (REE, Ti) deposit (Amazonas, Brazil)* - este artigo discorre sobre os depósitos de Elementos Terras Raras associados ao carbonatito, ao intemprismo do mesmo e associado a bacia cárstica formada durante esse intemperismo.

O fechamento da tese com a integração dos três artigos é realizado no capítulo 5 (Conclusões).

Em anexo, estão mais dois artigos sobre o Morro de Seis Lagos do qual o doutorando foi co-autor duranto o período da tese:

- *Aplicação de técnicas de sensoriamento remoto na investigação do controle do posicionamento do Complexo Carbonatítico Seis Lagos e no estudo do depósito (Nb) laterítico associado (Amazonas, Brasil)*

- *U-Pb zircon geochronologycal investigation on the Seis Lagos Carbonatite Complex and associated Nb-deposit (Amazonas, Brazil).*

2 CARBONATITOS

2.1 Classificação

Carbonatitos são definidos como rochas magmáticas com mais de 50% de minerais carbonáticos e geralmente apresentam uma forte tendência alcalina, geoquímicamente essas rochas tendem a ser muito ricas em Sr, Ba, P e terras raras leves (ETRL) (Nelson et al. 1988). Existem duas classificações utilizadas para carbonatito, uma delas mineralógica, na qual essas rochas são subdivididas conforme o carbonato formador principal (calcita-, dolomita-, siderita-carbonatito, etc.). Existe também uma classificação química com base na proporção em peso dos elementos maiores (Ca-, Mg-, Fe- e ETR-carbonatito) (Figura 3A) (Wooley 1982; Le Bas 1987; Wooley e Kempe 1989), essa classificação foi revisada por Gittins e Harmer (1997), que propuseram a utilização no diagrama de massas molares ao invés de proporções de peso (Figura 3B), uma vez que a classificação anterior não diferenciava carbonatitos com carbonatos ricos em ferro (siderita e ankerita) de carbonatitos que contém hematita e magnetita na composição modal.

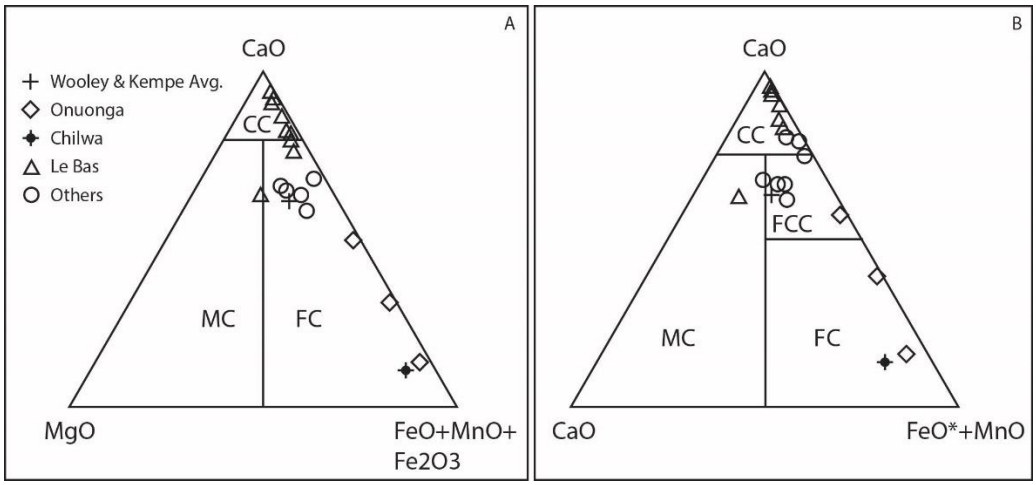

Figura 3. (A) Diagrama de classificação de carbonatitos definido por Wooley & Kempe (1989) e (B) Classificação revisada por Gittins & Harmer (1997). Modificado de Gittins & Harmer (1997).

Mitchell (2005) criou uma classificação genética para facilitar a interpretação, uma vez que qualquer rocha com mais de 50% de carbonatos e de origem magmática são chamados de carbonatitos. Portanto, esse termo, pode se referir a rochas calcíticas e dolomíticas plutônicas, veios de calcita hidrotermais formados em estágios tardi-magmáticos

de diversos magmas diferentes, ao albita-carbonatito de Great Glen na Escócia (Garson et al., 1984) e até veios tardios de calcita no analcima basanita de Calton Hill (Tomkeieff, 1928).

Visando resolver esse problema, e identificar o magma que pode gerar carbonatitos, através de diferenciação, Mitchell definiu que carbonatitos (sensu lato) são rochas que contém 30 % de volume de carbonatos ígneos primários, independente do conteúdo de sílica. Portanto, o nome carbonatito passa, além de se referir ao tipo de rocha específica, também se refere a uma suíte de rochas geneticamente associadas, que contém uma variedade de tipos de carbonatitos.

Além do interesse científico, essas rochas também são indicativos de uma variedade grande depósitos importantes do ponto de vista econômico. Fluidos carbotermais concentram elementos terras raras (ETR), Sr, Ba entre outros, e possuem baixas quantidades de Nb, enquanto carbonatitos associados a melilitos formam depósitos importantes de Nb, Ti e P, porém pobres em ETR.

Utilizando esse conceito de uma classificação mineralógica-genética, Mitchell (2005) subdividiu essas rochas em dois grupos:

(1) Carbonatitos primários: Calcita e dolomita carbonatito que são geneticamente associados a nefelinitos, melilitos, kimberlitos e outros magmas mentélicos.
(2) *Carbonathermal residua*. Carbonatitos como produtos residuais de magmas ricos em CO_2, que também contém flúor e H_2O. São formados em baixa temperatura.

2.2 Ocorrência

Tectonicamente carbonatitos apresentam uma forte ligação com processos de rifteamento e separação de placas (Jones et al. 2013). Baseado em base de dados mundial completa da ocorrência de carbonatitos que mostra um forte controle litológico, Wooley e Bailey (2012) propuseram que um forte processo de reativação ocorre sobre carbonatitos formados em crostas arqueanas, e isto está ligado com o fator de um manto subjacente rico em CO_2, o que também gera kimberlitos.

2.2 Geoquímica dos carbonatitos

Carbonatitos ocorrem como rochas que contém mais de 50% de minerais carbonáticos primários, com menos de 20% de SiO2 (Le Maitre 2002). A classificação química é com base na proporção em peso dos elementos maiores (Ca-, Mg-, Fe- e ETR-carbonatito) (Wooley 1982; Le Bas 1987; Wooley e Kempe 1989). O termo ETR-carbonatito se refere a carbonatitos com mais de 1% de ETR_2O_3 na rocha, porem essa classificação pode estar associada com Ca-, Mg- e Fe- carbonatitos, alguns exemplos de carbonatitos que podem ser classificados como ETR carbonatitos são Bayan Obo, Kagankunde e Mountain Pass. Esse alto teor de ETR nesses carbonatitos está associado a minerais carbonáticos como bastnasita, synchsita e ETR fluorcarbonatos, e minerais fosfáticos como monazita e ETR-fosfatos (Wall & Mariano 1996; Jones et al. 2013). Jones (2013) sugeriu que carbonatitos com mais de 1% de ETRO sejam classificados como ETR-carbonatitos. Altos valores de ETR (>5%) já são utilizados por geólogos de mina, mas esses valores geralmente estão ligados carbonatitos ricos em Fe, portanto são chamados de ferrocarbonatito. Altos teores de ETR em carbonatitos estão0 geralmente associados a altos teores de Th e U, o que sugere a cristalização fracionada de um magma carbonatítico associado a um enriquecimento secundário por fluidos metassomáticos ricos em voláteis (Le Bas et al. 2007; Yang et al. 2011; Jones et al. 2013).

Outro carbonatito que apresenta uma classificação diferente é o carbonatito de Oldoinyo Lengai na Tanzânia, é o único exemplo de um carbonatito cujo o principal formador de carbonato são o Na e K (~40% peso).

2.2.1 Elementos Maiores

Carbonatitos são ricos em Ba, Sr, P e ETR (principalmente os ETRL) e possuem anomalias negativas de Zr a Hf (Nelson, 1988). A composição média dos carbonatitos (Bell, 1989) mostra um enriquecimento de Si, Mn, Ba, Fe e F na evolução da série cálcio-, magnésio-, ferro- carbonatito. Teores de Al, Na, K, Sr, e P são variados e não apresentam uma tendência nessa série.

O natrocarbonatito não apresenta uma correlação com os outros carbonatitos, são formados essencialmente de Na_2O e K_2O (até 40%) e apresenta baixos teores SiO_2 e Al_2O_3. E

altos teores de CaO e CO_2, também apresenta valores consideráveis de Ba, Sr, P, S, Cl, F e Mn em comparação com as rochas ígneas (Ridley & Dawson 1975).

2.2.2 Elementos Traço

Diversos elementos traço assumem um papel de elemento maior nos carbonatitos, como por exemplo Ba, Sr e ETR em alguns casos. O alto enriquecimento em ETRL é típico em carbonatitos e pode gerar depósitos econômicos desses elementos. Na evolução da série de carbonatitos de cálcio- e magnésio- carbonatitos para ferrocarbonatito ocorre um empobrecimento em elementos como Co, Cr, Ni e V, enquanto os teores de ETR aumentam significativamente, acompanhados por U e Th (Jones et al. 2013). Natrocarbonatitos contém altos teores de ETRL com altas razões de La/Yb e U/Th (Dawson 2008). Os elementos HFSE (high strength field elements) apresentam uma variação entre os tipos de carbonatito (Chackmouradian, 2006), enquanto os valores de TiO_2 aumentam na evolução da série calcio- magnésio- ferro-carbonatitos, os valores de Zr, Hf, Nb e Ta diminuem com a evolução da série.

2.3 Assinaturas Isotópicas de Carbonatitos

Isótopos Radiogênicos: Carbonatitos são rochas com um volume de ocorrência insignificante comparado a rochas silicáticas, mesmo assim, devido a sua dispersão e ocorrência em diversos tempos geológicos, essas rochas fornecem informações importantes sobre a evolução do manto subcontinental. Rochas alcalinas e carbonatíticas do rift leste africano apresentam assinaturas isotópicas próximas a linha de mistura HIMU-EM1 (Jones et al. 2013). Essa mistura pode indicar

Isótopos Estáveis: Os primeiros estudos de isótopos estáveis de carbono e oxigênio foram realizados em carbonatitos intrusivos associados a rochas alcalinas afim de definir o campo de carbonatitos ígneos primários (primary igneous carbonatites) (Taylor et al. 1967). O campo definido possui δC13 entre -3.1 a -7.7 e δO18 entre +5.3 a +8.4 (Figura 4). Os carbonatitos comumente sofrem alteração secundária e isso afeta principalmente os valores de δO18. Essa variação de δO18 pode indicar o processo pelo qual o carbonatito passou. Se ocorre somente a variação de δO18, isso é uma indicação de alteração de baixa temepratura

ou de processos hidrotermais, se a variação de δO18 é acompanhada de uma variação de δC13 isso pode indicar uma contamição sedimentar, um fracionamento em alta temperatura (Rayleight) ou um processo carbohidrotermal (Pineau et al. 1973).

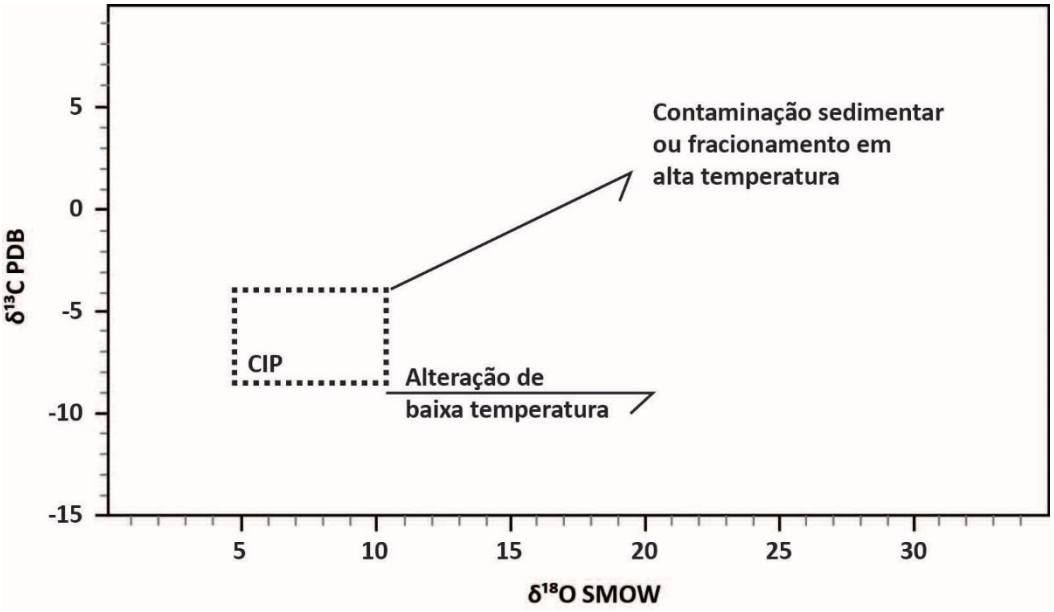

Figura 4. Campo de Carbonatitos ígneos primários definido por Taylor et al. 1967. Alteração de baixa temperatura e fracionamento/contaminação sedimentar (Pineau et al. 1973)

2.4 Depósitos minerais em carbonatitos

Carbonatitos são rochas distintas e concentram elementos com alto valor econômico, principalmente ETR, Nb, U e Ta, mas concentram também Fe, Cu, P, fluorita, barita, PGE, Ag e Au (Richardson & Brickett 1996; Hornig-Kjarsgaard 1998; Jones et al. 2013). Alguns dos depósitos de ETR mais importantes do mundo ocorrem em carbonatitos como por exemplo Bayan Obo, China que contem 37 Mt com média de 6% ETR_2O_3, Mountains Pass, EUA com 31.6 Mt com 6.57 % de ETR_2O_3 em média, entre outros. Carbonatitos também são considerados como principais fontes Nb do mundo. Os principais são o Oka, Canada. Depósitos secundários sobre rochas carbonatíticas são muito comuns, pois essas rochas são muito sucetíveis ao intemperismo, por isso formam-se grandes depósitos com enriquecimento secundário de Nb e ETR. São exemplos Mount Weld (Austrália), Araxá (Brasil) entre outros.

3 CROSTA LATERÍTICA

3.1 Nomenclatura

Os estudos de perfis de intemperismo abrangem diversas áreas das ciências de terra, e portanto muitos termos são utilizados com diferentes significados por essas áreas. Neste trabalho, usamos o termo laterita, que originalmente foi aplicado por Buchanan (1807) a um material rico em Fe em Kerala (Índia).

Anand and Payne, 2002, fizeram uma revisão geral sobre perfis de intemperismo e sua terminologia no trabalho *Regolith geology of the Yilgarn Craton*. A terminologia de um perfil laterítico idealizado pode ser resumido na figura 1. Um "típico" perfil de intemperismo laterítico (Figura 1) descrito por Anand and Butt (1988) compreende, da base para o topo, a rocha sã, o saprock, o saprólito, um horizonte rico em argila (plásmico) ou rico em areia (arenoso), a zona mosqueada e o resíduo laterítico. Terminologias utilizadas por outros autores (Walther, 1915; Millot, 1964; Ollier & Galloway, 1990; Nahon & Tardy, 1992; Aleva, 1994) estão resumidas na figura 1 (modificada de Anand and Payne, 2002), a fim de demonsrar a equivalência da nomenclatura utilizada neste trabalho com a literatura relacionada. A laterita de Morro dos Seis Lagos corresponde ao termo crosta ferrífera (Walter, 1915), e também engloba o cascalho laterítico e o duricrust laterítico (Anand e Butt, 1988), bem como o ferricrete (Ollier e Galloway, 1990).

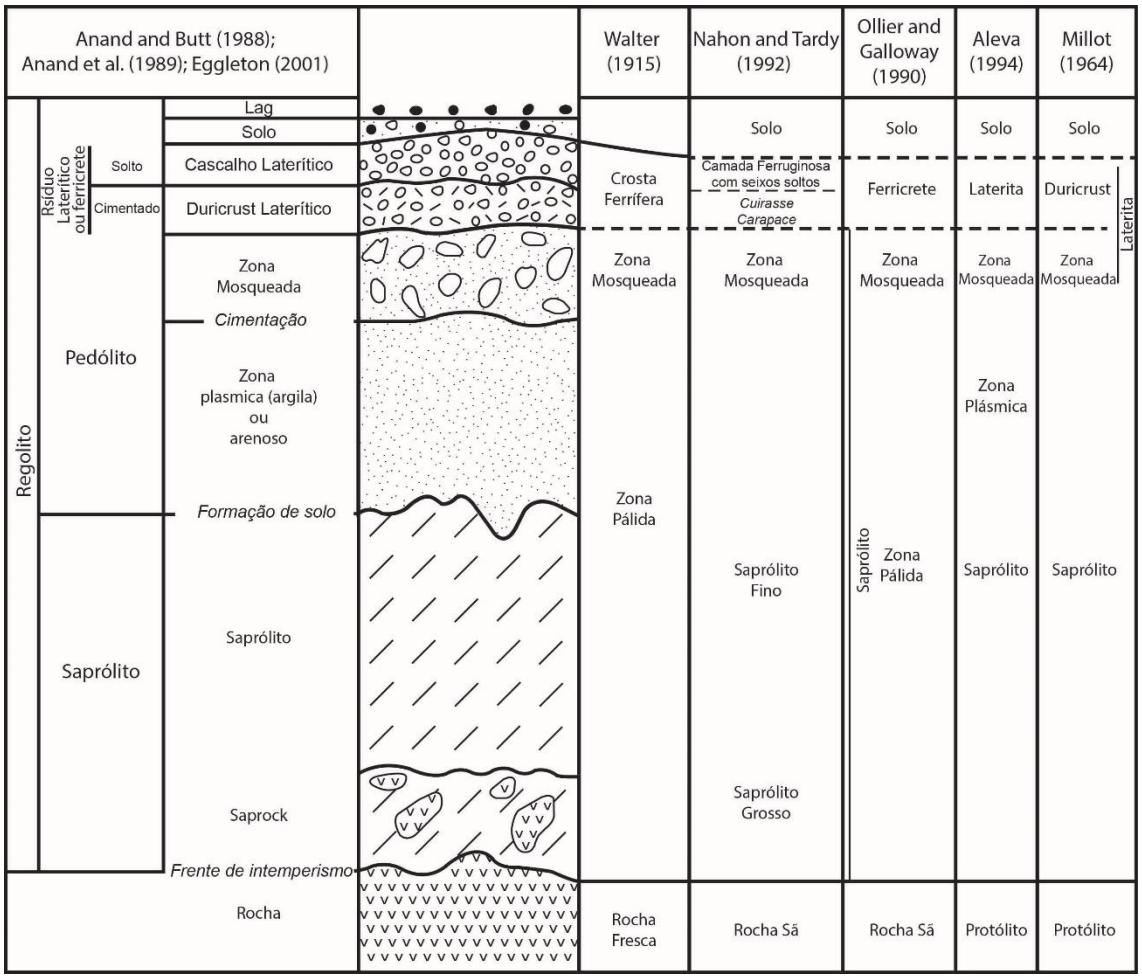

Figura 5. Nomenclatura de perfis lateríticos. (Modificado de Anand & Payne, 2002)

3.2 Típico Perfil de Intemperismo

Segundo Anand & Payne (2002), um perfil de intemperismo típico é constituído de dois grandes componentes, o saprólito e o pedólito, o saprólito está em contato com a rocha sã na base e em contato com o pedólito no topo.

O saprólito é a parte inferior do regolito, e é caracterizada por manter a estrutura da rocha original. O saprólito é dividido em dois horizontes, o *saprock* e o saprólito.

O saprock é uma rcoha compacta, pouco intemperizada com pouca porosidade, com menos de 20% dos minerais intemperisados. Os efeitos do intemperismo nesse horizonte ocorrem nas bordas dos grãos, nas fraturas e clivagens dos minerais, e afetam apenas alguns minerais. O primeiro sinal desse intemperismo aparece como a oxidação de sulfetos e silicatos portadores de Fe, e a sericitização do plagioclásio.

O *saprólito* é similar ao *saprock*, porém possui mais de 20% do minerais intemperisados, o que torna difícil diferenciar os dois sem um estudo petrográfico. O saprólito é o um produto do intemperismo isovolumétrico. Os minerais primários são pseudomorficamente substituídos por produtos do intemperismo, mantendo a estrutura e estrutura da rocha sã. Nesse horizonte a maioria dos minerais foram alterados para caolinita, goethita e hematita, somente os minerais mais resistentes ao intemperismo, como quartzo, zircão e etc. não são afetados. O saprólito pode perder a fábrica progressivamente com o aumento da argilização, aumento da cimentação por formação de sílica secundária e especialmete óxidos de Fe.

O *pedolith* é a parte superior do perfil, acima do *pedoplasmation front*, que sofreu processos de formação de solo, resultando numa perda da estrutura da rocha original e formação de uma nova estrutura, devido ao intemperismo não isovolumétrico. Os principais horizontes do pedolith são o horizonte arenoso, a zona mosqueada e o resíduo laterítico. Esses horizontes são caracterizados pela concentração de certos elementos químicos, como o Fe e o Al nos perfis ferruginosos e o Si, Ti e Zr nos silcretes.

O horizonte plasmático é o componente homogêneo do perfil de intemperismo desenvolvido sobre rochas pobres em quartzo, esse horizonte é dominado por argila e não possui estrutura de saprólito, nem a formação de estruturas secundárias, como nódulos e pisólitos. É uma zona de transição entre o saprólito e zona mosqueada, onde ocorre a perda da estrutura. A perda da estrutura ocorre principalmente pela dissolução de alguns minerais e por processos mecânicos, como a variação de tamanho dos argilominerais. Em rochas ricas em quartzo, esse horizonte corresponde a zona arenosa, que é composto de areia de quartzo angular, com uma estrutura supertada pelos grãos. A perda da estrutura, nesse caso, é causada pela dissolução e remoção de caulinita, e a compactação de minerais resistentes, predominantemente o quartzo. Esses horizontes não estão sempre presentes em perfis lateríticos.

A zona mosqueada é a parte de um perfil de intemperismo que possui segregações macroscópicas, as quais se diferem da matriz principalmente pela cor, geralmente são formadas por zonas ricas em ferro (avermelhadas) em uma matriz aluminosa/caulinitica (amarelada/acinzentada). Essas segragações são chamadas de manchas e podem ter limites angulosos ou difusos. Rochas félsicas apresentam uma zona mosqueada menos espessa, enquato rochas máficas apresentam sozas mosqueadas mais espessa, com manchas maiores.

Esse menor desenvolvimento de manchas nas rochas félsicas deve-se principalmente ao baixo conteúdo de ferro nessas rochas.

O duricrust laterítico, corresponde a o resíduo laterítico cimentado e o cascalhoso (não cimentado), esse termos são usados para descrever a parte superior do perfil ferruginoso. O duricrust laterítico pode ser utilizado como um termo geral para descrever os materiais regolíticos cimentados pelo Fe, independentemente da sua origem. O residuo laterítico é usado como termo coletivo para a zona ferruginosa superior do perfil laterítico e é composto predominantemente de óxidos e oxihidróxidos secundários de Fe (goethita, hematita, maghemita), hidróxidos de alumínio (gibbsita, boehmita) e caulinita, com ou sem quartzo. Essas parte do perfil se desenvolve essencialmente por processos residuais e, portanto, têm uma ampla relação genética e composicional com o substrato. O resíduo laterítico evolui por um colapso parcial do zona mosqueada envolvendo movimentação e a introdução e mistura de materiais exóticos através de processos de formação de solo e tranporte eólico. O uso do termo "residuo" não significa que todo o residuo seja in situ, porque se formou continuamente e foi modificado durante a intempérie. Pode ser maciço ou, mais comumente, conter várias segregações secundárias, tais como nódulos, pisólitos e oólitos, e estruturas como vazios vermiformes abertos e preenchidos. Os cascalhos lateríticos são o componente não consolidado do residuo laterítico, consistindo em segregações ferruginosas soltas (nódulos e pisolitos) e fragmentos, por convenção na faixa de tamanho de 0,25-64 mm. Os cascalhos são comumente suportados por grãos e podem ter uma matriz rica em argila ou arenosa. Os nódulos são irregulares com características reinantes, enquanto os pisolitos são elipsoidais ou esféricos. À medida que a esfericidade dos nódulos aumenta, eles se fundem com os pisolitos. Poucos solos que originalmente foram formados sobre essas lateritas são preservados.

Lag é o acúmulo residual de fragmentos grosseiros, geralmente rígidos, que se acumulam na superfície. É um resíduo que se forma a partir do desmantelamento físico e químico dos horizontes superiores do regolito e a remoção de materiais mais finos em solução, sheetwash ou ação do vento.

3.2 Mineralogia

O intemperismo é causado por entre os hidrosfera, biosfera, litosfera e atmosfera. Durante o intemperismo, a maioria dos minerais primários da rocha são destruídos. Alguns

componentes são lixiviados e alguns são retidos como minerais secundários. O produto final é uma rocha mais estável no ambiente intempérico. No produto final, todos os caminhos tendem para produzir conjuntos similares de minerais menos solúveis. A parte superior do perfil (o duricrust ferruginoso e zona mosqueada), que se desenvolveram a partir de uma variedade de rochas primárias, agora consistem em grande parte dos minerais menos solúveis (caulinita, hematita, goethita, maghemita, gibbsita, anatásio, boehmita e coríndon) e minerais mais resistentes (quartzo, zircão, cromita, moscovita e talco), um resumo dessas tranformações observadas está na figura 6.

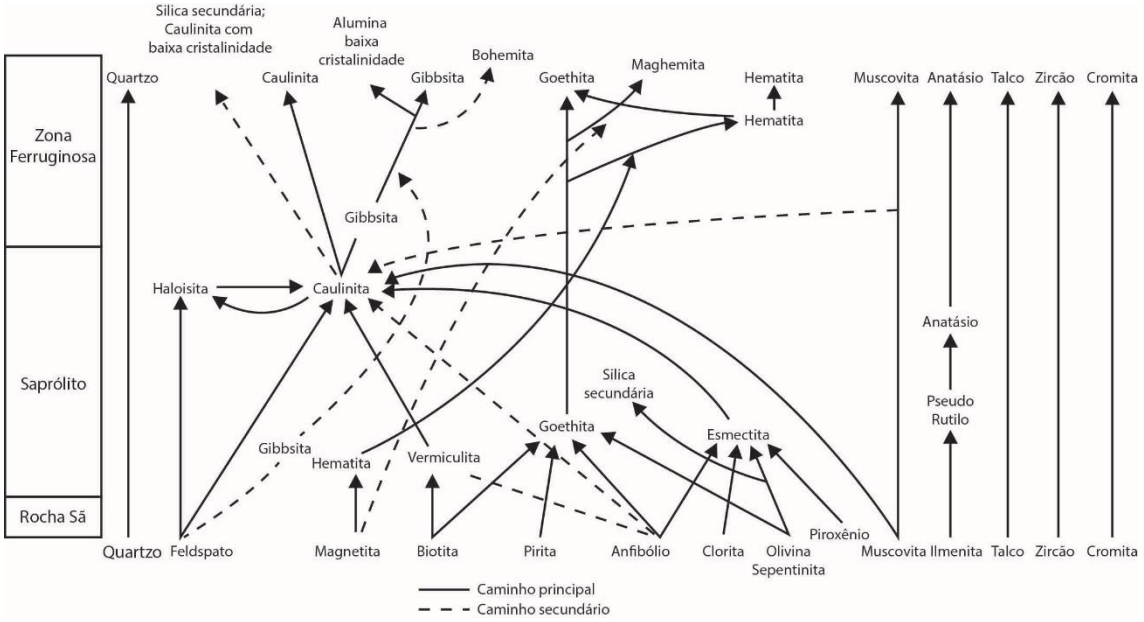

Figura 6. Caminhos para a formação de minerais secundários em perfis de intemperismo (modificado de Anand & Payne, 2002).

A dissolução dos minerais primérios pode ser congruente ou incongruente, se a dissolução for congruente o mineral secundário apresentara a mesma composição do mineral primário, se a dissolução for incongruente, ocorre a perda de alguns elementos, e o mineral secundário apresenta um composição diferente do mineral primário. Geralmente essas mudanças nos minerais primários ocorre lentamente, resultando em perfis de que há variações ne mineralogia com a profundidade. No entanto, a neoformação de várias gerações de hematita, goethite ou caulina pode ocorrer dentro de uma amostra de mão. Os principais minerais secundários que formam essas lateritas são as argilas e oxihidróxidos de Al (gibbsita e bohemita) e de Fe (hematita, goethita e maghemita).

3.2.1 Argilas (Caulinita, haloisita e esmectita)

Caulinita, halloysita e esmectita são os mais minerais comuns em saprólito. No entanto, a abundância deles varia de acordo com a rocha primária. Em rochas ultramáficas e carbonatíticas o desenvonvimeto de argilas no perfil lateritico é muito menor do que em rochas félsicas.

Esmectita é geralmente um produto de intemperismo sob ambientes secos ou mal drenados. É mais abundante na base do perfil e resulta do intemperismo de anfíbólio, olivina, piroxênio, clorita e, etc (Figura 6). Geralmente ocorre em pequenas quantidades em saprolite desenvolvido a partir de granítico rochas, e em rochas maficas, com alto teor de Fe e Al formam esmectite ferruginosa. Na parte superior do saprólito a esmectita geralmente altera-se para a caulina e goethita.

Caulinita e haloisita são os principais produtos de alteração do feldspato e, em menor grau, da muscovite (Figura 6). O feldspato pode ser inemperisado diretamente para caulinita, ou esta fase pode ser precedida por haloisita (Anand et al., 1985). Perto do topo do perfil, pode haver caulinita secundária. A proporção de haloisite geralmente diminui para o topo do perfil. Para a formação do haloisita é necessária a incorporação de água na intercamada, assim, a formação da mesma é mais comum nas partes mais úmidas e profundas do perfil laterítico (Churchman 1990, Anand & Payne, 2002).

3.2.2 Oxi hidroxidos de Al (Gibbsita)

Entre os oxihidróxidos de alumínio, a gibbsite é o principal mineral formado em perfis de intemperismo. Em um ambiente com uma drenagem mais efetiva, a caulinita é dissolvida e é precipitada a gibbsita. Gibbsita atinge concentrações máximas na zona da bauxita, diminuindo significativamente à medida que a zona bauxítica passa para saprólito. Sob fortes condições de lixiviação, os feldspatos se tranformam diretamente em gibbsita (Figura 6).

3.2.3 Oxihidróxidos de Fe (Hematita, goethita e maghemita)

A natureza dos óxidos de Fe (termo geral usado aqui para goethita, hematita e maghemita) que são formadas pelo intemperismo geralmente depende mais do ambiente condições do que do mineral primário a partir do qual o Fe foi liberado (Cornell & Schwertmann 1996). A quantidade de óxidos de ferro tendem geralmente a aumentar para o topo do perfil.

Goethite pode ocorrer em qualquer lugar do perfil, mas é especialmente comum nas partes superiores, está ausente apenas no zonas argilosas. Bandas ricas em goethita, possivelmente relacionadas a frentes redox, geralmente ocorrem em saprolite (Lawrance 1991). Em nódulos e os pisolitos, a hematita é mais comum do que a goethita. Os caminhos para formação dos diferentes óxidos de Fe são complexos. Os óxidos de ferro são os produtos do intemperismo de portadores de Fe (Figura 6). Sob condições aeróbicas e na faixa de pH normal de um ambiente intemérico, os óxidos de Fe^{3+} são muito estáveis e persistem por muito tempo. No entanto, em um ambiente anaeróbio os óxidos de Fe^{3+} podem ser reduzidos e dissolvidos por microorganismos através da transferência enzimática de elétrons da biomassa em decomposição. O Fe torna-se móvel através da redução e pode ser redistribuído em várias distâncias.

Hematita também forma-se por desidroxilação de goethita e por oxidação de magnetita (Anand & Gilkes 1984; Wells et al., 1989). Em alguns casos, hematita é um produto de intemperismo relativamente adiantado, ocorrendo seja disseminada ou segregada na base do perfil. Na parte superior do perfil, particularmente nos solos, a hematita altera-se comumente para goethite por reidratação (Tardy & Nahon, 1985).

Além da hematita, a maghemite também forma-se por desidroxilação de goethita porem em temperaturas mais altas (áreas expostas ao fogo). Em perfis de intemperismo sobre rochas ultramáficas a maghemita forma-se através da oxidação da magnetita primária (Fontes & Weed, 1991).

3.2.4 Subtituição de Fe por Al nos óxidos de Fe

A substituição de Fe por Al é comum em goethita e hematita, e afeta o tamanho da célula unitária, o tamacho da partícula e a cristalinidade (Taylor, 1987). A extensão da

substituição de Al em goethite e hematita é um indicador sensível do ambiente pedogênico da formação do óxido de Fe e depende da paragenese (Fitzpatrick & Schwertmann 1982; Schwertmann 1988).

A porcentagem de substituição de Al nas goethitas variam conforme a paragenese e o ambiente de formação. Em ambientes continentais, a substituição de Al varia de 6% a 28% de massa molar em goethites de lateritas ricas em caolinita (Davy & Gozzard 1995; Anand 1998). Isso contrasta com Al intervalos de substituição de 22-35% molar em goétias associadas com gibbsite em solos bauxíticos (Anand & Gilkes 1987). Valoresde substituições superiores a 33% não ocorrem na natureza e um limite semelhante tem sido observado em experiências de síntese de laboratório (Schwertmann, 1985). A hematita e a maghemita apresentam menos substituição por Al do que a goethite (Anand & Gilkes 1987; Singh & Gilkes 1992; Davy & Gozzard 1995)

4 RESULTADOS

4.1 Mineralogy and geochemistry of the Morro dos Seis Lagos siderite carbonatite, Amazonas, Brazil.

Artigo submetido à revista Lithos dia 19/12/2017

Acknowledgement of receipt of your submitted article

Lithos <eesserver@eesmail.elsevier.com>

Tue 12/19/2017 5:09 PM

To: artur.bastos@ufrgs.br <artur.bastos@ufrgs.br>; arturcbn@hotmail.com <arturcbn@hotmail.com>;

Re:Mineralogy and geochemistry of the Morro dos Seis Lagos siderite carbonatite, Amazonas, Brazil
by Arthur L Giovannini; Roger H Mitchell; Artur Cezar Bastos Neto, Ph.D; Candido V Moura; Luiz H Ronchi; Vitor P Pereira
Regular Article

Dear Dr. Bastos Neto,

Your submission entitled "Mineralogy and geochemistry of the Morro dos Seis Lagos siderite carbonatite, Amazonas, Brazil" has been received by Lithos

Please note that submission of an article is understood to imply that the article is original and is not being considered for publication elsewhere. Submission also implies that all authors have approved the paper for release and are in agreement with its content.

You will be able to check on the progress of your paper by logging on to https://ees.elsevier.com/lithos/ as Author.

Your manuscript will be given a reference number in due course.

Thank you for submitting your work to this journal.

Kind regards,

Lithos

LITHOS6833 - Notice of manuscript number

Lithos <eesserver@eesmail.elsevier.com>

Tue 12/19/2017 5:09 PM

To: artur.bastos@ufrgs.br <artur.bastos@ufrgs.br>; arturcbn@hotmail.com <arturcbn@hotmail.com>;

Dear Dr. Bastos Neto,

Your submission entitled "Mineralogy and geochemistry of the Morro dos Seis Lagos siderite carbonatite, Amazonas, Brazil" has been assigned the following manuscript number: LITHOS6833.

You will be able to check on the progress of your paper by logging on https://ees.elsevier.com/lithos/ as Author.

Thank you for submitting your work to this journal.

Kind regards,

Lithos

Mineralogy and geochemistry of the Morro dos Seis Lagos siderite carbonatite, Amazonas, Brazil.

Arthur L. GIOVANNINI [1], Roger H. MITCHELL [2], Artur C. BASTOS NETO [3], Candido A.V. MOURA[4], Luiz H. RONCHI [5], Vitor P. PEREIRA [3]

[1] Programa de Pós-graduação em Geociências, Instituto de Geociências, Universidade Federal do Rio Grande do Sul. Avenida Bento Gonçalves 9500, Porto Alegre, 91501-970, RS, Brasil, arthur_giovannini@hotmail.com

[2] Department of Geology, Lakehead University, 955 Oliver Road, Thunder Bay, Ontario P7B 5E1, Canada, rmitchel@lakeheadu.ca

[3] Instituto de Geociências, Universidade Federal do Rio Grande do Sul. Avenida Bento Gonçalves 9500, Porto Alegre, 91501-970, RS, Brasil. artur.bastos@ufrgs.br, vitor.pereira@ufrgs.br

[4] Departamento de Geoquímica e Petrologia, Universidade Federal do Pará, Rua Augusto Corrêa 1, Belém, PA, Brasil. candido@ufpa.br

[5] Centro de Desenvolvimento Tecnológico, Universidade Federal de Pelotas, Praça Domingos Rodrigues 2. Pelotas, RS, Brasil. lhronchi@hotmail.com

ABSTRACT

The Morro dos Seis Lagos Nb, rare earth element (REE), Ti-bearing lateritic deposit (Amazonas, Brazil) is derived from a primary siderite carbonatite. The country rock gneiss was affected by potassic fenitization, with formation of phlogopite and orthoclase together with monazite, fluorapatite and bastnäsite. At the current level of exposure the Morro dos Seis Lagos complex consists only of siderite carbonatite and silicate rocks are absent. Three types of siderite carbonatite are recognized: (1) a brecciated and oxidized core siderite carbonatite (CSC) consisting of up to 95 vol.% siderite together with: hematite; Ce-Ba-pyrochlore; Nb-brookite; Ti-maghemite; and thorobastnäsite; (2) a REE- and P-rich variety of the CSC consisting of siderite (up to 95 vol.%), hematite, minor Ce-Ba-pyrochlore, monazite and bastnäsite; (3) a border hydrothermal siderite carbonatite (BSC), with ~70 vol.% siderite, barite (~15 vol.%), gorceixite (~7 vol.%) and minor rabdophane and Pb-Ba-pyrochlore. The Ce-Ba-pyrochlore progressively weathers to Ce-pyrochlore in the lower part of the laterite profile. The observed substitution $3Ti^{4+} = Fe^{2+} + 2Nb^{5}$ recognized in Nb-rich brookite explains the enrichment in Nb in the CSC and indicates formation in a reducing environment. Magmatic two phase fluid inclusions occur in siderites from the CSC and REE-rich CSC. Low-temperature hydrothermal fluid inclusions occur in siderites from all carbonatites. The CSC and the REE-rich CSC are related to a late-magmatic-to-hydrothermal process; whereas the BSC is considered as a carbo-hydrothermal stage. The siderite carbonatites exhibit a wide variation of $\delta^{13}C$ (-5.39‰ to -1.40‰), accompanied by a significant variation in $\delta^{18}O$ (17.13‰ to 31.33‰), especially conspicuous in the REE-rich CSC, and related to the high concentrations of both H_2O and CO_2 in the magma. The CSC

is the richest in (48.64 – 70.85 wt.% Fe_2O_3) and the poorest in Ca (up 0.82 wt.% CaO) example of a siderite carbonatite yet recognized, and has high contents of Mn, Ba, Th, Pb and LREE, and a very high Nb (up to 7,667 ppm) content. The high Nb/Ta ratio (1408 - 11459) is compatible with residual liquids derived by fractional crystallization. The $^{87}Sr/^{86}Sr$ and $^{144}Nd/^{143}Nd$ isotopic data suggest the carbonatite has a mantle origin with essentially no crustal contamination and is younger than the maximum age of the carbonatite of 1328 ± 58 Ma previously proposed. We suggest that the Morro dos Seis Lagos Carbonatite Complex represents the upper-most parts of a differentiated carbonatite magmatic system, and that the siderite carbonatite is related to a late-magmatic-to- carbo-hydrothermal processes.

Key Words: carbonatite, ferrocarbonatite, siderite, niobium, Morro dos Seis Lagos, Brazil

1. INTRODUCTION

Carbonatites are igneous rocks which in the IUGS modal nomenclature scheme contain over 50 vol.% of primary carbonate and less than 20 wt.% SiO_2 (Le Maitre 2002) Recognizing the failure of the IUGS system to contend with the observation that carbonatites are usually members of a consanguineous suite of alkaline rocks and carbonatites, Mitchell (2005) using a mineralogical-genetic classification scheme, proposed that carbonatites are igneous rocks which contain more than 35 vol.% primary carbonate regardless of silica content. In either scheme carbonatites can be named on the basis of modal mineralogy or bulk composition (Woolley and Kempe, 1989). Thus, in modal nomenclature it is possible to recognize calcite, dolomite and siderite carbonatites. The corresponding compositional names are calciocarbonatite, magnesiocarbonatite and ferrocarbonatite. Note that the modal name might not correspond exactly with the compositional name. Most carbonatites are found in plutonic-to-subvolcanic alkaline rock-carbonatites complexes and effusive equivalents are exceedingly rare. The volcano Oldoinyo Lengai (Tanzania) which erupts natrocarbonatites is unique and cannot be used a model system for the genesis of plutonic carbonatites. Carbonatites can contain minerals of economic interest such as: pyrochlore (Nb); barite (Ba); rutile (Ti); zircon (Zr); magnetite (Fe); apatite (P, rare earth elements); monazite and bastnaesite (rare earth elements) (Pell, 1996, Mitchell, 2015, Chakhmouradian and Zaitsev 2012, Mariano and Mariano 2012).

The terminology of the Ca-Mg-Fe carbonates found in ferrocarbonatites is complex, and on the basis of composition, the major varieties recognized are:

Dolomite: $CaMg(CO_3)_2$ with < 2.0 wt% FeO_T

Ferrodolomite (*or ferroan dolomite*): $Ca(Mg,Fe)(CO_3)_2$ - $Ca(Fe,Mg)(CO_3)_2$ solid solutions with 2- 14 wt% FeO_T

Magnesian siderite or "breunnerite": $(Fe,Mg,Mn)(CO_3)_2$ with 30 -40 wt% FeO_T

Siderite: $(Fe,Mg,Mn)(CO_3)_2$ with 40-50 wt% FeO_T

Note that ferrodolomite can also be termed "ankerite". The original definition of ankerite [$Ca(Mg,Fe)(CO_3)_2$ with > 10 % $FeCO_3$; Luboldt ,1857] is an imprecisely-defined term which was "grandfathered" as a mineral name by the IMA-CNMNC as $Ca(Fe,Mg)(CO_3)_2$ with Fe>Mg. Given that most "ankerites" are actually ferrodolomite (Mg>Fe) and that these minerals are members of a continuous solid solution series between dolomite and 70 mol.% ferrodolomite (Davidson et al. 1993; Goldsmith et al. 1962), we prefer to use the name ferrodolomite for all *Ca-rich*, Mg and Fe bearing carbonates rather than ankerite. Breunnerite is not an IMA valid mineral name but has been used for Ca-poor members of the magnesite-siderite solid solution series.

Ferrocarbonatites are relatively uncommon and typically consist of ferrodolomite and magnesian siderite and more rarely of siderite. Examples include: Buru; Chilwa; Kugwe and Swartbooisdrif complexes (Africa) (Gittins and Harmer 1997; Thompson et al. 2002); Sallanlatvi, Finland (Zaitsev et al. 2004); Gifford Creek, Australia (Pirajno et al., 2014); Chipman Lake, Canada (Buckley and Woolley, 1990), the Fen complex, Norway (Anderson 1986); and the Ashram Zone of the Eldor Complex, Canada (Mitchell and Smith

2017). These ferrodolomite and siderite-carbonate rocks mainly occur as minor components of carbonatite complexes dominated by calcite and/or dolomite carbonatites. The Sallanlatvi Complex (Zaitsev et al. 2004) is one with large bodies of siderite carbonatite (two main bodies about 500m x 100m in size in the central part of the complex). These carbonatites are mineralized with pyrochlore, but have no associated laterites At the Ashram Zone of the Eldor complex (Gagnon et al., 2015) REE mineralization, extends approximately 700 metres along strike, is over 500 metres across and reaches depths exceeding 600 metres assigns a cut-off grade of 1.25% TREO, for 1.59 Mt averaging 1.77% TREO of measured resources, 27.67 Mt averaging 1.90% TREO of indicated resources, and 219.8Mt averaging 1.88 % TREO of inferred resources. In contrast to Seis Lagos and Sallanlatvi, pyrochlore is extremely rare and the main ore mineral is monazite (Mitchell and Smith, 2017)

Ferrocarbonatites are commonly considered as the low-temperature products of fractional crystallization of Ca-Mg "carbonate melts", although Thompson et al. (2002) propose that they form from carbo-hydrothermal fluids. The only magmatic ferrocarbonatite, in terms of C-O ratios, is that from Swartbooisdrif (Thompson et al. 2002). Other ferrocarbonatites such as Buru, Chilwa and Kugwe have C-O isotopic ratios indicating interaction with carbothermal systems (Simonetti and Bell 1994 and Onwonga et al. 1997dro). In reality, there is undoubtedly a continuum from magmatic through carbo-hydrothermal to hydrothermal stages in the differentiation of carbonatite-bearing magmatic systems. Carbo-hydrothermal fluids typically concentrate the rare-earth elements (REE), Sr, Ba, etc. and not Nb. In contrast intrusive carbonatites, and especially those associated with rocks of the melilitite clan, are typically important sources of Nb, Ti and P, but not the REE (Mitchell, 2005).

In this work we focus on the siderite carbonatite from the Morro dos Seis Lagos (Six Lakes Hill) carbonatite body, the lateritization of which formed the Morro dos Seis Lagos Nb (Ti, REE) deposit. This deposit stands out among the nineteen key examples of Nb deposits associated with carbonatites selected by Chakhmouradian et al. (2015) as being the world's largest Nb deposit (2897.9 Mt at 2.81 wt% Nb_2O_5, Justo and Souza, 1986) and for being the only one associated with siderite carbonatite. To our knowledge, the Morro dos Seis Lagos deposit is the only case of a world-class deposit, regardless of the type of metal, associated with siderite carbonatite. No work has been published on the siderite carbonatite to the present day, with the exception of some petrographic and geochemical data included in Giovannini et al. (2017) to provide broad overview of the mineralization. In the present investigation we present petrographic, mineralogical, fluid inclusion and isotopic (Sm-Nd, Rb-Sr, C and O) data.

2. PREVIOUS STUDIES

2.1 Geological setting

The Seis Lagos Carbonatite Complex (Issler and Silva, 1980) consists of three circular bodies discovered in the 1970's by the RADAM Project (Pinheiro et al., 1976). The carbonatite complex is located in the SW part of the Guyana Shield (Fig. 1A). In the model by Santos et al. (2006), the complex is located approximately at the boundary between the Rio Negro Province and the K'Kmudku Belt (Fig. 1A), which is an intracontinental shear zone related to Sunsás collisions along the margin of the Amazon Craton. This event generated mylonitization and magmatism between 1.49 and 1.14 Ga (Santos et al. 2000,

2009, Almeida et al. 2013, Souza et al. 2015). The carbonatite complex is in the Tarsira lithofacies (Fig. 1B), which is composed of monzogranite augen gneiss and granitoids with ages of 1810 to 1790 Ma (CPRM, 2006).

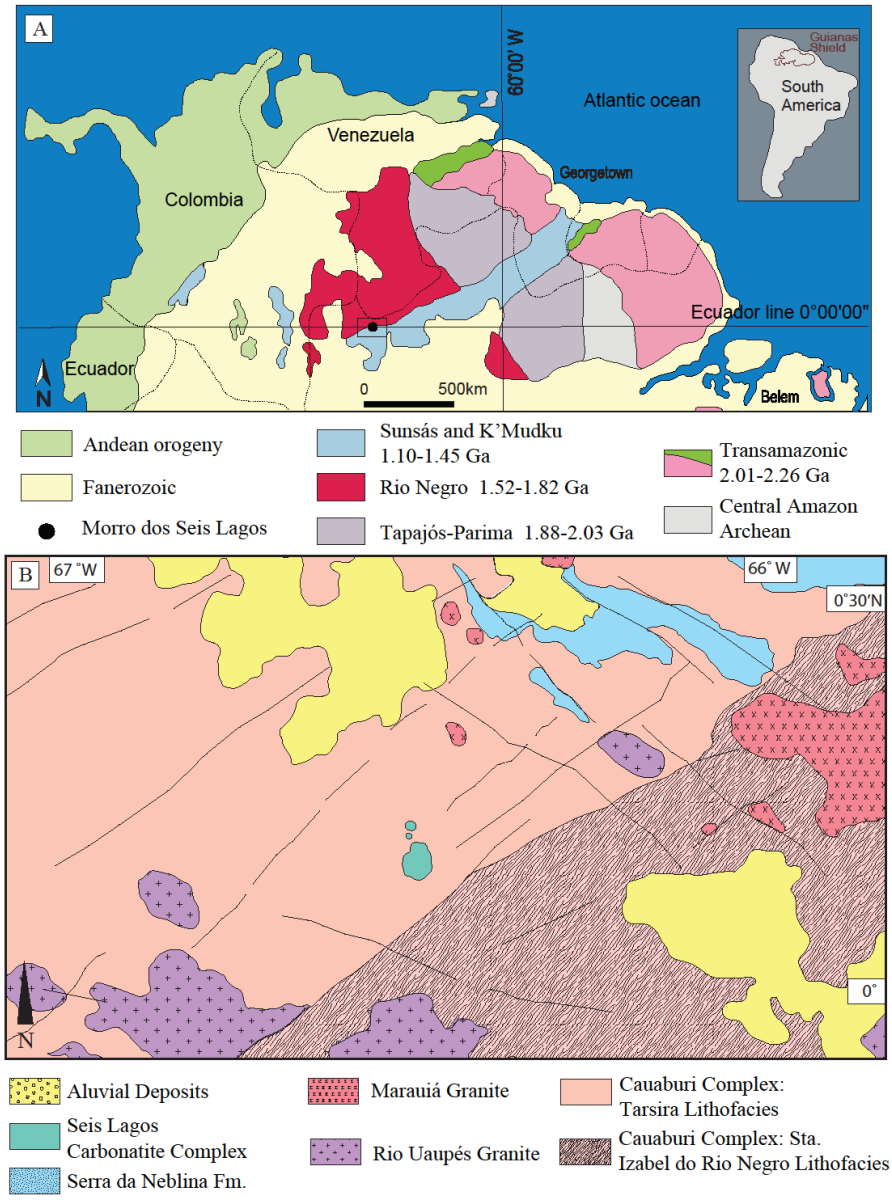

Fig. 1. (A) Geological provinces of the Guyana Shield (modified from Santos et al. 2006a). (B) Geological map of the area of the Seis Lagos Carbonatite Complex (modified from CPRM 2006).

CPRM (2006) related the complex emplacement to the Mesozoic reactivation of the K'Mudku Belt structures by the evolution of the Brazilian Equatorial Continental. However, other carbonatites in the southern part of the Guyana Shield, such as Maicurú (586 ± 18 Ma; Lemos and Gaspar 1998) and Mutum (1.0 Ga; Gomes et al. 1990), have ages that preclude being related to the continental margin. Rossoni et al. (2017) obtained 3 groups of U-Pb ages in zircons from carbonatite samples: inherited zircons with ages compatible with the gneissic host rock (~1820 Ma); with upper intercept ages of 1525 ± 21 Ma; and age 1328 ± 58 Ma (MSWD= 1.4; Th/U from 1.52 to 0.14). Mineralogical study indicates that the ~1.3 Ga zircons might have affinities with carbonatite, although this is not proven. The available data indicate the age of 1328 ± 58 Ma represents the maximum age of the carbonatite. According to Rossoni et al. (2016) the carbonatite emplacement was controlled by E-W structure, and the relief on the hill is controlled by NNE-SSW, NNW-SSE and E-W structures. All the lakes and a number of karstic depressions filled by clays are associated with these structures.

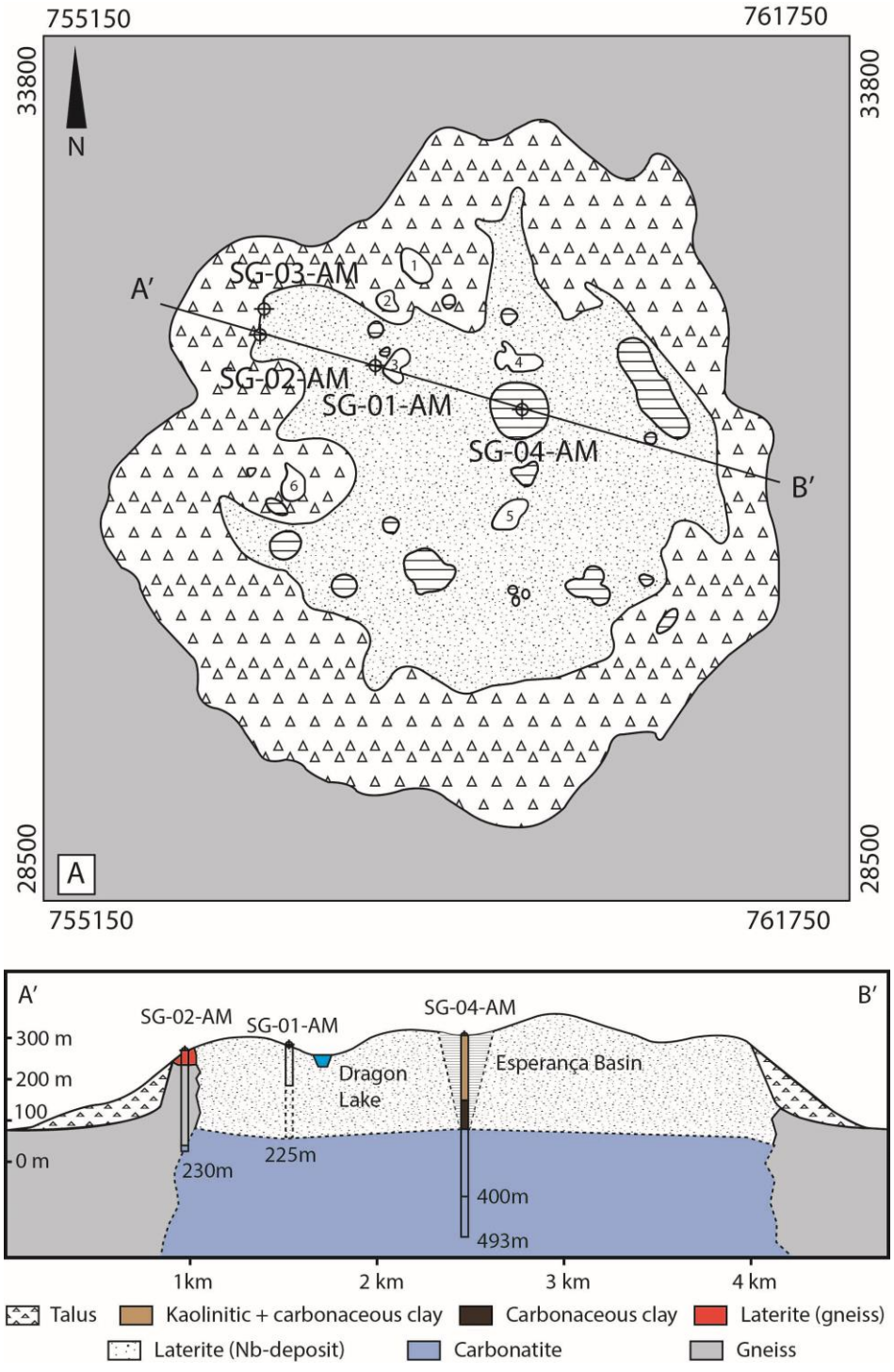

Fig. 2. Geological map (modified from Viegas and Bonow, 1976) and vertical section of the Morro dos Seis Lagos carbonatite body and associated Nb-deposit.

2.2 The Morro dos Seis Lagos Deposit

The Companhia de Pesquisa de Recursos Minerais (CPRM), who remains the holder of the mineral rights, conducted an exploration program (Viegas and Bonow, 1976) that included the drilling of 4 boreholes (Fig. 2A) in the major circular body - the Morro dos Seis Lagos (Six Lakes Hill). In 1982, CPRM drilled 4 additional boreholes in order to define the Nb resources (2897.9 Mt at 2.81% Nb_2O_5, Justo and Souza, 1986). Correa (1996) and Correa and Costa (1997) conducted detailed studies using surface samples and core pulps from drill cores obtained during the first CPRM campaign. Since then, no other study has been conducted until the recent investigations of Giovannini (2013) and Giovannini et al. (2017).

The primary carbonatite rock was intersected in only two drill holes and was classified by Viegas and Bonow (1976) as beforsite in SG-02-AM and as carbonatic breccia in SG-04-AM. Issler and Silva (1980) recognized this breccia as carbonatite and introduced the term Seis Lagos Carbonatite Complex.

The lateritic profile may be more than 200m in thickness according to information obtained from drill hole SG-01-AM. However, detailed description of this drill hole was possible only down to 100m due to poor core recovery below this depth. Six textural and compositional types of laterites were identified (from the top to the botton): (i) pisolitic laterite; (ii) fragmented laterite; (iii) mottled laterite; (iv) purple laterite; (v) manganiferous laterite; and (vi) brown laterite. All these types consist principally of goethite and hematite. Goethite predominates in the upper types (i to iii), which result from physical and chemical reworking near the surface, and in the brown laterite, whereas hematite predominates in the

purple laterites. In the manganiferous laterite (10m thick), manganese oxides (mainly hollandite, with associated cerianite) occur as veins or irregular masses formed in a late event during the development of the lateritic profile. The main Nb ore mineral is Nb-rich rutile (with 10.5 - 26.86 wt% Nb_2O_5), which occurs in all laterites, formed together with Nb-bearing goethite and secondary Ce-pyrochlore, probably derived from former pyrochlore. Minor Nb-rich brookite, formed from Nb-rich rutile, occurs as broken spherules with an oolitic structure. The laterites have average Nb_2O_5 concentrations of 2.91 wt% (Giovannini et al. 2017).

3. MATERIALS AND METHODS

This work is mainly based on the study of drill cores form boreholes SG-01-AM, SG-02-AM, SG-03-AM, and SG-04-AM (Fig. 2) which were completely re-logged and sampled in May 2011. The cores of the additional 4 boreholes drilled by CPRM in 1982 were also inspected but unfortunately these bore holes only transected laterite.

X-ray diffraction (XRD) work was performed at the Universidade Federal do Rio Grande do Sul (UFRGS) using a Siemens D-5000 diffractometer, equipped with Cu-Kα radiation and a Ni filter in the range from 2° to 70° 2θ with a velocity of 0.02º 2θ per second. X-ray data were processed with "MATCH! Phase identification from powder diffraction" developed by Cristal Impact, and compared to the Crystallography Open Database (COD) database. Semi-quantitative analysis of the XRD data was also performed by MATCH! on the basis based of peak height, and the results are considered relative

amounts. Energy-dispersive X-ray spectrometry (EDS) analyses were performed at the UFRGS using a JEOL-JSM5800 scanning electron microscope (SEM) with a voltage of 20 kV, 10nA, and a spot size of 5 μm.

Electron microprobe wavelength dispersive analyses were first performed at the CNRS/Universitéd'Orléans ISTO Laboratory (Orléans, France) using a Cameca SX50 instrument. The majority of the study was performed at the Universidade de Brasília using a GEOL JXA-8230 instrument. The concentrations of P, Si, Ca, Na, K, Ba, Sr, Al, Fe, Mn, Ti, and F were determined with an accelerating voltage of 15 kV and a beam current of 10 nA. The concentrations of Nb, Ta, W, REE, Y, U, Th, and Pb were determined with an accelerating voltage of 20 kV and a beam current of 20 nA and a spot size of 1 μm, for siderite only was used a spot size of 5 μm.

Whole rock geochemical analyses were performed at Analytical Laboratories Ltda (Canada). Major oxides (SiO_2, Al_2O_3, Fe_2O_3, MgO, CaO, Na_2O, K_2O, TiO_2, P_2O_5, MnO, Cr_2O_3) and trace elements (Ba, Be, Co, Cs, Ga, Hf, Nb, Ni, Rb, Sc, Sn, Sr, Ta, Th, U, V, W, Zr, plus 14 REE and Y) were analysed by ICP-MS after fusion and nitric acid digestion of 0.2g aliquots. Another set of trace elements (Ag, As, Au, Bi, Cd, Cu, Hg, Mo, Ni, Pb, Sb, Se, Tl, Zn) were analysed by ICP-MS after Aqua Regia digestion of 0.5 g aliquotes. Loss on ignition was obtained by weight difference after ignition at 1000^{o} C. A Leco furnace was used to measure total C and S.

Raman spectra in fluid inclusions were obtained using a Jobin Yvon/Horiba LABRAM-HR 800 spectrograph equipped with a He-Ne laser (632.8nm) at the INPE (São Paulo). The Raman signal was collected by an Olympus BX -41 microscope provided with objective magnifications of 10x, 50x and 100x. The detector used was a liquid N_2 cooled, back illuminated Spectrum One CCD. Depending on the sample, the acquisition time

ranged from 10 to 60s and the laser power from 0.08 to 8mW. To reduce signal/noise ratio, spectra were acquired in 5 to 10 accumulations. Collected Raman spectra were analyzed and optimized with Labspec 5. Spectra collected were averaged; the background was corrected and if necessary, normalized and peak deconvoluted. Data interpretation used Frezzotti et al. (2012) data as the main reference. Microthermometric runs were made using a Linkam THMSG600 Temperature Controlled Geology Stage. The Linkan stage temperature range is from a maximum of 600°C and to a minimum of -196 °C. The Linksys32 System control software and digital video capture was added to the precise temperature control from PC. Fluid inclusion studies were also performed with a Chaix Meca heating-freezing stage, calibrated at CO_2 and H_2O triple points and Merck standards (135°, 200°, 306° and 398°C). The estimated precision of the measurements is near 0.2°C and the accuracy is ±0.5°C up to 135°C, and up to 12°C at 398°C.

C and O isotopes analysis was conducted at the LABISE of the Universidade Federal de Pernambuco using SIRA II a mass spectrometer. Fe oxides in siderite samples were removed by Franz magnetic separator at 0,4 A. The siderite samples then were ground to 100 mesh. The O^{18}/O^{16} and C^{13}/C^{12} data are given in the usual permil deviation relative to the standard sample. The $\delta^{13}C$ samples were standarized to Vienne-Pee Dee Belemnite (PDB) and the $\delta^{18}O$ were standarized to Vienna-Standard Mean Ocean Water (SMOW).

Sm-Nd and Rb-Sr isotopic analysis were performed at the Isotope Geology Laboratory of the Universidade Federal do Pará. Powdered samples were spiked for Rb, Sr, Sm and Nd, dissolved with HF-HNO_3 in sealed teflon beakers, and then re-disolved with HCl (6N). Rare Earth Elements (REE), Rb and Sr were separated by cation exchange chromatography using Biorad Dowex AG-50W-X8 resin, and Sm and Nd were removed from the REE using Ln Resin SPS (50-100µm) Eichrom®. Isotopic compositions of Rb

and Sr were determined using a MAT 262 thermal ionization mass spectrometer (TIMS), while Sm and Nd isotopic compositions were obtained with a Triton Plus TIMS, both from ThermoFisher Scientific Instruments. The $^{87}Sr/^{86}Sr$ ratio of NBS987 and the $^{143}Nd/^{144}Nd$ ratio of the La Jolla standard determined during this study were 0.7102473±0.000004 and 0.511839±0.000005, respectively. Total procedural blank levels were less than 300 pg for Sr and 150 pg for Nd. The $^{143}Nd/^{144}N$ ratio was normalized to 0.7129 for the $^{146}Nd/^{144}Nd$ ratio. Neodimium isotope variations are expressed in the εNd notation (De Paolo and Wasserburg, 1976), using a present-day value of CHUR for $^{143}Nd/^{144}Nd$ = 0.512638 (Jacobsen and Wasserburg, 1979).

4. RESULTS

The re-logging and reinterpretation of the 4 boreholes of the first CPRM campaign resulted in geological profile (Fig. 2B) quite different from that presented by Justo e Souza 1986). Borehole SG-01-AM located over the Nb-mineralized laterite is described in detail in Giovannini et al. (2017). Borehole SG-02-AM intersected non-mineralized laterite (formed from gneiss) (0 – 34.00 m), fenitized gneiss (34.00 - 222.60 m), and border siderite carbonatite (BSC) (221.60 – 227.70 m); the 227.70 – 230.85 m interval was not recovered. Borehole SG-03-AM intersected non-mineralized laterite (0 – 9.00 m), saprolitized gneiss (9.00 – 50.00 m), and fresh gneiss (50.00 – 110.00 m). Borehole SG-04-AM (Fig. 2), located in the Esperança Basin, intersected: (0 to 233.65 m) sedimentary package; (233.65

to 288.00 m) core siderite carbonatite (CSC); (288.00 to 340 m) REE- rich CSC; (340.00 to 492.00 m) CSC.

4.1 Petrography and Scanning Electron Microscopy

4.1.1 Host rock fenitization

The host rock in borehole SG-03-AM is a biotite-hornblende gneiss with quartz-feldspathic bands interspersed with bands of mafic minerals, with fractures filled by iron oxides and clay minerals. Plagioclase is the most abundant mineral, subhedral- to- anhedral, in habit and sericitized. The K-feldspar is anhedral, fractured and contains argillitic alteration. The quartz exhibits wide variations in particle size and shape and always has undulous extinction. The chloritized biotite and hornblende are associated with, and commonly contain, apatite inclusions. Leucoxene, zircon and opaque minerals occur as accessories.

In the SG-02-AM bore hole, the gneiss is affected by fenitization, which increases in depth, closer to the carbonatite body, transforming the gneiss into pseudo-syenite. In the more distal parts the development of phlogopite with iron oxides inclusions occurs (Fig. 3A). Neoformation of K-feldspar occurs closer to the carbonatite. Most K-feldspar crystals were subsequently partially (Fig. 3B) or totally (Fig. 3C) kaolinitized and cut by numerous veins of Fe-oxides (Fig. 3B). Some of these kaolinitized K-feldspars have monazite (Fig. 3C)

inclusions, both as isolated crystals and alignments and, more rarely, inclusions of fluorapatite and bastnäesite. Monazite also occurs in veins associated with iron oxides (Fig. 3E). Fluorite (Fig. 3D) is very common and occurs mainly associated with aggregates of kaolinite and illite (Fig. 3D, E), which appear texturally to have been formed from micas. Barite occurs in veins (Fig. 3D, F), which can be very abundant and cut through the rock; the barite from these veins commonly has inclusions of Fe oxides (Fig. 3F) and more rarely forms intergrowth with sphalerite.

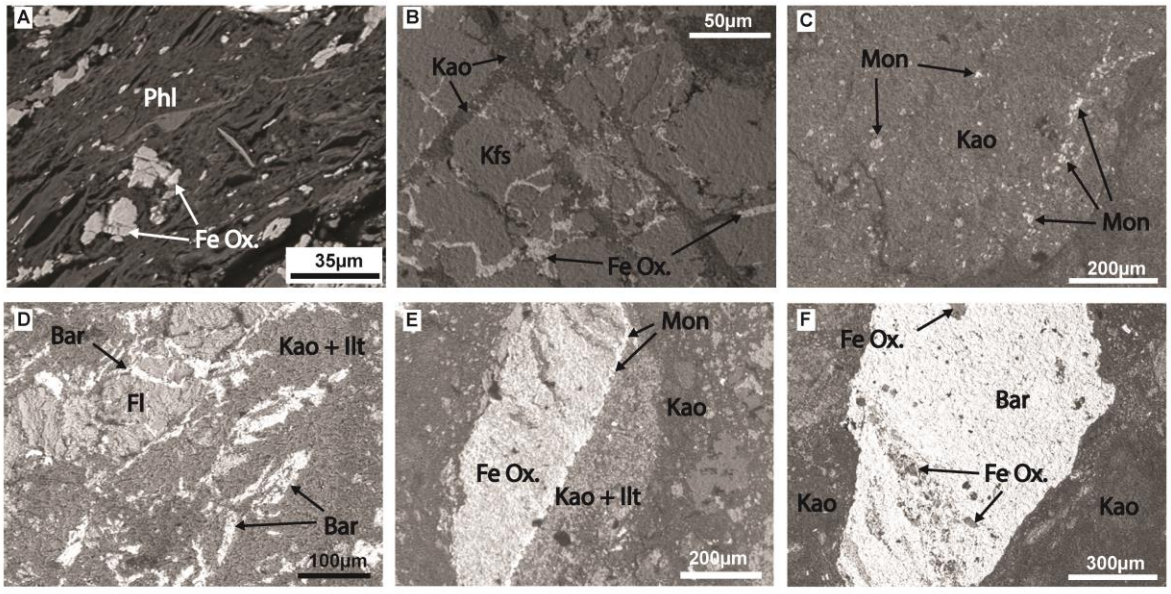

Fig. 3. Back-scattered electron images of fenites from the host rock of the Morro dos Seis Lagos carbonatite body. (A) Phogopite with inclusions of iron oxides. (B) K-feldspar with zones of kaolinization, cut by iron oxides veins. (C) K-feldspar completely kaolinitzed with monazite inclusions. (D) Fluorite and agglomerates of kaolinite and illite, both cut by barite veins. (E) Iron oxide vein with monazite in the edge, in the contact with agglomerate of kaolinite and illite (mica alteration). (F) Barite vein with iron oxide inclusions. Phl= phlogopite; Fe Ox= Fe oxide; Kao= kaolinite; Kfs= K-feldspar; Mon= monazite; Fl= fluorite; Bar= barite; Ilt= illite.

348 4.1.2 Border siderite carbonatite (BSC)

349

350

351 The siderite carbonatite in borehole SG-02-AM is light grey and highly friable,
352 possibly due to weathering because, regardless of the depth, the samples originate from a
353 level close to the base of the laterite (Fig. 2B). This rock is composed mainly of siderite,
354 barite, and gorceixite, with minor rhabdophane-(Ce) and pyrochlore.

355 Siderite (~70 vol.%) is the only carbonate identified. The crystals are euhedral, have
356 brownish color (Fig. 4A, B), average size of 700 µm and feature the typical rhombohedral
357 cleavage of carbonates. Some crystals are broken and have hematite at the edges and in
358 fractures (Fig. 4A, B). Some crystals exhibiting corrosional features are highlighted in
359 backscattered electron images in Fig. 6C.

360 Barite (~15 vol.%) occurs as aggregates of very fine grained crystals (up to 150
361 µm) that fill the interstices of siderite crystals, or in veins that cross-cut siderite. (Fig. 4A,
362 B, D, E). BSE images reveal that barite corrodes siderite crystals (Fig. 4C).

363 Gorceixite, a barium and aluminum phosphate of the crandalite group usually has
364 been formed by the alteration of primary phosphates. Gorceixite constitute up to 7.5 vol.%
365 of the rock. It occurs as the predominant mineral in aggregates (Fig. 4A, B) with
366 rhabdophane-(Ce) and pyrochlore. Gorceixite crystals are euhedral with size up to 5 µm
367 (Fig. 4F).

368 Rhabdophane-(Ce) is the only REE mineral in the border siderite carbonatite. It
369 constitutes up to 1 vol.% and occurs mainly as small crystals fibrorradiated with up to 5
370 µm. More rarely, rhabdophane-(Ce) fills gaps between siderite crystals (Fig. 4G). BSE
371 images reveal that this rhabdophane-(Ce) is actually aggregates of very small crystals (Fig

4E, H). Pyrochlore occurs as euhedral crystals with ~3 μm in the aggregates with rhabdophane-(Ce) and gorceixite.

4.1.3 Core siderite carbonatite (CSC)

All the carbonatite samples from the core drill SG-04-AM are classified as siderite carbonatite. In the zones preserved from weathering, the texture is similar to that illustrated in Figure 5A. In the most- altered zones, the crystals of siderite are partially dissolved, hematite is much more abundant and the texture resembles that of a breccia (Fig. 5B). Siderite probably composed at least 95 vol.% of the rock. Siderite crystals (where not partially- dissolved) are euhedral, brownish, with sizes up to 500 μm, display the typical rhombohedral cleavage of carbonates, and commonly contain trails of fluid inclusions (Fig. 5C). Optically, there are three types of siderite (Fig. 5D): a clear siderite (Sid. 1); a darker siderite (Sid. 2) that seems to replace the former; and an iron-oxide- rich siderite (Sid. 3). The siderite crystals are altered to hematite at their edges or along fractures. The hematite at the margins of the siderite crystals has the same texture as the small hematite crystals in the rock matrix (Fig. 5F). These latter hematite crystals contain relicts of siderite (Fig. 5F), which indicate that the growth of the matrix hematite occurred simultaneously with alteration at the edges of the large siderite crystals.

Petrographically, the only difference between the ordinary CSC and the REE-rich CSC is the presence of the REE minerals. The latter are mainly monazite and bastnäsite. Thorobastnäsite, pyrochlore, monazite, and bastnäsite were observed only in BSE-images.

Thorobastnäsite occurs as aggregations of acicular crystals filling interstices between matrix hematite crystals (Fig. 5D). Pyrochlore occurs as euhedral crystals (~5 μm) (Fig. 5E), more commonly zoned (Fig. 6A). Monazite occurs as aggregates (100 μm) consisting of 5 μm acicular crystals (Fig. 5F). Bastnäsite occurs as rare single small (<5 μm) crystals in the matrix. Gibbsite commonly occurs as veinlets that transect siderite and hematite crystals (Fig 5E). Quartz and gypsum were detected only by XRD in few samples.

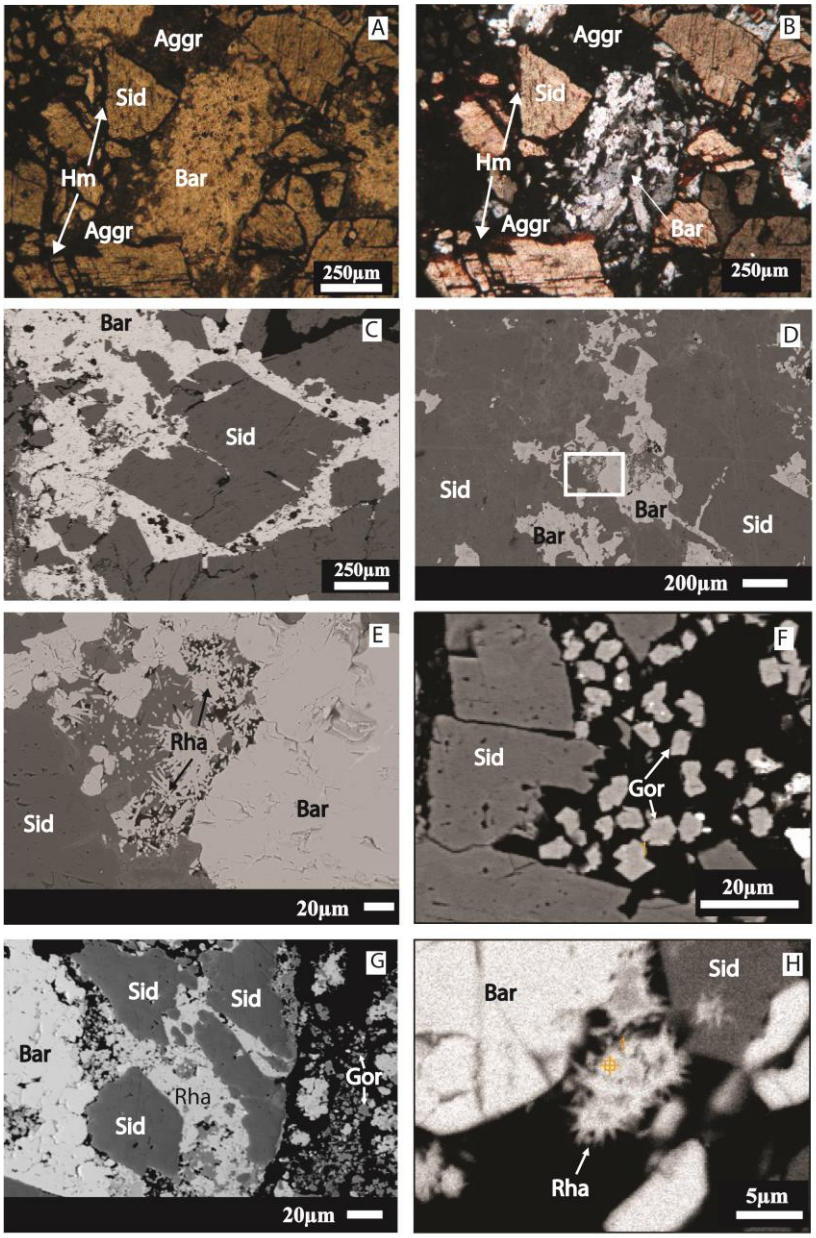

408

409 Fig. 4. Microscopic features of the border siderite carbonatite of the Morro dos Seis Lagos carbonatite body.
410 (A) Siderite with ferruginous rims, barite filling interstices between siderite crystals, and aggregates of
411 monazite, gorceixite and pyrochlore (non individualized at this scale), natural light. (B) Same as A, cross
412 polarized light. (C) Contact relations between siderite (gray) and barite (white): strait contact, corrosion
413 features and barite veins in siderite (BSE image). (D) Barite (white) filling residual spaces and fractures in
414 siderite (BES image). (E) Zoom of rectangle in D: rhabdophane in the interface between siderite and barite.
415 (F) Detail of aggregates as in A: gorceixite euhedral crystals. (G) rhabdophane-(Ce) mass filling gaps between
416 siderite crystals. (H) Fibrorradiated rhabdophane-(Ce) crystals. Sid= siderite; Aggr.= aggergates; Bar= barite;
417 Rha= rhabdophane; Gor= gorceixite.

418

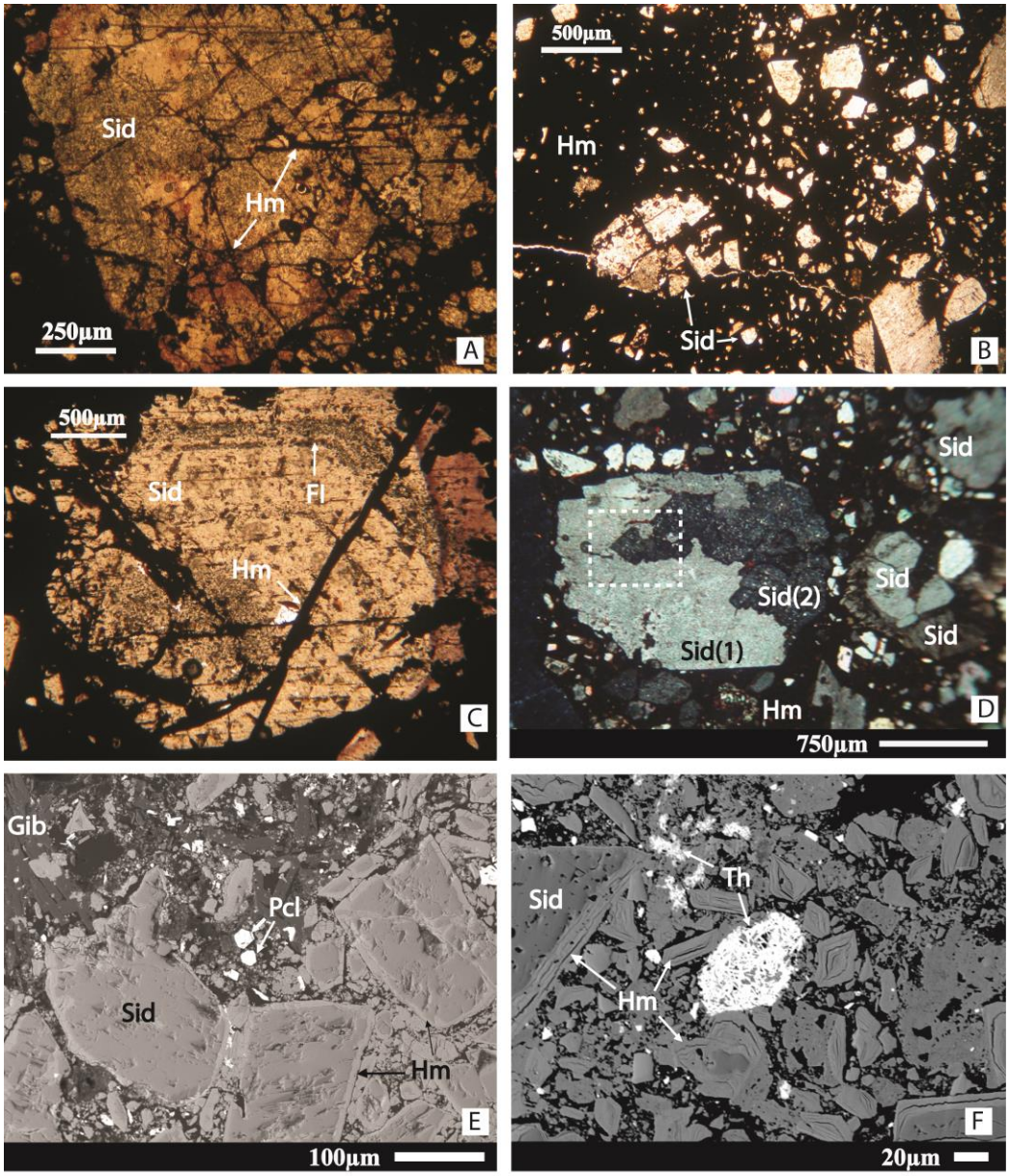

Fig. 5. Petrographic features of the core siderite carbonatite from Morro dos Seis Lagos. (A) Siderite crystals with hematitized rims and fractures filled by hematite, plane polarized light. (B) Carbonatic breccia formed by fractured siderite crystals in a hematitic matrix, plane polarized ligth. (C) Zoned siderite crystal, with trails of fluid inclusions, plane polarized ligth. (D) Siderite crystal (Sid 1) been replaced by siderite (Sid 2); Sid 3 is a third siderite generation associated with Fe oxides. (E) Euhedral pyrochlore crystals among siderite crystals with hematitized edges; gibbsite vein (BSE-image). (F) Agglomerate of acicular crystals of thorobastnäsite in a hematite matrix (BSE- image). Sid= siderite; Hm= hematite; FI= fluid inclusion; Pcl= pyrochlore; Gib= gibbsite; Th= thorobastnasite.

Titanomaghemite occurs as aggregates of small acicular crystals (up to 50 μm; commonly ~10-20 μm) that occur as coatings on or replace a primary cubic mineral; probably titanomagnetite (Fig. 6B,C). The titanomaghemite crystals are euhedral, have dimensions of up to 400 mm (commonly ~100 mm). They occur as isolated crystals or form aggregates with dimensions up to 1500 μm of ~10 crystals. Titanomaghmite is also observed as inclusions in siderite (Fig. 6C). Zonation of titanomagnetite is retained in the titanomaghemite (Fig. 6B, C). The growth of titanomaghemite crystals commonly exceeds the sizes of the primary mineral (Fig. 6C).

Nb-rich brookite was observed in just a few samples, as broken and more commonly fractured crystals which range in size from 100 μm to 3 mm (Fig. 6D). In contrast to Nb-rich brookite occurring in the laterite, the Nb-brookite in the siderite carbonatite is not zoned.

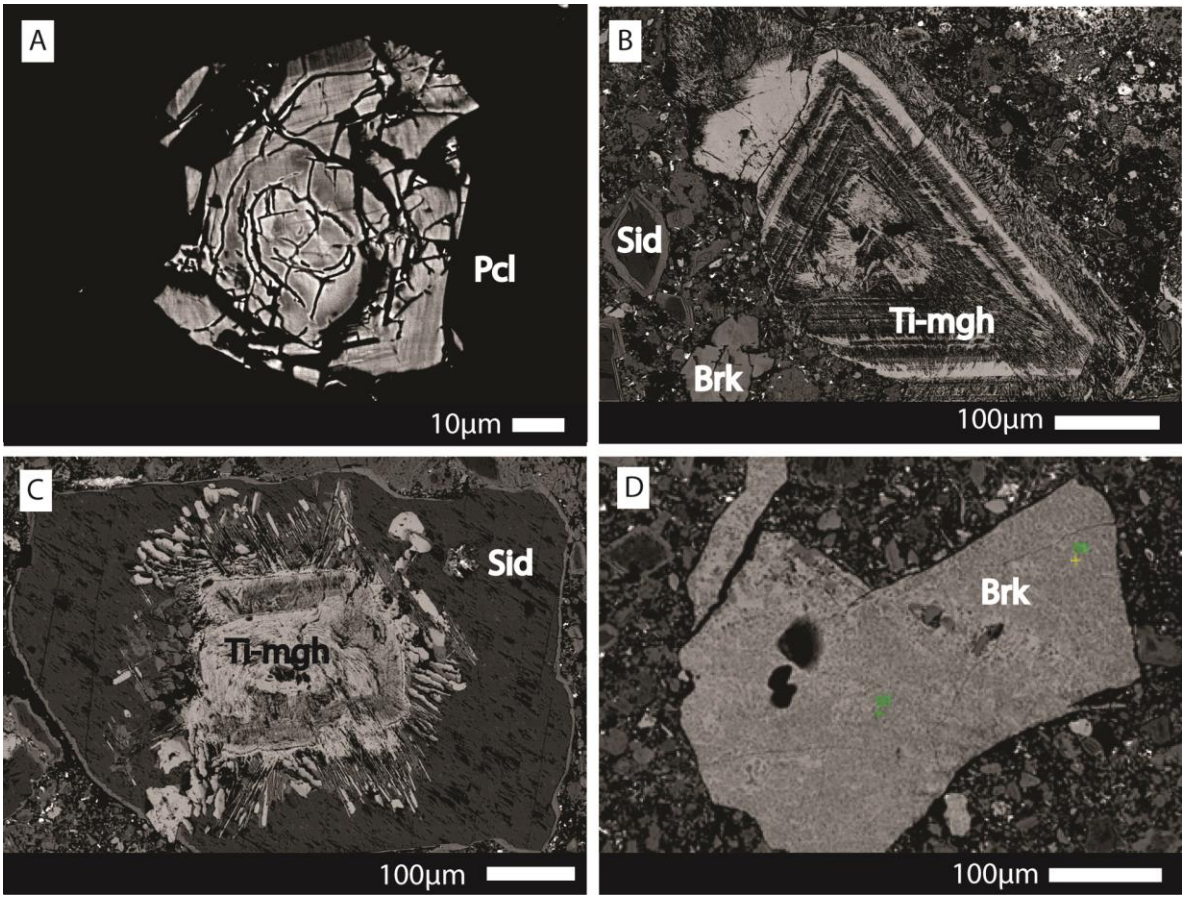

Fig. 6. BSE- images of siderite carbonatite. (A) Broken crystal of zoned pyrochlore. (B) Zoned crystal of titanomagnetite replaced by acicular crystals of titanomaghemite. (C) Titanomaghemite included in siderite crystal. (D) Broken crystal of Nb-rich brookite. Pcl= pyrochlore; Sid= siderite; Ti-mgh= titanomaghemite; Brk= Nb-rich brookite.

4.2 Mineralogy

The samples selected for analysis of minerals originate from the BSC, ordinary CSC, REE-rich CSC and a carbonatite clast (CSC- Frag.) deposited in the Esperança Basin.

456 *4.2.1 Siderite*

457

458 All siderite crystals consist (Tab. 1) essentially of Fe^{2+}, with minor amounts of Mg^{2+}
459 and Mn^{2+}; whereas Ca^{2+} contents are negligible. The main differences are relative to Mg
460 and Mn contents: BSC siderites are richer in Mg and Mn than CSC; CSC- Frag. siderite is
461 particularly poor in Mn (Fig. 7). REE-rich- CSC- siderite is similar to that of CSC. Siderite
462 is zoned from Fe- rich cores to Mg- poor margins, and constant Mn contents.

463

464 Table 1. Representative compositions of siderite.

	BSC			CSC				REE-rich CSC		CSC Frag.	
	53B		53C	18A		18B		14		8	
MgO	3.81	3.16	4.7	3.29	3.29	1.55	0.2	1.55	1.48	0.61	0.19
MnO	5.53	9.02	7.07	2.62	2.83	2.5	2.76	2.26	2.46	1.19	0.82
FeO	55.53	63.98	55.28	59.13	59.93	64.52	65.9	62.56	62.27	65.25	65.48
Sum	64.88	76.16	67.06	65.05	66.05	68.57	68.86	66.37	66.21	67.05	66.49
Structural Formulae											
Mg	0.100	0.072	0.118	0.087	0.085	0.040	0.005	0.041	0.039	0.016	0.005
Mn	0.083	0.116	0.101	0.039	0.042	0.036	0.041	0.034	0.037	0.018	0.012
Fe	0.817	0.812	0.781	0.874	0.873	0.924	0.954	0.925	0.924	0.966	0.982
Cations	1.000	1.000	1.000	1.000	1.000	1.000	1.000	1.000	1.000	1.000	1.000

BSC = Border siderite carbonatite; CSC = Core siderite carbonatite; REE-rich CSC= REE-rich core siderite carbonatite; CSC- frag.= Core siderite carbonatite fragment.

465

466

467

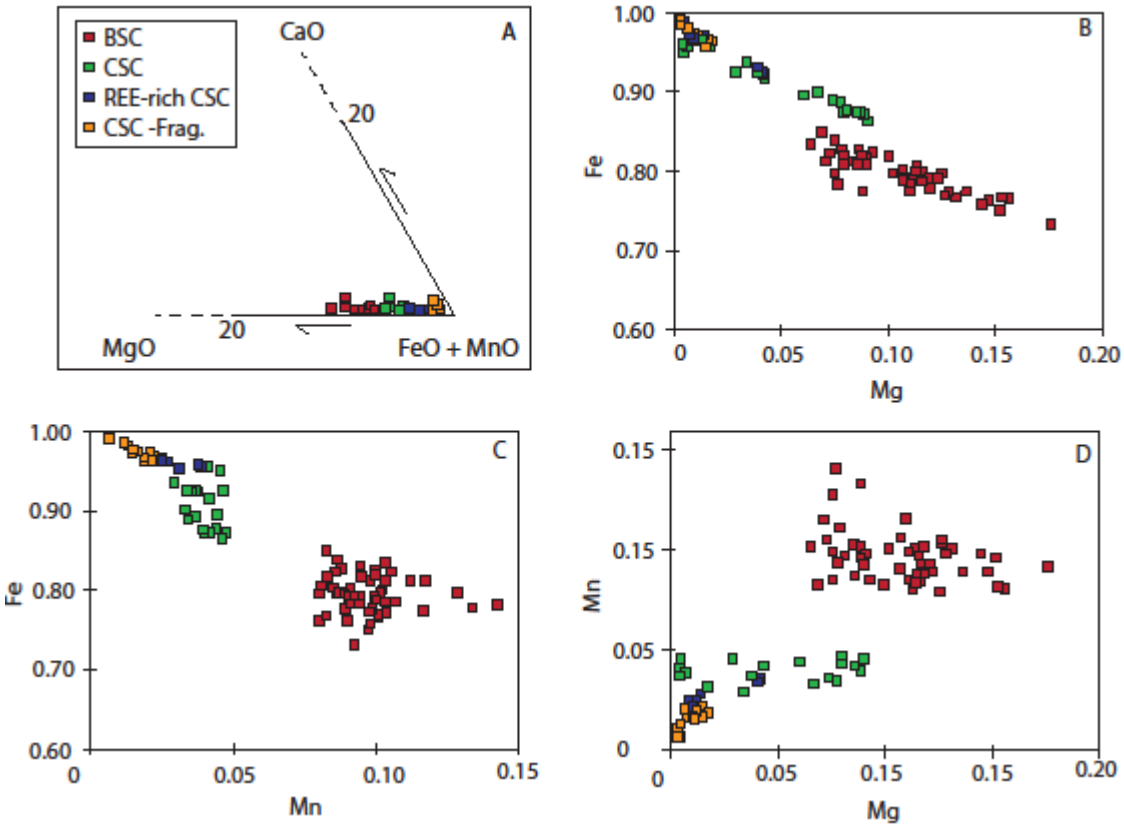

Fig. 7. Compositions of siderite from the border siderite carbonatite (BSC), core siderite carbonatite (CSC), REE-rich core siderite carbonatite CSC and carbonatite fragment from the Esperança Basin (CSC Frag.). (A) CaCO3-MgCO3-FeCO3 system; (B) Mg (apfu) vs. Fe(apfu); (C) Mn (apfu) vs. Fe (apfu); (D) Mg (apfu) vs. Mn (apfu).

4.2.2 Oxides

Pyrochlore occurs in all carbonatites, however in the BSC we found only one crystal larger enough for microprobe analysis. Representative compositions and structural formulae are given in Table 2. All the crystals plot in the pyrochlore compositional field in the Nb-Ti-Ta diagram (Fig. 8A). BSC- pyrochlore is a Pb-Ba-pyrochlore, relatively- poor in Ce and with the smallest vacancy (Fig. 8B). CSC and REE-rich CSC pyrochlore are Ce-

Ba-pyrochlores with vacancies greater than those of BSC (Fig. 8B, C). REE-rich CSC pyrochlore is richer in Pb than the CSC pyrochlore (Fig. 8C, E). The composition data show a negative correlation between Ce and Ba (Fig. 8D). We consider that this seems to be related to the composition of the primary pyrochlore rather than related to weathering.

Table 2. Representative compositions and respective structural formulae of pyrochlore.

	BSC	CSC					REE-rich carbonatite					CSC- Frag			
	54A	18A					14					8			
WO_3	n.d.	0.21	0.11	0.45	0.00	0.12	0.17	0.31	0.49	0.30	0.82	0.41	0.29	n.d.	0.44
Nb_2O_5	36.16	44.54	41.42	49.18	48.23	45.85	50.72	42.46	45.94	45.70	44.77	42.24	46.69	47.80	48.31
Ta_2O_5	n.d.	0.02	0.08	0.39	n.d.	n.d.	n.d.	n.d.	n.d.	n.d.	n.d.	n.d.	n.d.	0.18	n.d.
TiO_2	3.51	4.06	6.73	2.40	1.61	4.41	1.35	4.17	5.27	4.96	4.15	4.29	3.68	2.72	3.37
SiO_2	2.05	1.17	1.19	1.40	1.23	2.02	0.08	1.72	1.96	1.33	2.22	1.72	1.30	2.09	0.95
ThO_2	1.00	2.66	3.15	0.17	0.10	1.16	1.02	2.51	1.01	0.08	1.09	2.34	0.54	n.d.	1.37
Fe_2O_3	5.13	2.56	3.89	3.52	3.12	4.18	0.98	1.68	1.40	1.01	1.24	4.11	3.35	3.50	3.95
Al_2O_3	0.54	0.08	0.06	0.03	n.d.	0.18	n.d.	0.35	0.10	0.03	0.01	0.04	n.d.	0.04	0.09
La_2O_3	0.08	1.03	0.61	0.39	0.50	0.65	0.89	1.11	0.89	0.64	0.77	0.46	0.27	0.05	0.43
Ce_2O_3	1.48	6.20	4.01	3.44	3.75	4.48	6.51	8.55	6.92	5.22	6.38	3.05	2.40	1.30	2.53
Pr_2O_3	n.d.	0.25	0.10	n.d.	n.d.	n.d.	0.13	0.54	0.28	0.17	0.18	n.d.	n.d.	n.d.	n.d.
Nd_2O_3	0.70	2.51	1.72	1.28	1.39	1.72	0.94	1.30	1.25	0.86	0.99	0.94	0.57	0.15	0.67
Sm_2O_3	n.d.	0.91	0.80	0.05	n.d.	0.79	n.d.	0.33	0.24	0.19	0.14	0.88	0.54	0.14	0.55
Eu_2O_3	0.09	0.23	0.16	0.15	0.16	0.41	0.15	0.05	n.d.	0.13	0.06	0.57	0.37	n.d.	0.35
Gd_2O_3	n.d.	0.12	0.48	0.03	n.d.	0.16	n.d.	0.11	0.14	n.d.	0.02	0.02	n.d.	n.d.	0.14
Dy_2O_3	n.d.	0.13	0.10	0.26	n.d.	0.13	0.11	n.d.	n.d.	0.07	0.42	0.05	0.03	n.d.	0.19
Ho_2O_3	0.30	0.11	0.36	0.05	n.d.	n.d.	n.d.	0.07	n.d.	0.04	0.26	n.d.	0.06	0.16	n.d.
Er_2O_3	0.03	0.11	0.13	0.04	0.03	0.05	0.02	n.d.	n.d.	n.d.	n.d.	0.15	n.d.	n.d.	0.08
Y_2O_3	0.11	n.d.	0.46	0.05	0.05	0.04	n.d.	n.d.	n.d.	0.03	0.03	0.05	0.02	n.d.	0.07
BaO	12.09	13.39	16.51	18.16	20.00	15.37	12.87	9.78	9.55	13.17	14.17	14.43	18.56	20.73	17.04
PbO	12.21	4.71	4.91	3.78	3.55	4.40	8.27	7.64	7.89	8.92	8.23	7.54	6.41	5.41	6.37
SrO	1.35	n.d.	n.d.	0.23	0.01	0.03	0.15	0.24	0.54	0.28	0.31	0.29	n.d.	n.d.	0.20
CaO	2.60	0.17	0.13	0.07	0.03	0.22	n.d.	0.06	0.14	0.13	0.19	0.04	0.04	0.24	0.03
Sum	79.44	85.13	87.10	85.48	83.75	86.34	84.35	82.95	84.02	83.26	86.41	83.60	85.10	84.51	87.13
Structural Formulae															
Th	0.019	0.047	0.054	0.003	0.002	0.019	0.019	0.045	0.017	0.001	0.019	0.041	0.009		0.023
La	0.003	0.030	0.017	0.011	0.015	0.017	0.027	0.033	0.024	0.018	0.022	0.013	0.007	0.001	0.012
Ce	0.046	0.179	0.111	0.093	0.108	0.118	0.195	0.249	0.185	0.146	0.178	0.087	0.066	0.035	0.069
Pr		0.007	0.003				0.004	0.016	0.008	0.005	0.005				
Nd	0.021	0.070	0.046	0.034	0.039	0.044	0.028	0.037	0.032	0.024	0.027	0.026	0.015	0.004	0.018
Sm		0.025	0.021	0.001		0.019		0.009	0.006	0.005	0.004	0.024	0.014	0.003	0.014
Eu	0.003	0.006	0.004	0.004	0.004	0.010	0.004	0.001		0.003	0.002	0.015	0.009		0.009
Gd		0.003	0.012	0.001		0.004		0.003	0.003		0.001	0.001			0.003
Dy		0.003	0.002	0.006		0.003	0.003			0.002	0.010	0.001	0.001		0.005
Ho	0.008	0.003	0.009	0.001				0.002		0.001	0.006		0.001	0.004	0.000
Er	0.001	0.003	0.003	0.001	0.001	0.001						0.004			0.002
Y	0.005	0.001	0.018	0.002	0.002	0.001				0.001	0.001	0.002	0.001		0.003
Ba	0.593	0.608	0.719	0.777	0.910	0.638	0.609	0.449	0.402	0.581	0.624	0.648	0.810	0.883	0.729
Pb	0.279	0.100	0.100	0.076	0.075	0.085	0.183	0.164	0.155	0.184	0.169	0.158	0.130	0.107	0.127
Sr	0.045			0.007	0.001	0.001	0.005	0.007	0.015	0.008	0.009	0.009			0.006
Ca	0.237	0.014	0.011	0.006	0.002	0.017		0.005	0.011	0.010	0.015	0.003	0.003	0.019	0.003
SumA	1.260	1.099	1.129	1.021	1.159	0.977	1.076	1.020	0.858	0.989	1.091	1.032	1.068	1.057	1.021
W		0.004	0.002	0.009		0.002	0.004	0.006	0.009	0.006	0.016	0.008	0.006		0.009
Nb	1.387	1.581	1.410	1.646	1.716	1.487	1.877	1.526	1.513	1.576	1.541	1.484	1.592	1.591	1.616
Ta			0.002	0.008										0.004	
Ti	0.223	0.240	0.381	0.133	0.095	0.238	0.083	0.249	0.289	0.284	0.238	0.251	0.209	0.151	0.187
Si	0.174	0.092	0.090	0.104	0.097	0.145	0.006	0.137	0.143	0.102	0.169	0.134	0.098	0.154	0.070
Fe	0.164	0.076	0.110	0.098	0.093	0.113	0.030	0.050	0.038	0.029	0.036	0.120	0.095	0.097	0.110
Al	0.052	0.007	0.005	0.003		0.015		0.031	0.008	0.002	0.001	0.003		0.003	0.008
SumB	2.000	2.000	2.000	2.000	2.000	2.000	2.000	2.000	2.000	2.000	2.000	2.000	2.000	2.000	2.000
Vacancy	0.740	0.901	0.871	0.979	0.841	1.023	0.924	0.980	1.142	1.011	0.909	0.968	0.932	0.943	0.979

*Calculated on the basis of 2 B-site cations BSC = Border siderite carbonatite; CSC = Core siderite carbonatite; REE-rich CSC= REE-rich core siderite carbonatite; CSC- frag.= Core siderite carbonatite fragment.

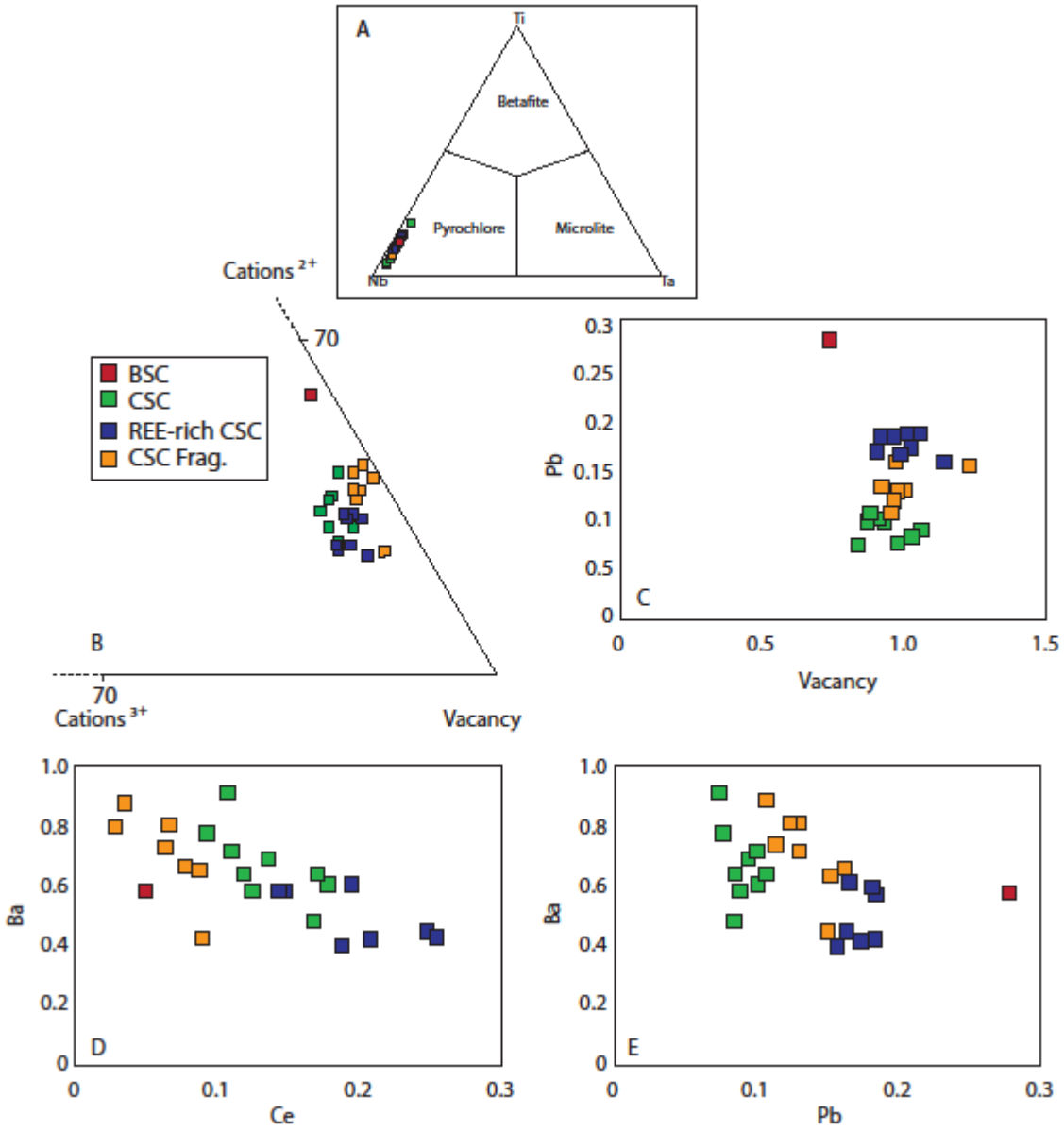

Fig. 8. Compositional variation of pyrochlore from border siderite carbonatite (BSC), core siderite carbonatite (CSC), REE-rich core siderite carbonatite REE-rich CSC and CSC fragment; (A) Pyrochlore-Microlite-Betafite classification (B) cation^{2+} vs. cation^{3+} vs. vacancy (C) Pr vs. vacancy; (D) Ba vs. Ce; (E) Ba vs. Pb.

Maghemites (γ-Fe_2O_3) are cation-deficient iron oxides with a structure related to that of spinel, which contain little or no ferrous iron. The ideal maghemite formula can be written: $[Fe^{3+}]\{Fe^{3+}_{5/3} + \square_{1/3}\}O_4$. Where [ ] represents the tetrahedral site (A-site) and {} represents the octahedral site (B-site) of the spinel structure. Al and Ti are common

substitutions at the octahedral site. The term titanomaghemite refers to cation-deficient spinels in the Fe^{3+}-rich field in the series Fe_3O_4 - Fe_2TiO_4 - $FeTiO_3$ - γ-Fe_2O_3 (Allan et al. 1989). Representative compositions of the titanomaghemite of Seis Lagos are presented in Table 3. The zonation, a relict from the primary titanomagnetite, corresponds to Fe and Nb variations. In Fe-rich and Nb poor bands, the Fe_2O_3 content ranges from 83.83 to 87.22 wt% and Nb_2O_5 ranges from 2.23 to 3.07 wt%. In Fe-poor and Nb-rich bands, Fe_2O_3 ranges from 55.12 to 71.37 wt% and Nb_2O_5 ranges from 15.75 to 19.18 wt%. Intermediate compositions (Tab. 3, analysis 3 and 9) also occur, but are rare. There is a strong negative correlation between the Nb_2O_5 content and the total oxides related to the vacancies created by the entry of Nb into the mineral. TiO_2 content varies from 1.50 to 8.08 wt%, without correlation with zonation or the presence of Nb. Considering all iron as Fe^{3+}, the structural formula is $Fe_1(Fe_{1.369}Nb_{0.036}Ti_{0.151}\square_{0.412})_2O_4$ for Fe-rich and Nb-poor bands and $Fe_1(Fe_{0.668}Nb_{0.353}Ti_{0.247}\square_{0.646})_2O_4$ for Fe-poor and Nb-rich bands.

Table 3. Representative compositions of titanomaghemite from the Seis Lagos siderite carbonatite.

	SG-04-AM-15									
	1	2	3	4	5	6	7	8	9	10
MgO	0.38	0.05	0.12	0.25	1.03	0.31	0.02	n.d.	0.05	0.06
MnO	0.06	n.d.	n.d.	0.14	0.68	0.08	0.07	0.04	0.05	0.10
Al_2O_3	0.53	0.07	0.40	0.45	0.12	0.55	0.04	0.11	0.28	0.08
Fe_2O_3	55.12	85.79	71.37	59.24	83.92	56.58	83.83	84.83	63.92	87.22
V_2O_3	0.23	0.15	0.15	0.21	0.06	0.08	0.15	0.12	0.19	0.19
SiO_2	0.21	0.22	0.65	0.27	0.15	0.08	0.22	0.21	0.16	0.43
TiO_2	8.08	6.31	3.33	5.97	1.50	6.76	6.30	7.60	3.16	5.56
Nb_2O_5	19.18	2.37	6.15	16.08	2.39	15.75	2.31	3.07	9.64	2.23
WO_3	0.07	0.08	0.06	0.07	0.08	0.03	0.09	0.13	0.02	0.14
Total	83.85	95.04	82.25	82.68	89.92	80.21	93.03	96.11	77.47	96.00
Mg	0.023	0.003	0.008	0.016	0.060	0.020	0.001		0.003	0.003
Mn	0.002			0.004	0.018	0.002	0.002	0.001	0.001	0.002
Al	0.024	0.003	0.019	0.021	0.005	0.026	0.002	0.004	0.014	0.003
Fe	1.688	2.350	2.263	1.856	2.469	1.821	2.347	2.290	2.163	2.369
V	0.007	0.004	0.005	0.007	0.002	0.003	0.004	0.003	0.007	0.005
Ti	0.247	0.173	0.106	0.187	0.044	0.217	0.176	0.205	0.107	0.151
Si	0.009	0.008	0.028	0.011	0.006	0.003	0.008	0.008	0.007	0.015
Nb	0.353	0.039	0.117	0.302	0.042	0.304	0.039	0.050	0.196	0.036
W	0.001	0.001	0.001	0.001	0.001	0.001	0.001	0.001	0.001	0.001

Formula calculated on the basis of 4 oxygens

The Nb-rich brookite from the siderite carbonatite (Tab. 4) is characterized by high Nb_2O_5 contents from 24.08 to 30.82 wt%, which are consistently higher than those found in Nb-rich brookite from the laterite (Nb_2O_5 from 10.43 to 16.03 wt%, Giovannini et al. 2017). The TiO_2 contents (from 57.77 to 66.04 wt%) and FeO (5.83 – 6.79 wt. %) are lower than those found in Nb-rich brookite from the laterites. This composition is compatible with the substitution $3Ti^{4+} = Fe^{2+} + 2Nb^{5+}$ (Fig. 9).

533 Table 4. Representative compositions of Nb-brookite from siderite carbonatite.

	SG-04-AM-15						
	1	2	3	4	5	6	7
CaO	0.40	0.75	0.63	0.68	0.30	0.68	n.d.
BaO	1.65	1.91	2.03	1.54	1.37	1.84	1.81
MgO	0.18	0.22	0.28	0.54	0.46	0.07	0.19
FeO	6.11	6.04	6.35	5.83	5.91	6.12	6.79
Al_2O_3	0.85	0.94	1.08	0.70	0.69	0.67	0.59
V_2O_3	0.50	0.60	0.55	0.53	0.48	0.47	0.49
SiO_2	0.22	0.34	0.37	0.17	0.25	0.29	0.20
ThO_2	0.44	0.44	0.47	0.11	0.09	1.21	0.78
TiO_2	66.04	57.77	61.31	60.86	58.77	58.04	58.28
Nb_2O_5	24.08	26.70	25.55	29.70	29.04	30.61	30.82
Total	100.46	95.70	98.61	100.66	97.35	100.01	99.92
Ca	0.006	0.012	0.010	0.010	0.005	0.011	
Ba	0.009	0.011	0.011	0.009	0.008	0.010	0.010
Mg	0.004	0.005	0.006	0.011	0.010	0.002	0.004
Fe	0.116	0.122	0.124	0.113	0.118	0.121	0.134
Al	0.013	0.016	0.017	0.011	0.011	0.011	0.010
V	0.006	0.007	0.006	0.006	0.006	0.005	0.006
Si	0.003	0.005	0.005	0.002	0.004	0.004	0.003
Th	0.001	0.001	0.002	0.001	0.001	0.004	0.003
Ti	0.690	0.642	0.655	0.647	0.646	0.631	0.631
Nb	0.151	0.178	0.164	0.190	0.192	0.200	0.201

Formula calculated on the basis of 1-cation

534

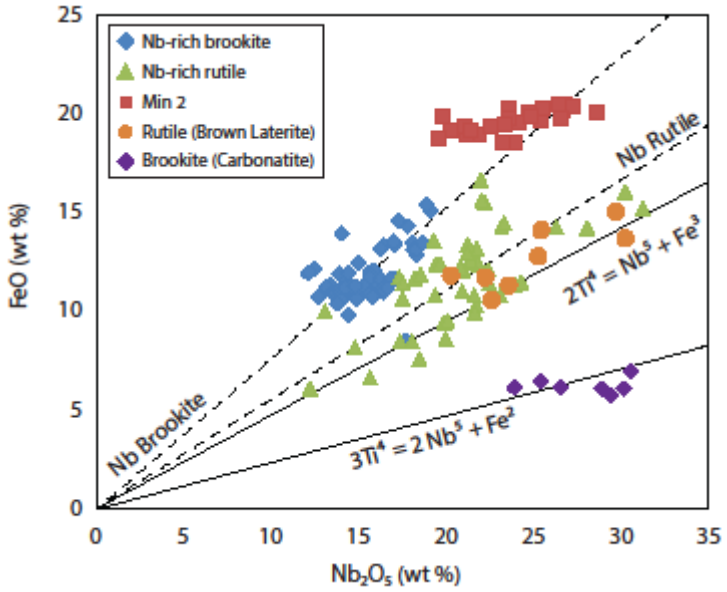

Fig. 9. Substitution diagram for Nb-rich brookite from the siderite carbonatite compared with Nb-rich brookite and Nb-rich rutile from the laterites (data in Giovannini et al. 2017).

4.2.3 REE minerals

The rhabdophane-(Ce) has a high Ca content and low La content compared to the other LREE (Tab. 5). Eu was not detected. As monazite, thorobastnäsite and bastnäsite crystals are very fine grained a satisfactory quantitative analysis was not possible. Semi-quantitative data for the REE compositions are reasonable and indicate (Fig. 10) that monazite does not exhibit the depletion in La observed in rhabdophane-(Ce). The bastnäsite is rich in LREE and has a REE distribution pattern similar to that of monazite from the core siderite carbonatite. Thorobastnäsite is rich in the MREE.

549 Representative compositions and structural formulae of gorceixite are presented in
550 Table 6. Among REE, only Ce (up to 6.36% Ce_2O_3) and Nd (up to 3.97% Nd_2O_3) are
551 highlighted. Sr is always present in concentrations up to 1.99% SrO.

552

553 Table 5. Representative compositions and respective structural formulae of rhabdophane-(Ce).

	Rabdophane-(Ce)			
	BSC			
P_2O_5	26.95	27.24	27.80	27.56
ThO_2	3.21	3.30	7.60	2.81
La_2O_3	2.28	2.31	2.58	3.87
Ce_2O_3	20.27	21.39	17.79	20.55
Pr_2O_3	3.76	3.73	3.05	3.42
Nd_2O_3	18.25	18.45	16.24	17.77
Sm_2O_3	2.70	2.82	3.48	3.23
Gd_2O_3	1.65	1.83	1.82	2.00
Dy_2O_3	1.20	1.30	0.89	1.42
CaO	4.94	4.91	5.56	5.01
SrO	0.82	0.85	2.06	0.54
BaO	2.69	2.17	2.28	2.66
H_2O	6.91	7.01	7.10	7.07
Sum	95.63	97.31	98.25	97.91
Th	0.030	0.030	0.069	0.025
La	0.036	0.036	0.040	0.060
Ce	0.322	0.335	0.275	0.319
Pr	0.059	0.058	0.047	0.053
Nd	0.283	0.282	0.245	0.269
Sm	0.040	0.041	0.051	0.047
Gd	0.024	0.026	0.025	0.028
Dy	0.017	0.018	0.012	0.019
Ca	0.229	0.225	0.251	0.228
Sr	0.021	0.021	0.050	0.013
Ba	0.046	0.036	0.038	0.044
Sum Cations	1.115	1.117	1.122	1.113
P	0.989	0.985	0.992	0.988

Calculated on the basis of 4 Oxygens

554

555

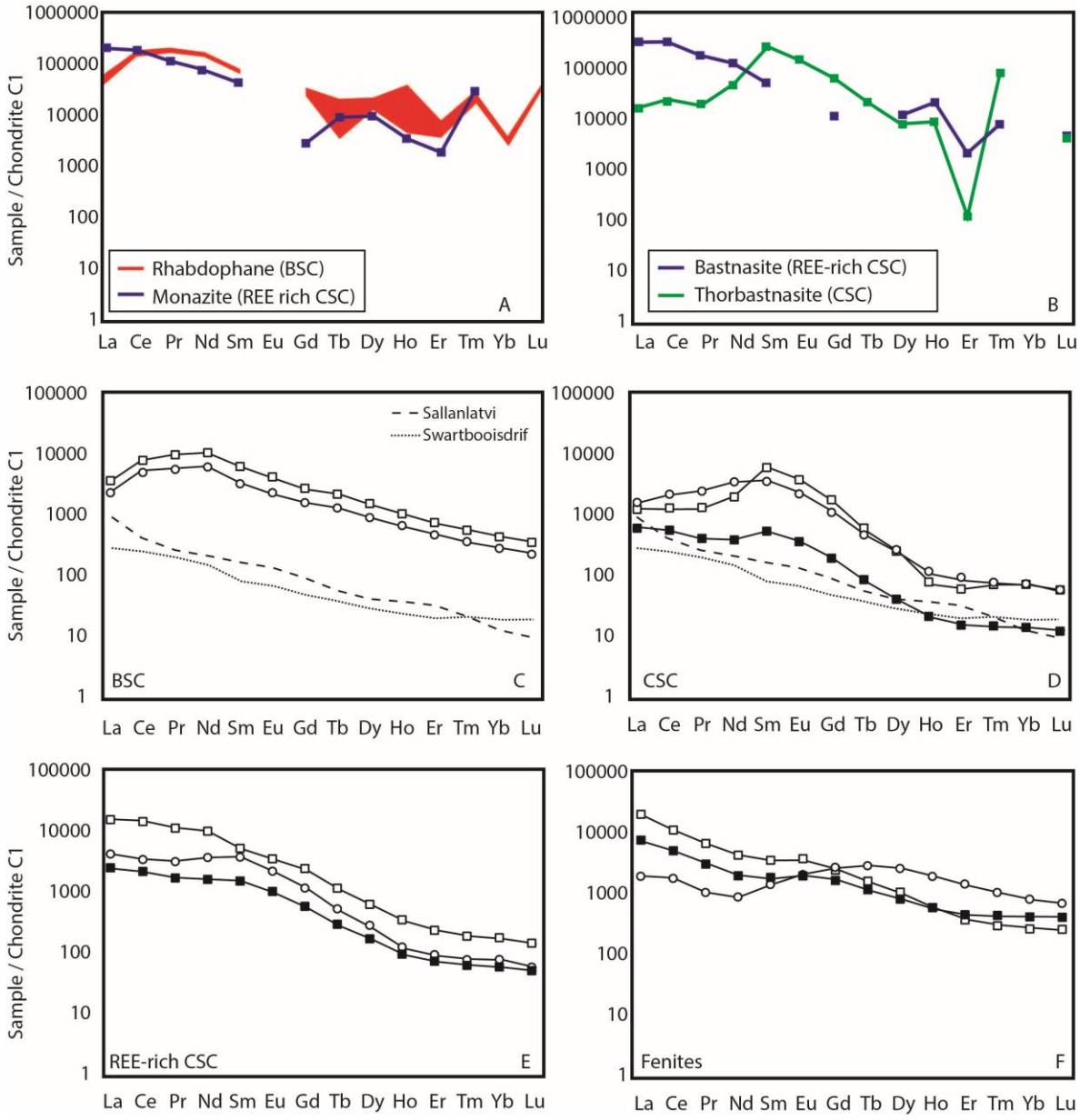

Fig. 10. REE normalized distribution patterns (chondrite C1; Sun and Mcdonuought, 1995) in carbonatite minerals, in the Seis Lagos siderite carbonatite (compared with othe carbonatites) and in fenites. (A) Rhabdophane-(Ce) from border siderite carbonatite (BSC) and monazites from REE-rich core siderite carbonatite (REE rich CSC). (B) Bastnäsite from REE-rich CSC and thorobastnäsite from core siderite carbonatite (CSC). (C) Border siderite carbonatite. (D) Core siderite carbonatite. (E) REE-rich core siderite carbonatite. (F) Fenites. Data from Sallanlatvi in Zeitsev et al. (2004) and from Swartbooisdrif in Thompson et al. (2002).

566 Table 6. Representative compositions and respective structural formulae of gorceixite.

	Border Siderite Carbonatite								
	53C-01	53C-02	53C-03	54A-01	54A-02	54A-03	54B-01	54B-02	54B-03
P_2O_5	23.47	22.96	22.93	21.30	22.24	21.60	21.99	22.25	22.29
La_2O_3	0.84	0.56	0.33	0.39	0.28	0.28	0.84	0.91	1.24
Ce_2O_3	6.36	4.06	3.21	3.09	2.53	2.63	4.32	4.99	5.86
Nd_2O_3	3.97	1.56	0.80	1.45	1.11	1.00	1.87	2.56	2.97
Sm_2O_3	0.59	0.02	n.d.	0.15	0.19	0.06	0.27	0.32	0.29
Eu_2O_3	n.d.	0.16	0.08	0.16	0.01	0.04	0.10	0.07	0.01
Dy_2O_3	0.55	0.01	0.08	0.24	0.22	0.12	n.d.	0.10	0.28
Er_2O_3	0.20	0.04	n.d.	0.01	0.07	0.12	0.06	0.02	n.d.
Al_2O_3	31.21	28.73	29.47	30.43	30.76	30.44	30.65	30.33	29.51
Fe_2O_3	1.03	0.54	0.38	2.18	2.44	2.72	3.64	1.71	1.96
BaO	22.29	24.24	24.70	22.08	22.81	23.98	19.77	22.59	22.11
SrO	1.67	1.97	1.55	1.99	1.90	1.39	1.78	1.71	1.00
CaO	0.61	0.46	0.56	0.55	0.35	0.40	0.77	0.50	0.48
MgO	0.04	0.15	0.07	0.12	0.05	0.17	0.08	0.16	0.11
Sum	92.81	85.48	84.16	84.13	84.93	84.96	86.14	88.21	88.09
La	0.024	0.017	0.010	0.012	0.008	0.008	0.025	0.027	0.036
Ce	0.177	0.120	0.095	0.093	0.074	0.078	0.125	0.145	0.169
Nd	0.108	0.045	0.023	0.042	0.032	0.029	0.053	0.072	0.084
Sm	0.015	0.001		0.004	0.005	0.002	0.007	0.009	0.008
Eu		0.005	0.002	0.004	0.000	0.001	0.003	0.002	
Dy	0.013	0.000	0.002	0.006	0.006	0.003		0.003	0.007
Er	0.005	0.001		0.000	0.002	0.003	0.001	0.001	0.000
Ba	0.666	0.769	0.786	0.709	0.716	0.762	0.613	0.701	0.683
Sr	0.073	0.092	0.073	0.094	0.088	0.065	0.081	0.078	0.045
Ca	0.049	0.040	0.049	0.048	0.030	0.035	0.065	0.042	0.041
Mg	0.005	0.018	0.009	0.014	0.006	0.021	0.010	0.018	0.013
ΣA	1.136	1.109	1.05	1.027	0.967	1.007	0.983	1.097	1.085
Al	2.802	2.742	2.821	2.937	2.905	2.909	2.858	2.83	2.741
Fe	0.059	0.033	0.023	0.134	0.147	0.166	0.217	0.102	0.116
ΣB	2.861	2.775	2.844	3.071	3.052	3.076	3.075	2.931	2.857
P	1.955	2.032	2.036	1.907	1.948	1.914	1.902	1.925	1.92

Formula calculated on the basis of 10.5 oxygens

567

568

569

570

571

572

573

574

4.3 Whole-rock geochemistry

Twenty eight samples were analyzed for their bulk compositions: BSC (5 samples), CSC (16 samples) and fenites (7 samples). Representative compositions are shown in Table 7. All 22 carbonatite samples are ferrocarbonatites according to the classifications of Gittings and Harmer (1997) (Fig. 11) and Le Maitre (1989). Twenty one samples characterize the siderite carbonatite as the richest in Fe and the poorest in Ca ever recognized.

599 Table 7. Representative bulk compositions of carbonatites and fenites.

	Fenites		BSC			CSC				REE-rich CSC	
%	02-46	02-52D	02-53C	02-54A	02-54B	04-81	04-19	04-92	04-59	04-72	04-76
SiO_2	34.98	26.97	0.38	0.32	0.36	0.12	0.48	0.08	0.77	1.29	0.26
Al_2O_3	14.7	17.71	1.34	0.92	1.34	1.05	0.27	0.33	0.45	1.85	1.1
Fe_2O_3	22.31	24.93	51.27	55.93	48.64	66.99	66.89	68.18	70.85	63.06	67.24
MgO	0.64	1.38	3.2	2.75	3.2	2.08	1.44	0.99	1.72	0.99	2.1
CaO	0.36	0.34	0.3	0.14	0.21	0.47	0.38	0.36	0.31	0.82	0.64
Na_2O	0.1	0.01	0.01	<0.01	<0.01	0.07	0.12	0.08	0.03	0.16	0.09
K_2O	5.91	1.35	0.05	0.03	0.05	0.08	0.11	0.08	0.12	<0.01	0.06
TiO_2	2.26	1.45	0.16	0.17	0.17	1.6	5.28	4.11	0.1	0.83	1.28
P_2O_5	0.38	0.24	2.01	0.81	1.56	0.27	0.23	0.14	0.13	0.87	0.28
MnO	1.71	1.85	6.73	11.69	5.1	2.39	1.87	1.49	2.14	2.18	2.06
LOI	9.2	12.4	24.6	22.8	25.2	22.3	20	21.1	22.4	24.3	21.8
Sum	92.58	88.67	90.08	95.56	85.81	97.48	97.33	97.08	99.01	96.49	97.02
ppm											
Cs	0.4	0.6	<0.1	<0.1	<0.1	0.1	0.1	<0.1	0.1	<0.1	0.3
Rb	111.2	41.9	1.2	0.6	0.8	5.6	6.6	3.4	1.2	0.5	2.6
Ba	42257	43899	>50000	28673	>50000	1928	1481	1485	1434	2743	2607
F	2020	4410	940	610	1030	476	n.a.	156	269	156	449
Sr	425.5	284.7	982.2	475.3	1028.3	212.4	87	86.9	45.6	554.6	282.3
Pb	89.6	844	1084.8	394.2	873.3	107.9	55.8	232.3	107.3	296.1	112.4
Th	3991.6	1160.9	1736.6	538.1	954.1	2807.7	5223	5973.3	1895.5	3059.9	2578.8
U	0.4	0.6	2.3	0.6	1.6	1	0.9	1.2	0.2	2.6	1
Zr	284.8	26857.9	142.9	102	145.1	58.6	32.6	34.3	155.2	140	103.5
Hf	8.2	215.4	3.3	2.4	3.6	1.1	0.8	0.5	4.7	2	2.3
Ta	0.6	1.2	0.2	0.2	1	1.5	1.3	1.9	0.4	2.3	1.8
Y	2134.8	847.5	1292.2	196.2	696	325.8	615.1	375.1	143.7	470.4	392.9
Nb	3426.8	4163.8	2291.6	1102.8	1532.7	6288.9	6152.2	7667.4	636.3	3240.4	6431.9
Sc	301	440	183	131	113	695	1590	1095	265	865	847
La	479.1	806.9	783.4	183.5	483.8	930.9	265.7	281	142.2	3795.2	1775.4
Ce	1159.9	1397.2	4604.8	2986.5	2875.2	1968.7	848.5	708.6	574.6	7450.3	3625.5
Pr	105.07	134.58	884.59	134.12	627.73	281.9	155.58	111.17	114.69	847.98	444.96
Nd	425.7	455.4	4662.4	709.8	3093.5	1578.1	1270.4	870.9	709.1	3205.4	2032.1
Sm	222.2	140.22	913.55	139.51	467.91	536.7	705.8	851.88	203.83	573.24	548.58
Eu	126.14	68.48	225.44	34.18	110.68	117.65	172.56	203.03	49.03	132.95	132.35
Gd	555.83	239.86	524.8	79.45	277	225.38	298.46	320.32	129.15	293.19	277.02
Tb	112.14	41.46	79.99	10.32	41.21	17.72	20.2	19.46	9.18	26.21	22.07
Dy	685.48	235.01	362.69	46.01	186.36	63.14	71.73	60.15	32.21	101.4	76.86
Ho	113.34	39.69	56.9	7.21	29.04	6.48	7.34	3.97	3.73	11.99	8.52
Er	235.46	96.17	117.23	17.8	59.77	14.53	17.05	9.97	8.15	27.39	18.02
Tm	27.62	14.21	14.26	2.2	7.07	1.97	2.52	1.79	1.02	3.42	2.3
Yb	141.86	86.49	73.58	12.44	35.98	12.78	16.12	11.89	6.55	19.86	13.81
Lu	18.39	13.55	8.99	1.58	4.54	1.44	1.94	1.33	0.79	2.43	1.67
REE	4408.2	3769.2	13312.6	4364.6	8299.8	5757.4	3853.9	3455.5	1984.2	16491	8979.2
Cr_2O_3	0.003	0.004	0.009	0.003	0.01	<0.002	<0.002	<0.002	<0.002	0.006	0.003
Ni	2.8	3.9	0.7	1.3	0.7	0.7	0.3	0.8	0.4	3.6	1.2
Co	12.8	20.5	25.7	41.9	18.5	58.3	73	69.8	59.9	64.7	55.6
V	439	2384	243	192	325	134	179	147	64	263	143
W	43.9	38	8.6	8.1	11.2	65.8	230	159.3	8.3	38	63.9
Ga	166.2	147.8	42.5	19.9	44.2	3.5	3.8	2	4.6	7.1	3.9
Zn	2293	2589	1268	1682	1242	1780	2296	2999	1254	1194	1513
Cu	5.1	5.1	1.8	3.6	1.4	1.2	1.6	1.1	0.4	7.5	1.4

BSC= Border siderite carbonatite; CSC= Core siderite carbonatite; REE-rich CSC= REE-rich core siderite carbonatite.

600

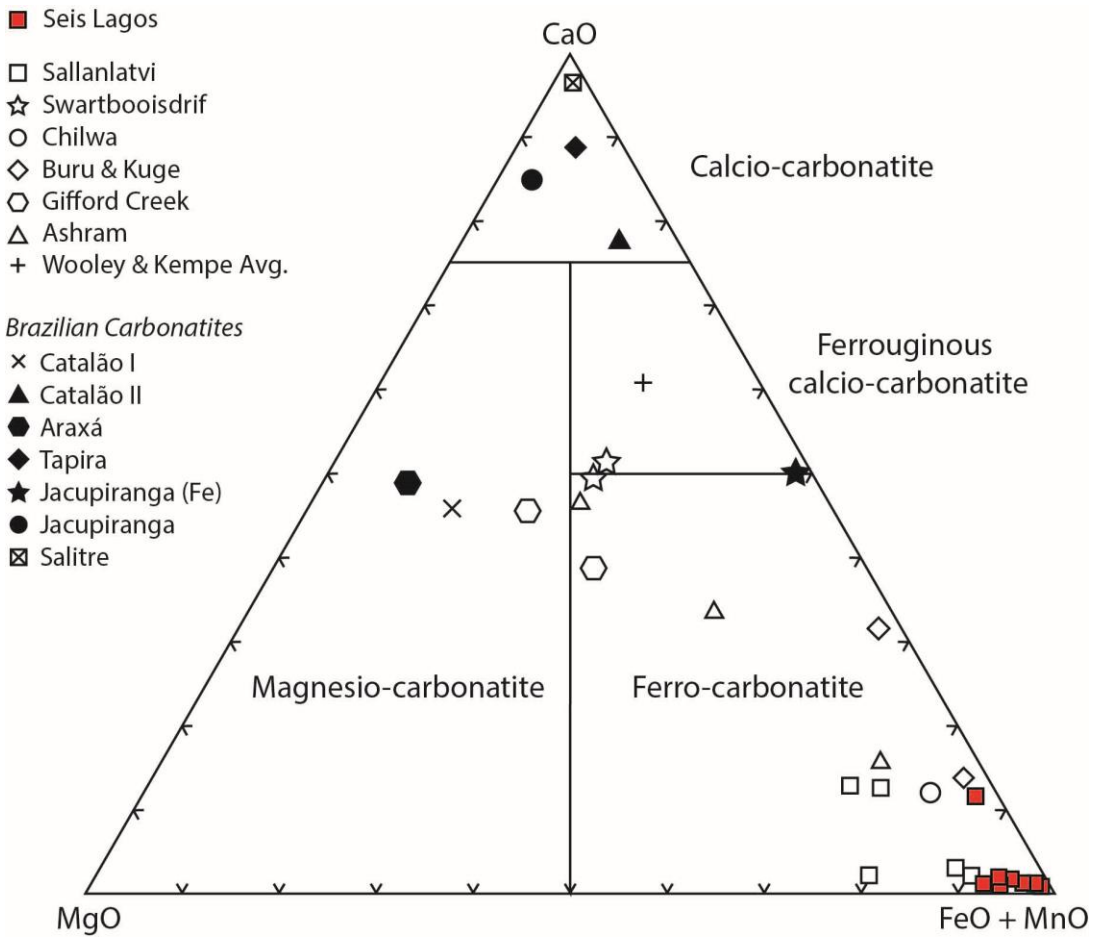

Fig. 11. Morro dos Seis Lagos siderite carbonatite compositions plotted in the Gittings & Harmer (1997) diagram for classification of carbonatites, together with other ferrocarbonatites and Brazilian Carbonatites. Data from Wooley & Kempe (1989), Simoneti & Bell (1994), Gittins & Harmer (1997), Onwonga (1997), Thompson et al. (2002), Zaitzev et al. (2004), Pirajno et al. (2014), Gomide et al. (2016), and Mitchell & Smith (2017).

The siderite carbonatite is richer in Fe (average of 67 wt% FeO in CSC and 63 wt% in REE-rich CSC) than the BSC (52 wt%). The BSC is much richer in Mn (up to 11 wt% MnO) than the core siderite (CSC and REE-rich CSC with ~2 wt% MnO). MgO contents are low in all carbonatites: BSC (up to 2.8 wt% MgO), CSC (up to 1.5 wt%) and REE-rich

614 CSC (up to 1.2 wt%). CaO content is extremely low with averages of: 0.2 wt% (BSC), 0.4
615 wt% (CSC) and 0.6 wt% (REE-rich CSC). BSC has higher contents of P_2O_5 (up to 2 wt%)
616 than core carbonatite (up to 0.2 wt% P_2O_5 in CSC and up to 0.9 wt% in REE-rich CSC).
617 SiO_2, Al_2O_3, Na_2O and K_2O contents are very low in all samples. LOI is high in all samples
618 with averages of 24 wt%, 20 wt%, and 23 wt%, respectively, in BSC, CSC and REE-rich
619 CSC due to the high contents of CO_2. As regard to the main major elements, the Sallanlatvi
620 siderite carbonatite (Zaitsev et. al, 2004) is the only one comparable to the Seis Lagos
621 carbonatite (Fig. 11).

622 The extended mantle-normalized distribution diagrams (Fig. 12) show that siderite
623 carbonatite and fenite have quite similar patterns. The fenites are similar to the border
624 siderite carbonatite except for La, Sm, and Pr which are more abundant in the fenite than in
625 the carbonatite. The major difference between the carbonatites is Ba which occurs with
626 higher content in the border siderite carbonatite and the fenites. All carbonatite samples
627 show positive anomalies of Nb, Th and REE, and negative anomalies of Rb, U, P, and Ta
628 (Fig.12).

629

630

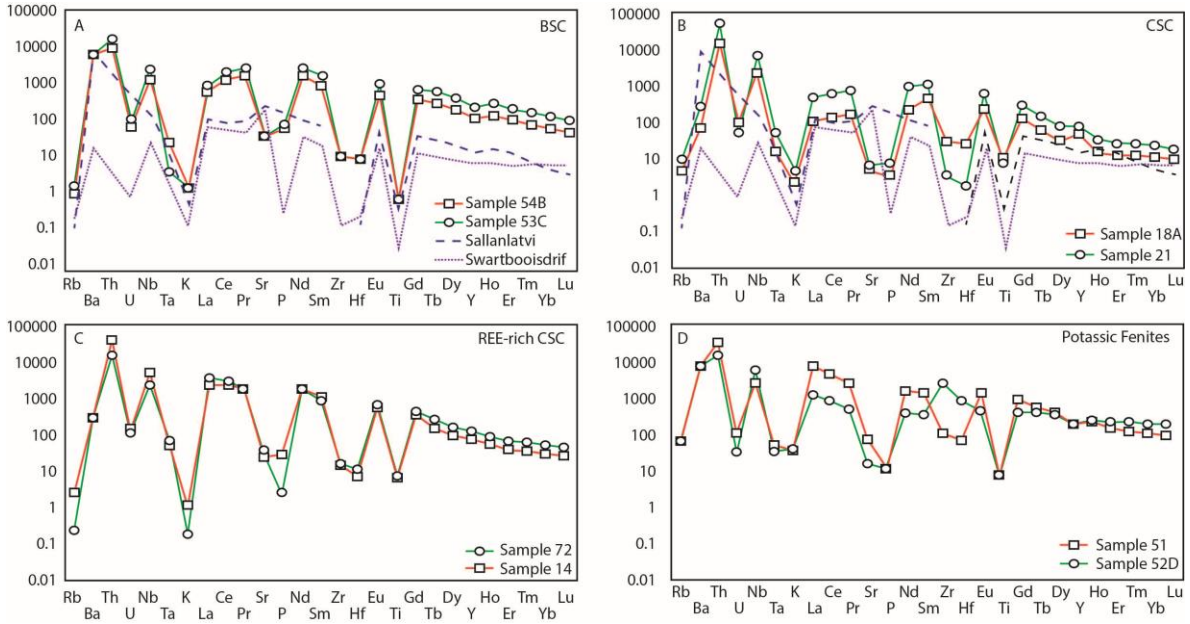

631

632 Fig. 12. Extended mantle-normalized distribution diagrams showing trace element variation in representative
633 border siderite carbonatite (BSC), core siderite carbonatite (CSC), REE-rich core siderite carbonatite (REE-
634 rich CSC) and fenites.

635

636

637 The Seis Lagos carbonatites samples enriched in Nb, Ti, Ba and REE. The
638 enrichment in Ba (>50,000 ppm) occurs only in the BSC and is accompanied by S
639 enrichment; reflecting the presence of barite veins. In the CSC, the Ba levels are low
640 (average of 1369 ppm in CSC and 2637 ppm in REE-rich CSC). The Sallanlatvi siderite
641 carbonatite has similar Ba contents (up to 80200 ppm) and also contains barite veins
642 (Zaitsev et al., 2004).

643 TiO_2 contents are low in BSC (up to 0.22 wt%; average 0.18 wt%), and are high in
644 CSC (up to 5.28 wt%, average 2.53 wt% in CSC; up to 6.77 wt%, average 1.89 wt% in
645 REE-rich CSC). These values are much higher than those found in other ferrocarbonatites
646 (up to 1.61 wt. %) (Chakhmouradian, 2006). This may reflect differences in mineralogy.
647 Nb-rich brookite is the only Ti-dominant mineral found to date.

Nb concentration in the BSC varies up to 2291.6 ppm (average of 1463.5 ppm). In the siderite carbonatite, higher contents are found (up to 7667.4 ppm, average of 5227 ppm in CSC and up to 22129.5 ppm an average of 5932 in REE-rich CSC). These values are much higher than those found in other ferrocarbonatites (up to 1980 ppm Nb) (Chakhmouradian, 2006). The contents of Ta in BSC (up to 1 ppm) and CSC (up to 1.9 ppm in CSC and up to 6ppm in REE-rich CSC) are much lower than those found in other ferrocarbonatites (average of 9.4 ppm Ta) (Chakhmouradian, 2006). Nb/Ta average values are 5786 in BSC and, in CSC, 3751 in CSC and 2072 in REE-rich CSC; the maximum value is 11000. These values are very high when compared to the primitive mantle ratio (35). Zr contents are higher in BSC (average of 365 ppm) than in CSC (average of 103 ppm in CSC and average of 143 ppm in REE-rich CSC). Hf is also richer in BSC (average of 6.4 ppm) than in CSC (average of 2.3 ppm in CSC and average of 2.7 ppm in REE-rich CSC). According to Chakhmouradian (2006), ferrocarbonatites present Zr average of 146 ppm and Hf average of 1.6 ppm. The Zr/Hf ratios in BSC, CSC, and REE-rich CSC are 48, 62, and 56, respectively. These values are compatible to mantle levels, approximately 60.

The Seis Lagos siderite carbonatite samples are rich in LREE especially La, Ce, Nd and Sm (Fig. 10). The BSC is particularly rich in Nd, the CSC is rich in Nd and Sm (related to thorobastnäsite) and the weathered CSC is rich in La and Ce. The LREE varies from 4187 ppm to 12074 ppm (average of 7886 ppm) in BSC, from 779 ppm to 5440 ppm (average of 3356 ppm) in CSC and from 2910 ppm to 17743 ppm (average of 8578 ppm) in REE-rich CSC.

The La/Yb ratio average values are 12.2 in BSC, 39.9 in core siderite carbonatite (CSC) and 107 in REE-rich CSC. This variation could reflect an evolution pattern, as this ratio tends to increase with magma evolution. However, BSC and CSC have low La

contents, and higher contents of Nd and Sm. All carbonatites have no Eu anomaly (Eu/Eu* ~1). HREE patterns are similar in all carbonatite samples.

In all samples, the REE distribution pattern of the whole-rock is quite similar to the REE pattern of the main REE-bearing mineral present i.e: rabdophane-(Ce) in the BSC; thorobastnäsite (rich in MREE) in the CSC; bastnäsite; and monazite in REE-rich CSC (Fig. 10).

The BSC is richer in Pb (up to 1028 ppm, average of 721 ppm) than the CSC (average of 90 ppm in CSC and of 153 ppm in the REE-rich CSC). This reflects the higher content of Pb in pyrochlore from the BSC. The contents of Zn are high and similar in all siderite carbonatite samples (up to 2593 ppm in BSC, up to 2999 ppm in CSC and up to 2149 ppm in REE-rich CSC. Although a Zn rich mineral was not found in siderite carbonatite, sphalerite was found in the associated fenites.

High Th contents occur in all carbonatite samples (up to 1736 ppm in BSC, up to 5973 ppm in CSC and up to 8239 ppm in REE-rich CSC). These contents reflect the high Th contents in monazite and thorobastnäsite (in CSC). U contents are very low in all siderite carbonatites (up to 3.2 ppm). The high Th/U ratio could reflect a high oxidation process, which transform U^{4+} in U^{6+}, which in highly mobile.

4.4 Fluid inclusions (FI) and solid inclusions

Twelve double-polished wafers of carbonatite were prepared for petrographic, Raman microspectroscopy and microthermometric studies. Samples included CSC (SG-02-

53B; 53C; 54A and 54B), BSC (SG-04-11; 15; 16; 17; 18B; 59), REE-rich CSC (SG-04-14 and 71) and core siderite carbonatite fragment (SG-04-08). In all these samples, siderite crystals are subhedral, with sizes up to 3mm, or present dissolution textures (Fig. 13A). The matrix is composed of dark red hematite and/or goethite. Four main fluid inclusions types were found in the carbonatite samples. They can be grouped in two Fluid Inclusions Assemblages (FIA; Goldstein & Reynolds 1994). FIA 1 is related to low temperature hydrothermal fluids. FIA 2 is represented by magmatic or melting inclusions.

FIA 1 is composed of pseudo-secondary fluid inclusions trails which lie parallel to crystal margins, cleavage and growth zones (Fig. 13A, B). There are three types of inclusions in the CSC and BSC samples. Type 1 are single phase mainly dark leaked inclusions or aqueous clear inclusions, both associated in the same trail and showing strong necking down (Fig. 13B). In the CSC, the size ranges from 10 - 30μm and are the predominant type. In the BSC, these inclusions are smaller than 5 μm and have less necking down.

The Type 2 inclusions are less common than Type 1, and are two-phase clear aqueous inclusions, which occur in the core and in border siderite carbonatites, usually associated with single phase inclusions, with evidence of strong necking down and sometimes with accidental carbonate rare solid inclusions. In the core siderite carbonatite, the shapes are irregular, the filling degrees ranges from 5 - 30% (Fig. 13B, D), the size ranges from 10 - 30 μm, and they can be associated with solid carbonate inclusions (Fig. 13A and 13B). In the border siderite carbonatite, they are rounded or have irregular shapes, the filling degree is usually lesser than 5%, and they have variable degrees of gas phase filling degree. They are smaller than 5μm and, in some example show pseudo-Brownian

719 movement (indication of low temperature, Roedder, 1984). Some Type 2 inclusions are
720 three-phase with accidental carbonate solid.

721 In the CSC the Type 1 and Type 2 inclusions are associated with rounded calcite
722 and nahcolite inclusions or opaque mineral inclusions, both with nearly the same size of the
723 fluid inclusions (10 - 30 μm). Such carbonate solid inclusions are smaller and corroded in
724 the BSC (Fig. 14A, B). Commonly, iron oxides occur as solid inclusions in siderite (Figure
725 14B, number 4).

726 Type 3 inclusions are single-phase triangular dark or clear inclusions with sizes
727 from 5 - 35 μm, which are more common in the border siderite carbonatite, but also occur
728 in the core siderite carbonatite (Fig.14B, number 5).

729 FIA 2 occurs only in the core siderite carbonatite. This association consists of two-
730 phase clear magmatic inclusions, with sizes lesser than 5 μm, regular filling degree of the
731 gas phase bubble (<5%), sometimes with two bubbles (Fig. 13E), and without necking
732 down evidence. Bubbles in FIA 2 can be deformed. These inclusions occur only in the core
733 siderite carbonatite, in siderites without solid carbonate or opaque inclusions. In the REE-
734 rich siderite carbonatite occur FIA 1 (hydrothermal) and FIA 2 (magmatic two-phase)
735 inclusions with similar textures as those from the core siderite carbonatite.

736 In all Raman experiments, siderite was identified as the enclosing mineral and the
737 presence of small nahcolite solid inclusions was confirmed by its main peak at 1022cm^{-1}.
738 The fluid inclusions of FIA 1 do not show CO_2, N_2 or CH_4 Raman peaks in the gas phase
739 (bubble or dark and clear one phase inclusions). In the magmatic two phase inclusion (FIA
740 2) the Raman spectra indicate that siderite is the enclosing mineral, and the inclusion
741 internal clear phase is characterized by non-identified Raman peaks at 604cm^{-1}, 816cm^{-1},
742 847cm^{-1}, 968cm^{-1}, which indicates this is a solid phase rather than an aqueous phase (Fig.

743 19). The gas phase (bubble) in the same inclusion presents a possible CH_4 Raman spectral
744 peaks at 2984cm^{-1}, 2870cm^{-1}, 2914cm^{-1}, 2948cm^{-1}. This could be related to contamination
745 during weathering (Ronchi et al. 2008).
746
747
748
749
750
751
752

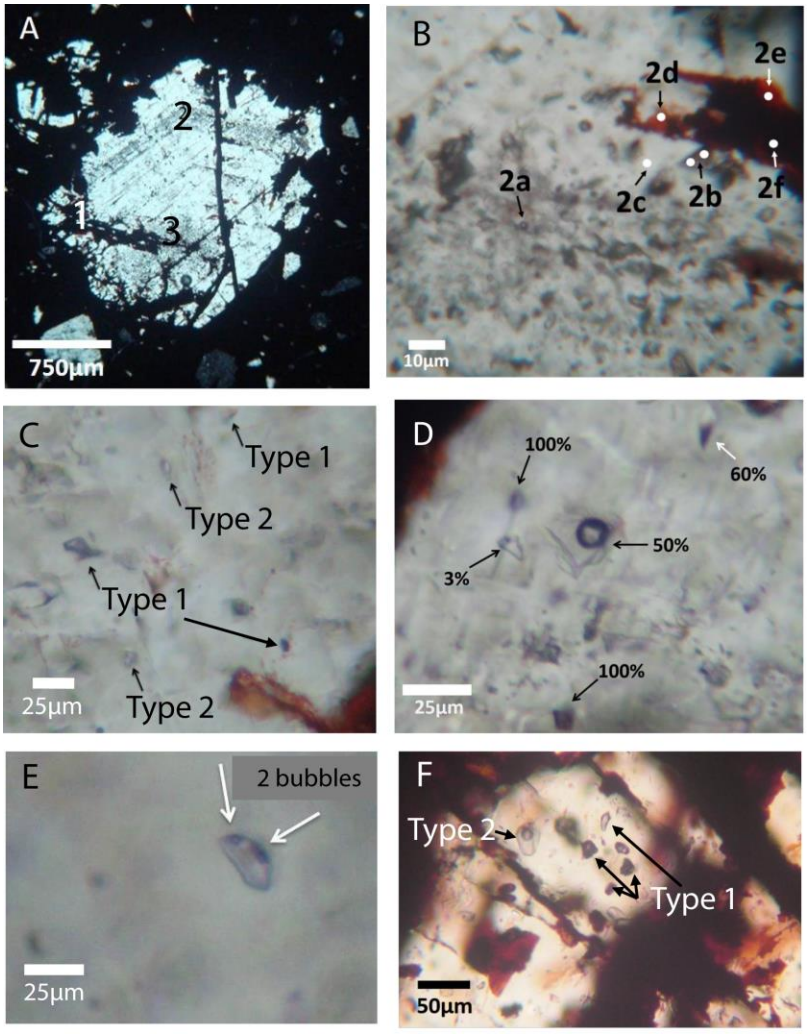

753

754 Fig. 13. Types of fluid and magmatic inclusions in the Seis Lagos siderite carbonatite. (A) Core carbonatite
755 fragment: siderite crystal with dissolution texture (in 1) and pseudo-secondary fluid inclusions (FIA 1)
756 defining growth zones (in 2 and 3); (2) also indicates the location of B; plane-polarized light. (B) Core
757 carbonatite fragment: FIA 1 three fluid inclusions types in the growth planes (see text): 2a is a two-phase type
758 2 fluid inclusion, 2b is the triangular type 3 inclusion; the numbers and letters indicate points of Raman
759 spectrometric analysis; plane-polarized light. (C) Core carbonatite fragment: FIA 1, types 1 and 2 one-phase
760 clear and dark inclusions in cleavage planes; some inclusions in this trails are two-phase due to leakage;
761 plane-polarized light. (D) Core carbonatite: FIA 1 association of type 1 one-phase and type 2 two-phase fluid
762 inclusions with different gas phase filling degree, indicated in %, strongly suggesting leaking and necking
763 down. Plane-polarized light. (E) REE-rich core siderite carbonatite: siderite hosting isolated magmatic
764 inclusion with two deformed bubbles corresponding to FIA 2; plane-polarized light. (F) Border siderite
765 carbonatite FIA 1 association of type 1 and 2 one-phase dark or clear inclusions and two-phase probably
766 aqueous necked and leaked inclusion; they are not associated with solid carbonate; plane-polarized light.

767

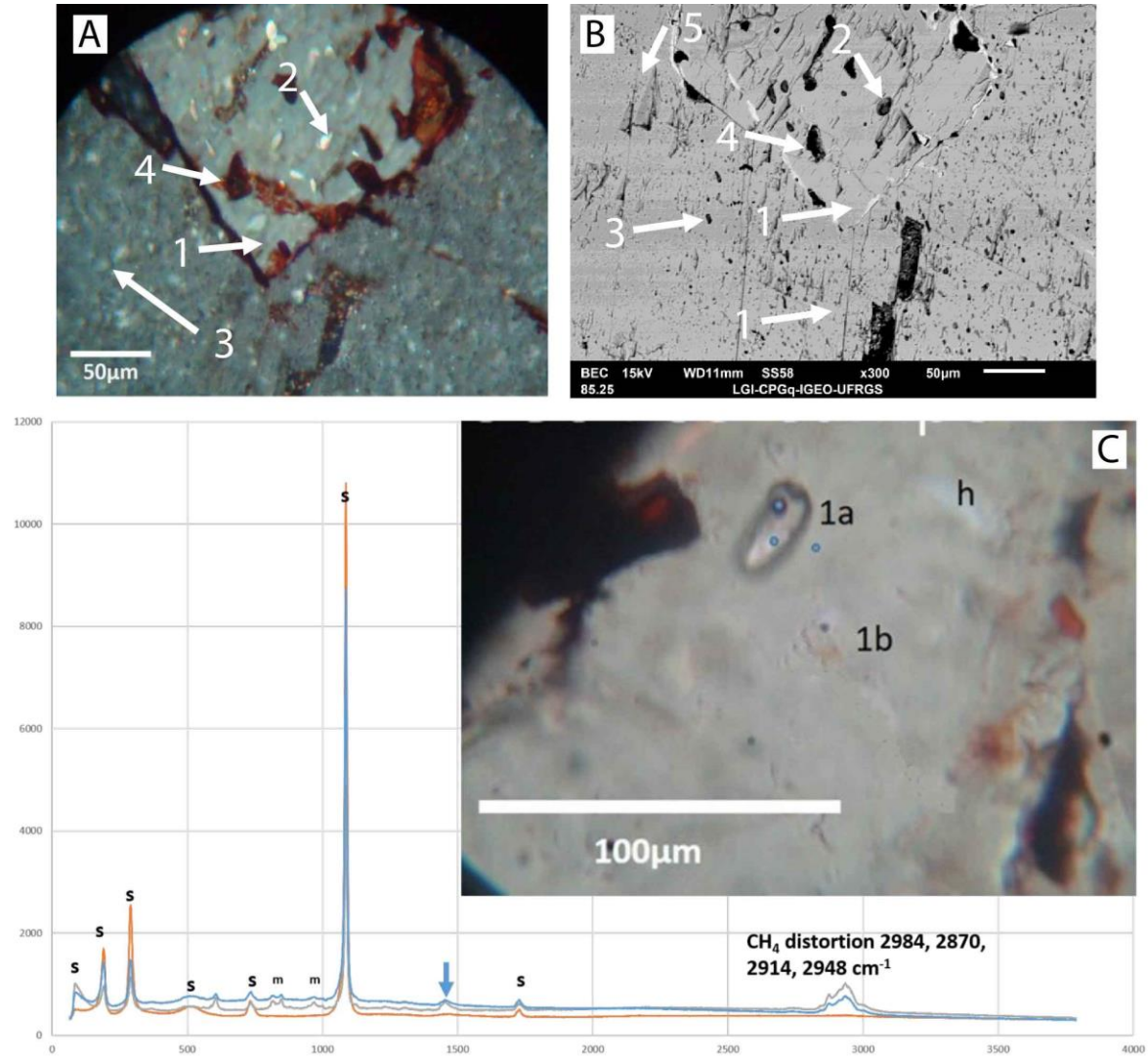

768

769 Fig. 14. Fluid and solid inclusions in the Seis Lagos siderite carbonatite. (A) Core siderite carbonatite: optical
770 image, crossed polars; B. SEM image. 1; enclosing siderite; 2: rounded solid inclusions probably a mix of
771 calcite and nahcolite; 3: corroded smaller calcite inclusion; 4: red iron oxides and 5: triangular cavities in the
772 enclosing siderite, similar to type 3 fluid inclusion. Raman Spectra of two-phase clear magmatic fluid
773 inclusion in core siderite carbonatite. 1a and 1b are magmatic fluid inclusion, h is a similar magmatic
774 inclusion out of focus. Blue dots indicate the sites where Raman spectra were obtained in the 1a magmatic
775 inclusion: orange line is the enclosing siderite Raman spectrum, gray line is the spectrum of the clear part of
776 the inclusion, blue line is the Raman spectrum of the bubble. Note that "s" are the siderite Raman peaks, "m"
777 are non-identified Raman peaks of the solid magmatic phase: 604cm-1, 816cm-1, 847cm-1, 968cm-1. There
778 is also a possible CH4 Raman spectral distortion at 2984cm-1, 2870cm-1, 2914cm-1, 2948cm-1 that only
779 appears on the bubble magmatic inclusion phase analysis. The blue arrow points to another non-identified
780 peak.

781

Microthermometric runs in FIA 1 three fluid inclusions types are meaningless due to their strong necking down and metastable behavior of the one-phase inclusions in freezing runs. The FIA 2 magmatic inclusions show no visible phase change during freezing to -190°C and heating to 400°C, suggesting that they are solid magmatic fluid inclusions with no H_2O or CO_2. Above 400°C they showed decrepitation as evidenced by, darkening and gas phase leakage. The dark red iron oxide spreads all over the samples precluding additional observations. In summary, FIA 1 is related to low temperature hydrothermal fluids whereas FIA 2 is represented by magmatic or melting inclusions.

4.5 Carbon and Oxygen Isotopes

The C and O isotopic compositions of siderite was analysed in 3 samples from BSC, 5 samples from CSC, and 2 samples from the RRE-rich CSC (Tab. 8). In the CSC, compositions are very similar ($\delta^{18}O$ ranges from 17.30‰ to 17.47‰ and $\delta^{13}C$ from -5.07‰ to -5.39‰). The samples from the BSC are characterized by higher values of $\delta^{18}O$ (from 19.11‰ to 20.08‰) and higher values of $\delta^{13}C$ (from -3.50‰ to -3.64‰). The REE-rich CSC samples show a wide range of $\delta^{18}O$ (20.79‰ and 31.33‰) and $\delta^{13}C$ (-4.62‰ and -1.40‰). These data are compared with those from other South American carbonatites (Fig. 15A) and ferrocarbonatites (Fig 15B).

Table 8. Isotopic compositions $\delta^{13}C$ and $\delta^{18}O$ of siderite from siderite carbonatite.

	Sample	$\delta^{13}C_{VPDB}$ ‰	$\delta^{18}O_{VSMOW}$ ‰
BSC	02-53A	-3.5	19.88
	02-53C	-3.57	19.11
	02-54A	-3.64	20.08
CSC	04-08	-5.3	17.21
	04-59	-5.22	17.13
	04-80	-5.07	17.47
	04-81	-5.14	17.44
	04-92	-5.39	17.3
REE-Rich CSC	04-72	-1.4	31.33
	04-76	-4.62	20.79

BSC= Border Siderite Carbonatite; CSC= CoreSiderite Carbonatite;
REE-rich CSC= REE-rich core siderite carbonatite

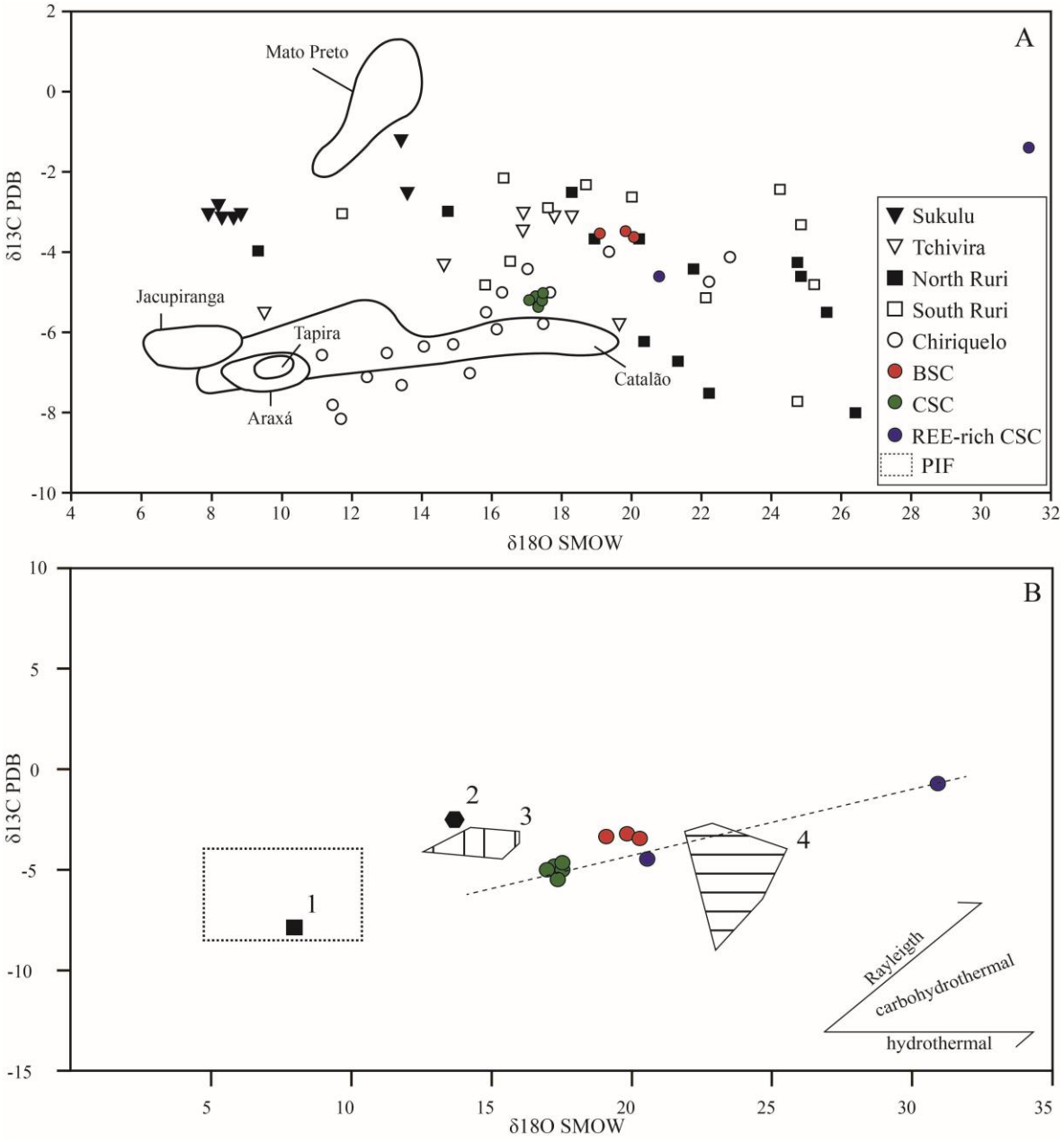

Fig. 15. Diagram $\delta^{13}C$ vs $\delta^{18}O$ for the Morro dos Seis Lagos carbonatite. (A) Comparison with other South American carbonatites and (modified from Santos and Clayton, 1995). (B) Comparison with other siderite carbonatites: (1) Swartbooisdrif (Thompson et. al. 2002); (2) Chilwa (Simoneti and Bell, 1994); (3) Buru and (4) Kuge (Onwonga, 1997).

Santos and Clayton (1995) studied the C and O isotopic compositions of carbonatites and metasomatic rocks (fenites) from carbonatite complexes from Brazil

816 (Jacupiranga, Araxá, Catalão, Tapira and Mato Preto). These carbonatites consist
817 principally of calcite and dolomite. There are no significant variations of $\delta^{13}C$ in the
818 samples from Jacupiranga, Araxá, Catalão and Tapira, and only Mato Preto shows a wide
819 range of $\delta^{13}C$, which is related to contamination by country rock limestone. There is a wide
820 range of oxygen isotopic composition in Araxa, Catalão, Tapira and Mato Preto, which are
821 accompanied by K-fenitization of the host rock, with the exception of Jacupiranga, which
822 has a narrow range of $\delta^{18}O$, and has not been extensively affected by fenitization.

823 Santos and Clayton (1995) concluded that fractional crystallization and liquid
824 immiscibility might not significantly affect the C and O isotopic compositions of
825 carbonatites. The large isotopic variations of C can be related to the host rock (e.g. Mato
826 Preto) and/or have been subjected to post-crystallization alteration processes. Variations in
827 both C and O composition can be explained by exchange between the rocks and H_2O-CO_2-
828 fluids; different H_2O/CO_2 ratios at different temperatures Santos and Clayton (1995) also
829 suggest that the C and O isotopic ratios are related to the emplacement level of the
830 carbonatite.

831 C isotopic variations are not strongly affected by C-free low-temperature processes,
832 such as weathering (Santos and Clayton, 1995). Therefore, the variation in $\delta^{13}C$ from the
833 REE-rich carbonatite samples cannot be accounted for these rocks being more weathered.

834 In figure 15A, C and O isotopic compositions from Brazil carbonatites are plotted
835 (Santos and Clayton, 1995), with Seis Lagos and other carbonatites. Samples from
836 Chiriguelo Complex (Paraguay) (white circles) have C and O isotopic compositions that
837 range from δC13 of -3.97 to -8.08, while the δO18 values display a wide range throughout
838 the same sequence (from + l1.22 to +22.91), with highest values of δC13 and δO18 related
839 to Fe-carbonatites (Censi et al., 1989). These samples form a trend which is interpreted by

Censi et al. (1989) as a similar to that expected from a Rayleigh distillation model of fractionation, between the crystalizing calcite and the coexisting vapor phase at 700°C having H_2O/CO_2 molar ratios between 0.4 and 0.5 in a closed system (see Pineau et al., 1973).

Figure 15B compares Seis Lagos samples to other Fe-carbonatites. Seis Lagos carbonatites has δC13 values similar to Chilwa (Simonetti and Bell, 1994), Buru and Kugwe (Onuonga et al. 1997), although the latter has a greater variance. The $\delta^{18}O$ values plot between Buru and Kugwe. According to Thompson et al. (2002), the Swartbooisdrift is the only ferrocarbonatite with magmatic isotopic values.

Pineau et al. (1973) divided the isotopic ratios of carbonatites into three groups: (1) rocks with isotopic ratios values in a primary carbonatite field; (2) rocks in which $\delta^{18}O$ variations are correlated with variations $\delta^{13}C$; and (3) rocks in which variations $\delta^{18}O$ are not correlated with variations of $\delta^{13}C$. When compared to the primary igneous field from Taylor (1967), Seis Lagos Carbonatite Complex samples show a greater enrichment in $\delta^{18}O$, as well as in $\delta^{13}C$. This is interpreted by Pineau (1973) as evidence of high concentrations of both H_2O and CO_2 in the magma, suggesting a carbohydrothermal process. The REE-rich zone in the carbonatite could be related to this carbohydrothermal process, at a late stage of the magma crystallization.

4.6 Sr and Nd Isotopes

Isotopic compositions of Sr and Nd for the Seis Lagos carbonatite are shown in Tables 9 and 10. The observed values of the $^{87}Sr/^{86}Sr$ ratio range from 0.70411 to 0.70573, which indicate low variation in this ratio. This range corresponds to the present values of the mantle compiled by Samoilov (1984) and Rukhlov et al. (2015). In general, the $^{87}Sr/^{86}Sr$ ratios of the Seis Lagos carbonatite are in the range of those reported for carbonatites elsewhere (Tab. 11). The $^{87}Sr/^{86}Sr$ initial ratio for Seis Lagos carbonatite was calculated for the age of magmatic and/or tectonic events reported in the Rio Negro Province as reference: the 200 Ma Penantecaua mafic magamatism related to the Pangea break up (CPRM 2006; Reis et al., 2006); the Maicurú carbonatite dated around 600 Ma (Lemos and Gaspar 1998); the K'Mudku event, that occurred around 1300 Ma (Santos et al. 2006, 2009, Almeida et al. 2013, Souza et al. 2015). Due to the low Rb/Sr ratio of the Seis Lagos carbonatite, the calculated initial $^{87}Sr/^{86}Sr$ ratio does not change significantly with time (Tab. 9). Thus the measured $^{87}Sr/^{86}Sr$ ratio of the Seis Lagos carbonatite might record values very near to those representative at the time of the emplacement.

The $^{143}Nd/^{144}Nd$ ratios for the Seis Lagos carbonatite range from 0.512663 to 0.512715, and did not vary significantly among the samples. However, the values of the Sm/Nd ratios are variable and affect directly the $^{147}Sm/^{144}Nd$ ratio as a function of time. A Depleted Mantle model age (T_{DM}) could be calculated only for two samples, which indicated T_{DM} ages of 829 and 1622 Ma (Tab. 10). These rocks are those with the lowest values for the $^{147}Sm/^{144}Nd$ ratio. This suggests that the Depleted Mantle model might not be used for these carbonatites. The values of $\varepsilon Nd_{(0)}$ are positive for all analyzed samples, and the two samples mentioned above present positive values of $\varepsilon Nd_{(t)}$ regardless of the age used for the calculation (Tab. 10). The other three samples gave negative values for $\varepsilon Nd_{(t)}$. In addition, the present day $^{143}Nd/^{144}Nd$ ratios for the Seis Lagos carbonatite are slightly

887 higher than the values reported for other carbonatite bodies (Comin-Chiaramonte et al.,
888 2001, 2005; Bizzi et al., 1994; Gibson et al., 1995; Traversa et al. 1996).

889

890 Table 9. Whole-rock Rb-Sr isotope data for the Seis Lagos carbonatite. Initial $^{87}Sr/^{86}Sr$ ratios for were
891 calculated for the ages of representative magmatic and/or tectonic events recognized in the Rio Negro
892 Province.

Sample	Rb (ppm)	Sr (ppm)	$^{87}Rb/^{86}Sr$	$^{87}Sr/^{86}Sr$	$^{87}Sr/^{86}Sr_{(200Ma)}$	$^{87}Sr/^{86}Sr_{(600Ma)}$	$^{87}Sr/^{86}Sr_{(1300Ma)}$
SG-02-53A	1.2	247	0.0141	0.70482	0.70478	0.7047	0.70456
SG-02-53B	0.42	525	0.0023	0.70497	0.70497	0.70495	0.70493
SG-02-53C	0.32	587	0.0031	0.70573	0.70572	0.70571	0.70567
SG-04-76	2.71	234	0.0335	0.70468	0.70459	0.70439	0.70406
SG-04-80	5.43	158	0.0992	0.70462	0.70433	0.70377	0.70277
SG-04-92	3.22	49,8	0.1873	0.70411	0.70357	0.7025	0.70062

893

894 Table 10. Whole-rock Sm-Nd isotope data for the Seis Lagos carbonatite. εNd values were calculated for the
895 the present time (εNd_0) and for ages of representative magmatic and tectonic events recognized in the Rio
896 Negro Province.

Sample	Rb (ppm)	Sr (ppm)	$^{87}Rb/^{86}Sr$	$^{87}Sr/^{86}Sr$	$^{87}Sr/^{86}Sr_{(200Ma)}$	$^{87}Sr/^{86}Sr_{(600Ma)}$	$^{87}Sr/^{86}Sr_{(1300Ma)}$
SG-02-53A	1.2	247	0.0141	0.70482	0.70478	0.7047	0.70456
SG-02-53B	0.42	525	0.0023	0.70497	0.70497	0.70495	0.70493
SG-02-53C	0.32	587	0.0031	0.70573	0.70572	0.70571	0.70567
SG-04-76	2.71	234	0.0335	0.70468	0.70459	0.70439	0.70406
SG-04-80	5.43	158	0.0992	0.70462	0.70433	0.70377	0.70277
SG-04-92	3.22	49,8	0.1873	0.70411	0.70357	0.7025	0.70062

897

898

899

900 **5. DISCUSSION**

901

902 Only siderite carbonatite is found at Morro dos Seis Lagos. Silicate rocks are absent
903 from the material found in drill cores. The absence of other rocks is corroborated by the

presence only of siderite carbonatite fragments in the Esperança Basin and by the mineralogy and geochemistry of the laterites (Giovanni et al., 2017). Anorogenic carbonatites are generally associated with alkaline complexes such as found at the Oka, Fen, Prairie Lake, Araxá, Afrikanda, and Kovdor carbonatite complexes (Mitchell, 2005, 2015). The absence of associated silicate rocks is not usual, but has also been described for other ferrocarbonatites such as Ashram Deposit (Mitchell and Smith, 2017). A possible explanation for their absence at Morro dos Seis Lagos is that these rocks may be present in deeper parts of the complex not yet investigated by deep core-drilling.

The gneissic host rock at Morro dos Seis Lagos is affected by potassic fenitization. The fenites are characterized by phlogopite and orthoclase (with monazite, fluorapatite and bastnäsite inclusions) accompanied by fluorite and iron oxides and monazite veins. Barite (with Fe iron oxides and sphalerite) veins cut the fenite, and are possibly related to the hydrothermal stage, which is well- developed in the border siderite carbonatite. The paragenesis of this potassic fenite is similar to that found at Gifford Creek (Pirajno et al., 2014), where the accessory minerals in fenitic haloes, both in siderite carbonatite and in the wall-rock, include fluorapatite, magnetite, phlogopite, pyrochlore, quartz, fluorite, barite, bastnäsite, and monazite. The fenitizing fluids (Le Bas, 2008) carrying the Na and K are halide-rich, principally F, and Ba; potassic fenites - characterized by a high proportions of K-rich orthoclase or microcline, or in some cases by concentrations of low-Al phlogopite or biotite - are considered to form in the apical parts of a carbonatite magmatic system, whereas sodic fenites form at deeper levels. We suggest that the Morro dos Seis Lagos Carbonatite Complex represents the upper-most parts of a carbonatite magmatic system.

Early- and late-stage carbonatites can be recognized (Kapustin, 1980; Zaitsev et al., 2004). The early stage carbonatites have calcite as the main mineral, whereas dolomite,

928 ankerite and siderite are typically late-stage carbonates. Siderite in most occurrences has
929 been described as formed from low-temperature (<150^{o}) hydrothermal fluids, and
930 commonly replaces other carbonate minerals (Simonetti and Bell, 1994; Schürman et al.,
931 1997; Onuonga et al., 1997; Buckley and Woolley, 1990; Woolley and Buckley, 1993). At
932 Sallanlatvi, the sequence of carbonatite formation is calcite-dolomite-ankerite-siderite, and
933 can be explained by fractional crystallization of hydrous carbonatite magma (Zaitsev et al.,
934 2004). The ferrocarbonatite from Ashram Deposit (Mitchell and Smith, 2017) is related to a
935 late-magmatic-to- hydrothermal process. At Morro dos Seis Lagos, the core siderite
936 carbonatite have either typically magmatic two phase inclusions (FIA 2) in siderite crystals
937 with no associated solid inclusions, as well as typical low temperature hydrothermal (FIA 1
938 fluid inclusions) belonging to, at least, two generations of siderite, both with solid
939 inclusions of Ca- carbonates. In the border siderite carbonatite only low temperature
940 hydrothermal fluid inclusions (FIA 1) were found. Our data suggest therefore that the
941 Morro dos Seis Lagos siderite carbonatite is related to a late-magmatic-to- hydrothermal
942 process.

943 In contrast to the great majority of carbonatite complexes, in which the variation of
944 $\delta^{13}C$ is relatively limited, the Morro dos Seis Lagos siderite carbonatite exhibits a
945 considerable large variation of $\delta^{13}C$, which is not attributable to low-temperature processes
946 such as weathering. A similar wide $\delta^{13}C$ range at the Mato Preto complex (Santos and
947 Clayton, 1995) is related to contamination by the country rock limestone, an explanation
948 not applicable to the Morro dos Seis Lagos complex where the country rocks are gneisses
949 and granites. In the present case, the $\delta^{13}C$ variation is accompanied by a variation in $\delta^{18}O$.
950 In other carbonatite complexes, such correlation was explained by exchange between the
951 rocks and H_2O-CO_2-fluids and by different fluid H_2O/CO_2 ratios at different temperatures

952 (Santos and Clayton 1995). At the Morro dos Seis Lagos complex both $\delta^{18}O$ and $\delta^{13}C$ are
953 higher than the primary igneous field (Taylor 1967) and the trend (Fig. 15), quite different
954 from that expected from a Rayleigh distillation model of fractionation (Censi et al., 1989),
955 is interpreted as evidence of high concentrations of both H_2O and CO_2 in the magma
956 (Pineau, 1973), suggesting a carbohydrothermal process. The REE-rich zone in the
957 carbonatite could be related to this carbohydrothermal process, at a late stage of the magma
958 crystallization. The border siderite carbonatite would be formed in the hydrothermal stage.

959 Petrological studies of carbonatites show that each Nb-deposit is unique with
960 respect to the assemblage of Nb-bearing minerals present (Mitchell 2015). The Morro dos
961 Seis Lagos Nb deposit is the only example where Nb-rich rutile (with minor Nb-rich
962 brookite formed from Nb-rich rutile) is the main Nb ore mineral. At the Morro dos Seis
963 Lagos, Nb-rich rutile is a secondary mineral whose formation results from the extreme
964 lateritization (Giovannini et al., 2017). The simplicity of the Nb-Ti-oxide paragenesis in the
965 Morro dos Seis Lagos siderite carbonatite, as well as Morro dos Seis Lagos Nb laterite
966 deposit, contrasts with all other carbonatites and associated laterites. For instance, at the
967 Ashram deposit (Mitchell and Smith, 2017) there occurs a diverse assemblage (Nb-rutile,
968 ferrocolumbite, aeschynite, nioboaeschynite, and samarskite - but no pyrochlore). This
969 assemblage, in veins and bands associated with quartz, is similar to that of NYF pegmatites
970 and not to carbonatites associated with undersaturated rocks.

971 The primary Nb-rich brookite from the core siderite carbonatite contains up to 30.82
972 wt.% Nb_2O_5, and is richer in Nb than the Nb-rich rutile and the Nb-rich brookite (up to
973 16.03 wt.% Nb_2O_5) from the laterites. The substitution $3Ti^{4+} = Fe^{2+} + 2Nb^5$ (Fig. 9) explains
974 the greater enrichment in Nb and characterizes a reducing environment, in contrast to the
975 substitution $Ti^{4+} = Fe^{3+} + Nb^5$ in Nb-rich brookite from the laterites. Although not common,

976 brookite occurs in some carbonatites. At Gross Brukkaross (Werner and Cook 2001), this
977 mineral is associated with hydrothermal fluids and formed under reducing conditions, from
978 direct precipation (high-Nb-brookite) and pseudomorphic replacement of perovskite (low-
979 Nb-brookite). At Salpeterkop (Verwoerd et al., 1995) disseminated grains of several
980 morphological types (oolitic; idiomorphic (not zoned); hypidiomorphic (zoned); and
981 radiating spherulitic) occur, with all considered of hydrothermal-metasomatic origin.
982 Titanomaghemite is also disseminated in Morro dos Seis Lagos carbonatite and is probably
983 formed by the alteration of titanomagnetite under oxidizing conditions (Zhou et al., 2001).
984 The Pb-Ba-pyrochlore in the border siderite carbonatite is less- altered than the Ce-
985 Ba-pyrochlore in the core siderite carbonatite, which progressively weathers to Ce-
986 pyrochlore until it is entirely destroyed in the lower part of the laterite profile (Giovannini
987 et al., 2017). Although the original composition of pyrochlore plays an important role in
988 determining the variety of secondary pyrochlores formed, these follow more- or - less well-
989 defined sequences (Wall et al., 1996; Lottermoser and England, 1988; Cordeiro et al., 2011;
990 Silva, 1986; Lumpkin and Ewing, 1995).
991 According to Thompson et al. (2002), minor ankerite- and siderite-carbonate rocks
992 occur in many complexes dominated by Ca–Mg carbonatite. Within a magmatic carbonatite
993 framework, such ferrocarbonatites are generally seen as the low-temperature product of
994 fractional crystallization of Ca–Mg carbonate melts (e.g. Le Bas, 1981, 1989; Gittins 1989;
995 Cooper and Reid 1998; Le Bas 1999). This process is usually inferred to concentrate Fe,
996 Mn, Co, Cr, V, Ba, Th, Pb and light rare-earth elements (REE) in ferrocarbonatites,
997 whereas Ti, P, Ni, Sr, Nb, Ta, Zr, Hf, U and heavy REE behave more erratically (e.g. Le
998 Bas 1989; Woolley and Kempe 1989; Cooper and Reid 1998; Le Bas 1999). The Seis
999 Lagos carbonatite appears to follow these trends.

1000 The Sallanlatvi carbonatite siderite is rich in Fe, Ba and S, with low Mg, Mn, Ca,
1001 Nb, Ta, Ti, Zr and Hf and REE contents. The Nb/Ta ratio (82 to 287) is higher than mantle
1002 values (~17.7). The Seis Lagos carbonatite has high levels of Nb (and Ti in some samples)
1003 and a very high Nb/Ta ratio (from 1408 to 11459). In the Swartbooisdrif ferrocarbonatite
1004 (Thompson et al., 2002), the high Nb/Ta ratio (372 to 2400) is suggested to have been
1005 inherited from an earlier episode of silicate-carbonate melt immiscibility in the evolution of
1006 the magma. This conclusion is contentious as, according to Veksler (1998), the strong
1007 preference of Zr, Nb and other HFSE for the silicate liquid does not support the origin of
1008 the Nb- and Zr-rich carbonatites by liquid immiscibility, and suggests that they are
1009 probably formed as residual liquids by fractional crystallization.

1010 The Seis Lagos siderite carbonatite has high REE contents in comparison with other
1011 ferrocarbonatites (Fig. 10C). The average La/Yb ratio is 39.9 in the core siderite carbonatite
1012 (CSC), and 107 in REE-rich CSC. This variation could reflect fractionation, as this ratio
1013 tends to increase with magma evolution. In the border siderite carbonatite the low La/Yb
1014 ratios and higher contents of Nd and Sm are characteristic of a hydrothermal stage
1015 (Formoso et al., 1989).

1016 The $^{87}Sr/^{86}Sr_i$ ratios calculated for 200 Ma are close to the values of the calculated
1017 CHUR for that age (0.70427), this can be interpreted as a mantle origin with practically no
1018 crustal contamination. The $^{87}Sr/^{86}Sr_i$ rations calculated for 1,300 Ma show a large deviation
1019 of the UR values for that age (0.70298). Only sample SG-04-80 has a $^{87}Sr/^{86}Sr_i$ ratio value
1020 close to the mantle value. To explain the deviation of the other samples is necessary to
1021 consider crustal contamination, however these samples do not present geochemical
1022 evidence (Rb, U, etc) of crustal contamination. Consequently, the Sr isotope data suggest a

younger age for the Morro dos Seis Lagos carbonatite than that previously proposed by Rossoni et al. (2017).

6. CONCLUSIONS

Only siderite carbonatite is found at the Morro dos Seis Lagos complex and the silicate rocks typically found in carbonatite-alkaline rock complexes are absent, although such rocks might present in the deeper and as yet unexplored parts of the complex, we suggest that the Morro dos Seis Lagos Carbonatite Complex represents the upper-most parts of a carbonatite magmatic system. Three types of siderite carbonatite are: (1) A brecciated oxidized core siderite carbonatite with: siderite (up to 95 vol.%), hematite; pyrochlore; Nb-brookite; Ti-maghemite; and thorobastnäsite; (2) A REE- and P-rich portion of the core siderite carbonatite with siderite (up to 95 vol.%), hematite, pyrochlore, monazite and bastnäsite; (3) A border carbo-hydrothermal siderite carbonatite, with siderite (~70 vol.%), barite (~15 vol.%), gorceixite (~7 vol.%) plus minor rabdophane and pyrochlore.

The Nb-Ti-oxide mineral assemblage is quite simple compared to that occurring in most Nb-deposits this being: Pb-Ba-pyrochlore in the border siderite carbonatite; Ce-Ba-pyrochlore, Nb-rich brookite, and titanomaghemite in the core siderite carbonatite); and Ce-Ba-pyrochlore in the REE-rich core siderite carbonatite. The Ce-Ba-pyrochlore progressively weathers to Ce-pyrochlore and is entirely destroyed in the lower parts of the laterite profile. The Nb-rich brookite in the carbonatite is much richer in Nb than the Nb-

rich brookite from the lateritic deposit. The substitution $3Ti^{4+} = Fe^{2+} + 2Nb^{5}$ explains this greater enrichment in Nb and indicates formation in a reducing environment. The absence of Nb-rich rutile in the carbonatite corroborates the laterite studies in that this mineral results from the complete decomposition of pyrochlore due to extremely intense lateritization.

Fluid inclusion and stable isotope studies indicate that the core siderite carbonatite is related to a late-magmatic-to- hydrothermal processes and the border siderite carbonatite is related to the hydrothermal stage.

The Morro dos Seis Lagos core siderite carbonatite is the richest in Fe and the poorest in Ca ferrocarbonanite yet recognized. The very high Nb content (up 7667 ppm) in all carbonatite samples is uncommon in ferrocarbonatites.

The Sr and Nd isotopic data suggest the Morro dos Seis Lagos Carbonatite Complex has a mantle origin with practically no crustal contamination. If this is correct, the age of the carbonatite is considered to be much younger than the previously proposed maximum age of the carbonatite of 1328 ± 58 Ma.

ACKNOWLEDGMENTS

The present work would not have been possible without the support given by the Companhia de Pesquisa de Recursos Minerais, through Roberto Ventura Santos, Eduardo Camozatto, and Renê Luzardo. Nilson Botelho (UNB) is thanked by the microprobe analysis, Alcides Sial and Milton Formoso are thanked for the C and O isotopic analysis.

The Conselho Nacional de Desenvolvimento Científico e Tecnológico CNPq is acknowledged for the financial support (projects 485415/2012-7 and 405839/2013-8).

REFERENCES

Allan, J.E.M., 1989. An Occurrence of a Fully-Oxidized Natural Titanomaghemite in Basalt. Mineral. Mag. 53, 299–304.

Almeida, M.E., Macambira, M.J.B., Santos, J.O.S., Nascimento, R.S.C., Paquette, J.-L., 2013. Evolução crustal do noroeste do cráton Amazonico (Amazonas, Brasil) baseada em dados de campo, geoquímicos e geocronologicos. In: Simpósio de Geologia da Amazonia, 13^{o}, Belem, CD-ROM.

Andersen, T., 1986. Compositional variation of some rare earth minerals from the Fen complex (Telemark, SE Norway): implication for the mobility of rare earths in a carbonatite system. Mineral. Mag., 50, 503-9.

Bizzi L.A., Smith B.C., De Wit M.J., Macdonald I., Armstrong R.A., 1994. Isotope characteristics of the lithospheric mantle underlying the SW São Francisco craton margin, Brazil. Intern. Symp. on the Phys. and Chem. of the Upper Mantle, 227–256.

Buckley, H.A., Woolley, A.R., 1990. Carbonates of the magnesite-siderite series from four carbonatite complexes. Mineral. Mag. 54, 413–418.

Censi P., Comin-Chiaramonti P., Demarchi G., Longinelli A., Orue D., 1989. Geochemistry and C-O isotopes of the Chiriguelo carbonatite, northeastern Paraguay. J. South Amer. Earth Sci. 3 (2/ 3), 295-303.

Chakhmouradian, A.R., 2006. High-field-strength elements in carbonatitic rocks: Geochemistry, crystal chemistry and significance for constraining the sources of carbonatites. Chem. Geol. 235, 138–160.

Chakhmouradian, A.R., Reguir, E.P., Kressall, R.D., Crozier, J., Pisiak, L.K., Sidhu, R., Yang, P., 2015. Carbonatite-hosted niobium deposit at Aley, northern British Columbia (Canada): Mineralogy, geochemistry and petrogenesis. Ore Geology Reviews 64, 642–666.

Chakhmouradian, A.R., Zaitsev, A.N., 2012. Rare earth mineralization in igneous rocks: Sources and processes. Elements 8, 347–353.

Comin-Chiaramonti, P., Gomes C. B., Ruberti E., Antonini P., Castorina F., Censi P., 2001. Mato preto alkaline-carbonatite complex: Geochemistry and Isotope (O-C. Sr-Nd) constraints. Geochimica Brasiliensis15. 23-34.

Comin-Chiaramonti, P., Gomes, C.B. (Eds.), 2005. Mesozoic to Cenozoic Alkaline Magmatism in the Brazilian Platform. Edusp/Fapesp, São Paulo, p. 751.

Cooper A.F., Reid D.L., 1998. Nepheline sövites as parental magmas in carbonatite complexes: evidence from Dicker Willem, southwest Namibia. J. Petrol. 39:2123–2136.

1110 Cordeiro, P.F. de O., Brod, J.A., Palmieri, M., de Oliveira, C.G., Barbosa, E.S.R., Santos,
1111 R.V., Gaspar, J.C., Assis, L.C., 2011. The Catalão I niobium deposit, central Brazil:
1112 Resources, geology and pyrochlore chemistry. Ore Geol. Rev. 41, 112–121.

1113 Corrêa, S.L.A. 1996. Evolução geoquímica das crostas lateríticas e dos sedimentos
1114 sobrepostos na estrutura de Seis Lagos (Amazonas). PhD. thesis, Universidade Federal
1115 do Pará (in Portuguese).

1116 Corrêa, S.L.A., Costa M.L., 1997. Mineralogia das crostas lateríticas ferruginosas de Seis
1117 Lagos (Amazonas). Geociências 16 (1), 141-156.

1118 CPRM, 2006. Geologia e recursos minerais do Estado do Amazonas. Map scale
1119 1:1.000.000. Companhia de Pesquisa de Recursos Minerais, Manaus. CD-ROM
1120 (abstract in English).

1121 Davidson, P. M., Symmes, G. H., Cohen, B. A., Reeder, R. J., Lindsey D. H., 1993.
1122 Synthesis of the new compound CaFe(CO3)2 and experimental constraints on the (Ca,
1123 Fe)CO3 join. Geochim. Cosmochim. Acta 46, 1-22.

1124 De Paolo D.J., Wasserburg,G.J.,1976.Nd isotopic variations and petrogenetic models.
1125 Geophysical Research Letters 3, 743-746

1126 Formoso M.L., Nardi, L.V.S., Hartmann, L.A., 1989. Geoquímica dos elementos terras
1127 raras no Brasil. Chapter 7: Fracionamento dos elementos terras raras e suas aplicações
1128 em metalogenese: Comportamento químico em sistemas diversos. 152p.

Gagnon, G., Rousseau, G., Camus, Y., Gagné, J., 2015. Ashram Rare Earth Deposit. Preliminary Economic Assessment. NI 43-101 Technical Report, Prepared by SGS Geostat Canada for Commerce Resources, 202 pp.

Gibson S.A., Thompson R.N., Leonardos O.H., Dickin A.P., Mitchell J.G., 1995. The Late Cretaceous impact of the Trindade mantle plume–evidence from large-volume, mafic, potassic magmatism in SE Brazil. J Petrol 36:189–229.

Giovannini, A.L., 2013. Contribuição à geologia e geoquímica do carbonatito e da jazida (Nb, ETR) de Seis Lagos. Msc thesis Universidade Federal do Rio Grande do Sul (in Portuguese).

Giovannini, A.L., Bastos Neto, A.C., Porto, C.G., Pereira, V.P., Takehara, L., Barbanson, L., Bastos, P.H.S., 2017. Mineralogy and geochemistry of laterites from the Morro dos Seis Lagos Nb (Ti, REE) deposit (Amazonas, Brazil). Ore Geol. Rev. 88, 461–480.

Gittins, J., 1989. The origin and evolution of carbonatite magmas. Bell, K. (ed.) Carbonatites. Genesis and Evolution. London: Unwin Hyman, Rare earth partitioning pp. 580–599.

Gittins, J., Harmer, R.E., 1997. What is ferrocarbonatite? A revised classification. Journal of African Earth Sciences 25, 159–168.

Goldsmith J.R., Graf D.L., Witters J., Northrup D.A., 1962. Studies in the system CaCO3-MgCO3-FeCO3: (1) Phase relations; (2) A method for major-element spectrochemical analysis; (3) Compositions of some ferroan dolomites. J Geophys Res 70:659–688

1150 Goldstein, R. H., Reynolds, T. J., 1994. Systematics of fluid inclusions in diagenetic
1151 minerals. SEPM, Society for Sedimentary Geology, Short Course 31. 199p.

1152 Gomes, C.B., Ruperti, E., Morbidelli, L., 1990. Carbonatite complexes from Brazil: A
1153 review. J. South Am. Earth Sci. 3, 51–63.

1154 Issler, R.S., Silva, G.G. 1980. The seis lagos carbonatite complex. In: Congresso Brasileiro
1155 de Geologia 31, Camboriu, 3, 1564-1572.

1156 Jacobsen S.B., Wasserburg, G.J.,1979. Sm-Nd evolution of chondrites. Earth and Planetary
1157 Science Letters 50,139-155

1158 Justo, L.J.E.C., Souza, M.M., 1986. Jazida de nióbio do Morro dos Seis Lagos, Amazonas.
1159 In: Schobbenhaus, C. and Coelho, C.E.S. (Eds), Principais Depósitos Minerais do
1160 Brasil - Ferro e Metais da Indústria do Aço. Departamento Nacional da Produção
1161 Mineral.

1162 Kapustin, I., 1980. Mineralogy of Carbonatites. Amerind Publishing Co., New Dehli.

1163 Le Bas, M.J., 1981. Carbonatite magmas. Mineral. Mag. 44, 133–40.

1164 Le Bas M.J., 1989. Diversification of carbonatite. In: Bell K (ed) Carbonatites: genesis and
1165 evolution. Unwin Hyman, London, pp 428–447.

1166 Le Bas M.J., 1999. Ferrocarbonatites: geochemistry and magma- fluid state. Mem Geol Soc
1167 India 43:785–802.

1168 Le Bas M.J., 2008. Fenites associated with carbonatites. Canadian Mineralogist 46, 915 –
1169 932.

1170 Le Maitre R.W., 1989. A classification of igneous rocks and glossary of terms. Blackwell,
1171 Oxford.

1172 Le Maitre, R.W., 2002. Igneous Rocks: A Classificarion and Glossary of Terms.
1173 Cambridge University Press. Cambridge UK.

1174 Lemos, R. L., Gaspar, J. C. 1998. Geologia do Complexo Ultramáfico-Alcalino-
1175 Carbonatítico de Maicuru, noroeste do Estado do Pará. In: XL Congresso Brasileiro de
1176 Geologia, Belo Horizonte. Anais do XL Congresso Brasileiro de Geologia, 1998. p.
1177 466.

1178 Lottermoser, B.G., England, B.M., 1988. Compositional variation in pyrochlores from the
1179 Mount Weld carbonatite laterite, Western Australia. Mineralogy and Petrology 38, 37–
1180 51.

1181 Luboldt, R., 1857. Über den Ankerit. Ann. Physik 178, 435–437.

1182 Lumpkin, G.R., Ewing, R.C., 1995. Geochemical alteration of pyrochlore group minerals:
1183 Pyrochlore subgroup 80, 732–743.

1184 Mariano, A.N., Mariano, A. Jr., 2012. Rare earth mining and exploration in North America.
1185 Elements 8, 369–376.

1186 Mitchell, R.H., 2005. Carbonatites and carbonatites and carbonatites. Can. Mineral. 43,
1187 2049–2068.

1188 Mitchell, R.H., 2015. Primary and secondary niobium mineral deposits associated with
1189 carbonatites. Ore Geology Reviews 64, 626–641.

1190 Mitchell, R.H., Smith, D.L., 2017. Geology and mineralogy of the Ashram Zone
1191 carbonatite, Eldor Complex, Québec. Ore Geol. Rev. 86, 784–806.

1192 Onuonga, I.O., Fallick, A.E., Bowden, P., 1997. The recognition of meteoric-hydrothermal
1193 and supergene processes in volcanic carbonatites, Nyanza Rift, western Kenya, using
1194 carbon and oxygen isotopes. J. African Earth Sci. 25, 103–113.

1195 Pell, J., 1996. Mineral deposits associated with carbonatites and related alkaline igneous
1196 rocks. In: Mitchell, R.R. (Ed.), Undersaturated Alkaline Rocks: Mineralogy,
1197 Petrogenesis, and Economic Potential. Mineralogical Association of Canada, Short
1198 Course Series, Winnipeg, pp. 271–310.

1199 Pineau F., Javoy M., Allègre C. J., 1973. Etude systématique des isotopes de l'oxygène, du
1200 carbone et du strontium dans les carbonatites. Geochim. Cosmochim. Acta 37, 2363-
1201 2377.

1202 Pinheiro, S.S.; Fernandes, P. E. C. A.; Pereira, E. P.; Vasconcelos, E. G.; Pinto, A. C.;
1203 Montalvão, R. M. G.; Issler, R. S.; Dallagnoll, R.; Teixeira, W.; Fernandes, C. A. C.
1204 1976. Folha NA.19 Pico da Neblina; geologia, geomorfologia, pedologia, vegetação e
1205 uso potencial da terra. Rio de Janeiro, Cap. 2, p.19-138. (Levantamento de Recursos
1206 Naturais).

1207 Pirajno, F., González-Álvarez, I., Chen, W., Kyser, K.T., Simonetti, A., Leduc, E., leGras,
1208 M., 2014. The Gifford Creek Ferrocarbonatite Complex, Gascoyne Province, Western

Australia: Associated fenitic alteration and a putative link with the ~1075Ma Warakurna LIP. Lithos 202–203, 100–119.

Reis N.J., Szatmari P., Wanderley Filho J.R., 2006. Dois eventos de magmatismo máfico mesozóico na fronteira Brasil – Guiana, Escudo das Guianas: enfoque à região do rifte Tacutu – North Savannas. In: SBG, Cong. Bras. Geol., 43, Aracaju. Resumos Simples.

Roedder, E. 1984. Fluid Inclusions. In: Paul. H Ribbe, Reviews in Mineralogy, Mineralogical Society of America. Vol. 12, 646p.

Ronchi, L.H.; Parente, C. V.; Fuzikawa, K., Bastos Neto, A. 2008. Genetic and metamorphic conditions constrained by fluid inclusions from Paleoproterozoic (c. 1.8 Ga) magnesite ore deposits, NE Brazil Journal of South American Earth Sciences 25 : 492–500.

Rossoni, M.B., Bastos Neto, A.C., Saldanha, D.L., Souza V.S., Giovannini, A.L., Porto, C.G., 2016. Aplicação de técnicas de sensoriamento remoto na investigação do controle do posicionamento do Complexo Carbonatítico Seis Lagos e no estudo do depósito (Nb) laterítico associado (Amazonas, Brasil). Revista Pesquisas 43, 111-125.

Rossoni, M.B., Bastos Neto, A.C., Souza V.S., Marques, J. C., Dantas, E., Botelho, N. F., Giovannini, A.L., Pereira, V. P., 2017. U-Pb zircon geochronologycal investigation on the Morro dos Seis Lagos Carbonatite Complex and associated Nb deposit (Amazonas, Brazil). Journal of South American Earth Sciences, 80, 1-17.

Rukhlov, A.S., Bell, K., Amelin, Y., 2015. Carbonatites , isotopes and evolution of the subcontinental mantle : An overview. Br. Columbia Geol. Surv. Pap. 2015–3, 39–64.

1230 Samoilov, V.S., 1984. Geochemistry of Carbonatites. Nauka, Moscow (in Russ.).

1231 Santos, J.O.S., Hartmann, L.A., Faria, M.S.G., Riker, S.R., Souza, M.M., Almeida, M.E.,
1232 McNaughton, N.J., 2006. A compartimentação do Cráton Amazonas em províncias:
1233 avanços ocorridos no período 2000-2006. In: SBG-NO, 9º Simposio de Geologia da
1234 Amazonia. CD-ROM, Belém.

1235 Santos, J.O.S., Hartmann, L.A., Gaudette, H.E., Groves, D.I., Mcnaughton, N.J., Fletcher,
1236 I.R., 2000. A new understanding of the provinces of the Amazon craton based on
1237 integration of field mapping and U-Pb and Sm-Nd geochronology. Gondwana Res. 3,
1238 453-488.

1239 Santos, J.O.S., McNaughton, N.J., Almeida, M.E., 2009. Magmatismo de idade Sunsás no
1240 centro-norte do cráton Amazonas. In: SBG-NO, 11º Simposio de Geologia da
1241 Amazonia. CD-ROM, Manaus.

1242 Santos, R. V., Clayton, R.N., 1995. Variations of oxygen and carbon isotopes in
1243 carbonatites: A study of Brazilian alkaline complexes. Geochim. Cosmochim. Acta 59,
1244 1339–1352.

1245 Schürman, L. V., Horstmann, U. E., Cloete, H.C.C., Africa, S., 1997. Geochemical and
1246 stable isotope patterns in altered volcaniclastic and intrusive rocks of the Kruidfontein
1247 Carbonatite Complex , South Africa 25, 77–101.Clayton, R.N., 1995.

1248 Silva, A. B. da, 1986. Jazida de nióbio de Araxá, Minas Gerais. (in Principais depósitos
1249 minerais do Brasil. Vol. II, Shobbenhaus C., editor and Coelho C. E. da S., editor)
1250 DNPM, 435 – 453.

1251 Simonetti, A., Bell, K., 1994. Isotopic and geochemical investigation of the Chilwa Island
1252 carbonatite complex, Malawi: evidence for a depleted mantle source region, liquid
1253 immiscibility, and open- system behaviour. Journal of Petrology 35, 1597–1621

1254 Souza, V.S., Souza, A.G.H., Dantas, E.L., Valerio, C.S., 2015. K'Mudku A-type
1255 magmatism in the southernmost Guyana Shield, central-north Amazon Craton
1256 (Brazil): the case of Pedra do Gavião syenogranite. Braz. J. Geol. 45 (2), 293-306.

1257 Taylor, H.P., Frechen, J., Degens, E.T., 1967. Oxygen and carbon isotope studies of
1258 carbonatites from the Laacher See District, West Germany and the Alnö District,
1259 Sweden. Geochim. Cosmochim. Acta 31, 407–430.

1260 Thompson, R.N., Smith, P.M., Gibson, S. a., Mattey, D.P., Dickin, a. P., 2002. Ankerite
1261 carbonatite from Swartbooisdrif, Namibia : the first evidence for magmatic
1262 ferrocarbonatite. Contrib. to Mineral. Petrol. 143, 377–395.

1263 Traversa, G., Barbieri, M., Beccaluva, L., Coltorti, M., La, R., Moro, P.A., Terra, S., La,
1264 R., Moro, P.A., Perugia, U., Università, P., 1996. Mantle sources and differentiation of
1265 alkaline magmatic suite of Lages , Santa Catarina , Brazil 193–208.

1266 Veksler, I. V., Petibon, C., Jenner, G.A., Dorfman, A.M., Dingwell, D.B., 1998. Trace
1267 Element Partitioning in Immiscible Silicate-Carbonate Liquid Systems: an Initial
1268 Experimental Study Using a Centrifuge Autoclave. J. Petrol. 39, 2095–2104.

1269 Verwoerd, W.J., Viljoen, E.A., Chevallier, L., 1995. Rare metal mineralization at the
1270 Salpeterkop carbonatite complex, Western Cape Province, South Africa. Journal of
1271 African Earth Sciences 21, 171–186.

Viegas Filho, J.R., Bonow, C.W., 1976. Projeto Seis Lagos (Internal Report). Companhia de Pesquisa de Recursos Minerais, Manaus.

Wall, F., Williams, C.T., Woolley, A.R., Nasraoui, M., 1996. Pyrochlore from weathered carbonatite at Lueshe, Zaire. Mineralogical Magazine 60, 731-750.

Werner, M., Cook, N.J., 2001. Nb-rich brookite from Gross Brukkaros, Namibia: substitution mechanisms and Fe2+/Fe3+ ratios. Mineral. Mag. 65, 437–440.

Woolley A.R., Buckley H.A., 1993. Magnesite-siderite series carbonates in the Nkombwa and Newania carbonatite complexes. South African Journal of Geology ; 96 (3): 126–130.

Wooley A.R., Kempe D.R.C., 1989. Carbonatites: nomenclature, average chemical compositions, and element distribution. In: Bell K (ed) Carbonatites: genesis and evolution. Unwin Hyman, London, 1–13.

Zaitsev, A. N., Sitnikova, M. A., Subbotin, V. V., Fernandez-Suarez J., Jeffries T. E.. 2004. Sallanlatvi Complex; a rare example of magnesite and siderite carbonatites (in Phoscorites and carbonatites from mantle to mine; the key example of the Kola alkaline province , (eds) Wall F., Zaitsev A. N.) Mineralogical Society Series 10: 201-246.

Zhou W., Van der Voo R., Peacor D.P., Wang D., Zhang Y., 2001. Low-temperature oxidation in MORB of titanomagnetite to titanomaghemite: A gradual process with implications for marine magnetic anomaly amplitudes. Journal of Geophysical Research 106, 6409 – 6421.

4.2 Mineralogy and geochemistry of laterites from Morro dos Seis Lagos Nb (Ti,REE) deposit (Amazonas, Brazil)

Artigo publicado na revista Ore Geology Reviews em agosto de 2017.

Ore Geology Reviews 88 (2017) 461–480

Contents lists available at ScienceDirect

Ore Geology Reviews

journal homepage: www.elsevier.com/locate/oregeo

Mineralogy and geochemistry of laterites from the Morro dos Seis Lagos Nb (Ti, REE) deposit (Amazonas, Brazil)

Arthur L. Giovannini [a], Artur C. Bastos Neto [b,*], Claudio G. Porto [c,d], Vitor P. Pereira [b], Lucy Takehara [e], Luc Barbanson [f], Pedro H.S. Bastos [a]

[a] Programa de Pós-graduação em Geociências, Instituto de Geociências, Universidade Federal do Rio Grande do Sul, Avenida Bento Gonçalves 9500, Porto Alegre 91501-970, RS, Brazil
[b] Instituto de Geociências, Universidade Federal do Rio Grande do Sul, Avenida Bento Gonçalves 9500, 91501-970 Porto Alegre, RS, Brazil
[c] Divisão de Geoquímica, DGM, Companhia de Pesquisa de Recursos Minerais CPRM, Avenida Pasteur 404, Urca, Rio de Janeiro 22290-240, RJ, Brazil
[d] Instituto de Geociências, Universidade Federal do Rio de Janeiro, Cidade Universitária, Ilha do Fundão, Avenida Athos da Silveira Ramos s/n, 21949-900 Rio de Janeiro, RJ, Brazil
[e] Companhia de Pesquisa de Recursos Minerais CPRM, SUREG/PA, Rua Banco da Província, 105, Porto Alegre, RS, Brazil
[f] Institut des Sciences de la Terre d'Orléans, UMR7327, Université d'Orléans/CNRS/BRGM Orléans France, 1A rue de la Férollerie, F45071 Orléans

ARTICLE INFO

Article history:
Received 19 July 2016
Accepted 7 May 2017
Available online 19 May 2017

ABSTRACT

The Morro dos Seis Lagos niobium deposit (2897.9 Mt at 2.81 wt% Nb_2O_5) is associated with laterites formed by the weathering of siderite carbonatite. This iron-rich lateritic profile (>100 m in thickness) is divided into six textural and compositional types, which from the top to the base of the sequence is: (1) pisolitic laterite, (2) fragmented laterite, (3) mottled laterite, (4) purple laterite, (5) manganiferous laterite, and (6) brown laterite. All the laterites are composed mainly of goethite (predominant in the lower and upper varieties) and hematite (predominant in the intermediate types, formed from goethite dehydroxylation). The upper laterites were reworked, resulting in goethite formation. In the manganiferous laterite (10 m thick), the manganese oxides (mainly hollandite, with associated cerianite) occur as veins or irregular masses, formed in a late event during the development of the lateritic profile, precipitated from a solution with higher oxidation potential than that for Fe oxides, closer to the water table. Siderite is the source for the Mn. The main Nb ore mineral is Nb-rich rutile (with 11.26–22.23 wt% Nb_2O_5), which occurs in all of the laterites and formed at expense of a former secondary pyrochlore, together with Ce-pyrochlore (last pyrochore before final breakdown), Nb-rich goethite and minor cerianite. The paragenesis results of lateritization have been extremely intense. Minor Nb-rich brookite formed from Nb-rich rutile occurs as broken spherules with an "oolitic" (or Liesegang ring structure). Nb-rich rutile and Nb-rich brookite incorporate Nb following the [Fe^{3+} + (Nb, Ta) for 2Ti] substitution and both contain up to 2 wt% WO_3. The laterites have an average Nb_2O_5 content of 2.91 wt% and average TiO_2 5.00 wt% in the upper parts of the sequence. Average CeO_2 concentration increases with increasing depth, from 0.12 wt% in the pisolitic type to 3.50 wt% in the brown laterite. HREE concentration is very low.

1. Introduction

Niobium is a lithophile transition metal that is mainly used as ferroniobium alloys in the manufacturing of high-strength low-alloy steels. The global production has quadrupled since 2000, and the demand is projected to rise. The average Nb abundance in the Earth's laterite is 8 ppm (Rudnick and Gao, 2003). Nb is concentrated to potentially economic levels in carbonatite and alkali-silicate igneous rocks and their weathering products. The bulk of global Nb production originates from pyrochlore mineralization associated with carbonatites or their weathering products. Consequently, the majority of currently active Nb exploration projects around the world are focusing on fresh or weathered carbonatites as their primary target (Mitchell, 2015; Chakhmouradian, 2006; Chakhmouradian et al., 2015; Mariano and Mariano, 2012).

The Brazilian reserve of Nb is 10,693,520 t Nb_2O_5 (Pereira, 2014). This country supplies approximately 92% of the world market, and the production essentially comes from the Araxá and Catalão mining districts, whose production capacities are, respectively, 6 Mt/year and 1.3 Mt/year of pyrochlore ore (ROM), with grades between 0.51 wt% and 2.71 wt%. In 2013, these districts produced 73,668 t of niobium contained in Nb_2O_5 concentrate, 46,555 t of Fe-Nb alloy and 6200 t of niobium oxide and derivatives. In addition, Brazil has the Morro dos Seis Lagos

* Corresponding author.
E-mail addresses: arthur_giovannini@hotmail.com (A.L. Giovannini), artur.bastos@ufrgs.br (A.C. Bastos Neto), claudio.porto@cprm.gov.br, porto@geologia.ufrj.br (C.G. Porto), vitor.pereira@ufrgs.br (V.P. Pereira), lucytakehara@gmail.com (L. Takehara), ph_bastos@hotmail.com (P.H.S. Bastos).

http://dx.doi.org/10.1016/j.oregeorev.2017.05.008
0169-1368/

deposit, whose reserves (2897.9 Mt at 2.81% Nb_2O_5, Justo and Souza, 1984, 1986) are still untouched.

The Morro dos Seis Lagos deposit, associated with the Seis Lagos Carbonatite Complex (Issler and Silva, 1980), is located in the Amazon rainforest, in the northwestern part of Amazon State (Brazil). This deposit stands out among the nineteen key examples of Nb deposits associated with carbonatites selected by Chakhmouradian et al. (2015) as being the world's largest Nb deposit and for being the only one associated with siderite carbonatite. To our knowledge, the Morro dos Seis Lagos deposit is the only case of a world-class deposit, no matter the type of metal, associated with siderite carbonatite. Regardless its economic importance and geological uniqueness, few studies have been conducted on the occurrence.

In 2011, this research team began to investigate the carbonatite and associate Nb deposit, followed by a study by Giovannini (2013). The primary objective of the present work is to characterize the texture, mineralogy and geochemistry of the laterites that correspond to the ore of the Morro dos Seis Lagos deposit. The Seis Lagos carbonatite will be the subject to a separate article (Giovannini et al., in prep.). However, to provide a broader vision of the mineralization, some of our data on the geological setting and the carbonatite are presented here.

2. Background information

The Seis Lagos Carbonatite Complex consists of three circular bodies discovered in the 1970's by the RADAM Project (Pinheiro et al., 1976). Some months after the discovery, the Companhia de Pesquisa de Recursos Minerais (CPRM), still the holder of the mineral rights, conducted an exploration program (Viegas Filho and Bonow, 1976) in the major body, the Morro dos Seis Lagos (Six Lakes Hill) (Fig. 1), that evidenced this hill is capped by an iron-rich laterite that corresponds to the Morro dos Seis Lagos Nb deposit. The Morro dos Seis Lagos deposit is located within the Balaio Indigenous Territory, within the Pico da Neblina National Park, and within the Morro dos Seis Lagos Biological Reserve of the Amazonas State. The national park and the biological reserve were created after the discovery of the deposit.

2.1. Geological setting

The Seis Lagos Carbonatite Complex is located in Guyana Shield, in the Amazonas Craton, in the southeastern part of the Rio Negro Province (Santos et al., 2000). The basement is represented by the Cauaburi Complex (Fig. 1), which groups together porphyritic metagranitoids, tonalites, monzonitic orthogneisses, augen gneisses, amphibolites, and migmatites, which are foliated in a NE-SW direction (Almeida et al., 2002, 2007), with an age of approximately 1.8 Ga (Santos et al., 2000, 2003; CPRM, 2006). The wall rock of the carbonatite body is a monzogranitic augen gneiss. The U-Pb age of zircons from the carbonatite provided two populations of ages: ~1.8 Ga and ~1.3 Ga (Rossoni et al., submitted). The age of 1.3 Ga is interpreted as the maximum age for the Seis Lagos Carbonatite Complex.

The emplacement of the carbonatite complex was controlled by an E-W lineament that can be followed in an aeromagnetic maps for more than 400 km. Near the complex, the most prominent

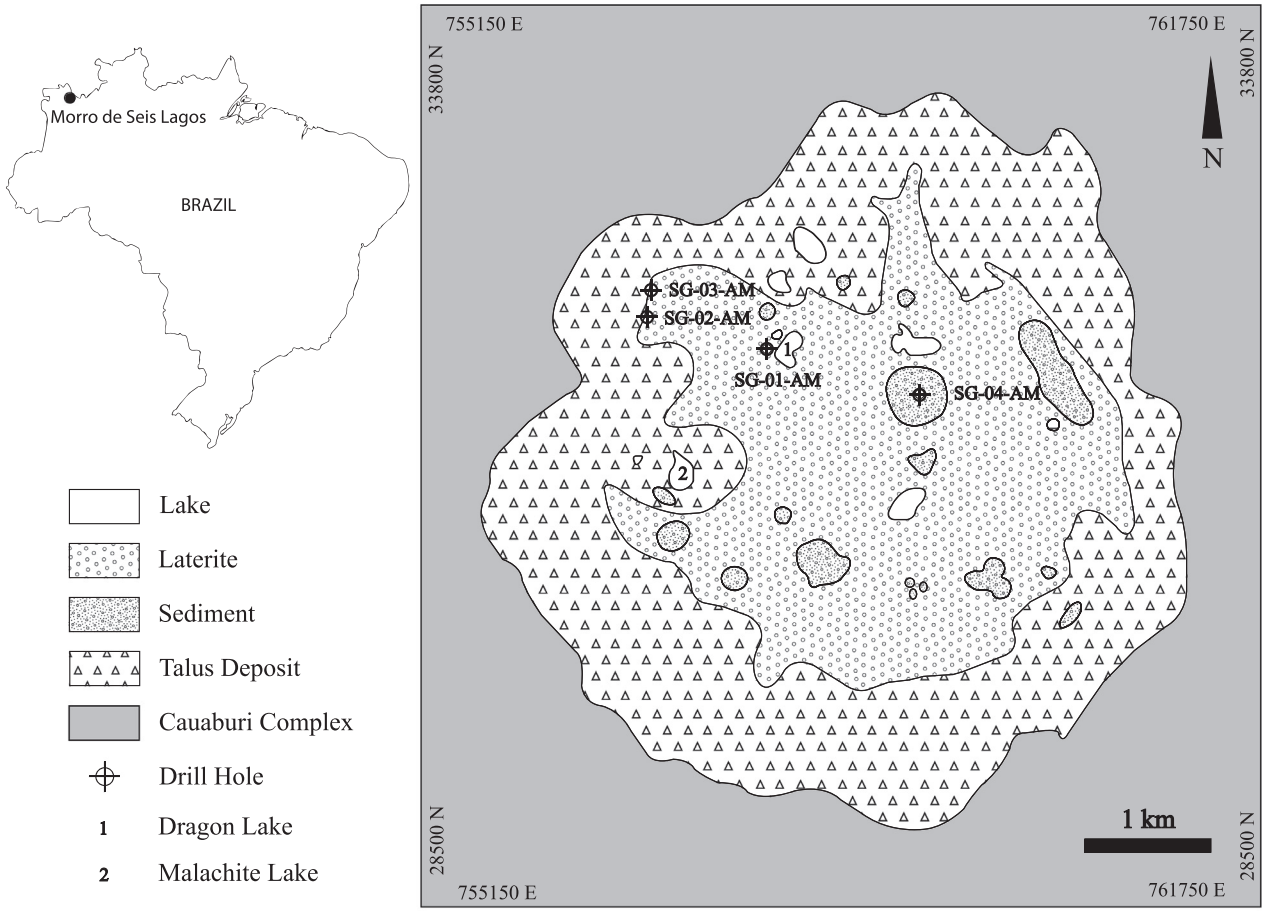

Fig. 1. Location and geological map of the Morro dos Seis Lagos deposit (Viegas Filho and Bonow, 1976).

structures have an E-W direction, although NE-SW and WNW-ESE structures are also found (Rossoni et al., 2016).

The Morro dos Seis Lagos (elevation approximately 400 m) stands out from a fairly flat terrain with an average elevation of approximately 90 m (Fig. 2). The six lakes occur on laterites (Figs. 1 and 3A) or at intermediate altitudes, in talus zones (Figs. 1 and 3B). The circular shape of the Morro dos Seis Lagos body is outlined by the base of the talus deposit (Figs. 1 and 2). However, the shape at a higher elevation (yellow and red) resembles a polygon (Fig. 2). The hill has linear edges on all sides of the polygon, except the NW edge, which presumably had a NE-SW direction but was interrupted by valleys controlled by NNW-SSE structures (Fig. 2). The remarkably rectilinear boundaries suggest that the intrusion was controlled by brittle structures. The relief on the hill is controlled by NNE-SSW structures in the NE part, by a NNE-SSW structure in the central part and by an E-W structure in the southern part (Fig. 2). All the lakes and a number of depressions filled by clays (assigned as sediments in Fig. 1) are associated with these structures (Rossoni et al., 2016).

The top of the lateritic profiles in many places in Amazonia are formed by hardened ferruginous horizons frequently called iron crust or ferricrete, which gives rise to landforms called "iron-hat" (Angélica and Costa, 1993). In this work we use the term laterite, which was originally applied by Buchanan (1807) to a Fe-rich material in Kerala (India). The Morro dos Seis Lagos laterite corresponds to iron crust (Walte, 1915), which, according to Anand and Paine (2002), encompasses the lateritic gravel together and the lateritic duricrust (Anand and Butt, 1988), as well as the ferricrete (Ollier and Galloway, 1990).

The Amazon region has been subjected to deep weathering under tropical conditions since at least the Eocene (Vasconcelos et al., 1994). The resulting regolith profile may be more than 100 m thick showing features that reflect successive weathering episodes such as in the Carajás region where the upper zones of iron crusts are overprinted by a late bauxitization event (Porto, 2016). The iron crusts may occur forming an approximately continuous layer following ancient planation surfaces or, more locally, reflecting bedrock types as in the case of the Seis Lagos Carbonatite Complex and other carbonatite complexes in the Amazon region (Angélica and Costa, 1993). Deep weathering under these conditions may result in the formation of numerous types of ore deposits as in the Carajás region (Porto et al., 2010; Costa, 1997) and elsewhere in the Amazon (Costa et al., 1993).

2.2. Previous investigations of the Morro dos Seis Lagos deposit

The first exploration program (Viegas Filho and Bonow, 1976) consisted of the geological mapping and the drilling of four boreholes (Fig. 1). Borehole SG-01-AM was located over the Nb-mineralized laterite and will be described in detail below. Borehole SG-02-AM intersected non-mineralized laterite (formed from the gneiss) (0–34.00 m), fenitized gneiss (34.00–222.60 m), and carbonatite (221.60–227.70 m); the 227.70–230.85 m interval was not recovered. Borehole SG-03-AM intersected non-mineralized laterite (0–9.00 m), saprolitized gneiss (9.00–50.00 m), and fresh gneiss (50.00–110.00 m).

Borehole SG-04-AM (Fig. 1), located in a depression named the Esperança basin, intersected from the surface to 233.65 m a sedimentary package composed of carbonaceous clays (lake sediments) and from 233.65 to 493.00 m "carbonatic" breccias. These breccias were recognized as carbonatite by Issler and Silva (1980). The palynological analysis of the lake sediments indicates a Neogene age (2.58 Ma to 23.03 Ma) (Viegas Filho and Bonow, 1976). Bonow and Issler (1980) highlighted the anomalous concentrations of rare earth elements (REE) in the carbonaceous clays from 14.65 to 73 m and estimated for this section a reserve of 7.8 Mt at 1.5 wt% REE_2O_3; the mineralogical characteristics of this REE mineralization are not mentioned.

In 1982, CPRM drilled an additional four boreholes in order to calculate the Nb ore reserve (Justo and Souza, 1984, 1986). These boreholes were stopped at depths of approximately 90 m and still within the mineralized laterite. Corrêa (1996) and Corrêa and Costa (1997) conducted studies using surface samples and core pulps from drill cores collected during the first CPRM campaign. They

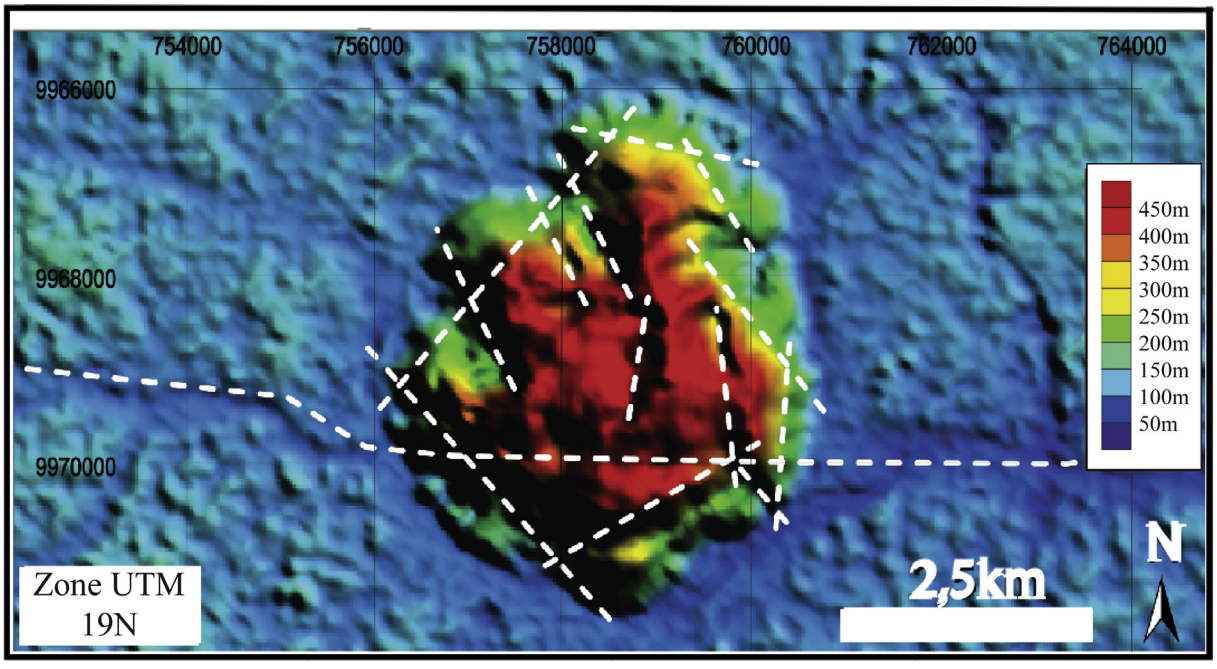

Fig. 2. Digital terrain model of the Morro dos Seis Lagos Carbonatite Body (Rossoni et al., 2016), whose lateritic cover corresponds to the Morro dos Seis Lagos deposit. N-S, NW and NE morphostructures correspond to faults that control the relief on the deposit. The E-W structure controlled the positioning of the carbonatite body; it was reactivated and affected the southern part of the deposit, where it controls a series of depressions filled by sediments (see Fig. 1).

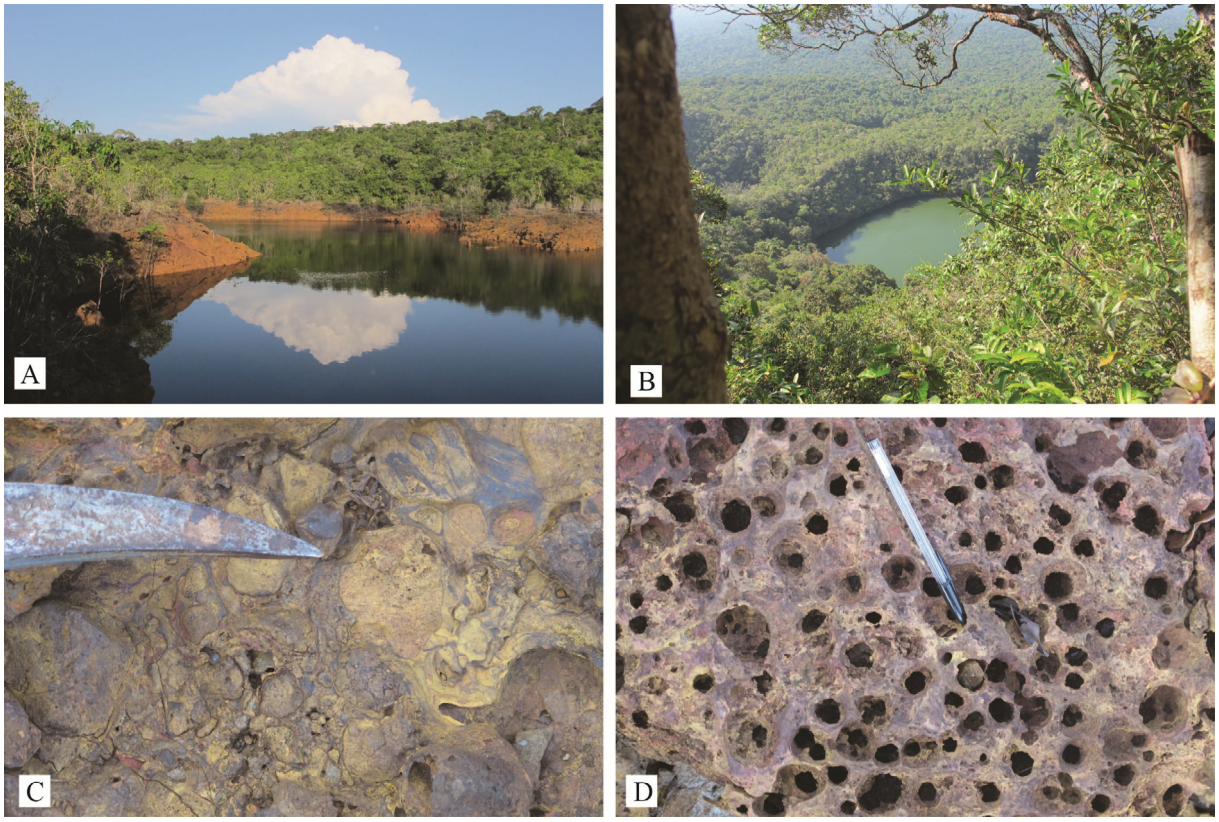

Fig. 3. (A) Dragon lake (located in Fig. 1B) formed in the laterite. (B) Malaquita lake formed in the talus zone, seen from the top of the laterite; on the third plane is observed the plain formed by the basement. (C) Outcroup of laterite with Mn-oxides, near Dragon lake. (D) Laterite with vertical cavities interpreted as ancient pedoturbation, near Dragon lake.

identified mostly the same minerals described in the laterite recognized in this paper. Subsequently, the only investigations of the area have been by Giovannini (2013), which are integrated into this work.

3. Research material and methods

This work is based mainly on drill cores of boreholes SG-01-AM, SG-02-AM, SG-03-AM, and SG-04-AM, which were completely re-logged and sampled in May 2011 at the Departamento Nacional da Produção Mineral office in the city of Manaus, Amazonas State. The cores of the additional four boreholes drilled by CPRM in 1982 were also inspected, but the types of laterite present were found to be similar to those described in borehole SG-01-AM, upon which our analytical work is concentrated, and were thus not further investigated.

The samples were examined using optical microscopy in transmitted polarized and reflected light. X-ray diffraction (XRD) work was performed at the Instituto de Geociências of the Universidade Federal do Rio Grande do Sul (UFRGS) using a Siemens D-5000 diffractometer, equipped with Cu-Kα radiation and a Ni filter in the range from 2° to 70° 2θ with a velocity of 0.02° 2θ per second. X-ray data were processed with "MATCH! Phase identification from powder diffraction" developed by Cristal Impact, and compared to the Crystallography Open Database (COD) database. Semi-quantitative analysis from XRD data was also performed by MATCH! based on peak height, and the results are considered relative amounts. The unit cell parameters were calculated through the UnitCellWin program using the Holland and Redfern method, 1995, goethite was refined in the orthorhombic system using the wavelength 1.540593 Å. In the 95% confidence interval the sigma parameters are as follows: a = 0.00126, b = 0.00033, c = 0.00089. Energy-dispersive X-ray spectroscopy (EDS) analyses were performed at the Centro de Microscopia Eletrônica (CME-UFRGS) using a JEOL-JSM5800 scanning electron microscope (SEM) with a voltage of 20 kV and a spot size of 5 μm.

Electron microprobe wavelength dispersive analyses were first performed at the CNRS/Université d'Orléans ISTO Laboratory (Orléans, France) using a Cameca SX50 instrument. The majority of the study was performed at the Instituto de Geociências of the Universidade de Brasília using a GEOL JXA-8230 instrument. The concentrations of P, Si, Ca, Na, K, Ba, Sr, Al, Fe, Mn, Ti, and F were determined with an accelerating voltage of 15 kV and a beam current of 10 nA. The concentrations of Nb, Ta, W, REE, Y, U, Th, and Pb were determined with an accelerating voltage of 20 kV and a beam current of 20 nA and a spot size of 1 μm.

Whole rock geochemical analyses were provided by ACME Analytical Laboratories Ltd (Canada). Major oxides (SiO_2, Al_2O_3, Fe_2O_3, MgO, CaO, Na_2O, K_2O, TiO_2, P_2O_5, MnO, Cr_2O_3) and trace elements (Ba, Be, Co, Cs, Ga, Hf, Nb, Ni, Rb, Sc, Sn, Sr, Ta, Th, U, V, W, Zr, plus 14 REE and Y) were analyzed by ICP-MS after fusion and nitric acid digestion of 0.2 g aliquots. Another set of trace elements (Ag, As, Au, Bi, Cd, Cu, Hg, Mo, Ni, Pb, Sb, Se, Tl, Zn) was analyzed by ICP-MS after aqua regia digestion of 0.5 g aliquots. Loss on ignition was obtained by weight difference after ignition at 1000 °C. A Leco furnace was used to measure total C and S.

4. Results

4.1. Siderite carbonatite

The carbonatite in drill cores of the borehole SG-02-AM (border of the Morro dos Seis Lagos carbonatite body) is a siderite carbonatite, light grey and highly friable. It is composed by siderite, barite

and gorceixite, and minor monazite and pyrochlore. Siderite (~70 vol%) crystals are euhedral, brownish, with average size of 700 μm. Some crystals are broken and present hematite at the edges and in fractures (Fig. 4A). Barite (~15 vol%) occurs as aggregates of fine crystals (up to 150 μm) that fill the interstices of siderite crystals (Fig. 4A) or in veins in siderite crystals. Gorceixite (up to 7.5 vol%) occurs as the predominant mineral in aggregates (Fig. 4A, B) with monazite and pyrochlore; the crystals are euhedral, with size up to 5 μm. Monazite (up to 1 vol%) occurs mainly as small crystals fibrorradiated with up to 5 μm. More rarely monazite occurs filling gaps between siderite crystals (Fig. 4B). BSE images reveal that this monazite is actually aggregates of very small crystals. Pyrochlore (<1 vol%) occurs as euhedral crystal, with ~3 μm in the aggregates with monazite and gorceixite.

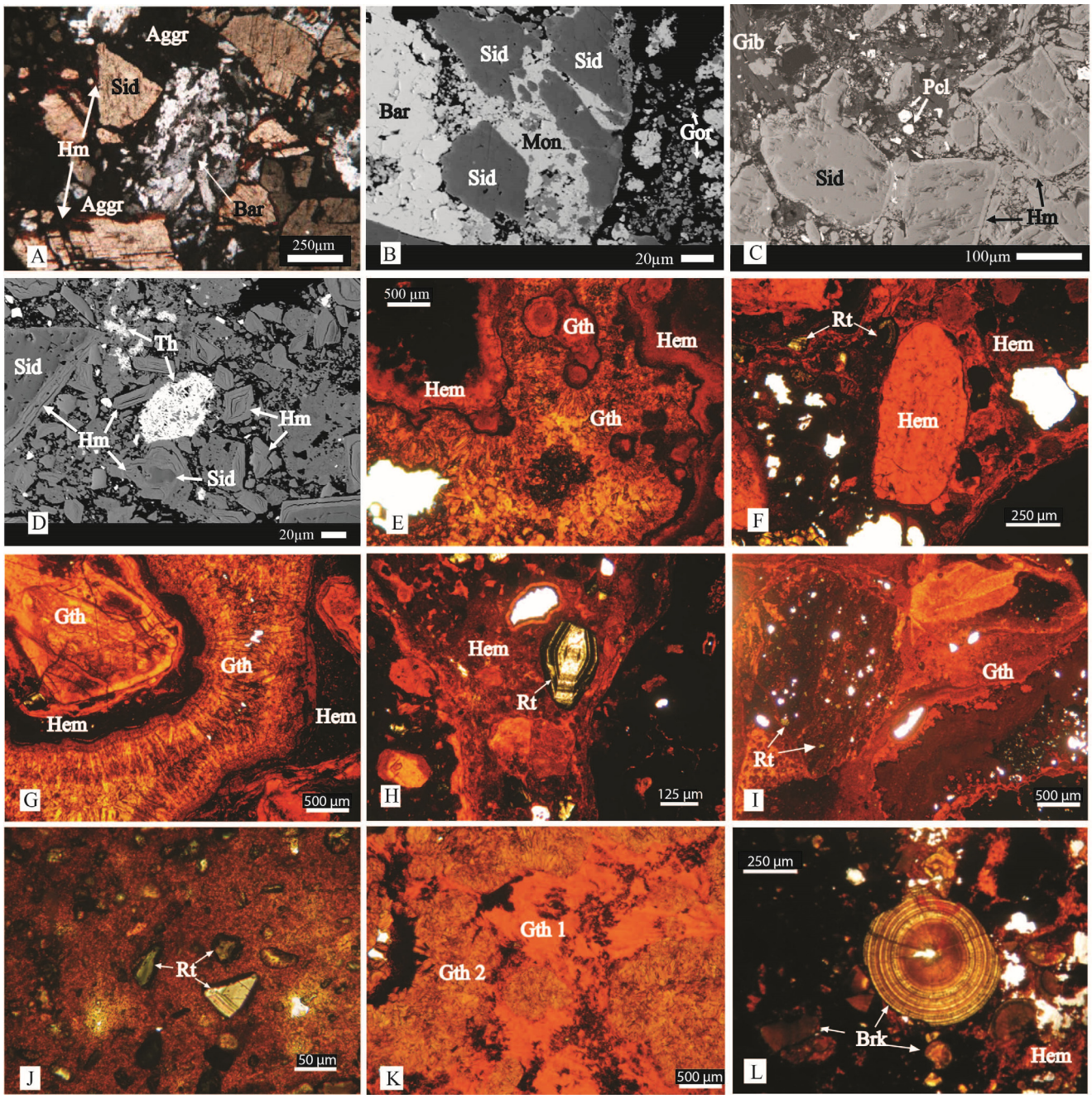

Fig. 4. Microscopic features of the carbonatite and laterites of the Morro dos Seis Lagos deposit. (A) Typical border siderite carbonatite formed by siderite crystals cut by hematite and the matrix formed of aggregates of barite crystals and aggregates (dark zones) of gorceixite, monazite and pyrochlore (PL). (B) BSE image of border siderite carbonatite formed by siderite crystals with monazite rich zones and matrix formed by aggregate rich in gorceixite, cut by a barite vein. (C) Core siderite carbonatite with siderite, pyrochlore euhedral crystals and gibbsite veilets (BSE image). (D) Core siderite carbonatite with siderite crystals within a hematitic matrix with relicts of siderite and thorbastnäsite filling spaces in the matrix (EDS image).: (E) Fibrous goethite filling tubular cavities and as pisolites, darker red Fe-bands are more hematitic (pisolitic laterite). (F) Sub-rounded Fe fragment set in porous matrix, where Fe precipitates in irregular masses and bands, with specks of Nb-rich rutile (fragmented laterite). (G) Fibrous goethite growing over darker red Fe hematitic bands around fragments formed by massive goethite (fragmented laterite). (H) Zoned Nb-rich rutile crystal (fragmented laterite). (I) Specks of Nb-rich rutile grains immersed in a banded ferruginous fragment (fragmented laterite). (J) Zoned and fractured Nb-rich rutile crystals set in a ferruginous cavity (mottled laterite). (K) Early goethite (Gth1) and late goethite (Gth2) (purple laterite); (L) Spherules of Nb-rich brookite (purple laterite). Abbreviations: Sid (siderite), Bar (barite), Mon (monazite), Gor (gorceixite), Aggr. (aggregates), Hmt (hematite), Gth (goethite), Rt (Nb-rich rutile), Brk (Nb-rich brookite).

The carbonatite in the borehole SG-04-AM (central part of the Morro dos Seis Lagos carbonatite body) occurs below the sedimentary package (0–233 m). There is a "transitional zone" between the sedimentary package and the carbonatite. In this zone occur intercalations of: sediments with carbonatite fragments; carbonatite; and sediment and carbonatite fragments deposited in karstic pockets or fractures opened by dissolution of the carbonatite. Below 290 m, the carbonatite intercalations become more abundant, thick and less weathered. Below 400 m, the carbonatite is almost continuous and seems to be unaltered, but evidences of weathering are clear under optical microscope. All carbonatite samples are siderite carbonatite. In less altered zones, the texture is that in the Fig. 4C. In most altered zones, the siderite crystals are partially dissolved, the hematite is much more abundant (Fig. 4D) and the texture both macroscopic and microscopic (optical) resembles that of a breccia.

Siderite grains (weather not partially dissolved) are euhedral, brownish, with sizes up to 500 μm, and frequently present trails of fluid inclusions that can be very abundant. The crystals present hematite at the edges or along fractures. The hematite zone at the edge of siderite crystals has the same texture as the small hematite crystals in the rock matrix; these hematite crystals may contain relicts of siderite (Fig. 4D), indicating that the growth of the matrix hematite occurred simultaneously with alteration on the edge of the large siderite crystals. Pyrochlore, monazite, bastnäsite, and thorbastnäsite were observed only in BSE images. Pyrochlore occurs as euhedral crystals of ~5 μm (Fig. 4C). Monazite occurs as agglomerate with 100 μm made by crystals with 5 μm. Bastnäsite occurs as rare single small (<5 μm) in the matrix. Thorbastnäsite occurs as acicular crystals fulfilling spaces between hematite crystals of the matrix (Fig. 4D). Gibbsite occurs as veinlets that cut siderite and hematite crystals (Fig. 4C). Quartz and gypsum were detected only by DRX in few samples.

All siderite is formed essentially by Fe^{2+} (55.26–66.25 wt% FeO), with minor amounts of Mg^{2+} and Mn^{2+}; Ca^{2+} contents are almost negligible. Siderite from the border carbonatite is richer in Mg (~4.00 wt% MgO) and Mn (5.53–11.82 wt% MnO) than siderite from the core carbonatite (0.19–3.12 wt% MgO; 0.82–2.16 wt% MnO). Pyrochlore from border siderite carbonatite is a Pb-Ba-pyrochlore and from the core siderite carbonatite is a Ce-Ba–pyrochlore with up to 6.0 wt% TiO_2.

Representative compositions of the siderite carbonatite are provided in Table 1. Samples from the core siderite carbonatite are the most affected by weathering because of the carstic processes that

Table 1
Representative compositions of siderite carbonatite from the Morro dos Seis Lagos carbonatite body. Samples 02 are from the borehole SG-02-AM (border); samples 04 are from the borehole SG-04-AM (core).

	Border			Core					
%	02-53C	02-54A	02-54B	04–59	04–72	04–76	04–81	04–19	04–92
SiO_2	0.38	0.32	0.36	0.77	1.29	0.26	0.12	0.48	0.08
Al_2O_3	1.34	0.92	1.34	0.45	1.85	1.1	1.05	0.27	0.33
Fe_2O_3	51.27	55.93	48.64	70.85	63.06	67.24	66.99	66.89	68.18
MgO	3.20	2.75	3.20	1.72	0.99	2.10	2.08	1.44	0.99
CaO	0.30	0.14	0.21	0.31	0.82	0.64	0.47	0.38	0.36
Na_2O	0.01	<0.01	<0.01	0.03	0.16	0.09	0.07	0.12	0.08
K_2O	0.05	0.03	0.05	0.12	<0.01	0.06	0.08	0.11	0.08
TiO_2	0.16	0.17	0.17	0.10	0.83	1.28	1.60	5.28	4.11
P_2O_5	2.01	0.81	1.56	0.13	0.87	0.28	0.27	0.23	0.14
MnO	6.73	11.69	5.10	2.14	2.18	2.06	2.39	1.87	1.49
LOI	24.60	22.80	25.20	22.40	24.30	21.80	22.30	20.00	21.10
Sum	90.08	95.56	85.81	99.01	96.49	97.02	97.48	97.33	97.08
ppm									
Nb	2291.6	1102.8	1532.7	636.3	3240.4	6431.9	6288.9	6152.2	7667.4
Ta	0.2	0.2	1	0.4	2.3	1.8	1.5	1.3	1.9
La	783.4	183.5	483.8	142.2	3795.2	1775.4	930.9	265.7	281
Ce	4604.8	2986.5	2875.2	574.6	7450.3	3625.5	1968.7	848.5	708.6
Pr	884.59	134.12	627.73	114.69	847.98	444.96	281.9	155.58	111.17
Nd	4662.4	709.8	3093.5	709.1	3205.4	2032.1	1578.1	1270.4	870.9
Sm	913.55	139.51	467.91	203.83	573.24	548.58	536.7	705.8	851.88
Eu	225.44	34.18	110.68	49.03	132.95	132.35	117.65	172.56	203.03
Gd	524.8	79.45	277	129.15	293.19	277.02	225.38	298.46	320.32
Tb	79.99	10.32	41.21	9.18	26.21	22.07	17.72	20.2	19.46
Dy	362.69	46.01	186.36	32.21	101.4	76.86	63.14	71.73	60.15
Ho	56.9	7.21	29.04	3.73	11.99	8.52	6.48	7.34	3.97
Er	117.23	17.8	59.77	8.15	27.39	18.02	14.53	17.05	9.97
Tm	14.26	2.2	7.07	1.02	3.42	2.3	1.97	2.52	1.79
Yb	73.58	12.44	35.98	6.55	19.86	13.81	12.78	16.12	11.89
Lu	8.99	1.58	4.54	0.79	2.43	1.67	1.44	1.94	1.33
Y	1292.2	196.2	696	143.7	470.4	392.9	325.8	615.1	375.1
Sc	183	131	113	265	865	847	695	1590	1095
Rb	1.2	0.6	0.8	1.2	0.5	2.6	5.6	6.6	3.4
Ba	>50000	28673	>50000	1434	2743	2607	1928	1481	1485
Sr	982.2	475.3	1028.3	45.6	554.6	282.3	212.4	87	86.9
Pb	1084.8	394.2	873.3	107.3	296.1	112.4	107.9	55.8	232.3
Th	1736.6	538.1	954.1	1895.5	3059.9	2578.8	2807.7	5223	5973.3
U	2.3	0.6	1.6	0.2	2.6	1	1	0.9	1.2
Zr	142.9	102	145.1	155.2	140	103.5	58.6	32.6	34.3
Hf	3.3	2.4	3.6	4.7	2	2.3	1.1	0.8	0.5
Co	25.7	41.9	18.5	59.9	64.7	55.6	58.3	73	69.8
V	243	192	325	64	263	143	134	179	147
W	8.6	8.1	11.2	8.3	38	63.9	65.8	230	159.3
Zn	1268	1682	1242	1254	1194	1513	1780	2296	2999
Cu	1.8	3.6	1.4	0.4	7.5	1.4	1.2	1.6	1.1
F	940	610	1030	269	156	449	476	n.a.	156

formed the Esperança basin. Low total values in samples from the border siderite carbonatite are due to the high values of Ba, above the upper limit of detection (50,000 ppm Ba) in 2 cases. Even so, these results evidence the Seis Lagos siderite carbonatite as an extremely Fe-rich ferrocarbonatite (Fig. 5). Regarding some immobile elements important to this work, it can be noted that core siderite carbonatite has: 0.1–5.28 wt% TiO_2; 636.3–7667.4 ppm Nb; 3455.46–16490.96 ppm REE. The border siderite carbonatite is poorer in all these elements: ~0.16 wt% TiO_2; ~1500 ppm Nb; 4364.62–13312.62 ppm REE.

4.2. Petrography of the laterites

The laterites considered in this work were identified in drill hole SG-01-AM by re-logging of the cores. Six types were defined by descriptions of macroscopic structure, texture, color and mineralogy. They are described sequentially from top to the bottom of the core as follows (Fig. 6): (1) pisolitic laterite; (2) fragmented laterite; (3) mottled laterite; (4) purple laterite; (5) manganiferous laterite; and (6) brown laterite. This drill core had a good recovery until 97.50 m. From there to 255.25 m, the recovery was extremely low. The material was described by Viegas Filho and Bonow (1976) as lateritic crust, but it was not retained in the drill core boxes.

Semi-quantitative analysis of the X-ray diffraction results shows that goethite and hematite are the dominant minerals in the laterites. In the brown laterite, goethite is overwhelmingly dominant over hematite. Hematite becomes relatively more important in the lower purple laterite, manganiferous laterite, and upper purple laterite. From the fragmented laterite upwards, goethite is again enriched in relation to hematite, suggesting that these units were hydrated closer to the surface (Nahon and Tardy, 1992; Nahon, 1986). In the manganiferous laterite, the main Mn-oxide mineral is hollandite, with pyrolusite occurring only in the lowermost sample. Other important minerals detected by XRD in the fragmented laterite are Nb-rich rutile, Nb-rich brookite, florencite-(Ce), and rare ankerite. Nb-rich brookite is also detected in the lower and upper purple laterite. Pyrochlore peaks were detected in the manganiferous laterite, but petrographically this mineral was only observed in the brown laterite. Detailed petrographic analysis was conducted on 35 samples selected along the drill hole length covering the 6 types of laterites (Fig. 6). These data were supported by microprobe/EDS microanalysis as given below.

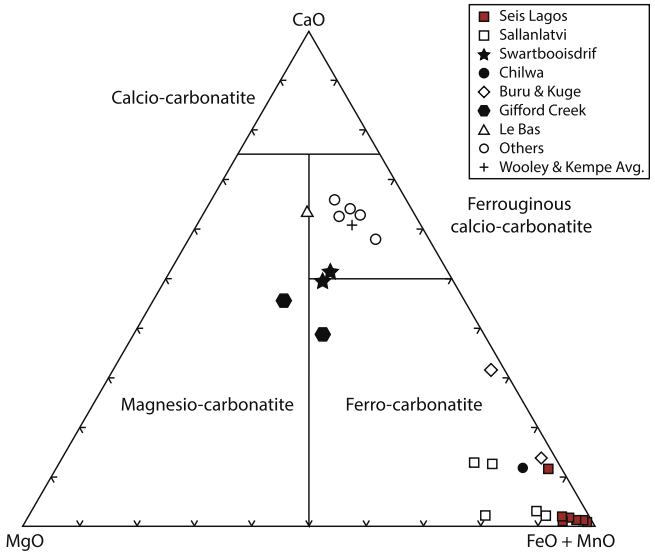

Fig. 5. Seis Lagos siderite carbonatite classification (modified from Gittins and Harmer, 1997). Other ferrocarbonatites: Sallanlatvi (Zaitsev et al., 2004); Swartbooisdrif (Thompson et al., 2002); Chilwa (Simonetti and Bell, 1994); Buru & Kuge (Onuonga, 1997), Le Bas (1981), Gifford Creek (Pirajno et al., 2014), other data from Gittins and Harmer, 1997.

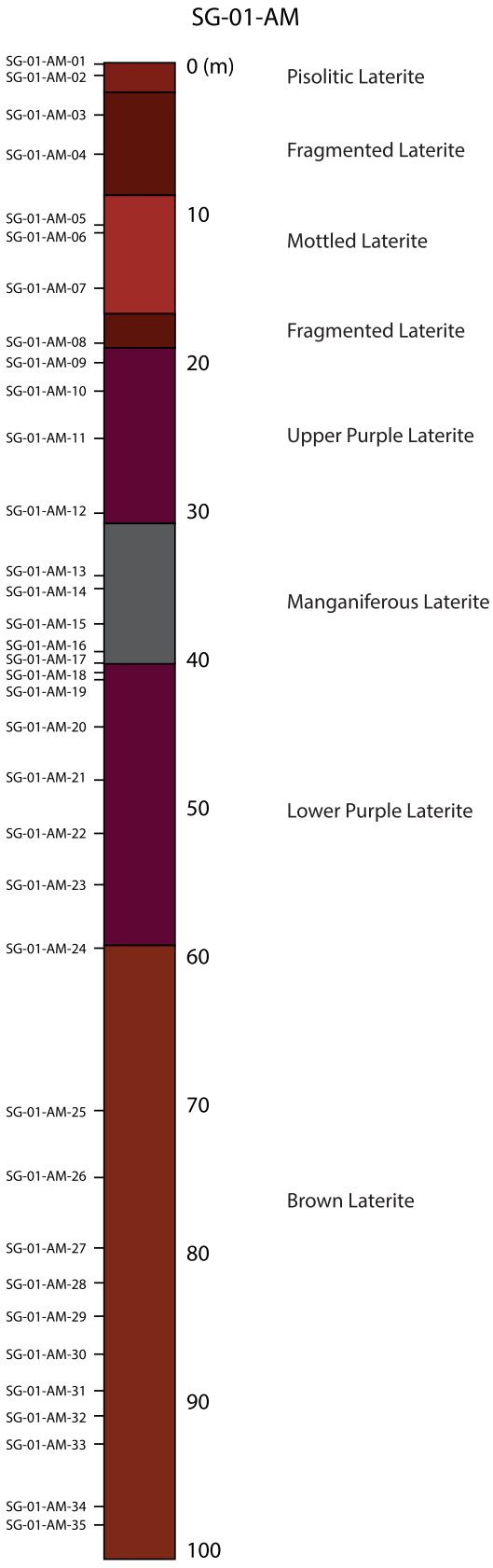

Fig. 6. Distribution of the different types of laterite and studied samples in drill hole SG-01-AM.

4.2.1. Pisolitic laterite

The pisolitic laterite occurs from the surface down to a depth of 2.2 m and is characterized by the predominance of a pisolitic structure alternating with more-massive ferruginous bands of different generations ranging in color from dark brown to light red and orange. Its composition is mostly goethitic (~80 vol%) and hematitic (~20 vol%). The pisolites have an average size of 500 μm, and are composed of fibrous radiating goethite, which also occurs as a filling of tubular cavities (Fig. 4E). Hematite is interpreted to constitute the darker red domain which occurs lining the walls of the cavities forming a substrate onto which more-abundant goethite has precipitated (Fig. 4E). Nb-rich rutile, occurring as broken spherules, is an important accessory. These features suggest that several episodes of iron precipitation in cavities occurred, as these laterites are created closer to the surface (Nahon and Tardy, 1992; Nahon, 1986). As the precipitated Fe phases, mostly as fibrous goethite, became better crystallized, new tubular cavities developed allowing further Fe precipitation. The continuation of this process led to a reworked laterite with an intricate pattern of Fe phases precipitated in micro channels with different degrees of recrystallization, and eventually leading to a pisolitic structure.

4.2.2. Fragmented laterite

The fragmented material occurs in two intervals to a depth of 19.75 m separated by the mottled laterite (Fig. 6). It is characteristically composed of sub-rounded ferruginous fragments in different orientations. These fragments are surrounded by more-porous domains, where Fe phases were precipitated in masses or bands of different compositions (Fig. 4F). The typical fragmented texture may be due to internal collapse close to the surface, where dissolution and pedoturbation have been stronger (Anand and Paine, 2002). Goethite is the dominant mineral, but the relative importance of hematite increases compared to the overlying pisolitic laterite. Goethite occurs around nodules and fragments in a fibroous-radiating pattern or filling cavities over darker red hematitic bands (Fig. 4G). Nb-rich rutile occurs as zoned and fractured greenish grains up to 125 μm in size (Fig. 4H). Also found are small Nb-rich rutile crystals enclosed in a banded ferruginous clast representing reworked tubular cavities where these grains are concentrated (Fig. 4I). Minor Nb-rich brookite occurs as broken spherules. In some Nb-rich rutile, there is a breakdown of the structure in parts of the crystal, with the formation of a gel in which the early formation of spheroidal structures can be seen. Florencite-(Ce) is a minor component; it occurs as veinlets and fills residual spaces in the laterite.

4.2.3. Mottled laterite

The mottled laterite occurs between 9.00 m and 17.00 m. It shows vertical bands alternating between highly ferruginous hematitic dark bands and light red to orange bands of a more goethitic composition. Goethite occurs in botryoidal aggregates sometimes forming a fibro-radiating pattern. Florencite-(Ce) veinlets was identified by SEM images and EDS analysis. Nb-rich rutile (Fig. 4J) occurs as fine-zoned greenish, commonly fractured grains 75 μm in size, preferentially along more-porous tubular cavities filled by iron oxide-hydroxides. In some crystals, two types of malformed spherules occur, both apparently originating from the alteration of Nb-rich rutile. In the first case, it seems that part of the Nb-rich rutile turned into gel in which there is the incipient formation of spherules (Min 1 in Fig. 7A). In the second case, malformed spherules can already be individualized (Min 2 in Fig. 7B and 8A). Columbite is very rare and occurs as a relictal mineral in goethite (Fig. 8B). Veinlets of unidentified mineral rich in Fe and Nb, observed only in SEM images (Fig. 8C), cut the goethite. From this depth downwards, the Al content of goethite, as determined by the electron microprobe, diminishes drastically. This probably reflects the hydrodynamics of the environment under to which these laterites have been subjected to closer to the surface, where Fe is frequently remobilized and reprecipitated as goethite, which is able to incorporate larger quantities of Al compared to hematite (Tardy and Nahon, 1985). Mottling has been interpreted in many lateritic profiles as a result of vegetation root penetration into softer lateritic material before the hardening of the laterite (Anand and Paine, 2002).

4.2.4. Purple laterite

The purple laterite is divided into the upper and lower portions, separated by the manganiferous laterite. The upper portion, between 19.75 m and 31.00 m, is generally more porous, although it contains horizons that are more massive. It is typically more hematitic compared to the laterites above. Hematite occurs as nodules approximately 2 cm in size, while goethite occurs as botryoidal aggregates or forms two generations of fibro-radiating crystals (Fig. 4K). Nb-rich rutile is rare, and some crystals are cut by veinlets composed exclusively by cerianite. An outstanding feature is the more abundant occurrence of spherules of Nb-rich brookite. They occur as nearly perfect rounded grains immersed in the ferruginous matrix (Fig.4L and 8D) or as fractured spherules indicating brittle deformation after formation.

The lower purple laterite is 19 m thick and shows a similar texture to the upper purple laterite but is less porous. Goethite is mostly fibrous. Goethite and hematite are equally abundant. Nb-rich rutile grains are more often fractured, and Nb-bearing brookite spherules are more often malformed and commonly found as 100 μm grains.

4.2.5. Manganiferous laterite

The manganiferous laterite occurs in the interval between 31 m and 40 m. Manganese oxides in large quantities occur as veins or irregular masses that cut through the fabric of the iron-rich material. They are sub-millimeter to- centimeter in size and can

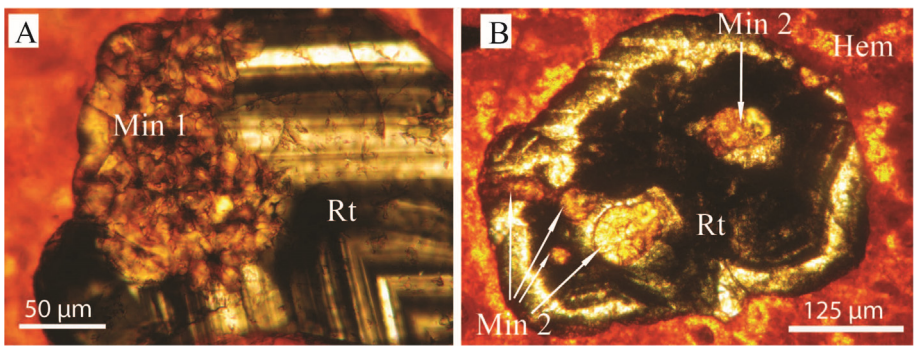

Fig. 7. (A) Zoned crystal of Nb-rich rutile from fragmented laterite with edge turned into gel (Min 1) in which there is the incipient formation of spherules. (B) Spherules of Min 2 (Fe-Nb-rich brookite?) in Nb-rich rutile from mottled laterite.

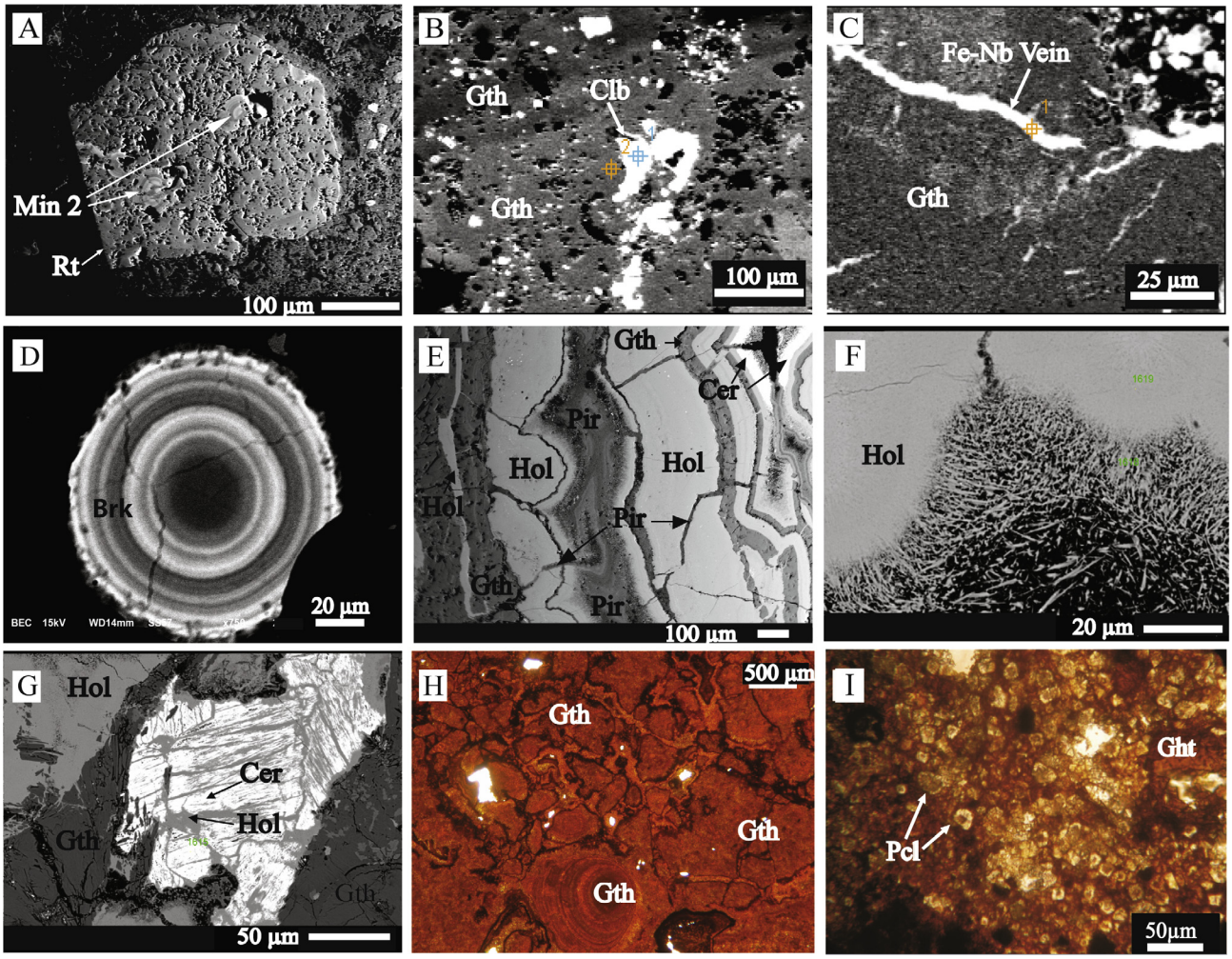

Fig. 8. SEM images and photomicrographys. (A) Nb-rich rutile with spherules of Min2 (Nb-rich brookite?) (mottled laterite). (B) Columbite as a relict mineral in goethite (mottled laterite). (C) Veinlets of unidentified mineral rich in Fe and Nb (mottled laterite). (D) Zoned Nb-rich brookite spherule (purple laterite). (E) Banded Mn-rich veins constituted of hollandite, pyrolusite, cerianite and Mn-bearing goethite (manganiferous laterite). (F) Fibrous growing front of hollandite (Mn laterite). (G) Hollandite and cerianite intergrow (Mn laterite). (H) Typical microscopic texture formed by botryoidal goethite evenly distributed (brown laterite). (I) Pyrochlore small crystals with core transformed to goethite (brown laterite). Abbreviations: Gth (goethite), Min2 (non-identified mineral, possibly Nb-rich brookite), Hol (holandite), Cer (cerianite), Pir (pyrolusite), Pcl (pyrochlore), Clb (columbite), Rt (Nb-rich rutile). (For interpretation of the references to colour in this figure legend, the reader is referred to the web version of this article.)

form banded or brecciated patterns. The modal composition (vol%) of this laterite is hematite (20% to 45%), goethite (30% to 68%), hollandite (~12%), and cerianite (1%). The parageneses in the wider Mn-bearing veins (1 cm) is hollandite, pyrolusite, goethite, and cerianite combined in different ways and proportions. In these veins, hollandite bands (Fig. 8E) are very homogeneous, without mineral inclusions (except for cerianite) and without alteration zones. The growth fronts of hollandite are fibrous (Fig. 8F). Hollandite also commonly occurs in the form of very thin veinlets with complex relationships. Cerianite occurs as thinner and more discontinuous bands in comparison with the other minerals (Fig. 8E) and as numerous small crystals within the hollandite bands, distributed along growing surfaces. By examining these crystals in more detail, an intergrowth between hollandite and cerianite is noted (Fig. 8G). Pyrolusite is the later mineral in the Mn-bearing veins, and occurs filling residual spaces or forming veinlets which crosscut all other minerals (Fig. 8E). Nb-rich rutile in the manganiferous laterite is a trace small (<100 µm) mineral.

4.2.6. Brown laterite

The brown laterite has a characteristically homogeneous texture. It occurs below 58 m, although its entire thickness could not be determined due to the poor drill core recovery. Goethite is the dominant mineral, making up to 96 vol% of the laterite. Compared to the other laterites, this unit has fewer tubular cavities filled with iron precipitates, and the goethite is more evenly distributed (Fig. 8H). This shows that Fe has been less remobilized, suggesting it has developed closer to the carbonatite protolith and therefore represents a less-developed laterite. Nb-rich rutile (fractured) and Nb-rich brookite (malformed spherules) are commonly found as isolated grains, as in the laterites above. This Nb-rich rutile is similar to those described in the other laterites.

Additionally, the Nb-rich rutile was observed in sample SG-01-AM-27 (Fig. 6) and below this depth in two types of associations. In both cases, the Nb-rich rutile is malformed, contains abundant and very small mineral inclusions and the zoning is incipient. In the first association (Fig. 9A), the Nb-rich rutile occurs within a larger crystal of a non-identified mineral that is transformed into smaller crystals of secondary Ce-pyrochlore, Nb-bearing goethite, cerianite (observed only in SEM images), and Nb-rich rutile. In one case, the Nb-rich rutile in this association is euhedral (Fig. 9B). In the second association, which is very rare, malformed Nb-rich rutile occurs together with very small columbite (?) crystals partially altered to goethite. In the goethite matrix, below sample SG-01-AM-27,

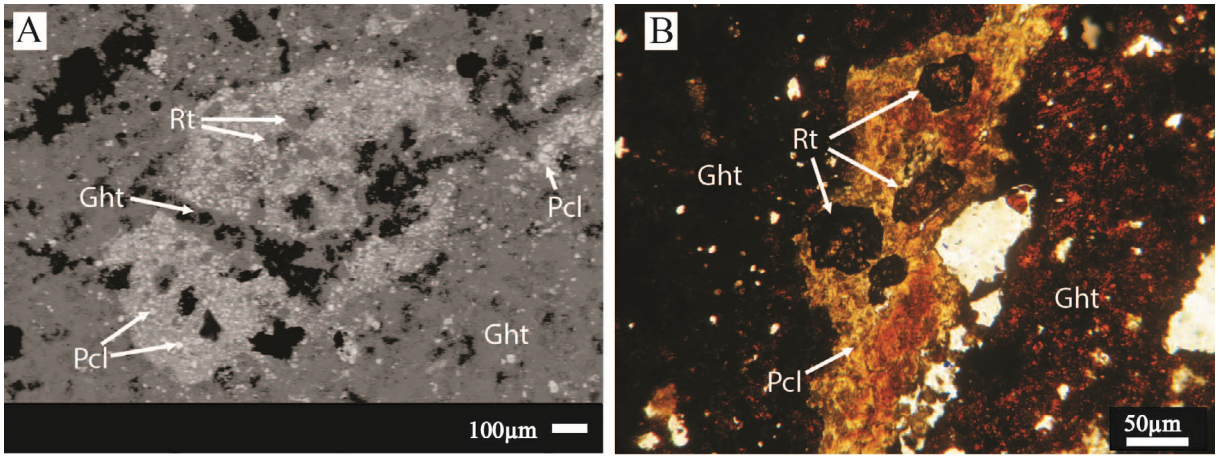

Fig. 9. (A) Former mineral (white area) transformed into smaller crystals of secondary Nb-rich rutile, Ce-pyrochlore and Nb-bearing goethite. (B) Euhedral Nb-rich rutile in association with a deeply weathered Ce-pyrochlore.

small relict isolated crystals of Ce-pyrochlore partially altered to goethite commonly occur. In one case, we observed an association of Ce-pyrochlore and goethite (Fig. 8I) without any other mineral. In all cases, the Ce-pyrochlore presents evidences of weathering (Fig.8I and 9B).

4.3. Esperança basin

The Esperança Basin is the name given by CPRM to a karst depression filled with consolidated clay and carbonate breccia, which occurs in the upper portion of borehole SG-04-AM (Fig. 1C). CPRM subdivided these sediments into: kaolinite clay (9.00–14.65 m), carbonaceous clay (14.65–73.10 m), clay sediment (73.10–99.45 m), very oxidized carbonaceous clay (99.45–123.85 m) and carbonaceous clay plus calciferous clay (123.85–166.55 m). The consolidated clay overlies a sedimentary carbonate breccia (166.55–222.00 m). The carbonatite occurs below 222.00 m. By SEM and XRD, we identified kaolinite as the main constituent of all clay layers, with minor quartz, jarosite, and florencite in all layers. Gibbsite occurs to a depth of 15 m. Hematite occurs just below 70 m. Illite was identified only in highly oxidized carbonaceous clay. Florencite-(Ce), identified by EDS analysis, occurs as aggregates of authigenic crystals.

4.4. Mineralogy

4.4.1. Fe oxides

Fe oxide-hydroxides in the laterites are goethite and hematite, whose relative proportions in the vertical profile invert twice (Fig. 10A). Goethite is predominant in the lower laterites. Hematite becomes predominant in the upper purple laterite. Goethite becomes more abundant again in pisolitic and fragmented laterites, suggesting that these units have been reworked.

Representative compositions of goethite from fragmented, mottled, purple laterites and from Mn-rich rich veins are presented in Table 2. The Al_2O_3 concentration increases upwards up to 6 wt% (Fig. 11). Silica occurs in all goethite crystals, with a concentration up to 0.9 wt% SiO_2, decreasing upward. Niobium and Ti were detected commonly in goethite crystals from the laterites, especially in the fragmented and mottled types, with concentrations up to 3.19 wt% Nb_2O_5 and 2.76 wt% TiO_2. Manganese was detected in only half of the goethite crystals from laterites at low concentrations (~0.15 wt% MnO), reaching up to 1.1 wt% MnO. Tungsten (up to 0.12 wt% WO_3) and Ce (up to 0.2 wt% Ce_2O_3) were detected in most goethites. The goethite associated with Mn-rich veins has a distinctive composition: Mn was detected in all crystals with an average 2.0 wt% MnO. The Ce concentration reaches 0.60 wt% Ce_2O_3, and Nb, Ti, and W were not detected.

4.4.2. Manganes oxides

Hollandite, generally $A_{0\text{-}2}(B^{2+}, B^{3+}, Mn^{4+})_8O_{16}$, has a structure consisting of double chains of MnO_6 octahedra sharing vertices along the *c*-axis which form a square tunnel arrangement The tunnels are partially filled with large *A*-site cations, which may be mono- or divalent (K, Ba, Sr etc). Charge compensation is achieved by substitution for Mn^{4+} at the octahedral *B*-sites by tri- and divalent cations, and some OH^- may replace O^{2-} (Pasero, 2005). Representative compositions of hollandite are provided in Table 3. The structural formula can be written as: $(Ba_{0.78\text{-}0.95}\ K_{0\text{-}0.03}\ Pb_{0\text{-}0.01})$ $(Mn^{4+}_{6.42\text{-}7.18}\ Mn^{2+}_{0.32\text{-}0.85}\ Fe^{3+}_{0.02\text{-}0.90}\ Al_{0.03\text{-}0.36})\ O_{16}$.

4.4.3. Niobium minerals

In the laterites, Nb minerals are Nb-rich rutile (notably predominant), Nb-rich brookite, secondary Ce-pyrochlore (below 79 m depth) and extremely rare columbite. Nb-rich rutile has been known for 150 years, mainly under its currently varietal name ilmenorutile. Nb-rich rutile occurs in all laterites, with the crystals showing omnipresent oscillatory zoning with respect to the Ti, Nb, and Fe contents. The zoning is evident in optical or BSE images. Representative compositions and structural formulae are provided in Table 4. The main oxides have the following ranges: TiO_2 (57.84–80.92 wt%), Nb_2O_5 (11.26–22.23 wt%), Fe_2O_3 (8.96–14.95 wt%), up to 1.27 wt% WO_3, and up to 1.09 wt% SiO_2. The average structural formula is: $(Ti_{0.75}\ Fe_{0.13}\ Nb_{0.11}\ Si_{0.01}\ W_{0.01})O_2$. A distinctive feature of the Nb-rich rutile is the absence of Ta corroborated by whole-rock analyses (Ta < 2.3 ppm in carbonatite and Ta < 0,70 ppm in the laterites).

The Nb-rich rutile of the brown laterite, which occurs in paragenesis with Ce-pyrochlore, Nb-bearing goethite and cerianite, has composition (Table 4) very similar to that of the isolated crystals of Nb-rich rutile. Fig. 12A suggests that there are two compositional types with respect to the main elements (Ti, Fe and Nb), but more analysis is needed to confirm this division.

Nb-rich brookite occurs in all types of laterites in small amounts, except in the purple variety, in which there is a concentration of spherules, in contrast to the rarity of Nb-rich rutile in this unit. Representative compositions and structural formulae are provided in Table 5. The main oxides have the following ranges: TiO_2 (68.23–82.99 wt%), Nb_2O_5 (10.43–16.446 wt%), Fe_2O_3 (7.65–13.87 wt%), up to 1.2 wt% WO_3, and up to 0.97 wt% SiO_2. The aver-

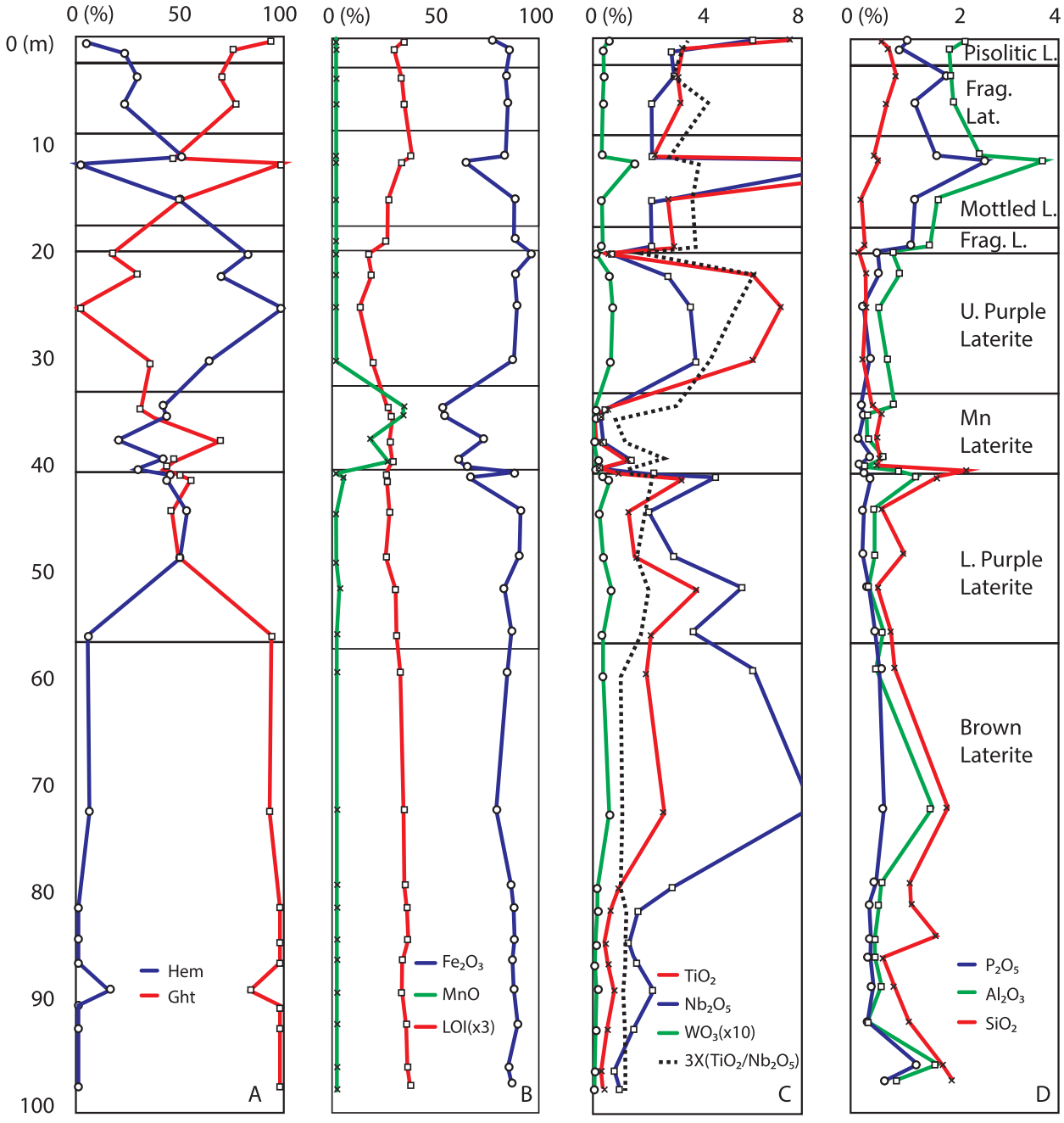

Fig. 10. Vertical distribution of (A) hematite and goethite, (B) Fe_2O_3, MnO and LOI, (C) TiO_2, Nb_2O_5, WO_3 and TiO_2/Nb_2O_5 and (D) P_2O_5, Al_2O_3 and SiO_2 in laterites from the Morro dos Seis Lagos deposit.

age structural formula is $(Ti_{0.79}\ Fe_{0.11}\ Nb_{0.08}\ Si_{0.01}\ W_{0.01})O_2$. Compared with Nb-rich brookite, the Min 2 spherules are richer in Nb and Fe and poorer in Ti. This is likely a Nb-Fe-rich brookite.

These spherules exhibit structures similar to Liesegang rings. Some of these structures are perfect, apparently without any interference in growth. They also occur in pairs of rings with initial growth from two distinct nuclei that do not touch, i.e. they began to grow simultaneously. Some fragments have overgrowth of other bands. The colors of the bands reflect compositional variations. The BSE images show that these bands are composed of other minor bands.

The best charge balance for Nb-rich rutile and Nb-rich brookite was achieved with all iron as Fe^{3+}. Nb-rich rutile incorporates Nb following the coupled substitution [Fe^{3+} +(Nb, Ta) for 2Ti] (Fig. 12B) with few deviations from the ideal. Nb-rich brookite presents a significant deviation, while Min 2 diverges from this substitution.

Representative compositions of the Ce-pyrochlore are given in Table 6. Many crystals present low total and are very poor in Na and Ca corroborating the petrographic evidences of weathering (Wall et al., 1996). Fluorine was not detected. Ce_2O_3 varies from 12.16 to 28.25 wt%. Pb concentration varies from 1.4% a 11.36 wt %. Ba concentration varies from 0.18 to 4.61 wt%. The correlation between vacancy at A-site, loss of Ce and the vertical distribution of the samples is very prominent (Fig. 13).

4.4.4. Rare earth elements minerals

The Rare Earth Elements (REE) minerals in the laterites are cerianite and florencite-(Ce). REE were also detected in low concentrations in several microprobe analyses performed in amorphous,

Table 2
Representative compositions and structural formulae of Fe oxides from the Morro dos Seis Lagos deposit. Samples from borehole SG-01-AM (Fig. 6): fragmented crust (sample 04), mottled crust (sample 06), upper purple crust (sample 12), manganiferous crust (sample 15) and brown crust (samples 27 and 31).

	04.1	04.2	06.1	06.2	12.1	12.2	15.1	15.2	27.1	31.1
Crust	Fragmented		Mottled		Upper Purple		Manganiferous		Brown	
Fe_2O_3	86.86	90.68	90.92	91.12	94.10	98.71	86.08	85.48	90.74	80.90
Al_2O_3	1.30	n.d.	0.34	0.07	0.21	0.05	0.15	0.20	0.06	0.13
SiO_2	0.10	0.69	0.08	0.08	0.20	0.08	0.53	0.44	0.35	0.80
MnO_2	0.22	n.d.	n.d.	n.d.	0.52	0.12	2.03	2.26	n.d.	n.d.
TiO_2	0.10	0.09	0.11	0.02	n.d.	n.d.	n.d.	n.d.	1.53	0.16
Nb_2O_5	0.16	0.01	n.d.	0.04	0.05	n.d.	n.d.	n.d.	3.19	0.25
Total	88.74	91.47	91.45	91.33	95.08	98.96	88.79	88.38	95.87	82.24
Structural Formulae										
Fe^{3+}	1.936	1.958	1.981	1.992	1.968	1.991	1.908	1.905	1.871	1.933
Al	0.045		0.012	0.002	0.007	0.002	0.005	0.007	0.002	0.005
Si	0.004	0.030	0.003	0.003	0.008	0.003	0.023	0.020	0.014	0.038
Mn^{4+}	0.005				0.010	0.002	0.041	0.046		
Ti	0.002	0.002	0.002	0.000					0.032	0.004
Nb	0.002	0.000		0.001	0.001				0.040	0.004
Total	1.994	1.990	1.998	1.998	1.994	1.998	1.977	1.978	1.959	1.984

Atoms per formula unit calculated on the basis of 3 oxygens.

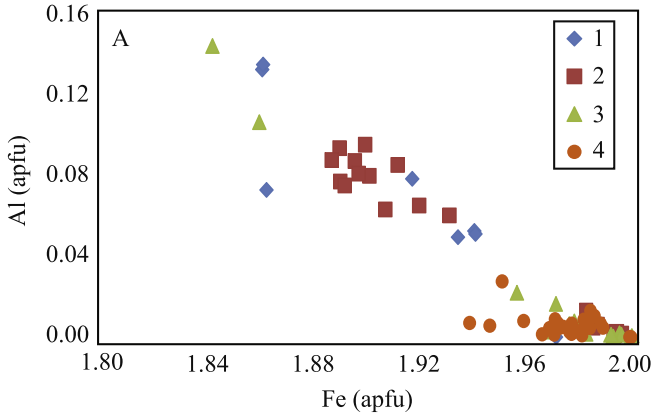

Fig. 11. Binary diagrams for Fe oxides. Al vs Fe. (1) Fragmented laterite; (2) mottled laterite; (3) upper purple laterite; (4) goethite from Mn-rich veins in manganiferous laterite.

poorly crystalline and crystalline Fe-oxide-hydroxides. Ce, with a concentration up to 0.2 wt% Ce_2O_3, is the main REE in these minerals. Microprobe analysis show that both cerianite associated with hollandite in the manganiferous laterite and cerianite in veinlets from the purple laterite are almost entirely composed of Ce with low concentrations of Gd, Nd, Yb, and Lu; F is present in many cases.

Florencite occurs in the upper laterites, where it was detected only by XRD, and in sediments of the Esperança basin. EDS analysis indicates that Ce is the main REE in almost all cases. Nd is always present but is the main REE only in a few cases.

4.5. Geochemistry

The compositions of representative samples of all types of laterites are presented in Table 7. The LOI values range from 6 to 10 wt% (Fig. 10B), and reflect the goethite abundance. All samples from the laterite profile have high iron content (~80 wt% Fe_2O_3), except the manganiferous type, which can contain up to 32 wt% MnO, diluting the iron concentration to as low as nearly ~55 wt% Fe_2O_3 (Fig. 10B). MgO, CaO, Na_2O and K_2O occur with very low concentrations or are not detected (<0.01 wt%).

The Al_2O_3 content of the fragmented, mottled and pisolitic laterites may reach 3.6 wt% (Fig. 10D). A similar enrichment trend

Table 3
Representative compositions and structural formulae of hollandite from manganiferous crust from the Morro dos Seis Lagos deposit. Samples located in borehole SG-01-AM (Fig. 6).

	13.01	13.02	15.01	15.02	15.03	15.04	15.05	17.01
K2O	0.07	0.05	0.01	0.11	0.07	0.08	0.16	0.19
BaO	17.22	14.66	17.59	16.88	16.43	15.94	16.52	14.62
PbO	0.03	0.20	n.d.	0.04	n.d.	n.d.	n.d.	0.13
MnO	6.46	6.50	2.72	7.15	7.05	6.53	7.35	6.66
MnO2	70.99	75.89	67.47	73.24	73.30	73.73	73.51	75.74
Al2O3	1.10	0.43	2.22	0.72	0.46	0.50	0.40	0.17
Fe2O3	1.82	0.18	8.72	0.58	0.62	1.24	0.31	0.38
Total	97.69	97.91	98.73	98.72	97.93	98.02	98.24	97.89
Structural Formulae								
Mn2	0.758	0.740	0.317	0.824	0.823	0.756	0.848	0.751
Mn4	6.870	7.172	6.419	6.998	7.037	7.034	7.055	7.183
Al	0.181	0.069	0.360	0.118	0.076	0.081	0.065	0.027
Fe	0.192	0.019	0.904	0.060	0.064	0.129	0.032	0.039
ΣB	8.000	8.000	8.000	8.000	8.000	8.000	8.000	8.000
K	0.013	0.009	0.001	0.020	0.012	0.014	0.028	0.033
Ba	0.944	0.784	0.949	0.913	0.893	0.861	0.897	0.784
Pb	0.001	0.007		0.002				0.005
ΣA	0.958	0.800	0.950	0.935	0.905	0.875	0.925	0.822

n.d. = not detected; Mn^{2+}/ Mn^{4+} and analysis totals calculated on a basis of stoichiometry (ΣB = 8; O = 16).

Table 4
Representative compositions and structural formulae of Nb-rich rutile from the borehole SG-10-AM (Fig. 6) from the Morro dos Seis Lagos deposit: fragmented crust (sample 4), mottled crust (5 crystals in sample 6) and upper purple crust (sample 12) and brown crust (5 crystals in sample 34).

Nb-rich rutile								Nb-rich rutile (brown crust)				
	4.1	6.1	6.2	6.3	6.4	6.5	12.1	34.1	34.2	34.3	34.4	34.5
Fe_2O_3	8.96	12.18	13.94	11.12	14.95	10.52	17.78	14.92	11.64	11.67	11.18	12.43
SiO_2	n.d.	1.09	0.45	0.63	0.62	0.52	1.00	0.33	0.27	0.34	0.30	0.28
TiO_2	80.92	70.73	68.92	72.45	66.26	74.08	57.84	58.26	67.34	68.66	66.92	57.86
Nb_2O_5	11.26	16.59	19.08	16.71	18.89	14.89	22.23	25.46	19.16	17.47	20.28	27.61
WO_3	0.16	0.35	0.31	0.70	0.33	0.64	1.27	0.20	0.33	0.19	0.85	0.62
Total	101.30	100.94	102.70	101.61	101.05	100.65	100.12	99.17	98.74	98.33	99.53	98.80
Structural Formulae												
Fe^{3+}	0.093	0.130	0.148	0.118	0.162	0.112	0.198	0.168	0.128	0.128	0.123	0.140
Si		0.015	0.006	0.009	0.009	0.007	0.015	0.005	0.004	0.005	0.004	0.004
Ti	0.841	0.753	0.729	0.766	0.715	0.786	0.643	0.653	0.740	0.754	0.732	0.653
Nb	0.070	0.106	0.122	0.106	0.123	0.095	0.149	0.172	0.127	0.115	0.134	0.187
W	0.001	0.001	0.001	0.003	0.001	0.002	0.005	0.001	0.001	0.001	0.003	0.002
Cations	1.005	1.005	1.006	1.002	1.010	1.002	1.010	0.999	1.000	1.003	0.996	0.986

n.d. = not detected; Atoms per formula unit calculated on the basis of two oxigens.

is observed for P_2O_5 (Fig. 10D), which may reach up to 2.5 wt% in the mottled variety. Below that, it is typically <0.6 wt%, which is consistent with the low levels of P_2O_5 (<2.0 wt%) in the primary carbonatite. The contents of Zr, Hf, and U follow similar trends. The MnO content (Fig. 10B) is generally low, except for the manganiferous laterite (up to 32.6 wt%), with concomitant enrichment in Ba, Co, Cd, and Tl. Cerium is also enriched in the manganiferous laterite, but there are also similarly rich Ce intervals in the lower purple and brown varieties. From the fragmented laterite upwards, Ce is depleted. The other LREE are generally depleted in the manganiferous laterite but enriched in the fragmented, mottled and pisolitic varieties. In the lower purple and brown laterites, the LREE show a more variable concentration. The concentrations of HREE and Y tend to be higher in the lower purple and upper portions of the brown type, but above it, including the manganiferous variety, they show an upward depletion trend.

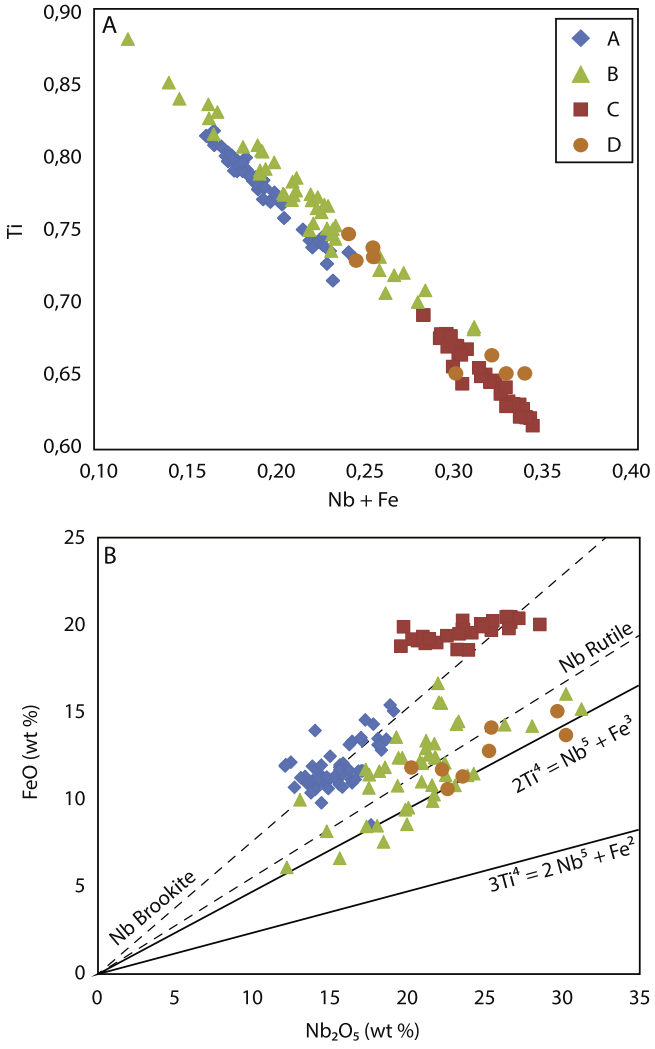

Fig. 12. Binary diagrams for Nb-rich rutile, Nb-rich brookite, and Min 2 (see text). (A) FeO (wt%) vs Nb_2O_5 (wt%). (B) Ti vs Nb + Fe^{3+}. (A): Nb-rich brookite; (B) Nb-rich rutile (isolated crystals all laterites); (C): Min 2; (D): Nb-rich rutile associated with Ce-pyrochlore.

Niobium and Ti are typically accompanied by W. High concentrations of these elements occur in the upper and lower purple laterites and upper portions of the brown type (Fig. 10C) - for instance, sample SG-01-AM-11 (Tab. 7) with 13217.10 ppm Nb, 7.23 wt% TiO_2, and 380.20 ppm W – and may reflect the presence of concentrated Nb-Ti-W mineralization in the carbonatite. In the fragmented laterite and upwards, they are enriched, in common with Al, P, Zr, Hf, and U.

The parallelism between the TiO_2/Nb_2O_5 ratios and the textural/mineralogical classification of the laterites is remarkable. In the reworked laterites (pisolitic, fragmented, and mottled), the TiO_2/Nb_2O_5 ratios are approximately 1 (Fig. 10C). In the upper purple laterite, the TiO_2/Nb_2O_5 ratios are approximately 2. In the lower purple laterite and brown laterite the TiO_2/Nb_2O_5 ratios invert to ~0.70 and ~0.35 respectively.

The upward enrichment of Al, P, Zr, Hf, U, and LREE observed in the fragmented laterite suggests that these elements are residually enriched closer to the surface. However, the enrichment of Al and P may also be influenced by their incorporation into goethite, although P may also occur as secondary phosphate minerals.

Fig. 14 compares the normalized distribution diagrams of lanthanides for all types of laterite, the siderite carbonatite and the clays from Esperança Basin. As is characteristic of carbonatites, the distribution pattern of the siderite carbonatite (Fig. 14) is strongly enriched in LREE, but with an unusual feature represented by a relative depletion of the La, Ce, and Pr. The siderite carbonatite has no Eu anomaly. The brown and the lower purple laterites (Fig. 14C, D) – the lowest laterites in the profile and, therefore, the least evolved – display similar REE distribution; they differ from this rock in being slightly poorer in REE (from Pr to Lu) and by the presence of a positive Ce anomaly which is more pronounced in the brown laterite. The manganiferous and upper purple laterites (Fig. 14B) have similar REE distribution patterns; with

Table 5
Representative compositions and structural formulae of Nb-rich brookite from the upper purple crust from the Morro dos Seis Lagos deposit. Samples from borehole SG-01-AM (Fig. 6): 3 crystals in sample 10; 2 crystals in sample 12.

	Nb-rich brookite				
	10.1	10.2	10.3	12.1	12.2
Fe_2O_3	12.08	12.53	9.86	10.89	10.69
SiO_2	0.97	1.24	0.64	0.72	0.78
TiO_2	69.60	73.45	76.68	76.93	78.02
Nb_2O_5	16.03	12.09	11.77	10.75	10.43
WO_3	0.69	0.32	0.74	1.10	0.80
Total	99.37	99.63	99.69	100.39	100.72
Structural Formulae					
Fe^{3+}	0.131	0.134	0.105	0.115	0.112
Si	0.014	0.018	0.009	0.010	0.011
Ti	0.753	0.783	0.814	0.812	0.818
Nb	0.104	0.078	0.075	0.068	0.066
W	0.003	0.001	0.003	0.004	0.003
Cations	1.005	1.014	1.006	1.009	1.010

Atoms per formula unit calculated on the basis of two oxigens.

regard to the carbonatite, these are depleted in REE (from Pr to Lu), show an accentuated positive Ce anomaly and the presence of a positive Gd anomaly (Fig. 14B). The pisolitic and fragmented laterites have similar REE patterns (Fig. 14A); with regard to the carbonatite they are poorer in REE from Pr to Lu; they have small positive Ce and Gd anomalies. The REE patterns of mottled laterite and of clays from Esperança basin are similar; they are richer in LREE with respect to all of the laterites. In case of La and Ce, there is an enrichment compared to the primary rock and no positive Ce and Gd anomalies. The upper laterites (pisolitic, fragmented and mottled) and the clays of Esperança Basin are the poorer in HREE (Fig. 14A).

4.6. Metals of economic interest

The ranges of variation and the average concentrations of oxides representing potential economic interest for each laterite are shown in Table 8. Although our sampling was not made specifically for economic evaluation, we draw attention to the similarity between the Nb_2O_5 concentrations we obtained and the average concentration for the Morro dos Seis Lagos deposit obtained by CPRM in the 1970 s (2.81 wt% Nb_2O_5, Justo and Souza, 1984).

The TiO_2 concentrations (Table 8) are quite significant, especially to a depth of 30 m (pisolitic, fragmented, mottled and upper purple laterites), with an average of 5.00 wt% in this section. From 31 m to 70 m [manganiferous, lower purple, and brown (upper portion) laterites], the TiO_2 concentrations decrease.

The W concentrations of 250 ppm in the upper laterites (Table 7) are associated with Nb-rich rutile, which contains up to 2 wt% WO_3, so the possibility of W extraction as byproduct may be considered. Zinc (~1500 ppm in the middle and lower laterites) and Th (~2500 ppm in all laterites) (Table 7) may also be of interest to exploration, but further mineralogical studies are required.

Ce is by far the most abundant REE in the laterites, in which the CeO_2 concentrations range from 0.12 to 3.50 wt%. The increase in concentration with increasing depth is very clear, ranging from an average of 0.15 wt% in the pisolitic laterite up to 1.07 wt% in the brown laterite (Table 8). The sum of all other LREE ranges from an average of 0.13 wt% $LREE_2O_3$ in the manganiferous laterite up to 0.63 wt% $LREE_2O_3$ in the mottled laterite; La is the most abundant, whose content ranges from 0.02 to 0.90 wt% La_2O_3 (average all laterites: 0.20 wt% La_2O_3). Nd may also have economic interest. The HREE concentration is very low, as commonly occurs in carbonatites and associated deposits.

5. Discussion

The most abundant carbonates in carbonatites are calcite and dolomite, whereas ankerite, siderite, magnesite, and rhodochrosite are relatively rare. Other typical rock-forming constituents include apatite, magnetite, and ferromagnesian silicates (Mitchell, 2005; Woolley and Kjarsgaard, 2008; Chakhmouradian and Zaitsev, 2012). These minerals are virtually absent at the Seis Lagos Carbonatite Complex where siderite is the only rock-forming mineral. The revised nomenclature for ferrocarbonatites (Gittins and Harmer, 1997) reclassified all previous ferrocarbonatites, except three African carbonatites: Buru, Chilwa and Kugwe. Subsequently, others ferrocarbonatites have been recognized: Swartbooisdrif (Thompson et al., 2002), Sallanlatvi (Zaitsev et al., 2004), and Gifford Creek (Pirajno et al., 2014). These ankerite- and siderite-carbonate rocks mainly occur as a minor component in many carbonatite complexes dominated by Ca-Mg carbonatite. The Sallantvi Complex is the one with the largest bodies of siderite carbonatite (two main bodies with about 500 m × 100 m in the central part of the complex) that are mineralized in pyrochlore, but have no associated lateritic deposit. The ferrocarbonatites are generally seen as the low-temperature product of fractional crystallization of Ca-Mg carbonate melts, nevertheless, some carbonatite specialists are sceptical as to whether Fe-rich carbonate magmas exist (Thompson et al., 2002). The siderite carbonatite of Sallantvi precipitated from carbo-hydrothermal fluid (Zaitsev et al., 2004). The origin of the Seis Lagos siderite carbonatite is uncertain at this point and will be the subject of a separate contribution.

With regard to Ti and Nb concentrations in siderite carbonatite, most samples from the central part of the carbonatite body (up to 5.28 wt% TiO_2 and up to 7667 ppm Nb, Table 1) allow consider this rock as a viable protolith to the deposit. TiO_2/Nb_2O_5 ratio in Nb-rich rutile and the Nb-rich brookite ranges more frequently from ~4 to ~7. The TiO_2/Nb_2O_5 ratios in the laterites are quite different. The differences can correspond to different protoliths but can also be interpreted as mainly due to the weathering process. In this sense, the low values in the brown laterite (~0.35) are attributable to the presence of relict pyrochlore; the increasing to ~0.70 in the lower purple laterite and to 2.0 in the upper purple laterite can reflect the remobilization of Nb liberated from pyrochlore decomposition that was not retained in Nb-rich rutile and in iron-oxides; the pisolitic, fragmented, and mottled laterites present values ~1 and these are the three laterites that were reworked.

The sequence of pyrochlore transformation with progressive weathering has been investigated in several locations. Although

Table 6
Representative compositions of Ce-pyrochlore from the brown crust from the Morro dos Seis Lagos deposit.

	SG-01-AM-27				SG-01-AM-31		SG-01-AM-34			
	1	2	3	4	1	2	1	2	3	4
Na_2O	0.05	0.02	0.02	0.27	0.37	0.68	0.04	0.13	1.67	1.01
K_2O	0.03	0.02	0.00	0.04	0.03	0.12	0.02	0.03	0.08	0.16
BaO	4.03	2.05	0.57	3.60	4.61	4.47	0.18	1.73	3.10	1.47
PbO	1.55	8.33	11.36	1.50	8.13	8.09	1.40	8.99	6.13	4.66
SrO	0.07	0.03	n.d.	0.11	0.17	0.04	0.01	n.d.	0.03	0.02
CaO	0.16	0.35	n.d.	0.65	0.62	0.14	0.22	n.d.	n.d.	n.d.
MnO	0.00	0.11	0.03	0.07	0.14	0.22	0.00	0.10	0.04	n.d.
La_2O_3	6.92	6.13	1.79	6.41	4.41	3.81	0.41	1.73	2.66	2.20
Ce_2O_3	12.43	18.92	24.13	12.16	15.63	15.66	28.25	17.28	21.48	23.36
Pr_2O_3	1.92	2.59	0.33	1.97	1.10	1.13	0.08	0.77	0.55	0.98
Nd_2O_3	3.26	3.66	0.34	3.25	1.74	1.40	0.31	1.48	1.37	2.35
Sm_2O_3	0.19	0.05	n.d.	0.21	0.17	0.13	0.03	0.04	0.07	0.07
Eu_2O_3	0.24	0.04	0.06	0.35	0.17	0.16	0.04	0.08	0.06	0.23
Gd_2O_3	0.02	0.25	0.35	0.08	0.32	0.32	0.57	0.30	0.27	0.42
Dy_2O_3	0.00	0.02	n.d.	n.d.	n.d.	0.02	0.00	0.14	n.d.	n.d.
Er_2O_3	0.11	0.03	0.09	0.01	0.01	0.04	0.05	0.12	n.d.	n.d.
Y_2O_3	0.57	0.12	0.02	0.46	0.14	0.32	0.03	0.62	1.56	0.22
ThO_2	0.29	0.38	0.40	0.15	1.16	1.05	13.76	3.80	0.90	2.55
Fe_2O_3	1.71	3.11	3.50	2.61	1.27	2.59	2.59	1.53	1.35	2.23
Al_2O_3	0.02	0.13	0.05	0.17	0.10	0.06	0.06	0.15	0.01	0.10
TiO_2	8.91	4.41	2.61	9.16	4.82	6.39	2.72	8.43	7.86	4.89
SiO_2	0.07	0.18	0.10	0.11	2.85	4.54	0.31	3.30	1.62	0.91
Nb_2O_5	49.35	49.04	51.46	46.76	45.93	44.27	35.27	40.03	43.25	39.66
Ta_2O_5	0.01	n.d.	0.01	n.d.	n.d.	0.16	n.d.	n.d.	n.d.	n.d.
Sum	91.91	99.97	97.22	90.10	93.89	95.81	86.35	90.78	94.06	87.49
Structural Formula										
Na	0.006	0.003	0.003	0.035	0.051	0.084	0.008	0.017	0.230	0.161
K	0.003	0.002	0.000	0.003	0.003	0.010	0.003	0.003	0.007	0.017
Ba	0.104	0.057	0.016	0.093	0.128	0.112	0.007	0.047	0.086	0.047
Pb	0.027	0.159	0.218	0.027	0.155	0.139	0.037	0.167	0.117	0.103
Sr	0.003	0.001		0.004	0.007	0.001	0.001		0.001	0.001
Ca	0.011	0.027		0.046	0.047	0.010	0.023			
Mn	0.000	0.007	0.002	0.004	0.008	0.012	0.000	0.006	0.002	
La	0.168	0.161	0.047	0.156	0.115	0.089	0.015	0.044	0.070	0.067
Ce	0.299	0.492	0.631	0.294	0.404	0.365	1.018	0.435	0.560	0.704
Pr	0.046	0.067	0.009	0.047	0.028	0.026	0.003	0.019	0.014	0.029
Nd	0.077	0.093	0.009	0.077	0.044	0.032	0.011	0.036	0.035	0.069
Sm	0.004	0.001		0.005	0.004	0.003	0.001	0.001	0.002	0.002
Eu	0.005	0.001	0.001	0.008	0.004	0.003	0.001	0.002	0.001	0.006
Gd	0.000	0.006	0.008	0.002	0.007	0.007	0.019	0.007	0.006	0.011
Dy	0.000	0.000				0.000	0.000	0.003		
Er	0.002	0.001	0.002	0.000	0.000	0.001	0.002	0.003		
Y	0.020	0.005	0.001	0.016	0.005	0.011	0.002	0.023	0.059	0.010
Th	0.004	0.006	0.006	0.002	0.019	0.015	0.308	0.060	0.015	0.048
ΣA	0.779	1.089	0.953	0.819	1.029	0.920	1.459	0.873	1.205	1.275
Fe	0.085	0.166	0.188	0.130	0.068	0.124	0.192	0.079	0.072	0.138
Al	0.002	0.011	0.004	0.013	0.008	0.005	0.007	0.012	0.001	0.010
Ti	0.440	0.235	0.140	0.454	0.256	0.306	0.201	0.436	0.420	0.302
Si	0.005	0.013	0.007	0.007	0.201	0.289	0.031	0.227	0.115	0.075
Nb	1.468	1.575	1.661	1.396	1.467	1.274	1.570	1.246	1.391	1.475
Ta	0.000		0.000			0.003				
ΣB	2.000	2.000	2.000	2.000	2.000	2.000	2.000	2.000	2.000	2.000
Vacancy	1.221	0.911	1.047	1.181	0.971	1.080	0.541	1.127	0.795	0.725

n.d = not detected; calculated on the basis of 2 B-site cations.

the original composition of pyrochlore plays an important role in determining the variety of pyrochlore that formed, secondary pyrochlores formed by weathering processes follow more or less well-defined sequences at each locality. According to Entin et al. (1993) (in Wall et al., 1996), fresh predominantly Ca, Na pyrochlore weathers to give successive generations of strontio-, Sr,Ba-, Ba,Sr- and then plumbopyrochlore. The trend at Mount Weld is one of progressive leaching of Ca and Na and partial replacement by varying proportions of Sr and Ce rather than K, Ba and Sr (Lottermoser and England, 1988). At the Yenisei Ridge, bariopyrochlores are reported to occur lower in the profile than strontiopyrochlore (Lapin and Kulikova, 1989). At Lueshe (Wall et al., 1996), the most K-Nb-rich pyrochlore occurs at intermediate levels, the most Ba-rich pyrochlore occurs in quartz- and clay-rich ores and close to the surface in some other drill holes, and the highest levels of Sr occur in the Ba-rich pyrochlore and near the base of weathering profiles throughout the deposit. In the Nb-deposit of Catalão I, the pyrochlore is secondary and, with increasing weathering, it presents Ba enrichment and increasing in vacancy due to Ca and Na losses (Cordeiro et al., 2011). In the Catalão II Nb-deposit, the pyrochlore alteration is marked by Ba and REE enrichment (Rocha et al., 2001). Secondary Ba-pyrochlore is the Nb ore mineral exploited at Araxá (Silva, 1986). Given the data above, we are inclined to interpret the Pb-Ba-pyrochlore (border siderite carbonatite) as an early product of primary pyrochlore weathering, followed by Ce-Ba-pyrochlore (core siderite carbonatite, strongly weathered because of the karstic process that formed the Esperança Basin) and then by Ce-pyrochlore (lower part of the brown

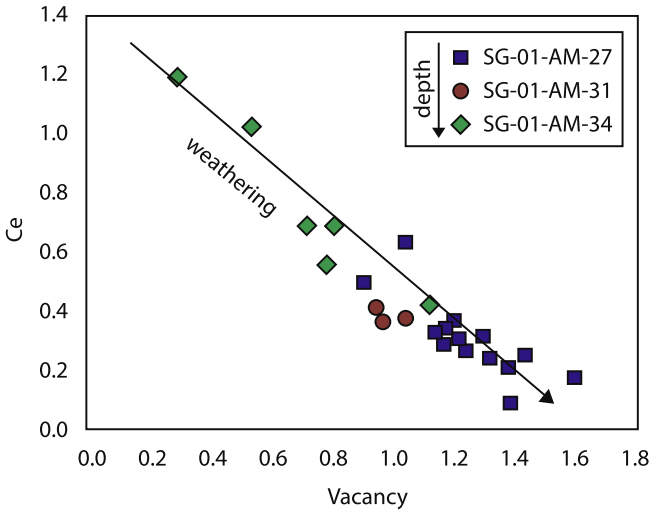

Fig. 13. Binary diagram Ce (apfu) vs Vacancy (apfu) showing progressive weathering of Ce-pyrochlore from brown laterite.

laterite) which is progressively weathered (Fig. 13) until disappearing in the upper part of the brown laterite.

The Morro dos Seis Lagos is the only example of a Nb-deposit where Nb-rich rutile is the main ore mineral. Minor Nb-rich rutile (together with minor ferrocolumbite) occurs in the Tomtor deposit (Kravchenko and Pokrovsky, 1995), where pyrochlore is the main ore mineral. Petrological studies of carbonatites have shown that each Nb-deposit is unique with respect to the assemblage of Nb-bearing minerals present (Mitchell, 2015). Hence, the Oka (Bond Zone) calcite carbonatites (Canada) contain pyrochlore, perovskite and niocalite, whereas the St. Honoré dolomite carbonatites (Canada) lack perovskite and niobium silicates and, in addition to pyrochlore, contain abundant ferrocolumbite and magnetite together with minor niobian rutile. Another point to consider is the intensity of lateritization. According to Mitchell (2015), intense lateritization ultimately leads to complete decomposition of pyrochlore and the formation of Nb-rich rutile, brookite, and anatase. Indeed, the lateritic profile we described is a case of extreme lateritization, where very small amounts of pyrochlore were preserved only in the deepest least evolved laterite.

Table 7
Representative composition of iron and manganiferous laterites from Morro dos Seis Lagos deposit.

	Pisolitic	Fragmented	Mottled		Upper Purple		Manganiferous		Lower Purple		Brown			
%	F1-02	F1-03	F1-05	F1-07	F1-10	F1-11	F1-14	F1-16	F1-18	F1-23	F1-24	F1-27	F1-30	F1-35
SiO_2	0.64	0.78	0.36	0.12	0.2	0.21	0.49	0.47	2.1	0.68	0.75	1.04	0.53	1.85
Al_2O_3	1.78	1.82	2.37	1.56	0.86	0.43	0.23	0.55	0.8	0.54	0.4	0.5	0.38	0.77
Fe_2O_3	81.35	79.2	79.28	83.22	83.4	84.46	50.55	57.09	83.29	82.09	80.16	81.74	82.39	81.98
MgO	<0.01	<0.01	<0.01	<0.01	<0.01	0.02	<0.01	<0.01	0.44	0.04	<0.01	0.01	<0.01	<0.01
CaO	<0.01	0.02	<0.01	<0.01	<0.01	0.01	<0.01	<0.01	0.35	0.05	<0.01	<0.01	<0.01	0.01
Na_2O	<0.01	0.01	<0.01	<0.01	<0.01	0.01	<0.01	0.01	0.01	<0.01	<0.01	<0.01	<0.01	<0.01
K_2O	0.02	<0.01	0.02	<0.01	<0.01	0.02	0.02	0.04	0.04	0.02	0.02	<0.01	<0.01	<0.01
TiO_2	3.46	3.25	2.33	2.88	6.14	7.23	0.06	1.31	1.07	2.23	2.06	0.99	0.57	0.37
P_2O_5	0.87	1.74	1.53	1.14	0.47	0.16	0.21	0.33	0.16	0.38	0.46	0.4	0.29	0.58
MnO	0.07	0.07	0.02	0.26	0.24	0.21	32.2	25.27	0.22	0.36	0.23	0.39	0.31	0.43
LOI	9.3	10.5	12.1	8.4	6.0	4.0	9.2	9.1	8.1	9.7	10.3	10.9	10.6	11.8
ppm														
Nb	10419.3	10744.5	8194.3	7772.3	9969.8	13217.1	796.6	5075.2	8253.3	13311.2	21548.1	10983.6	5444.1	3419.1
Ta	0.5	0.7	0.5	0.2	0.1	0.3	0.1	0.4	<0.1	<0.1	0.2	<0.1	<0.1	<0.1
La	474.4	730.0	667.4	807.1	415.7	319.2	262.6	480.0	343.4	980.8	1622.0	1042.9	503.2	1560.5
Ce	1695.1	2304.7	1536.4	2637.6	1857.8	2365.0	11156.7	4233.4	10041.6	5224.4	5185.6	9331.7	28520.6	4500.2
Pr	78.65	134.89	118.07	123.85	68.26	75.9	89.57	113.05	101.81	281.66	591.76	252.42	105.77	248.77
Nd	202.7	373.3	323.3	298.3	166.9	117.7	302.5	341.4	187.9	492.9	1413.4	407.3	226.4	627.1
Sm	32.86	52.05	41.23	47.89	32.04	22.58	73.24	70.96	38.01	57.91	152.59	53.03	41.47	74.66
Eu	9.7	13.05	9.33	14.87	11.96	7.72	22.09	22.96	14.67	19.89	40.94	13.6	12.13	17.00
Gd	39.45	30.39	30.76	60.24	61.58	38.15	154.91	62.03	52.97	76.18	116.34	35.61	63.22	36.81
Tb	4.23	4.18	2.55	5.82	8.34	3.75	11.21	9.77	9.53	12.63	19.95	6.02	5.38	5.18
Dy	17.09	16.16	8.98	20.87	39.68	14.77	40.04	43.86	51.14	65.38	101.29	32.43	28.26	25.65
Ho	2.85	2.59	1.3	3.62	7.11	2.46	6.13	6.98	8.98	11.07	18.01	6.63	4.25	3.77
Er	5.95	5.96	3.24	7.68	14.96	5.94	13.1	16.42	22.78	25.32	39.99	17.86	10.00	8.83
Tm	0.75	0.73	0.36	0.92	1.83	0.89	1.67	2.00	2.72	2.99	4.7	2.32	1.48	1.21
Yb	4.26	4.37	2.14	5.5	8.67	4.56	8.75	10.37	14.95	16.35	24.83	13.37	8.28	6.39
Lu	0.59	0.51	0.25	0.62	1.29	0.67	1.14	1.39	1.97	2.06	3.15	1.61	0.92	0.78
Y	71.2	74.3	28.5	105.2	220.1	64.1	163.5	203.5	256.8	377.0	558.4	168.5	88.1	97.1
Sc	241	194	146	261	368	350	243	193	433	381	382	482	285	417
Rb	0.9	0.5	1.1	<0.1	<0.1	1.6	0.2	0.6	0.9	0.4	0.6	0.1	0.2	<0.1
Ba	367	448	315	868	783	738	44024	34729	518	753	1810	557	431	978
Sr	66.2	101.4	83.1	237.9	90.5	41.1	19.1	49.9	25.1	81.4	161.5	75.9	107.2	236.0
Pb	200.9	139.6	113.8	231.8	306.6	278.7	261.4	211.5	172.1	172.3	174.0	509.6	395.0	199.6
Th	2989.7	2224.5	1943.0	2856.8	2723.9	1956.2	2076.5	1216.5	1826.7	3234.9	2186.0	3451.5	2314.0	2373.6
U	0.5	0.8	0.8	0.3	0.1	0.2	<0.1	0.2	0.1	0.2	0.4	0.8	0.5	0.2
Zr	188.1	204.5	147.1	75.3	54.7	49.7	32.0	70.6	38.4	88.3	108.8	109.4	39.8	18.2
Hf	5.5	5.4	3.7	2.0	1.4	3.2	0.7	1.9	1.0	3.2	3.5	3.8	1.3	0.7
Co	7.8	8.2	2.9	21.4	27.7	14.9	222.4	144.2	35.8	87.0	33.0	41.1	51.1	43.8
V	183	201	291	118	162	191	20	106	116	262	377	208	125	122
W	203.5	208.8	168.4	172.4	326.5	380.2	11.1	84.1	128.2	195.6	193.5	88.1	38.3	30.8
Zn	328	287	118	896	1560	2287	1444	1296	2201	2079	2391	1543	1592	1553
Cu	5.7	7.2	4.6	7.3	4.3	2.6	6.2	8.1	11.5	4.1	5.0	7.0	22.9	7.6
F	210	171	90	210	130	160	210	142	201	99	209	583	310	503

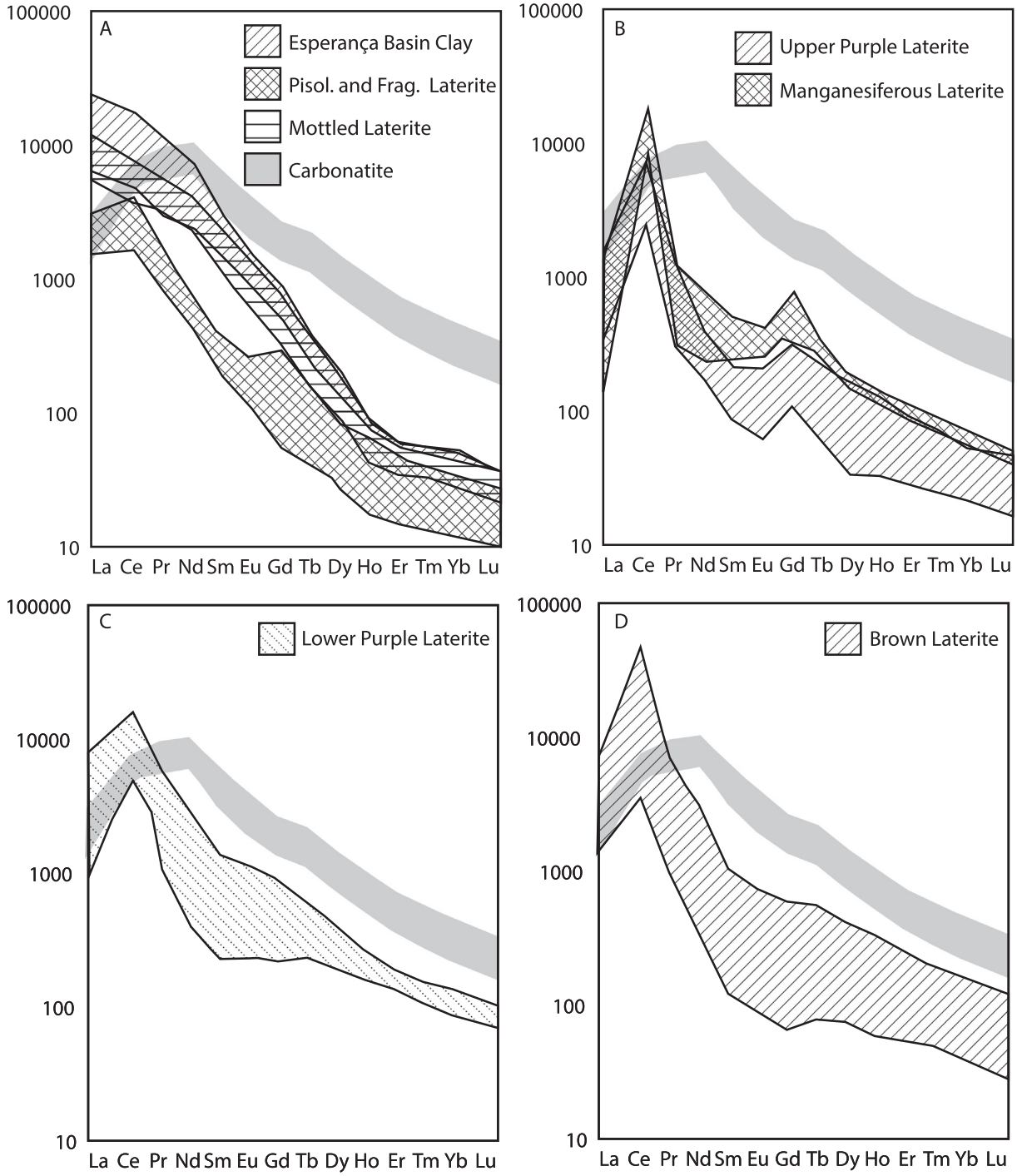

Fig. 14. Rare earth element patterns in the Morro dos Seis Lagos deposit. Normalized to chondrite C1 (McDonough and Sun, 1995).

At the Seis Lagos deposit, a non-identified mineral altered to form Nb-rich rutile together with Ce-pyrochlore and Nb-bearing goethite (Fig. 9). We think that this mineral was likely a secondary pyrochlore, possibly a Ce-Ba-pyrochlore, richer in Ti than those already found in the core siderite carbonatite (with up to 6.0 wt% TiO_2). Alternatively, it could be perovskite or loparite-(Ce). As the Nb-rich rutile crystals from the different laterites are petrographically and chemically similar, there is no reason to suppose they formed from different minerals.

Nb-bearing goethite formed by the weathering of carbonatites was described at Lueshe (Democratic Republic of the Congo) by Wall et al. (1996), who noted the difficulty of discriminating between Nb incorporated into the goethite structure and inclusions of pyrochlore or other secondary minerals. In some of their samples, the presence of Nb in goethite occurring as anhedral inclusions in crandallite was unambiguous. In other samples, from highly weathered ores, between 1.4 and 3.0 wt% Nb_2O_5 was found in goethite with no evidence of inclusions. In our samples, there is no evidence of inclusions and there is no evidence of replacement of Nb-rich rutile by goethite, as described in the Longonjo carbonatite, Angola (Castellano et al., 2012). Thus, we consider that Nb-bearing goethite is a product of pyrochlore transformation with progressive weathering.

Spherules of Nb-rich brookite occur in the rare metal mineralization at the Salpeterkop carbonatite complex, South Africa, where the mode of occurrence was considered compatible with

Table 8
Concentrations of Nb_2O_5, TiO_2 and REE of the Morro dos Seis Lagos deposit.

Laterites	Nb_2O_5			TiO_2			CeO_2			$LREE_2O_3 - CeO_2$			$HREE_2O_3$		
%	Min.	Max.	Avg.	Min.	Max.	Avg.	Min.	Max.	Avg.	Min.	Max.	Avg.	Min.	Max.	Avg.
Pisolitic	2.98	6.14	4.56	3.46	7.57	5.52	0.12	0.17	0.15	0.18	0.19	0.18	0.01	0.02	0.01
Fragmented	2.24	3.07	2.54	3.10	3.39	3.25	0.13	0.29	0.24	0.19	0.33	0.28	0.01	0.02	0.01
Mottled	2.22	10.55	5.04	2.33	14.68	6.63	0.19	0.77	0.43	0.27	1.31	0.63	0.01	0.03	0.02
Upper Purple	0.72	3.25	2.38	0.44	7.23	4.99	0.19	0.56	0.32	0.06	0.20	0.14	0.01	0.03	0.02
Manganiferous	0.23	1.45	0.62	0.06	1.31	0.45	0.52	1.37	0.90	0.06	0.24	0.13	0.04	0.05	0.05
Lower Purple	2.13	5.73	3.62	1.07	4.01	2.29	0.38	1.23	0.75	0.16	1.05	0.46	0.04	0.09	0.05

metasomatic crystallization from permeating hydrothermal solutions, even though subsequent fragmentation is evident (Verwoerd et al., 1995). Our petrographic and analytical data suggest that the Nb-rich brookite formed from Nb-rich rutile. It is, however, an extremely complex issue. In Nb-Ta-bearing geochemical environments, rutile readily accepts Nb and Ta into its structure, mainly in tapiolite-like stoichiometry with Fe > Mn. The rutile incorporates the tapiolite component through the substitution of $3Ti^{4+}$ by $(Fe,Mn)^{2+} + 2(Nb,Ta)^{5+}$ (Hirtopanu et al., 2015). Černý et al., (1999) considered 2 additional substitutions: [Fe^{3+} +(Nb, Ta) for 2Ti] and [(Fe^{2+}, Mn) + W for 2Ti]. These authors observed that Nb-rich rutile is, in most cases, exsolved into a (Fe, Nb)-depleted rutile + titanian ferrocolumbite or titanian ixiolite and that the relics of the original homogeneous phase are scarce and only microscopic in size. Oxidation of the primary niobian rutile phase and exsolution products is controlled by the (Nb, Ta, W) vs (Fe, Mn) budget and by the Fe^{3+}/Fe^{2+} budget in the primary phase. In cases of highly Fe^{2+} dominant rutile with (Nb, Ta) balanced by (Fe, Mn), titanian ferrocolumbite to manganocolumbite or ixiolite are the only exsolution products. In (Fe^{3+}, Sc) dominant rutile with (Nb, Ta) balanced by (Fe, Mn), a titanian (Fe^{3+}, Sc)NbO_4 phase with a subordinate ferrocolumbite component is the only exsolution product (Černý et al., 1999).

At the Morro dos Seis Lagos Deposit, the Nb-rich rutile accommodates Nb following [Fe^{3+} +(Nb, Ta) for 2Ti] substitution with few deviations from the ideal, whereas Nb-rich brookite presents a little more significant deviation (Fig. 11B). Furthermore, the stage preceding the formation of the Nb-rich brookite is represented by a breakdown of the structure in parts of the Nb-rich rutile crystals, with the formation of a gel in which the incipient formation of spherules can be seen (Min 1, Fig 7A). The first formed spherules (Min 2, Fig. 7B) have a composition of Nb-Fe-rich brookite, but further studies are required to prove whether it is brookite. The oolitic texture can be attributed to the phenomena known as Liesegang rings (Liesegang, 1896). Liesegang rings are bands formed when diffusion leads to supersaturation and nucleation. Fine precipitation occurs when two components separate through chemical segregation during weathering, thus forming self-organizing periodic patterns.

According to Smith (1984), many experiments produce Liesegang rings. Common to most of these systems is the presence of gel/water and supersaturated solution and the product of reaction is stable. Hedges (1932) and Stern (1954), in Krug et al. (1996), argue that the interaction of specific chemical reactions and diffusion precipitation and the competitive growth of particles are responsible for the formation of ring pattern over time. In addition, several factors are involved in the formation of these rings, such as the concentration and temperature of chemical solutions, to promote the precipitation of colloids or the existence of nuclei that facilitate mineral growth. According to Krug et al. (1996), self-organizing patterns are very regular but may have many types of irregularities, with apparent displacement or branches, gaps in bands or transitions between bands and skeletal patterns.

Under oxidizing conditions siderite becomes unstable, the formation of iron oxides and hydroxides occurs. These are stable under oxidizing conditions at a wide pH range (Krauskopf, 1985). The occurrence of siderite is practically limited to neutral or basic conditions. The Eh elevation or pH decrease destabilizes siderite, which turns into different mineral phases or remains in solution. In the case of Seis Lagos, where the activity of S was low, the input of oxidizing and acid solutions easily destabilized siderite and formed Fe oxi-hydroxide. Goethite and hematite can be formed from weathering of Fe-bearing primary minerals in the early stages of weathering. Goethite is the dominant weathering product of most primary Fe-bearing minerals (siderite, biotite, pyrite, olivine and others). Hematite is mainly formed by oxidation of magnetite (Anand and Gilkes, 1984; Anand and Paine, 2002). However, in more advanced weathering profiles, which is the case of Morro dos Seis Lagos deposit, hematite can be formed from dehydroxylation of goethite (Wells et al., 1989). The occurrence of hematite together with goethite may be a result of variations in hydrological conditions that affect the ageing product of goethite. These variations can explain the existence of successive phases of Fe oxi-hydroxides precipitation. Under aerobic conditions and in the pH range of a normal weathering environment, the Fe^{3+} oxides are very stable and persist for a long time (Anand and Paine, 2002). In the upper part of the lateritic profiles, hematite is commonly altered to goethite by rehydration (Tardy and Nahon, 1985). This occurred in the Morro dos Seis Lagos deposit during the reworking of the three upper laterites.

The precipitation of Mn oxide minerals within the laterite seems to be a late event since Mn oxides occur in fractures and cavities. The source of Mn is most likely the siderite. Under oxidizing conditions Fe and Mn can behave in different ways if such solutions are made basic suddenly, both metals will precipitate, resulting in the formation of Fe minerals with a small admixture of Mn. If, on the other hand, the pH increases very slowly, Fe compounds reach the limit of solubility before Mn compounds and so can precipitate while Mn is left in solution. The Mn remaining in solution may be deposited as an oxide if conditions are oxidizing and the solution becomes still more alkaline. As the precipitation of Mn oxides from solutions requires a higher oxidation potential than that for Fe oxides, the Mn tends to precipitate closer to the water table (Krauskopf, 1985).

The configuration presented by the REE (Fig. 14) in the Morro dos Seis Lagos deposit indicates that the HREE were leached along the entire lateritic profile, especially in its upper part. The LREE were leached in the uppermost part of the profile, but were precipitated at the base of the reworked laterites (mottled laterite) and in the clays of the Esperança Basin. The positive anomalies of Ce are related to its tetravalent state that favors its fixation by the formation of cerianite in the laterites, with increasing concentrations with increasing in depth. Low REE contents at the top of the laterite are likely due to mobility and removal of REE after decalcification of the upper part of the profile, and thus during the acid stage of weathering. A similar REE distribution was described in Mount

Weld (Lottermoser, 1990), where the REE were complexed by carbonate, fluoride or chloride anions, and transported down through the laterite profile. These complexes were subsequently destabilised when they encountered higher carbonate anion concentrations, increasingly higher groundwater pH and higher alkalinity conditions in deeper parts of the profile. LREE were deposited as phosphates and aluminophosphates in the middle portion of the supergene horizon. The LREE were separated from the HREE and Y because the latter remained stable in solutions characterised by elevated pH and alkalinity conditions. Lottermoser also indicated that LREE formed a high-concentration REE zone in the center of the profile due to variations in pH and Eh and groundwater lateral circulation. In the Morro dos Seis Lagos deposit, the LREE were deposited at the mottled laterite and the high-concentration central zone is exemplified by the high concentrations of LREE in the Esperança Basin associated with neoformed florencite-(Ce). Lottermoser (1990) also identified a high concentration of phosphates at the interface between the carbonatite and the base of the lateritic profile, which cannot be accessed in the case of Morro dos Seis Lagos Deposit. Our data indicate that this interface may also be an HREE enrichment zone, which were leached along the entire studied profile, especially in the upper levels.

The Araxá Nb-deposit (Silva, 1986) is associated to a carbonate complex with 4.5 km in diameter, consisting of sovitos, beforsitos, and glimerites, where carbonatites occur as veins and dikes that cut the glimerites. The predominant carbonate is dolomite, with subordinate calcite and ankerite. Ba-pyrochlore, barite, phlogopite, apatite and magnetite occur as accessory minerals. The lateritic cover (thickness ranging from few meters to 230 m) is composed of limonite, goethite, and magnetite, with minor chalcedony, Ba-pyrochlore and barite. Phosphorus released by apatite decomposition was deposited at the lower levels of the profile, in the form of neoformed apatite, or at the higher levels as phosphates of the crandalite and monazite group. The Morro dos Seis Lagos deposit differs in many respects: type and continuity of primary rock (siderite carbonatite only), mineralogy and textural complexity of laterite (hematite and goethite, 6 textural types), weathering intensity (much stronger, decomposition of pyrochlore, formation of Nb-rich rutile, its transformation to Nb-rich brookite and laterite reworking).

6. Conclusion

The Morro dos Seis Lagos Nb (Ti, REE) deposit consists of a complex lateritic profile formed by the weathering of siderite carbonatite. This is the only type of carbonatite observed and has chemical and mineralogical characteristics compatible with a primary rock for the deposit.

The lateritic profile (>100 m in thickness) is formed by six textural and compositional types of laterite (from the surface downwards): (1) pisolitic laterite, (2) fragmented laterite, (3) mottled laterite, (4) purple laterite, (5) manganiferous laterite, and (6) brown laterite. All the laterites are mainly formed by goethite (predominant in the lower laterites) and hematite (predominant in the intermediary laterites). Goethite becomes more abundant again in the upper laterites as a result of reworking. In the manganiferous laterite (10 m thick), the manganese oxides (mainly hollandite, with associated cerianite) occur as veins formed in a late event during the development of the lateritic profile, precipitated from a solution with higher oxidation potential than that for Fe oxides, closer to the water. Siderite is the source for the Mn.

The Nb-ore minerals are essentially Nb-rich rutile with minor Nb-rich brookite. Nb-rich rutile occurs as isolated crystals in all laterites, with a composition 57.84 to 80.92 wt% TiO_2, 11.26 to 22.23 wt% Nb_2O_5 and 8.96 to 14.95 wt% Fe_2O_3. Nb-rich brookite formed at the expense of Nb-rich rutile, has similar composition to that of Nb-rich rutile, occurs as spherules more commonly broken by collapsing of the laterites during the reworking of the upper laterites and has fine banded structure interpreted as Liesegang ring. Nb-rich rutile and Nb-rich brookite accommodate Nb following [Fe^{3+} +(Nb, Ta) for 2Ti] substitution. The late mineral presents some deviation from the ideal substitution; the stage preceding its formation is represented by a breakdown of the structure in parts of the Nb-rich rutile crystals, with the formation of a gel in which the incipient formation of spherules can be seen.

The presence of Nb-rich rutile rather than other common Nb minerals is related to the extremely intense lateritization. The primary pyrochlore was progressively weathered forming successive secondary pyrochlores until the Ce-pyrochlore that disappears in the upper part of the brown laterite. The formation of rutile Nb-rich, observed in the brown laterite, occurred, together with Ce-pyrochlore, Nb-bearing goethite, and cerianite, from the alteration of a mineral presumably a former secondary pyrochlore.

The laterites have an average Nb_2O_5 content of 2.91 wt%. The TiO_2 concentrations are significant as well, with an average of 5.00 wt% in the upper laterites. The HREE were leached along the entire lateritic profile, especially in its upper part. The LREE were leached in the uppermost part of the profile, but were precipitated at the base of the reworked laterites (mottled laterite) and in the clays of the Esperança Basin as florencite-(Ce). Positive anomalies in Ce occur from upper purple crust to the base of the sequence. The analogy with Mount Weld deposit suggests that HREE and phosphate concentrations are likely to occur at lower deposit levels not accessed in the present study.

Acknowledgments

The present work would not have been possible without the support given by the Companhia de Pesquisa de Recursos Minerais, through Roberto Ventura Santos, Eduardo Camozatto, and Renê Luzardo. Gert Rodolfo Woeltje (DNPM-Amazonas) is also thanked. The manuscript has benefitted from very constructive reviews by Roger Mitchell and Anton Chakhmouradian. The Conselho Nacional de Desenvolvimento Científico e Tecnológico CNPq is acknowledged for the financial support (projects 485415/2012-7 and 405839/2013-8).

References

Almeida, M.E., Macambira, M.J.B., Faria, M.S.G. de, 2002. A granitogênese paleoproterozoica do sul de Roraima. In: Congresso Brasileiro de Geologia, 41, João Pessoa, 434.

Almeida, M.E., Macambira, M.J.B., Oliveira, E.C., 2007. Geochemistry and zircon geochronology of the I-type high-K calc-alkaline and S-type granitoid rocks from southeastern Roraima, Brazil: Orosirian collisional magmatism evidence (1.97–1.96 Ga) in central portion of Guyana Shield. Precambr. Res. 155, 69–97.

Anand, R.R., Butt, C.R.M., 1988. The terminology and classification of a deeply weathered regolith. CSIRO Division of Exploration Geoscience Discussion Paper.

Anand, R.R., Gilkes, R.J., 1984. Mineralogical and chemical properties of weathered magnetite grains from lateritic saprolite. J. Soil Sci. 35, 559–567.

Anand, R.R., Paine, M., 2002. Regolith geology of the Yilgarn Craton, Western Australia: implications for exploration. Aust. J. Earth Sci. 49, 3–162.

Angélica, R.S., Costa, M.L., 1993. Geochemistry of rare-earth elements in surface lateritic rocks and soils from the Maicuru complex, Para, Brazil. J Geochem. Explor. 47, 165–182.

Bonow, C.W., Issler R.S., 1980. Reavaliação e aspectos económicos do jazimento de terras raras e ferro-ligas do Lago Esperança, Complexo carbonatítico de Seis Lagos – Amazonas, Brasil. In: Congresso Brasileiro de Geologia, 31, Camboriu, 3, 1431.

Buchanan, F., 1807. A Journey From Madras Through the Countries of Mysore. Canara and Malabar. East India Company, London, pp. 436–461.

Castellano, A., Melgarejo, J., Alfonso, P., Bambi, A.C.J.M., Alves, A.G.O.N., 2012. Subsolidus Processes in the Longonjo and Bailundo Carbonatites (Angola) 8–9.

Černý, P., Chapman, R., Simmons, W.B., Chackowsky, L.E., 1999. Niobian rutile from the McGuire granitic pegmatite, Park County, Colorado: Solid solution, exsolution, and oxidation. Am. Mineral. 84, 754–763.

Chakhmouradian, A.R., 2006. High-field-strength elements in carbonatitic rocks: geochemistry, crystal chemistry and significance for constraining the sources of carbonatites. Chem. Geol. 235, 138–160.
Chakhmouradian, A.R., Reguir, E.P., Kressall, R.D., Crozier, J., Pisiak, L.K., Sidhu, R., Yang, P., 2015. Carbonatite-hosted niobium deposit at Aley, northern British Columbia (Canada): mineralogy, geochemistry and petrogenesis. Ore Geol. Rev. 64, 642–666.
Chakhmouradian, A.R., Zaitsev, A.N., 2012. Rare earth mineralization in igneous rocks: sources and processes. Elements 8, 347–353.
Cordeiro, P.F., de, O., Brod, J.A., Palmieri, M., de Oliveira, C.G., Barbosa, E.S.R., Santos, R.V., Gaspar, J.C., Assis, L.C., 2011. The Catalão I niobium deposit, central Brazil: resources, geology and pyrochlore chemistry. Ore Geol. Rev. 41, 112–121.
Corrêa, S.L.A., 1996. Evolução geoquímica das crostas lateríticas e dos sedimentos sobrepostos na estrutura de Seis Lagos (Amazonas) (PhD. thesis). Universidade Federal do Pará, (in Portuguese).
Corrêa, S.L.A., Costa, M.L., 1997. Mineralogia das crostas lateríticas ferruginosas de Seis Lagos (Amazonas). Geociências 16 (1), 141–156.
Costa, M.L., Costa, J.A.V., Angélica, R.S., 1993. Gold bearing bauxitic laterite in a Tropical rainforest climate. Cassiporé, Amapá, Brazil. Chron. Rec. Min. 510, 41–51.
Costa, M.L., 1997. Lateritization as a major process of ore deposit formation in the Amazon region. Explor. Mining. Geol. 6 (1), 79–104.
CPRM, 2006. Geologia e recursos minerais do Estado do Amazonas. Map scale 1:1.000.000. Companhia de Pesquisa de Recursos Minerais, Manaus. CD-ROM (abstract in English).
Entin, A.R., Yerernenko, G.Y., Tyan, O.A., 1993. Stages of alteration of primary pyrochlores. Transactions (Dokaldy) of the U.S.S.R. Academy of Sciences: Earth Science Sections 320 (1991), 236–239 (Translated from O stadiynosti izmeneniya pervichnykh pirokhlorov. Doklady Akademii Nauk SSSR, 1991, 319, 1218-21).
Giovannini, A.L., 2013. Contribuição à geologia e geoquímica do carbonatito e da jazida (Nb, ETR) de Seis Lagos (Msc thesis). Universidade Federal do Rio Grande do Sul, (in Portuguese).
Gittins, J., Harmer, R.E., 1997. What is ferrocarbonatite? A revised classification. J. Afr. Earth Sc. 25, 159–168.
Hedges, E.S., 1932. Liesegang rings and other periodic structures. Chapman and Hall, London, p. 122.
Hirtopanu, P., Fairhurst, R.J., Jakab, G., 2015. Niobian rutile and its associations at Jolotca, Ditrau alkaline intrusive massif, East Carpathians. Geonomy 17 (1), 39–55.
Issler, R.S., Silva, G.G. 1980. The seis lagos carbonatite complex. In: Congresso Brasileiro de Geologia 31, Camboriu, 3, pp. 1564–1572.
Justo, L.J.E.C., Souza, M.M., 1984. Jazida de nióbio do Morro dos Seis Lagos, Amazonas. In: Simpósio Amazonense 2, Manaus, pp. 467–472.
Justo, L.J.E.C., Souza, M.M., 1986. Jazida de nióbio do Morro dos Seis Lagos, Amazonas. In. Schobbenhaus, C., and Coelho, C.E.S. (Eds), Principais Depósitos Minerais do Brasil - Ferro e Metais da Indústria do Aço. Departamento Nacional da Produção Mineral, 2, pp. 463–468.
Krauskopf, K.B., 1985. Introduction to Geochemistry. McGraw-Hill book Company, Auckland, p. 617.
Kravchenko, S.M., Pokrovsky, B.G., 1995. The Tomtor alkaline ultrabasic massif and related REE-Nb deposits, northern Siberia. Econ. Geol. 90, 676–689.
Krug, H.-J., Brandstädter, H., Jacob, K.H., 1996. Morphological stabilities in pattern formation by precipitation and crystallization processes. Geol. Rundsch. 85, 19–28.
Lapin, A.V., Kulikova, I.M., 1989. Processes of pyrochlore alteration and their products in the carbonatite weathering crusts. Zap. Vses. Mineral. Obshch., 118, (in Russian), p 419.
Le Bas, M.J., 1981. Carbonatite magmas. Mineral. Mag. 44, 133–140.
Liesegang, R.E., 1896. A-Linien. Lieseg Photogr. Arch 21, 321–326. Reprinted in: Kuhnert and Niedersen (1987).
Lottermoser, B.G., 1990. Rare-earth element mineralisation within the Mt. Weld carbonatite laterite, Western Australia. Lithos 24, 151–167.
Lottermoser, B.G., England, B.M., 1988. Compositional variation in pyrochlores from the Mount Weld carbonatite laterite, Western Australia. Mineral. Petrol. 38, 37–51.
Mariano, A.N., Mariano Jr., A., 2012. Rare earth mining and exploration in North America. Elements 8, 369–375.
McDonough, W.F., Sun, S.S., 1995. The composition of the Earth. Chem. Geol. 120, 223–253.
Mitchell, R.H., 2005. Carbonatites and carbonatites and carbonatites. Can. Mineral. 43, 2049–2068.
Mitchell, R.H., 2015. Primary and secondary niobium mineral deposits associated with carbonatites. Ore Geol. Rev. 64, 626–641.
Nahon, D., 1986. Evolution of iron crusts in tropical landscapes. In: Colman, S.M., Dethier, D.P. Eds., Rates Ž. of chemical weathering of rocks and minerals. Academic, London, pp. 169–191.
Nahon, D., Tardy, Y., 1992. The ferruginous laterites. In: Butt, C.R.M., Zeegers, H. (Eds.), Regolith Exploration Geochemistry in Tropical and Sub-tropical Terrains. Handbook of Exploration Geochemistry, 4. Elsevier, pp. 41–55.
Ollier, C.D., Galloway, R., 1990. The laterite profile, ferricrete an unconformity. Catena 17, 97–109.
Onuonga, I.O., 1997. Geochemistry and mineralisation of Buru and Kuge volcanic carbonatite centres, western Kenya Ph.D. Thesis. University of St Andrews, Scotland, UK, p. 288.
Pasero, M., 2005. A Short Outline of the Tunnel Oxides. Rev. Mineral. Geochemistry, p. 57.
Pereira, R.F., 2014. Nióbio. In: Sumário Mineral 2014. Departamento Nacional da Produção Mineral, Brasília, pp. 94–95.
Pinheiro, S.S., Fernandes, P.E.C.A., Pereira, E.P., Vasconcelos, E.G., Pinto, A.C., Montalvão, R.M.G., Issler, R.S, Dallagnoll, R., Teixeira, W., Fernandes, C.A.C., 1976. Folha NA.19 Pico da Neblina; geologia, geomorfologia, pedologia, vegetação e uso potencial da terra. Rio de Janeiro, Cap. 2, pp. 19–138. (Levantamento de Recursos Naturais).
Pirajno, F., Gonzalez-Alvarez, I., Chen, W., Kyser, K.T., Simonetti, A., Leduc, E., leGras, M., 2014. The Gifford Creek Ferrocarbonatite Complex, Gascoyne Province, Western Australia: Associated fenitic alteration and a putative link with the ~1075Ma Warakurna LIP. Lithos 202–203, 100–119.
Porto C.G., Imbernon, R. A. L., Toleto, M. C. M., Menezes, R. O. G., Souza, J. J., Borges, C. E. P., 2010. Depósito de Cobre e Ouro em regolitos lateriticos no Brasil: casos de Chapada (GO) Igarapé Bahia e Salobo (Carajás, PA). (in, Modelos de depósitos de cobre no Brasil e sua resposta ao itemperismo. (eds) Brito, R. S. C., Silva, M. da G., Kuyumijan, R. M.), Brasília, CPRM, 189–213.
Porto, C.G., 2016. Geochemical exploration challenges in the regolith dominated IgarapéBahia gold deposit, Carajás, Brazil. Ore Geol. Rev. 73, 432–450.
Rocha, E., Nasraoui, M., Soubiès, F., Bilal, E., De Parseval, P., 2001. Évolution géochimique du pyrochlore au cours de l'altération météorique du gisement de Catalao II (Goiás, Brésil). Comptes Rendus l'Academie Sci. – Ser. IIa Sci. la Terre des Planetes 332, 91–98.
Rossoni, M.B., Bastos Neto, A.C., Saldanha, D.L., Souza, V.S., Giovannini, A.L., Porto, C. G., 2016. Aplicação de técnicas de sensoriamento remoto na investigação do controle do posicionamento do Complexo Carbonatítico Seis Lagos e no estudo do depósito (Nb) laterítico associado (Amazonas, Brasil). Rev. Pesquisas 43, 111–125.
Rudnick, R.L., Gao, S., 2003. The composition of the continental crust. In: Rudnick, R. L., Holland, H.D., Turekian, K.K. (Eds.), Treatise on Geochemistry – The Crust. Elsevier, Oxford, pp. 1–64.
Santos, J.O.S., Hartmann, L.A., Gaudette, H.E., Groves, D.I., Mcnaughton, N.J., Fletcher, I.R., 2000. A new understanding of the provinces of the Amazon craton based on integration of field mapping and U-Pb and Sm-Nd geochronology. Gondwana Res. 3, 453–488.
Santos, J.O.S., Potter, P.E., Reis, N.J., Hartmann, L.A., Fletcher, I.R., McNaughton, N.J., 2003. Age, source and regional stratigraphy of the roraima supergroup and roraima-like sequences in Northern South America, based on U-Pb Geochronology. Geol. Soc. Am. Bull. 115 (3), 331–348.
Silva, A.B. da, 1986. Jazida de nióbio de Araxá, Minas Gerais. (in Principais depósitos minerais do Brasil. Vol. II, Shobbenhaus C., editor and Coelho C. E. da S., editor) DNPM, pp. 435–453.
Simonetti, A., Bell, K., 1994. Isotopic and geochemical investigation of the Chilwa Island carbonatite complex, Malawi: evidence for a depleted mantle source region, liquid immiscibility, and open- system behaviour. J. Petrol. 35, 1597–1621.
Smith, D., 1984. On Ostwald's supersaturation theory of rhythmic precipitation (Liesegang's rings). J. Chem. Phys. 81, 3102–3115.
Stern, K.H., 1954. The Liesegang phenomenon. Chem. Revs. 54, 79–99.
Tardy, Y., Nahon, D., 1985. Geochemistry of laterites, stability of Al-goethite, Al-hematite, and Fe^{3+} kaolinites in bauxites and ferricretes: an approach to the mechanism of concretion formation. Am. J. Sci. 285, 865–903.
Thompson, R.N., Smith, P.M., Gibson, S.a., Mattey, D.P., a.P., Dickin, 2002. Ankerite carbonatite from Swartbooisdrif, Namibia: the first evidence for magmatic ferrocarbonatite. Contrib. Mineral. Petrol. 143, 377–395.
Vasconcelos, P.M., Becker, T.A., Renne, P.R., Brimhall, G.H., 1994. Direct dating of weathering phenomena by K-Ar and 40Ar/39Ar analysis of supergene-Mn oxides. Geochim. Cosmochim. Acta 58, 1635–1665.
Verwoerd, W.J., Viljoen, E.A., Chevallier, L., 1995. Rare metal mineralization at the Salpeterkop carbonatite complex, Western Cape Province, South Africa. J. Afr. Earth Sci. 21, 171–186.
Viegas Filho, J.R., Bonow, C.W., 1976. Projeto Seis Lagos (Internal Report). Companhia de Pesquisa de Recursos Minerais, Manaus.
Wall, F., Williams, C.T., Woolley, A.R., Nasraoui, M., 1996. Pyrochlore from weathered carbonatite at Lueshe, Zaire. Mineral. Mag. 60, 731–750.
Walte, R.J., 1915. Laterit in West Australien. Zeitschrift de Deutshens Geologischen Gesellchaft 67B, 113–140.
Wells, M.A., Gilkes, R.J., Anand, R.R., 1989. The formation of corundum and aluminous hematite by the thermal dehydroxylation of aluminous goethite. Clay Miner. 24, 513–530.
Woolley, A.R., Kjarsgaard, B.A., 2008. Paragenetic types of carbonatite as indicated by the diversity and relative abundances of associated silicate rocks: evidence from a global database. Can. Mineral. 46, 741–752.
Zaitsev, A.N., Sitnikova, M.A., Subbotin, V.V., Fernandez-Suarez J., Jeffries T.E., 2004. Sallanlatvi Complex; a rare example of magnesite and siderite carbonatites (in Phoscorites and carbonatites from mantle to mine; the key example of the Kola alkaline province, (eds) Wall F., Zaitsev A.N.) Mineralogical Society Series 10, pp. 201–246.

4.3 REE mineralization (primary, supergene and sedimentary) associated to the Morro dos Seis Lagos Nb (REE, Ti) deposit (Amazonas, Brazil)

Artigo submetido à revista Ore Geology Reviews dia 13/11/2017.

Track your co-authored submission to Ore Geology Reviews

Ore Geology Reviews <EviseSupport@elsevier.com>

Wed 11/15/2017 7:32 AM

To: arthur_giovannini@hotmail.com <arthur_giovannini@hotmail.com>;

Dear Mr Giovannini,

Submission no: ORGEO_2017_733
Submission title: REE mineralization (primary, supergene and sedimentary) associated to the Morro dos Seis Lagos Nb (REE, Ti) deposit (Amazonas, Brazil).
Corresponding author: Dr Artur C. BASTOS NETO
Listed co-author(s): Mr Arthur Giovannini, Dr LUCY CHEMALE, Dr Claudio Porto, Mr Mauricio H. Bidone, Dr Vitor Pereira

Dr BASTOS NETO has submitted a manuscript to Ore Geology Reviews and listed you as a co-author. This email is to let you know we will be in contact with updates at each decision stage of the submission process.

The link below takes you to a webpage where you can sign in to our submission system using your existing Elsevier profile credentials or register to create a new profile. You will then have the opportunity to tailor these updates and view reviewer and editor comments once they become available.

http://www.evise.com/profile/api/navigate/ORGEO?resourceUrl=%2Fco-author%2F%3Fdgcid%3Dinvite_email_coauthoroutreach01691368%23%2FORGEO%2Fsubmission%2FORGEO_2017_733

If you are not a co-author of this manuscript, please contact Researcher Support at: https://service.elsevier.com

Thank you very much for your submission and we will be in touch as soon as we have any news to share.

Ore Geology Reviews

If you do not wish to receive further update emails on your co-authored submission, you can unsubscribe via this link:

http://www.evise.com/co-author/#/ORGEO/unsubscribe/arthur_giovannini@hotmail.com/vSqT3EZOMQ2GxPUxLli-m_enxIOPexdO1z6mnc-E0xD16uWF38bm7mXpO6Ak-6fbdDv5OGZApXz0pnBcKecsiA

ELSEVIER

My Co-authored Submissions

Ore Geology Reviews

Overview

Research paper | ORGEO_2017_733

REE mineralization (primary, supergene and sedimentary) associated to the Morro dos Seis Lagos Nb (REE, Ti) deposit (Amazonas, Brazil).

Artur Bastos Neto, Arthur Giovannini, Claudio Porto, LUCY CHEMALE, Mauricio H. Bidone, Vitor Pereira

Submitted 13 Nov 2017

Under Review 15 Nov 2017

View PDF

Alert: keep me informed about the submission status for this manuscript

Abstract +

REE mineralization (primary, supergene and sedimentary) associated to the Morro dos Seis Lagos Nb (REE, Ti) deposit (Amazonas, Brazil).

Arthur L. GIOVANNINI[1], Artur C. BASTOS NETO[2], Claudio G. PORTO[3,4], Lucy TAKEHARA[5], Vitor P. PEREIRA[2], Mauricio H. BIDONE[2]

[1] Programa de Pós-graduação em Geociências, Instituto de Geociências, Universidade Federal do Rio Grande do Sul. Avenida Bento Gonçalves 9500, Porto Alegre, 91501-970, RS, Brasil. arthur_giovannini@hotmail.com.

[2] Instituto de Geociências, Universidade Federal do Rio Grande do Sul. Avenida Bento Gonçalves 9500, 91501-970, Porto Alegre, RS, Brasil. artur.bastos@ufrgs.br, vitor.pereira@ufrgs.br.

[3] Divisão de Geoquímica, DGM, Companhia de Pesquisa de Recursos Minerais CPRM. Avenida Pasteur 404, Urca, Rio de Janeiro, 22290-240, RJ, Brasil. claudio.porto@cprm.gov.br.

[4] Instituto de Geociências, Universidade Federal do Rio de Janeiro. Cidade Universitária, Ilha do Fundão, Avenida Athos da Silveira Ramos s/n, 21949-900, Rio de Janeiro, RJ, Brasil. porto@geologia.ufrj.br.

[5] Companhia de Pesquisa de Recursos Minerais CPRM. SUREG/PA. Rua Banco da Província, 105, Porto Alegre, RS, Brasil. lucytakehara@gmail.com.

Key-words: Rare earth elements; carbonatite; laterite; Morro dos Seis Lagos; Amazon.

ABSTRACT

In the Morro dos Seis Lagos Nb (Ti, REE) deposit there are three types of REE mineralization: primary, associated to siderite carbonatite; supergene, associated to laterite profile; sedimentary (detrital and authigenic). The mineralogical and geochemical evolutions of the REE in these three domains are integrated into a comprehensible metallogenic model. The main primary ore in the core siderite carbonatite (42 m thick) has 1.47 wt% REE_2O_3 mainly in monazite-(Ce) and bastnäsite. However, considering the entire section intersected in the core siderite carbonatite, the average grade drops to 0.7 wt% REE_2O_3 mainly contained in thorbastnasite. In the border siderite carbonatite, the REE mineralization is hydrothermal [rhabdophane-(Ce) and REE-rich gorceixite]. LREE and phosphates were concentrated at the reworked laterites from where the HREE were leached. With the advance of lateritization pyrochlore was completely decomposed. The final secondary Ce-pyrochlore was progressively enriched in Ce^{4+}, with loss in REE^{3+}, until the breakdown of the structure and release of Ce under strongly oxidizing conditions (high Ce^{4+}/Ce^{3+}) thus forming extremely pure cerianite-(Ce). This mineral occurs intercalated with goethite bands in the lower part of the weathering profile, represented by the brown laterite, and forms intergrowth with hollandite in the manganiferous laterite, which was formed in a more alkaline environment closer to the water table. The brown laterite has 1.30 wt% REE_2O_3, the manganese laterite has 1.54 wt% REE_2O_3, of which 1.42 wt% is Ce_2O_3. Tectonic and karstic processes over the carbonatite formed several sedimentary basins. In the Esperança Basin, the sedimentary record (233 m thick) shows the whole evolution of the MSLD. The base of the basin (layer 5) is formed by abundant carbonatite fragments, have florencite-(Ce) mineralization, and 1.07 wt% REE_2O_3; layer 4 is formed by carbonatite fragments interbedded with clayey bed; layer 3 is a rhythmite deposited in lacustrine environment, with clasts of ferruginous materials related to early stages of carbonatite alteration; layer 2 is made up by clays, is rich in organic matter, has autigenic florencite-(Ce), florencite-(La) and base metals. This layer marks the inversion of the relief and the input into the basin of REE leached from the upper laterites, carried by the groundwater flow; layer 1 was formed by the oxidation of the upper part of layer 2. Layers 1 + 2 have 73 m thick and average of 1.72 wt% REE_2O_3.

1. INTRODUCTION

The rare earth family consists of 17 transition metals forming Group 3 of the periodic table and comprising Sc, Y, and the lanthanide series (La to Lu). Lanthanides from La to Eu are conventionally termed light REE (LREE), whereas lanthanides from Gd to Lu are termed heavy REE (HREE). Yttrium is grouped with the HREE because its ionic radius is nearly identical to that of Ho. Some authors also classify REE with intermediate atomic numbers (Nd to Gd) as medium REE (Chakhmouradian and Wall, 2012). The REE are lithophile elements, which occur invariably together in natural systems. In rock-forming minerals, they have very similar ionic radius and typically present as trivalent cations in carbonates, oxides, phosphates and silicates, although europium and cerium can also occur as Eu^{+2} and Ce^{+4}. The term "rare" is inadequate because they are not rare elements, although rocks with significant concentrations of these elements are unusual (Formoso et al., 2016). A number of geological processes can lead to the concentration of REE in specific types of rocks and sediments and the enrichment of both LREE and HREE by fractionation of the REE series. Deposits of REE in placer and paleoplacer, that already occupied a prominent position in the world production of REE, are becoming again attractive due to the major economic interest of the HREE contained in xenotime. However, because these minerals may also contain high levels of Th and U, the commercial success of these projects depends on the resolution of the radioactive waste implications and other environmental problems. Presently, the main deposits in production and the main prospects of REE are related to magmatic rocks (Chakhmouradian and Wall, 2012).

Chakhmouradian and Zaitsev (2012) divide REE deposits associated with igneous rocks into 5 groups: (1) carbonatites, (2) peralkaline silica undersaturated rocks, (3) peralkaline granites and pegmatites, (4) pegmatites associated with sub- to metaluminous granites, and (5) Fe oxide–phosphate deposits. According to the authors, of the 50 major advanced projects of REE exploration outside China, 20 are related to carbonatites and their alteration products and 13 are related to different types of alkali silicate rocks. In many of these deposits, high levels of REE cannot be explained by magmatic processes alone and require a source enriched in incompatible elements and, in some cases, late-stage remobilization of these elements by fluids (Williams-Jones et al. 2012) or by weathering processes. In this sense, Mariano et al. (2010) highlight the

difficulty in the detailed characterization of REE deposit. In addition to the formation of secondary REE minerals, such as florencite, cerite, and cerianite, REE also occur as ions on the surface of clay minerals such as kaolinite, halloysite and smectites ("ionic clays"). According to Bau (1991), the preferential concentration of HREE in the clay minerals is due to the high charge/radius ratio of these elements. This process enriches lateritic deposits up to 5 times in relation to the igneous protolith (Kynicky et al., 2012). China is the largest REE producer in the world; where most of its HREE production is are from "ionic clays REE deposits". Table 1 presents the main characteristic of some key-examples of REE deposits. The importance of carbonatites is highlighted.

Carbonatites are rocks that contain more than 50 vol% of primary igneous carbonate minerals (Streckeisen 1980) and with less than 20% SiO_2 (Le Maitre 2002). Woolley and Kempe (1989) classified the carbonatites in: calciocarbonatite, dolomite carbonatite, ferrocarbonatite [(FeOT+MnO)>MgO], magnesiocarbonatite, and natrocarbonatite. Mitchell (2005) redefined carbonatites using a mineralogical-genetic classification and divided them into two groups: primary carbonatites and carbothermal residua. Jones et al. (2013) proposed the category of REE-carbonatites which can be associated with variable Ca:Mg:Fe carbonatites and widely varying grain sizes and textures from fine-grained (Bayan Obo, Inner Mongolia, China), to pegmatitic (Kangankunde, Malawi), and porphyritic (Mountain Pass, California). These authors suggested a whole-rock value of >1% RE_2O_3 as a working definition of REE carbonatite and mentioned that higher values (>5%) have been used by some mining geologists (Castor 2008); however, these deposits are often also rich in iron and thus have been termed ferrocarbonatite. The classification of ferrocarbonatites was revised by Gittins and Harmer (1997). These ankerite- and siderite-carbonate rocks mainly occur as a minor component in many carbonatite complexes dominated by Ca-Mg carbonatite. The ferrocarbonatites are generally seen as the low-temperature product of fractional crystallization of Ca-Mg carbonate melts, nevertheless, some carbonatite specialists are sceptical as to whether Fe-rich carbonate magmas exist (Thompson et al., 2002). According to Mitchell (2005), carbothermal fluids typically concentrate the REE, Sr, Ba, *etc*. and not Nb, whereas intrusive carbonatites associated with rocks of the melilitite clan are typically important sources of Nb, Ti and P, but not the REE.

When China announced in 2009 the intention to change the trade policy for REE, prioritizing the supply of its domestic market, a global race for new REE deposits

133 began, as well as the development of feasibility studies for the production of these
134 elements as by-products of operating mines. As a consequence, the following REE
135 projects have been developed in Brazil (i) CBMM mining is producing REO in the
136 Araxá Mine from niobium tailings (Carneiro, 2015) (ii) Serra Verde Mining is
137 performing feasibility studies in the Serra Dourada REE deposit located in the Goiás tin
138 Province (Marini et al., 1992); (iii) feasibility studies have been developed to extract
139 REE from the Madeira Sn-Nb-Ta deposit in the Amazonas state (Garcia, 2012). There
140 has also been renewed interest in further studying REE mineralization in the Morro dos
141 Seis Lagos Nb deposit (MSLD) associated with carbonatite. Although this is the world's
142 largest Nb deposit it is very poorly studied.

143 In 2011, this research team began to investigate the MSLD, followed by a study
144 by Giovannini (2013) and by a detailed description of the laterites focused in the Nb
145 mineralization (Giovannini et al., 2017). These laterites formed by the weathering of
146 siderite carbonatite and the deposit has very unusual characteristics: the lateritic profile
147 is more than 200 m thick and shows six textural and compositional types of laterites;
148 reworking of the upper laterites; complete decomposition of pyrochlore in the laterite
149 profile; and the paragenesis of Nb-rich rutile and Nb-rich brookite which result from the
150 extreme lateritization that affected the carbonatitic rocks. In addition, the REE
151 mineralization that is focused in this article also has unique characteristics. Unlike other
152 secondary deposits, where REE-phosphates predominate, the secondary REE
153 mineralization in the laterites is mainly formed by a REE-oxide [cerianite-(Ce)], which
154 is of a purity never before described. In karst basins, the REE mineralization is
155 distributed along a sedimentary column of ~200m, in which it is related to 4 different
156 staged processes. All this is associated to an ambiguous siderite carbonatite, whose
157 weathering generated the overlapping mineralization of Nb and REE. As in the case of
158 the Nb mineralization, extreme weathering has been the main cause of the formation of
159 a REE mineralization.
160
161
162
163
164
165

166 Table 1. Major REE deposits including former and current producers.
167

Deposit	Economic Parameters	Host Rock	Major Ore Minerals	Licence Holder	Phase
Mount Weld, Western Australia, Australia 1	14.9 Mt at 9.7% REE_2O_3	Lateritic profile over calcite and dolomite carbonatite.	REE phosphates (florencite, monazite)	Lynas Coorporation Ltd.	Operation
Nolans Bore, Australia's Northern Territory, Australia	55.9 Mt at 2.59% REE_2O_3	Hydrothermal veins in an orthogneiss	Fluorapatite	Arafura Resources Ltd.	Advanced project (pilot plants)
Hoidas Lake, Saskatchewan, Canada	2.8 Mt at 2.4% REE_2O_3	Hydrothermal veins in Archean and Paleoproterozoic gneiss.	REE rich-Apatite	Great Western Minerals Group Ltd.	Project
Mountain Pass, California, USA	31.6 Mt at 6.57% REE_2O_3	Carbonatite associated with ultrapoassic rocks	Bastnaesite	Molycorp Inc.	Suspended (maintnence)
Bear Lodge, Wyoming, USA	18.0 Mt at 3.05% REE_2O_3	Carbonatite and silicocarbonatite dykes	Ancylite and fluorcarbonates (bastnaesite group)	Rare Element Resources Ltd	Project suspended (pre-feasibility)
Zandkopsdrift, South Africa	46.8 Mt at 1.89% REE_2O_3	Calciocarbonatite, ferrouginous and ferrocarbonatites associated with ultrapoassic rocks	Monazite	Frontier Rare Earths Ltd.	Project
Steemkampskraal, South Africa	0.7 Mt at 14% REE_2O_3	REE mineral veins in quarts diorite and leucotonalite.	Monazite, apatite, allanite	Great Western Minerals Group Ltd.	Suspended (low prices)
Kagankunde, Malawi	2.5 Mt at 4.24% REE_2O_3	Carbonatite	Monazite, bastnasite	Lynas Coorporation Ltd.	Project
Songwe Hill, Malawi	38.4 Mt at 1.6% REE_2O_3	Calciocarbonatite and fe-rich carbonatite.	Synchysite	Mkango Resources Ltd.	Project (pre-feasibility completed)
Tambreez, Greenland, Denmark	4300 Mt at 0.65% REE_2O_3	Agpaitic kakortokite. (Layered alkaline intrusion)	Eudyalite	Rimbal Pty Ltd.	Project (explotation license)
Kvanefjeld, Greenland, Denmark.	673 Mt at 1.09% REE_2O_3	Layered alkaline intrusion	Steenstrupine	Greenland Minerals and Energy	Project
Bayan Obo, Inner Mongolia, China	--	Dolomite/Hydrothermal	Bastnasite, parisite, monazite	--	Operation
Maoniuping, Sishuan, China	--	Carbonatite	Bastnasite	--	Operation
Jaingxi, China	--	Clay-bearing saprolite produced by the deep weathering of granite	Ion adsorption clay	--	Operation
Lovozero Massif, Kola Province, Russia	--	Layered alkaline intrusion	Loparite	--	Operation
Tomtor, Siberia, Russia	150 Mt at 6% REE_2O_3	Lateritic profile with reduced horizons over carbonatites	REE phosphates (florencite, monazite, xenotime, rabdophane)	Rostec Coorporation	Project

Araxá, Mins Gerais, Brazil	28.3 Mt at 4.21% REE_2O_3	Lateritic profile over calcite and dolomite carbonatites	Monazite, apatite	CBMM	Operation
Serra Verde, Minas Gerais, Brazil	911 Mt at 0.12% REE_2O_3	Clay-bearing saprolite produced by the deep weathering of granite	Ion adsorption clay	Mining Ventures Brasil Ltda.	Project

(This table was compiled using the following sources, listed alphabetically: Andreoli et al., 1994; Arzamastsev et al., 2008; Broom-Fendley et al., 2016; Castor, 2008; Chakhmouradian et al., 2015; Hatch, 2015; Huston et al., 2016; Kravchenko and Pokrovsky, 1995; Lottermoser, 1990; Mariano and Mariano, 2012; Pandur et al., 2016; Ray and Clark, 2015; Thrane et al. 2014; Voncken, 2016).

2. PREVIOUS WORKS

2.1 Geological setting

The Seis Lagos Carbonatite Complex (Issler and Silva, 1980) consists of three circular bodies discovered in the 1970's by the RADAM Project (Pinheiro et al., 1976). The carbonatite complex is located in the SW part of the Guyana Shield (Fig. 1). This region is covered by the Amazon rain forest and is geologically one of the least studied regions in the world. In the model by Santos et al. (2006a), the carbonatite complex is located approximately at the boundary between the Rio Negro Province and the K'Kmudku Belt (Fig. 1). The carbonatite complex is embedded in the Tarsira lithofacies (Fig. 2), which is composed by monzogranite augen gneiss and granitoids with ages of 1810 to 1790 Ma (Almeida et al. 2013), and is part of the Cauaburi Complex (CPRM, 2006).

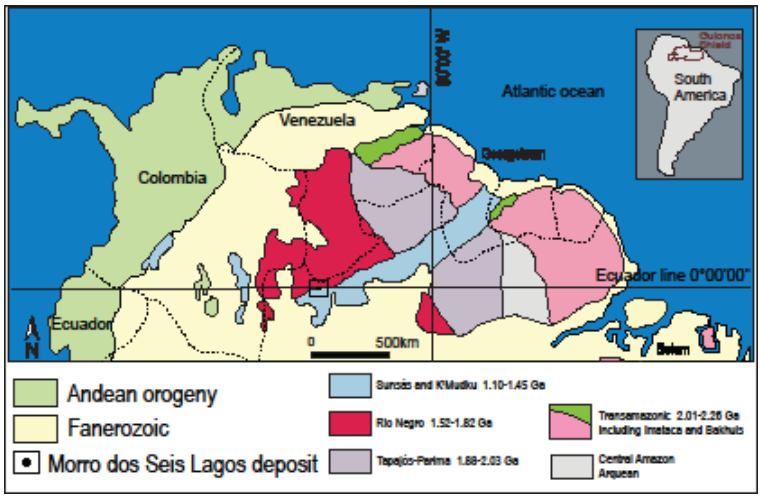

Figure 1. Geological provinces of the Guyana Shield (modified from Santos et al. 2006a) showing the location of the Morro dos Seis Lagos deposit.

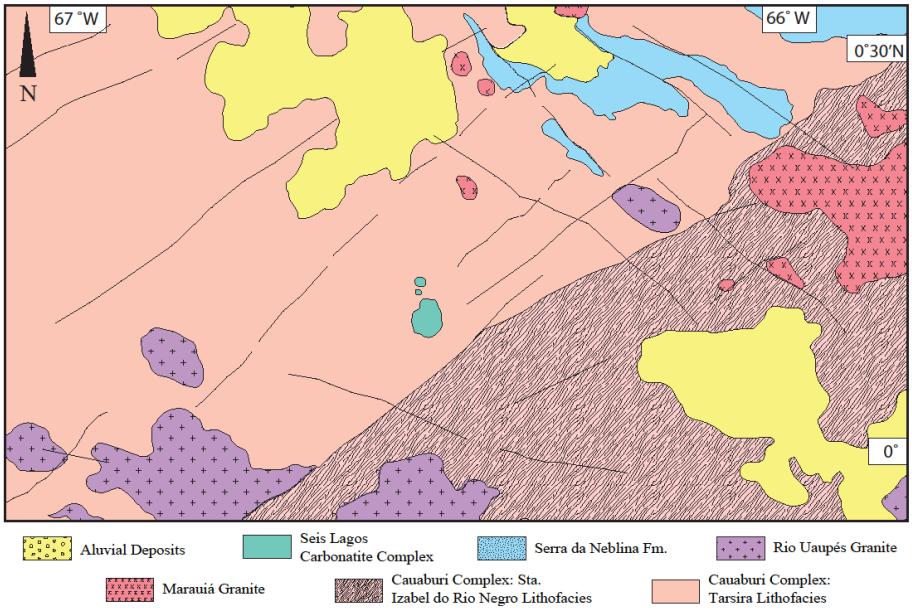

Figure 2. Geological map of the area of the Seis Lagos Carbonatite Complex (modified from CPRM 2006).

During the mid-Proterozoic, the region was affected by the formation of the K'Mudku Belt (Fig. 1), an intracontinental shear zone, reflection of Sunsás collisions along the margin of the Amazon Craton (Santos et al. 2000a). This event generated mylonitization and magmatism between 1.49 and 1.14 Ga (Santos et al. 2006a, 2006b, 2009, Almeida et al. 2013, Souza et al. 2015). CPRM (2006) related the complex emplacement to the Mesozoic reactivation of the K'Mudku Belt structures by the evolution of the Brazilian Equatorial Continental. However, other carbonatites in the southern part of the Guyana Shield, as the Maicurú (586 ± 18 Ma; Lemos and Gaspar 1998) and the Mutum (1.0 Ga; Gomes et al. 1990), have ages that preclude being related to the continental margin. Rossoni et al. (2017) obtained 3 groups of U-Pb ages in zircons from carbonatite samples: inherited zircons with ages compatible with the gneissic host rock (~1820 Ma); the superior intercept age of 1525 ± 21 Ma; the superior intercept age of 1328 ± 58 Ma (MSWD= 1.4; Th/U from 1.52 to 0.14). The mineralogical study indicates that the ~1.3 Ga zircons have affinity with carbonatite. It is, however, a tendency rather than a well-defined result. The available data allow to state the age of 1328 ± 58 Ma represents the maximum age of the carbonatite.

Aeromagnetometric data suggests that the Seis Lagos Carbonatite Complex positioning was controlled by a structure in the E-W direction (Rossoni et al. 2016). The circular shape of the hill is outlined by the base of the talus deposit (Fig. 3 and 4). However, the shape at a higher elevation resembles a polygon (Fig. 3). The hill has linear

edges on all sides of the polygon, except the NW edge, which presumably had a NE-SW direction but was interrupted by valleys controlled by NNW-SSE structures (Fig. 3). The remarkably rectilinear boundaries suggest that carbonatite emplacement has been controlled by brittle structures. The relief on the hill is controlled by NNE-SSW, NNW-SSE and E-W structures (Fig. 3). All the lakes and a number of karstic depressions filled by clays (assigned as sediments in Fig. 4) are associated with these structures (Rossoni et al., 2016).

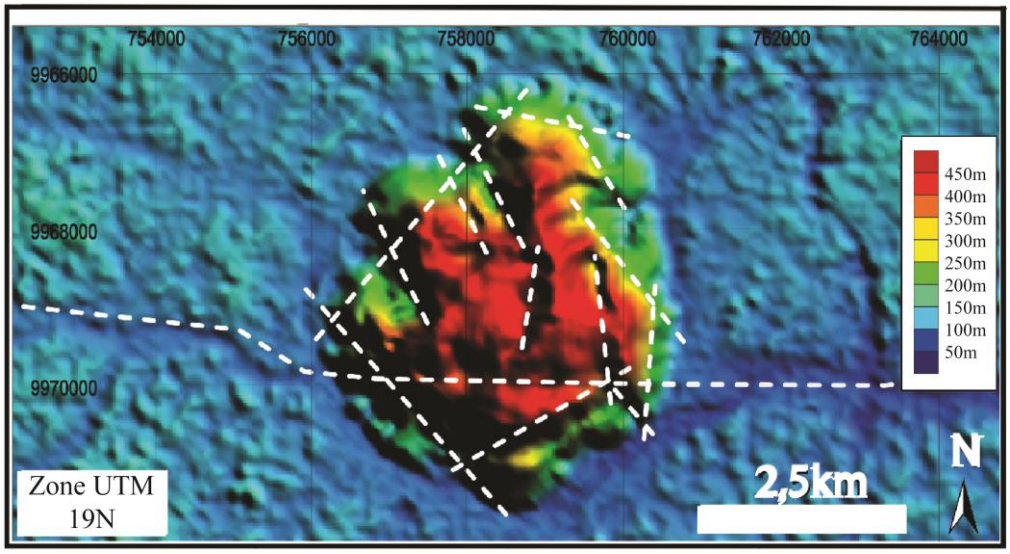

Figure 3. Morphostructures in the Morro dos Seis Lagos carbonatite body (modified from Rossoni et al., 2016).

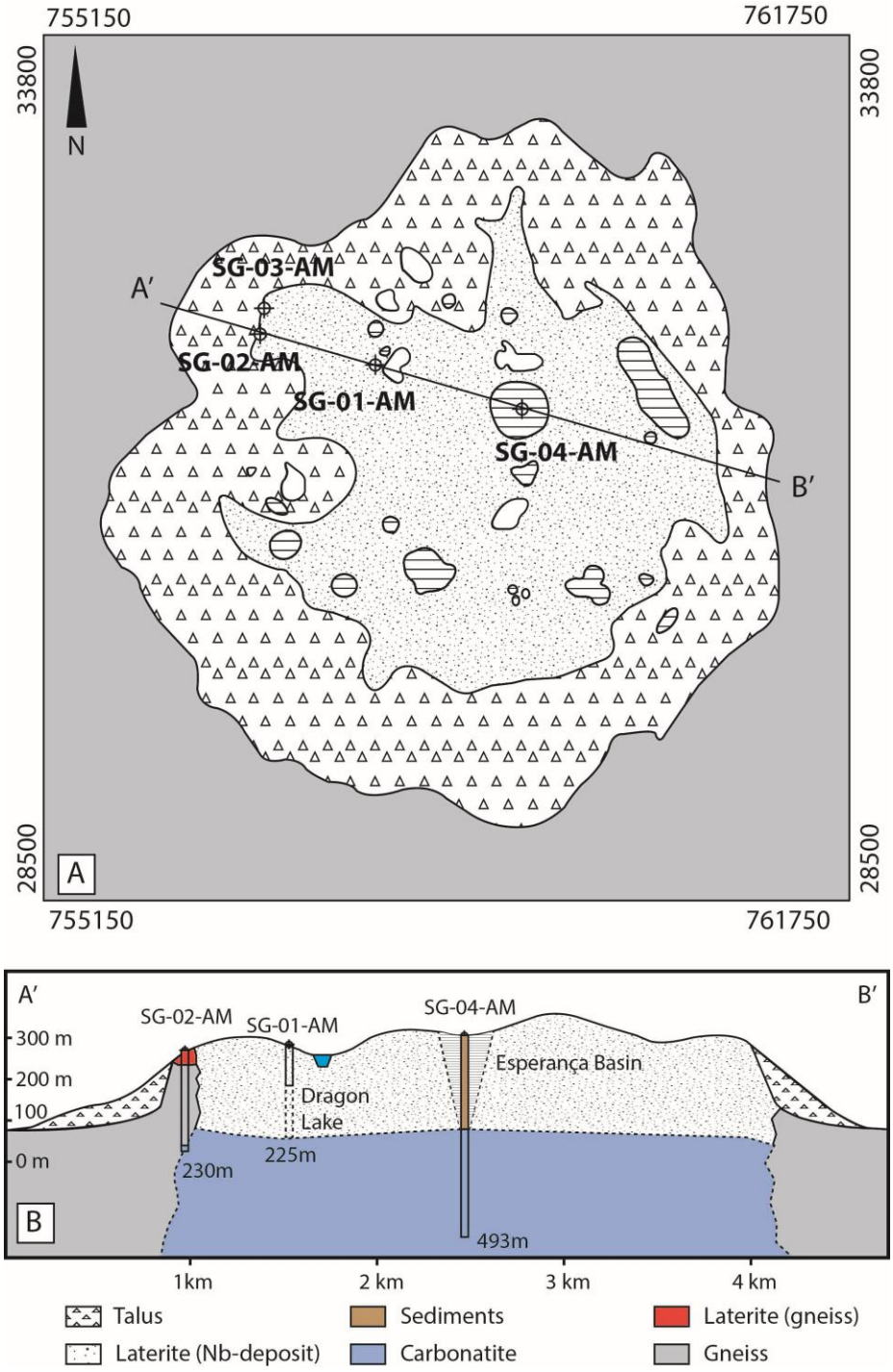

Figure 4. Geological map (modified from Viegas & Bonow, 1976) and vertical section of the Morro dos Seis Lagos carbonatite body and associated Nb-deposit.

2.2 The Morro dos Seis Lagos Deposit

The Companhia de Pesquisa de Recursos Minerais (CPRM), implemented an exploration program (Seis Lagos Project) (Viegas and Bonow, 1976) on the Morro dos

Seis Lagos carbonatite body that included the drilling of 4 boreholes (located in Fig. 4A). In 1982, CPRM drilled 4 additional boreholes (Uaupés Project) in order to block Nb resources (2897.9 Mt at 2.81% Nb_2O_5, Justo and Souza, 1984, 1986). Corrêa (1996) and Corrêa and Costa (1997) conducted detailed mineralogical and chemical studies using surface samples and core pulps from drill cores from the first CPRM campaign. Since then, no other study was conducted until Giovannini (2013).

The Morro dos Seis Lagos carbonatite body is covered by a thick lateritic crust that corresponds to the MSLD. The primary carbonatite rock was intersected in only two drill holes (SG-02-AM and SG-04-AM, Fig. 4). It was classified by Viegas & Bonow (1976) as beforsite (?) in SG-02-AM and as carbonatic breccia in SG-04-AM. Issler & Silva (1980) were the firsts to recognize this breccia as carbonatite and to use the term Seis Lagos Carbonatite Complex.

The lateritic profile may be more than 200m thick according to information obtained in drill hole SG-01-AM. However, detailed description of this drill hole was possible only down to 100m due to poor recovery below this depth. Six textural and compositional types of laterites were identified (from the top to the botton): (i) pisolitic laterite; (ii) fragmented laterite; (iii) mottled laterite; (iv) purple laterite; (v) manganiferous laterite; and (vi) brown laterite. All these types are mainly formed by goethite and hematite. Goethite predominates in the upper types (i to iii), that result from the physical and chemical reworking near the surface, and in the brown laterite, whereas hematite predominates in the purple laterites. In the manganiferous laterite (10m thick), the manganese oxides (mainly hollandite, with associated cerianite) occur as veins or irregular masses crosscutting the ferruginous laterite.. Manganese precipitation is a late event during the development of the lateritic profile. The main Nb ore mineral is Nb-rich rutile (with 10.5 - 26.86 wt% Nb_2O_5), which occurs in all iron laterites, formed together with Nb-bearing goethite and secondary Ce-pyrochlore, likely from a former pyrochlore. Minor Nb-rich brookite, formed from Nb-rich rutile, occurs as broken spherules with oolitic structure. The laterites have average Nb_2O_5 concentrations of 2.91 wt% (Giovannini et al. 2017).

The upper section (0 – 233 m) of the drill hole SG-04-AM (Fig. 4) is composed by sediments of the Esperança Basin deposited in a lacustrine environment (Viegas and Bonow 1976; Corrêa 1996). Bonow & Issler (1980) highlighted the high REE

concentrations in the interval 14.65 – 73.10 m for which they inferred a reserve of 7,839 Mt with 1.5 wt% REE_2O_3; the nature of the mineralization is not mentioned.

3. RESEARCH MATERIAL AND METHODS

This work is based mainly on drill cores of boreholes SG-01-AM, SG-02-AM, SG-03-AM, and SG-04-AM, which were completely relogged and sampled in May 2011 at the Departamento Nacional da Produção Mineral office of Manaus city, Amazonas State. The cores of the additional four boreholes drilled by CPRM in 1982 were also inspected but the types of laterites they intercepted are all similar to those described in borehole SG-01-AM, upon which our analytical work in laterites is concentrated.

The samples were examined using optical microscopy in transmitted polarized and reflected light. The X-ray diffraction (XRD) work was performed at the Instituto de Geociências of the Universidade Federal do Rio Grande do Sul (UFRGS) using a Siemens D-5000 diffractometer, equipped with Cu-Kα radiation and a Ni filter in the range from 2° to 70° 2θ with a velocity of 0.02º 2θ per second. The clay minerals were separated by decanting and submitted to the process of saturation with ethylene glycol (glycollate) and heating at 550 ºC for two hours (calcined), in order to identify them. XRD data were processed with "MATCH! Phase identification from powder diffraction" developed by Cristal Impact, and compared to the Crystallography Open Database (COD) database.

The Esperança Basin minerals were separated also by gently crushing these samples, concentrating the resulting powder onto a stub and submitted to SEM analyses. EDS analyses were performed at the Centro de Microscopia Eletroônica (CME-UFRGS) using a JEOL-JSM5800 scanning electron microscope (SEM) with a voltage of 20 kV and a spot size of 5 μm, and in Laboratório de Geologia Isotópica (LGI-UFRGS) using a JEOL 6610-LV, scanning electron microscope (SEM) with a voltage of 15 kV and a spot size of 1 μm.

The electron microprobe analyses were performed at the Instituto de Geociências of the Universidade de Brasília using a JEOL JXA-8230 instrument. In the first session the concentrations of P, Si, Ca, Na, K, Ba, Sr, Al, Fe, Mn, Ti and F were

determined with an accelerating voltage of 15kV and a beam current of 10nA. The concentrations of Nb, Ta, W, REE, Y, U, Th, and Pb were determined with an accelerating voltage of 20kV and a beam current of 20nA and a spot size of 1 μm. In the second session the concentrations of F, Cl, Ca, Mg, Al, Si, Ti, Nb, Ta, P, Zr, Hf, Fe, Mn, Y and V were determined with an accelerating voltage of 15kV and a beam current of 10nA. The concentrations of REE, U, Th, Ba, Sr, K, Pb, Na, Zn, Sc, S and W were determined with an accelerating voltage of 20kV and a beam current of 50nA.

Whole rock geochemical analyses of 86 individual core samples were performed at ACME Analytical Laboratories Ltda (Canada). Major oxides (SiO_2, Al_2O_3, Fe_2O_3, MgO, CaO, Na_2O, K_2O, TiO_2, P_2O_5, MnO, Cr_2O_3) and trace elements (Ba, Be, Co, Cs, Ga, Hf, Nb, Ni, Rb, Sc, Sn, Sr, Ta, Th, U, V, W, Zr, plus 14 REE and Y) were analyzed by ICP-MS after fusion and nitric acid digestion of 0.2 g aliquots. Another set of trace elements (Ag, As, Au, Bi, Cd, Cu, Hg, Mo, Ni, Pb, Sb, Se, Tl, Zn) was analyzed by ICP-MS after aqua regia digestion of 0.5g aliquots. Loss on ignition was obtained by weight difference after ignition at 1000^{o}C. Total C and S were obtained by Leco analysis.

Subsequently, the boreholes SG-01-AM and SG-04-AM were re-sampled by CPRM as 194 continuous core sample intervals. These samples were prepared for XRD and whole-rock analyzes. XRD analyzes were carried out on PANalytical X'PERT PRO MPD (PW 3040/60) Diffractometer, with goniometer PW3050/60 (Theta/Theta) and x-ray tube in Cu (Kα1 1,5406 Å) model PW3373/00, long thin focus, 2200W, 60kv, with detector RTMS Pixcel/1D. Data acquisition was done with X'Pert Data Collector software, version 2.1a, and data processing with PANalytical X'Pert HighScore software version 3.0d. The analytical conditions were 40 kV, 40mA, scan range (2θ) 5-70, step size (°2θ) 0.02, scan mode continuous, counting time 50s, divergence slit fixed 1/2°, mask fixed 10mm, anti-scatter slit name 5.7mm. SGS-Geosol Laboratories provided geochemical analyses for 66 elements. For major element oxides (SiO_2, Al_2O_3, Fe_2O_3, CaO, MgO, Na_2O, K_2O, MnO, TiO_2, P_2O_5) samples were fused with LiBO2, and analyzed by X-Ray fluorescence. The same fusion was utilized for trace elements including 14 REE plus Ba, Be, Cs, Ga, Hf, Nb, Rb, Sn, Sr, Ta, Th, U, W, Y, Zr but analysis were performed by ICP-MS after nitric acid digestion. In the cases where RRE results were above upper detection limit samples were re-analysed by X-ray fluorescence. For other trace metals like Ag, As, Au, B, Bi, Cd, Co, Cr, Cu, Ge, Hg, In,

Li, Mo, Ni, Pb, Re, S, Sb, Sc, Se, Te, Tl, V, Zn samples were digested by Aqua Regia and analyzed by ICP-MS. Loss on ignition was obtained by weight difference after ignition at $1000C^0$. A Leco furnace was used to measure total C and S.

4. RESULTS

The re-logging and reinterpretation of the 4 boreholes of CPRM first campaign (located in Fig. 4A) led to propose a geological profile (Fig. 4B) quite different from that presented by Justo e Souza (1984, 1986).

Borehole SG-01-AM is described in detail in Giovannini et al. (2017) with focus on the laterite features and Nb minerals. However, detailed logging of this drill hole was not possible from 97.50 to 255.25m due to very poor recovery. The few remaining cores available in that interval led Viegas and Bonow (1976) to describe it as lateritic crust, but they were not retained in the drill core boxes.

Borehole SG-02-AM intersected non-mineralized laterite (formed from the gneiss) (0 – 34.00 m), fenitized gneiss (34.00 - 222.60 m), and carbonatite (221.60 – 227.70 m); the 227.70 – 230.85 m interval was not recovered. Borehole SG-03-AM intersected non-mineralized laterite (0 – 9.00 m), saprolitized gneiss (9.00 – 50.00 m), and fresh gneiss (50.00 – 110.00 m). Borehole SG-04-AM (Fig. 4A), located in the Esperança Basin, intersected: (0 to 233.65 m) sedimentary package; (233.65 to 288.00 m) siderite carbonatite; (288.00 to 340 m) REE rich siderite carbonatite; (340.00 to 492.00 m) siderite carbonatite.

In this paper we present detailed descriptions of the REE mineralization associated to the laterites (borehole SG-01-AM), to the border siderite carbonatite (SG-02-AM), to the sedimentary package of the Esperança Basin and to the core siderite carbonatite (both in the borehole SG-04-AM). There is no REE mineralization in the laterite and the corresponding gneiss from borehole SG-03-AM.

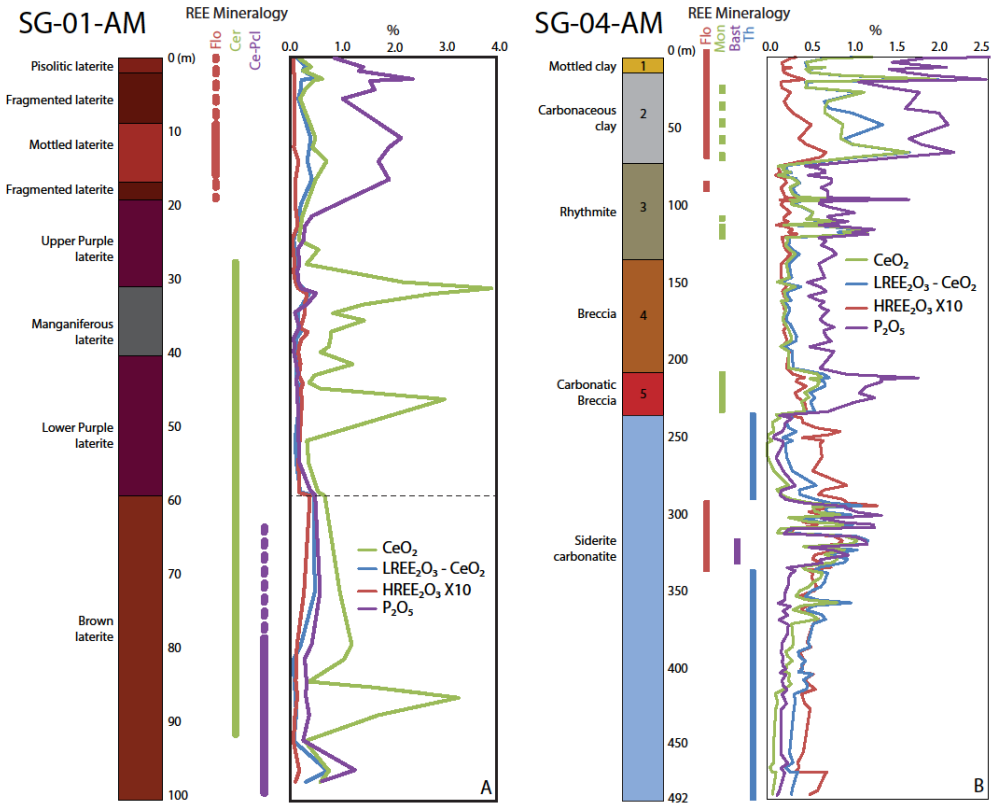

Figure 5. Geological profile, REE mineralogy, and vertical distribution of REE oxides and P_2O_5 in two boreholes (locations in Fig. 4) from the Morro dos Seis Lagos deposit. (A) Laterite profile in borehole SG-01-AM (Giovannini et al. 2017). (B) Esperança basin and core siderite carbonatite in borehole SG-04-AM.

4.1. REE mineralization in the siderite carbonatite

The carbonatites intersected in drill holes SG-02-AM (border of the carbonatite body) and SG-04-AM (center) are invariably a light grey siderite carbonatite. Siderite is the only carbonate present. On the other hand, border and center siderite carbonatites present many mineralogical differences concerning accessory minerals and REE minerals.

The border siderite carbonatite is composed by siderite, barite, and gorceixite, with minor hematite, rhabdophane-(Ce) and pyrochlore. Siderite (~70 vol.%) crystals are euhedral, with average size of 700 µm, some crystals are broken and present hematite at the edges and in fractures. Barite (~15 vol.%) occurs as aggregates of fine crystals (up to 150 µm) that fill the interstices of siderite crystals (Fig. 6A) or occurs in veins in siderite crystals. Gorceixite (up to 7.5 vol.%) occurs as the predominant mineral in aggregates (Fig. 5C) with rhabdophane-(Ce) and pyrochlore; the crystals are

euhedral, with size up to 5 µm. Rhabdophane-(Ce) (up to 1 vol.%) occurs mainly as fibrous radiated crystals, more commonly smaller than 5 µm, but frequently reaching 40 µm (Fig. 6B). More rarely rhabdophane-(Ce) occurs filling gaps between siderite crystals (Fig. 6C). BSE images reveal that this rhabdophane-(Ce) is actually aggregates of smaller crystals. The textures suggest that gorceixite and rhabdophane-(Ce) are hydrothermal. Pyrochlore (<1 vol.%) occurs as euhedral crystal, with ~3 µm in the aggregates (Fig. 6C) with monazite and gorceixite.

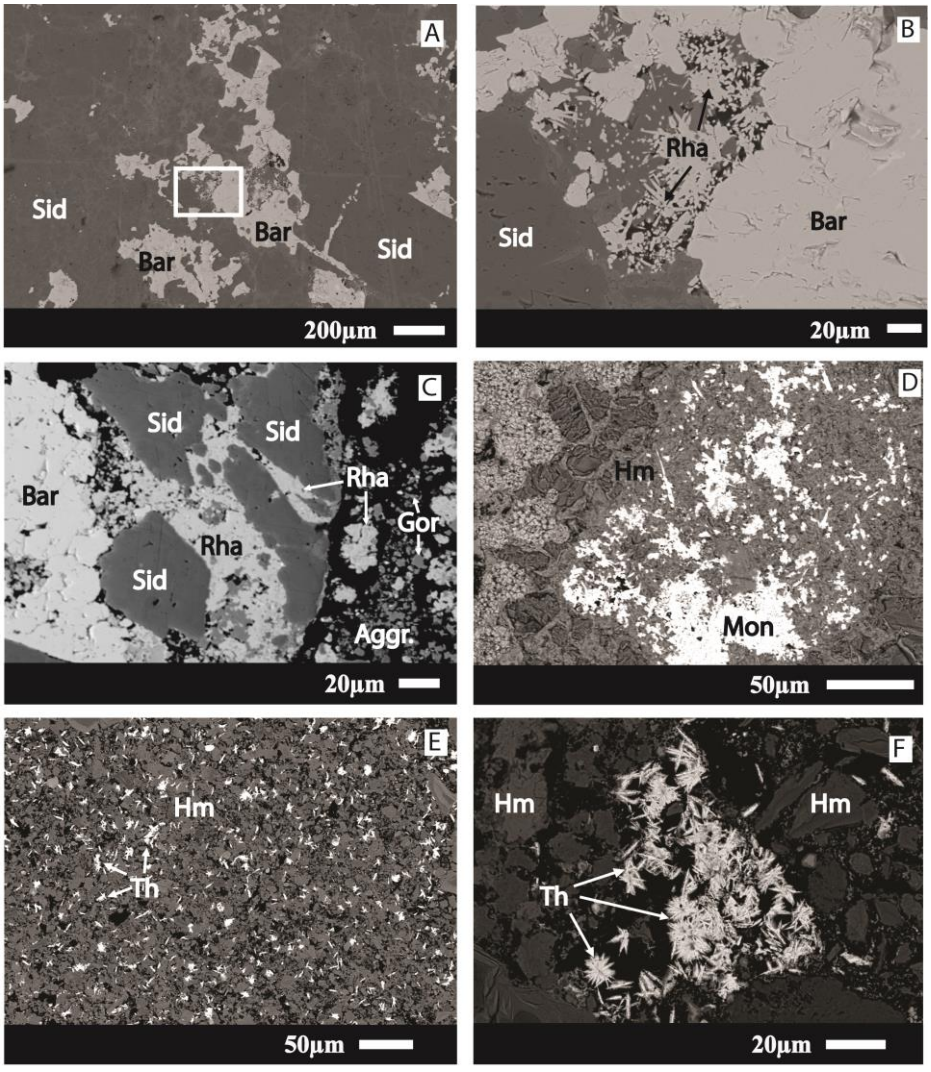

Figure 6. REE minerals from the Seis Lagos primary rock. Border siderite carbonatite: (A) barite veins filling interstices between siderite euhedral crystals, and small monazite crystals (BES image); (B) zoom of rectangle in A: fibroradiated crystals of rhabdophane-(Ce) in the interface between siderite and barite; (C) rhabdophane-(Ce) mass filling gaps between siderite crystals. Core siderite carbonatite: (D) Monazite agglomerate in hematitic matrix; (E) small throbastnäsite acicular crystals in a hematitic matrix; (F) acicular thorbastnäsite crystals fulfilling spaces in a hematitic matrix.

399 The core siderite carbonatite is mainly composed by siderite with subordinate
400 hematite and minor monazite, thorbastnäsite, bastnäsite, pyrochlore, titanomaghemite,
401 NB-rich brookite, and gibbsite. Quartz and gypsum were detected only by DRX in few
402 samples. Siderite grains are more commonly partially dissolved, but some euhedral
403 crystal also occurs, they are brownish, with sizes up to 500 μm, and frequently present
404 trails of fluid inclusions that can be very abundant. The crystals present hematite at the
405 edges or along fractures. The rock matrix is essentially made of hematite (Fig. 6D, E,
406 F).
407 Petrographically the only difference between the ordinary core siderite
408 carbonatite and the REE-rich core siderite carbonatite is given by the REE minerals.
409 The latter has mainly monazite and bastnasite and the first has almost exclusively
410 thorbastnasite. Pyrochlore, monazite, bastnäsite, and thorbastnäsite were observed only
411 in BSE images. Pyrochlore occurs as euhedral crystals of ~5 μm. Monazite occurs as
412 agglomerate with 100 μm made by crystals with 5 μm (Fig. 6D). Bastnäsite occurs as
413 single small crystals (<5 μm) dispersed in the matrix. Thorbastnäsite occurs as acicular
414 crystals fulfilling spaces between hematite crystals of the matrix (Fig. 6E, F). Gibbsite
415 occurs as veinlets that cut siderite and hematite crystals.
416 Nb-rich brookite likely primary and titanomaghemite secondary were observed
417 in only few samples. Titanomaghemite occurs as agglomerate of small acicular crystals
418 (up to 50 μm; more commonly ~10-20 μm) that overgrowths as coatings on or replaces
419 a primary cubic mineral likely titanomagnetite. Nb-brookite occurs as broken and more
420 commonly fractured crystals with size from 100μm to 3mm dispersed in the rock.
421
422
423 4.2 REE mineralization in the laterites
424
425 The REE minerals in the laterites are florencite-(Ce), which was observed in the
426 reworked laterites (pisolitic, fragmented, mottled laterites), and cerianite-(Ce), which
427 was observed in the upper purple, manganiferous, lower purple and brown laterites,
428 being particularly abundant in manganiferous laterite.
429 The florencite-(Ce) occurs as agglomerates more commonly with 30 μm to 50
430 μm, which fill interstitial/residual spaces between the crystals of iron-oxides (Fig. 7A).
431 The agglomerates are formed by elongated florencite-(Ce) crystals, with a length of ~5

μm (rarely reaching 20 μm). Some agglomerates have a fibroradial appearance. The crystals contain numerous inclusions of Fe-oxides and very small minerals unidentified.

Cerianite-(Ce) in the upper purple laterite is rare and occurs filling very small residual spaces in Fe-oxides. It has also been observed inside of Nb-rich rutile crystals (Fig. 7B), filling cavities and fractures resulting from the alteration and fracturing of this mineral. Such spaces are similar to those observed in Nb-rich rutile when this mineral is transformed to Nb-rich brookite.

The manganiferous laterite thick is 9 m (interval between 31 m and 40 m) in the borehole SG-01-AM. Manganese oxides in large quantities occur as veins or irregular masses that cut through the fabric of the iron-rich material. They are sub-millimeter to-centimeter in size and can form banded or brecciated patterns. The modal composition (vol%) of the manganiferous laterite is hematite (20% to 45%), goethite (30% to 68%), hollandite (12%), and cerianite-(Ce) (1%). Cerianite-(Ce) occurs as small crystals ($\leq$ 5 μm), that locally may be abundant, and fill residual spaces in the iron-rich material (Fig. 7C) and within the Mn-bearing veins (Fig. 7D, E, F). The paragenesis in the wider Mn-bearing veins (1 cm) is hollandite, pyrolusite, goethite, and cerianite-(Ce) combined in different ways and proportions (Fig. 7D). In these veins, hollandite bands (Fig. 7D) are very homogeneous, without mineral inclusions (except for cerianite-(Ce)) and without alteration zones. In thinner hollandite veins, cerianite-(Ce) forms "crystals" that occupy the whole thickness of the vein (Fig. 7E). Examining in more detail these "crystals" it is observed that they have parts formed by pure cerianite-(Ce) and part formed by the intergrowth of cerianite-(Ce) and hollandite (Fig. 7F).

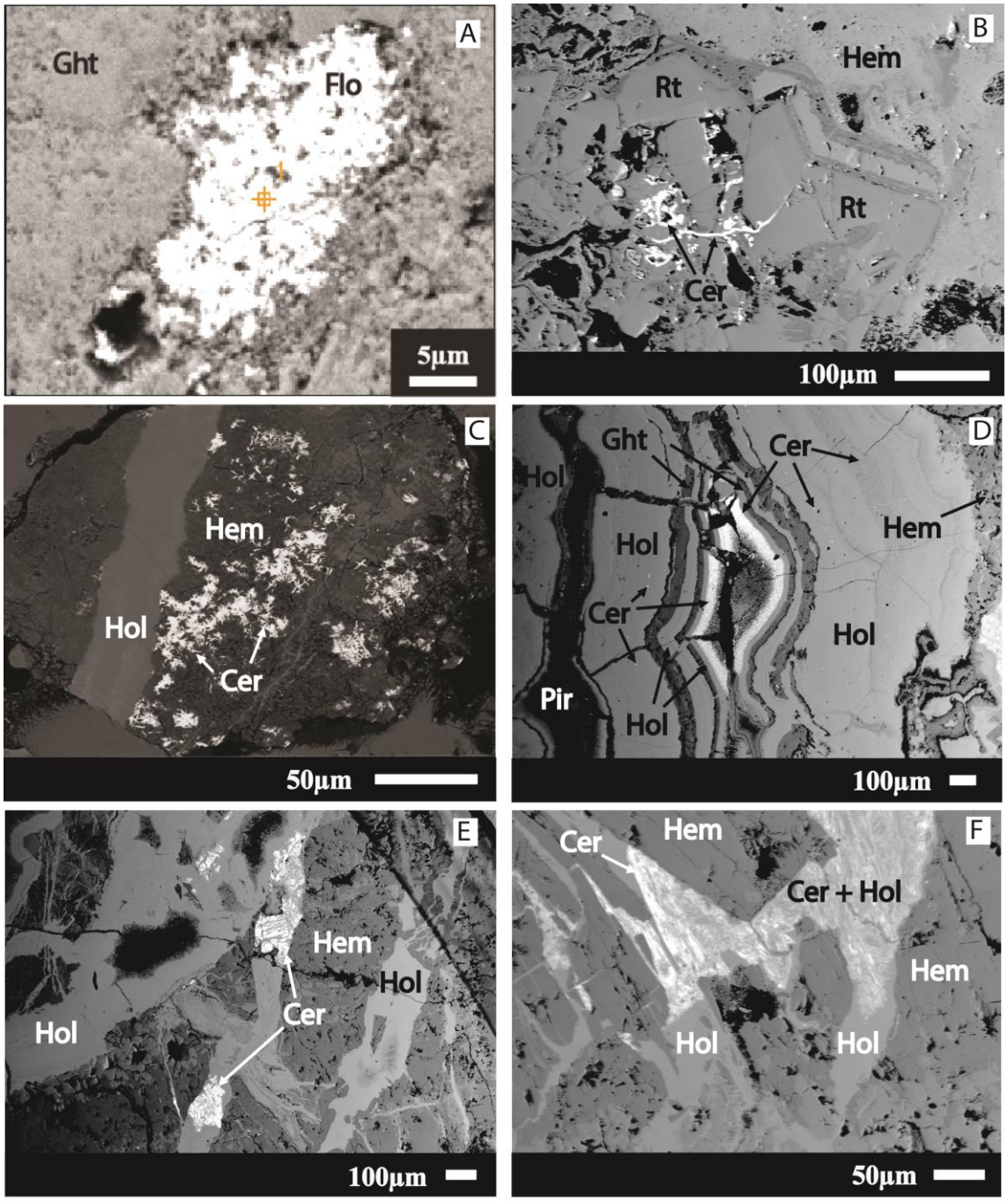

Figure 7. REE minerals in laterites from the Morro dos Seis Lagos deposit; (A) florencite-(Ce) agglomerate filling spaces between goethites; (B) cerianite-(Ce) small vein filling cavities in Nb-rich rutile; (C) hematite with small cerianite-(Ce) crystals cut by hollandite vein; (D) banded Mn-rich veins constituted by hollandite, pyrolusite, cerianite-(Ce) and goethite; (E) hollandite veins intergrown with cerianite-(Ce) crosscutting hematite crystals; (F) pure cerianite-(Ce) and cerianite-(Ce) intergrowth with hollandite in veins cutting hematite crystals.

The lower purple and brown laterites, especially for the last, compared to the reworked laterites, has fewer tubular cavities filled with iron precipitates. Goethite is the dominant mineral, making up to 96 vol% of the laterite, and is more evenly distributed.

This shows that Fe has been less remobilized, suggesting it has developed closer to the carbonatite protolith and therefore represents a less-developed laterite. In these laterites, cerianite-(Ce) occurs more commonly as “discontinuous bands” intercalated with the goethite (Fig. 8A). In the detail (Fig. 8B) these "discontinuous bands" are individual crystals or clusters of crystals formed on goethite growth surfaces. These crystals have characteristically a biconvex shape and length of the order of 10 μm. In many cases, cerianite-(Ce) is the last mineral to precipitate in theses cavities, which frequently are not completely filled (Fig. 8D).

The main REE bearing mineral in the laterites is the Ce-pyrochlore (Fig. 8D), which occurs in the middle and lower section of the brown laterite (below 79.00 m). This Ce-pyrochlore formed, together with Nb-rich rutile and Nb bearing goethite, from the weathering of a not identified former mineral (whole white area in Fig. 8D), more likely a pyrochlore. The Ce-pyrochlore weather and disappear in the upper part of brown laterite and laterites above this one.

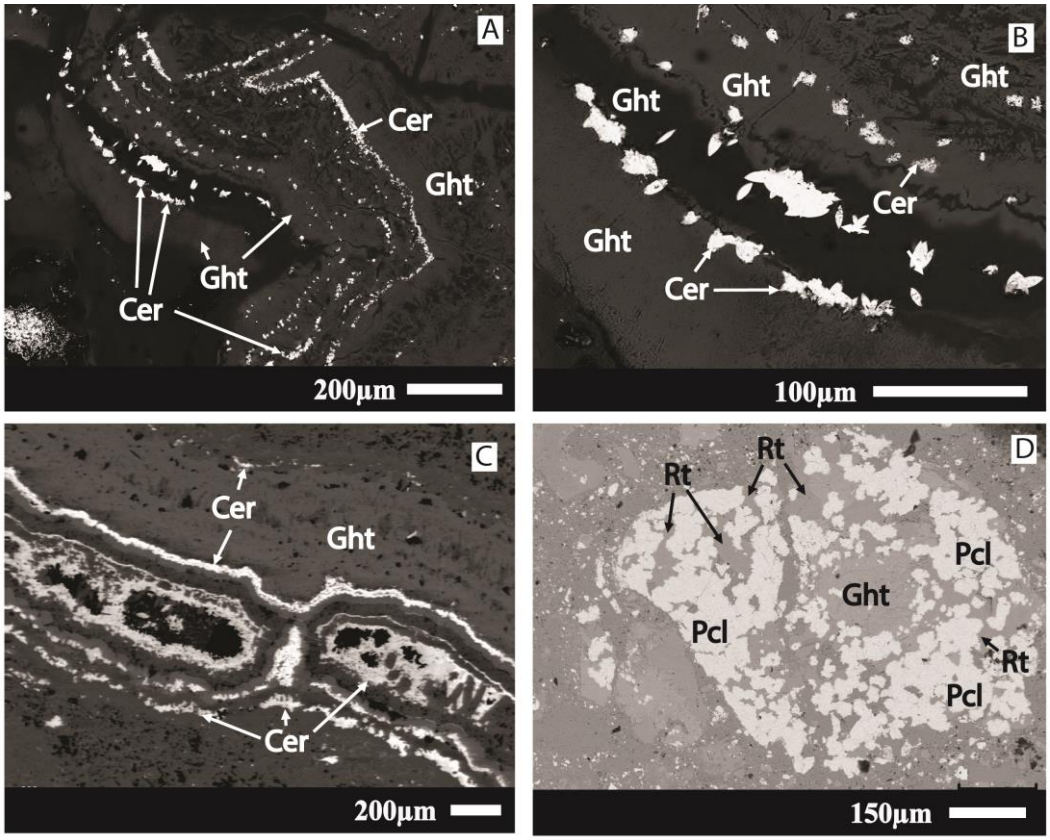

Figure 8. REE minerals from the Seis Lagos lateritic deposit; (A) cerianite-(Ce) crystals forming a descontinuos band intercalated with goethite; (B) detail of the image A, individual and agglomerates of cerianite-(Ce) crystal which forms the cerianite-(Ce) band; (C) Continuous cerianite-(Ce) band intercalated with goethite, filling cavities; (D) Ce-pyrochlore, Nb-rich rutile and Nb bearing goethite formed by weathering of an unidentified former mineral. (A) and (B) from Takehara et al. (2015).

4.3 Esperança Basin and REE mineralization

The whole basin is essentially filled by clays. Intercalations of coarser material (mainly carbonatite fragments) are frequent only in the lower layers (layers 4 and 5), and the finest and purest sediments occur at the top (layer 1). Our data by x-ray diffraction of selected samples (Tab. 2) indicate kaolinite as the major clay mineral in all layers; illite was identified only in layer 3. The other minerals in the basin (Tab. 2) allow regroup the 5 layers into two packages: the lower package (layers 3, 4 and 5) characterized by the presence of quartz and hematite (and monazite in layer 4) and the upper package (layers 1 and 2) characterized by the almost total absence of these two minerals, by the presence of florencite-(Ce) and gibbsite (only in layer 1) and carbonaceous material (layer 2).

The florencite-(Ce) is much more common in the upper 50 m of the sedimentary package. It occurs more often as clusters of crystals developed in voids in the clayey material. In some clusters, the crystals are abundant, thin and tabular (Fig. 9A). In other clusters, the crystals are less abundant, but are better developed and better crystallized (Fig. 9B). Rounded agglomerates of fine crystals of florencite-(Ce) (Fig. 9C) are also common. In many cases, better developed crystals of florencite-(Ce) stand out from the clusters (Fig. 9D). Agglomerates of florencite-(Ce) crystals may also develop on the surface of kaolinite (Fig. 9E). Due to these characteristics, the crystallization of the florencite-(Ce) within the sediments of the Esperança Basin is considered authigenic. Detritic grains of monazite (Fig. 9F) occur at the intermediate part of the sedimentary package.

521 Table 2. Sediment layers, studied samples and minerals identified in the Esperança Basin.

Layer	Sediment type	Sample	Depth (m)	Minerals								
				Kao	Qz	Hem	Sid	Flo	Mon	Gbs	Ill	Jar
1	Mottled clay, light yellow.	SG04-AM-02	9.30	x				x		x		
		SG04-AM-28	14.50	x				x		x		
2	Carbonaceous clay, homogeneous, oleaginous, with preserved organic matter	SG04-AM-29	16.40	x				x				x
		SG04-AM-03	34.00	x				x				
		SG04-AM-32	50.00	x				x	x			x
		SG04-AM-34a	70.00	x	x							
		SG04-AM-34b	70.00	x		x						
3	Rhythmites, intercalations of ferruginous and grey quartz-kaolinitic bands. Some ferrougionous argilite portions.	SG04-AM-36	78.00	x	x	x						
		SG04-AM-04	86.00	x	x	x		x				
		SG04-AM-05	93.00	x	x	x						
		SG04-AM-40	99.80	x	x	x						
		SG04-AM-06	105.00	x	x	x			x		x	
		SG04-AM-43	119.00	x	x	x			x			
		SG04-AM-07	133.00	x	x	x			x			
4	Breccia with fragmentes of rytmite and carbonatite (mainly in the lower portion)	SG04-AM-45	148.20	x	x							x
		SG04-AM-46	148.50	x		x						
		SG-04-AM-09	200.00	x	x	x						
5	Breccia with carbonatite fragmentes with interlayers of caolinitic clay	SG-04-AM-10	227.50	x		x						

522

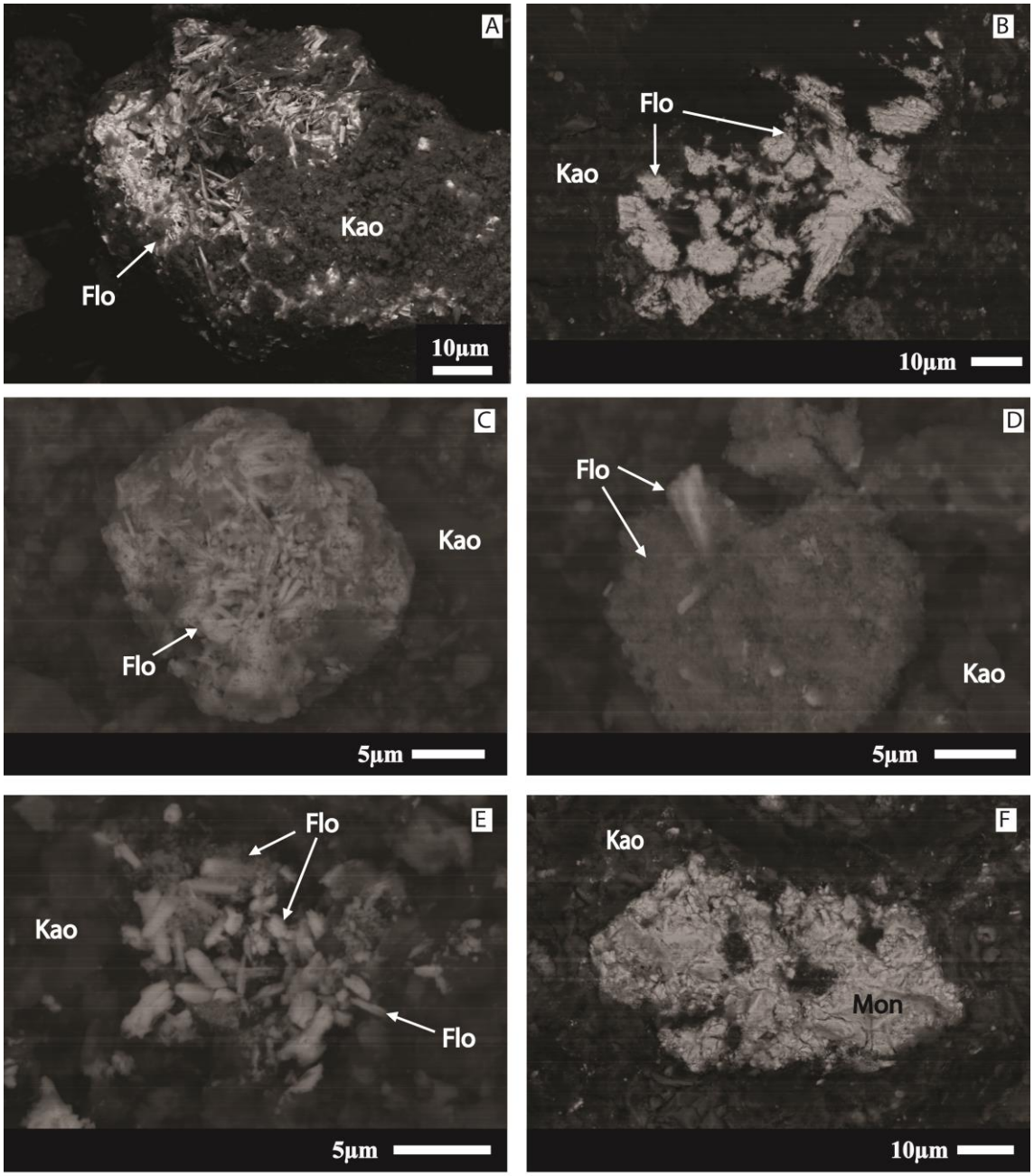

Figure 9. SEM images of: (A) Aggregates of tabular florencite-(Ce) crystals (white) developed in void spaces in the clayey sediment. (B) Euhedral florencite-(Ce) crystals developed in void spaces in the clayey sediment. (C) Grain of the clayey material formed by agglomerates of florencite-(Ce) crystals. (D) Florencite-(Ce) grain formed by a mass consisting of agglomerate of smaller crystals from which bigger florencite-(Ce) crystals developed. (E) Cluster of florencite-(Ce) crystals developed on the surface of kaolinite. (F) Monazite fragment in sediment from the lower portion of the Esperança Basin.

534

535 4.4 REE Mineralogy

536

537 The REE minerals are cerianite-(Ce) (secondary mineral in the laterites),
538 florencite-(Ce) (authigenic mineral in the Esperança Basin), rabdophane, monazite,
539 bastnäsite and thorbastnäsite (primary and secondary minerals in the siderite
540 carbonatite; detrital minerals in the Esperança Basin). The REE bearing minerals are
541 pyrochlore (siderite carbonatite and laterites) and gorceixite (secondary in the siderite
542 carbonatite).

543

544 4.4.1 REE minerals

545

546 Cerianite-(Ce) is usually described by the formula $(Ce^{+4}, Th)O_2$ and by the
547 empirical formula $Ce_{0.75}Th_{0.25}O_2$ (Min Data 2017). Table 3 shows representative
548 compositions and respective structural formulae of cerianite-(Ce) from the
549 manganiferous and brown laterites. Compared to the ideal composition, both are rich in
550 Ce and poor in Th, notably by the cerianite-(Ce) from the brown laterite, in which the
551 concentration of Ce_2O_3 reaches 94.80 wt%, corresponding to 0.958 Ce apfu, and the
552 concentration of ThO_2 varies between 0 and 0.6 wt%, contrasting with the cerianite-(Ce)
553 from the manganiferous laterite, where ThO_2 ranges from 2.57 to 7.32 wt%. Nd is
554 $REE^{+3}$the most regularly present, with concentrations between 0.26 and 0.55 wt%
555 Nd_2O_3, without significant differences between cerianites-(Ce) from the two types of
556 laterite. Sm occurs with much lower concentrations (up to 0.1 Sm_2O_3) in almost all
557 analyzed crystals. On the other hand, Gd occurs with a much higher concentration in the
558 cerianite-(Ce) from brown laterite (Gd_2O_3 ~2.75 wt%) than in cerianite-(Ce) from the
559 manganiferous laterite (Gd_2O_3~ 0.04 wt%). Also noteworthy are the presences, in all
560 analysed cerianite crystals, of Nb (up to 0.75 wt% Nb_2O_5), P (up to 1.90 wt% P_2O_5), Si
561 (up to 0.54 wt% SiO_2), and F (up to 2.62 wt%) without major differences between
562 laterite types. Contrastingly, Fe has higher concentrations in cerianite-(Ce) from
563 manganiferous laterite (1.40 to 3.48 wt% Fe_2O_3) than in cerianite-(Ce) from brown
564 laterite (0.11 to 1.10 wt% Fe_2O_3).

565 The composition of the florencite mineral was determined by the EDS analysis
566 (Fig. 10). The most frequent composition is that of florencite-(Ce), ideally

567 [$CeAl_3(PO_4)_2(OH)_6$] (Min Data 2017). More rarely, florencite-(La) occurs. In the same
568 cluster of crystals (Fig. 10 A) may occur both types of florencite (Fig 10B, C).
569 Rhabdophane-(Ce) is usually described by the formula $CePO_4.H_2O$. Table 4
570 shows representative composition and respective structural formulae of rhabdophane-
571 (Ce) from the border siderite carbonatite. Besides Ce (17.79 to 21.39 wt% Ce_2O_3) the
572 mineral is also rich in Nd with Nd_2O_3 ranging from 16.24 to 18.45 wt%. The mineral
573 also have high concentrations of ThO_2 (2.81 to 7.60 wt%), CaO (4.91 to 5.56 wt%),
574 BaO (up to 2.69 wt%), and SrO (up to 2.06 wt%). Representative composition of
575 monazite-(Ce) from Esperança Basin (Tab. 4) show that the mineral is rich in Ce_2O_3 (up
576 to 32.25 wt%), La_2O_3 (up to 18.74 wt%) and Nd_2O_3 (up to 14.42 wt%). Monazite-(Ce)
577 have low CaO contents (up to 1.05 wt%) and low ThO_2 (up to 3.42 wt%).
578
579
580
581
582
583
584
585
586
587
588
589
590
591
592
593
594
595
596
597
598

599 Table 3. Representative composition and respective structural formulae of cerianite-(Ce) from laterites of
600 the Morro dos Seis Lagos Nb deposit.

	Manganiferous Crust					Brown Crust		
	13-01	15-01	15-02	17-01	17-02	31-01	31-02	34-01
Nb_2O_5	0.75	0.22	0.09	0.57	0.29	0.25	0.20	0.61
P_2O_5	0.96	1.18	1.75	0.31	1.29	1.90	0.21	1.52
SiO_2	0.20	0.20	0.08	0.54	0.17	0.12	0.01	0.23
TiO_2	0.27	0.53	0.20	0.03	0.15	0.47	0.06	0.35
CeO_2	86.22	90.66	85.90	88.93	85.41	89.48	94.80	93.14
ThO_2	2.57	4.05	7.32	6.82	3.75	0.60	0.00	0.59
Fe_2O_3	3.48	1.57	1.94	1.40	1.58	1.10	0.11	0.99
Al_2O_3	0.27	0.13	0.11	0.10	0.06	0.18	0.02	n.d.
La_2O_3	n.d.	n.d.	n.d.	n.d.	n.d.	0.83	n.d.	n.d.
Nd_2O_3	0.55	0.26	0.32	0.34	0.42	0.66	0.28	0.47
Sm_2O_3	0.10	0.00	0.08	0.03	0.13	0.10	n.d.	0.01
Eu_2O_3	n.d.	0.06	n.d.	n.d.	n.d.	n.d.	n.d.	n.d.
Gd_2O_3	0.02	0.08	0.04	0.03	0.02	2.33	2.75	3.14
Ho_2O_3	0.05	0.10	0.14	n.d.	0.10	n.d.	n.d.	0.03
Y_2O_3	n.d.	n.d.	0.14	0.02	0.02	0.09	n.d.	0.01
BaO	0.19	0.34	0.29	0.06	0.14	0.77	0.01	0.06
PbO	0.08	0.01	n.d.	n.d.	n.d.	2.39	0.03	0.13
MnO	n.d.	1.63	1.38	0.40	1.69	0.05	n.d.	0.02
K_2O	0.03	0.13	0.05	0.08	0.10	0.03	0.01	0.05
F	2.08	1.01	1.72	2.18	1.88	1.82	1.21	2.62
O=F	0.88	0.42	0.72	0.92	0.79	0.77	0.51	1.10
Total	96.93	101.72	100.79	100.92	96.42	102.40	99.17	102.86
Nb	0.009	0.003	0.001	0.007	0.004	0.003	0.003	0.008
P	0.023	0.027	0.040	0.007	0.031	0.044	0.005	0.035
Si	0.006	0.005	0.002	0.015	0.005	0.003	0.000	0.006
Ti	0.006	0.011	0.004	0.001	0.003	0.010	0.001	0.007
Ce	0.847	0.845	0.820	0.875	0.845	0.844	0.958	0.883
Th	0.016	0.025	0.046	0.044	0.024	0.004	0.000	0.004
Fe	0.074	0.032	0.040	0.030	0.034	0.022	0.002	0.020
Al	0.009	0.004	0.003	0.003	0.002	0.006	0.001	
La						0.008		
Nd	0.006	0.003	0.003	0.003	0.004	0.006	0.003	0.005
Sm	0.001	0.000	0.001	0.000	0.001	0.001		0.000
Eu		0.001						
Gd	0.000	0.001	0.000	0.000	0.000	0.021	0.026	0.028
Ho	0.000	0.001	0.001		0.001			0.000
Y			0.002	0.000	0.000	0.001		0.000
Ba	0.002	0.004	0.003	0.001	0.002	0.008	0.000	0.001
Pb	0.001	0.000				0.017	0.000	0.001
Mn	0.000	0.037	0.032	0.010	0.041	0.001		0.000
K	0.001	0.004	0.002	0.003	0.003	0.001	0.000	0.002
Total	1.000	1.000	1.000	1.000	1.000	1.000	1.000	1.000
F	0.185	0.085	0.148	0.194	0.168	0.156	0.111	0.225
O	1.874	1.905	1.884	1.877	1.864	1.885	1.932	1.878
Total	2.060	1.990	2.032	2.071	2.033	2.040	2.042	2.102

Formula calculated on the basis of 1 cation

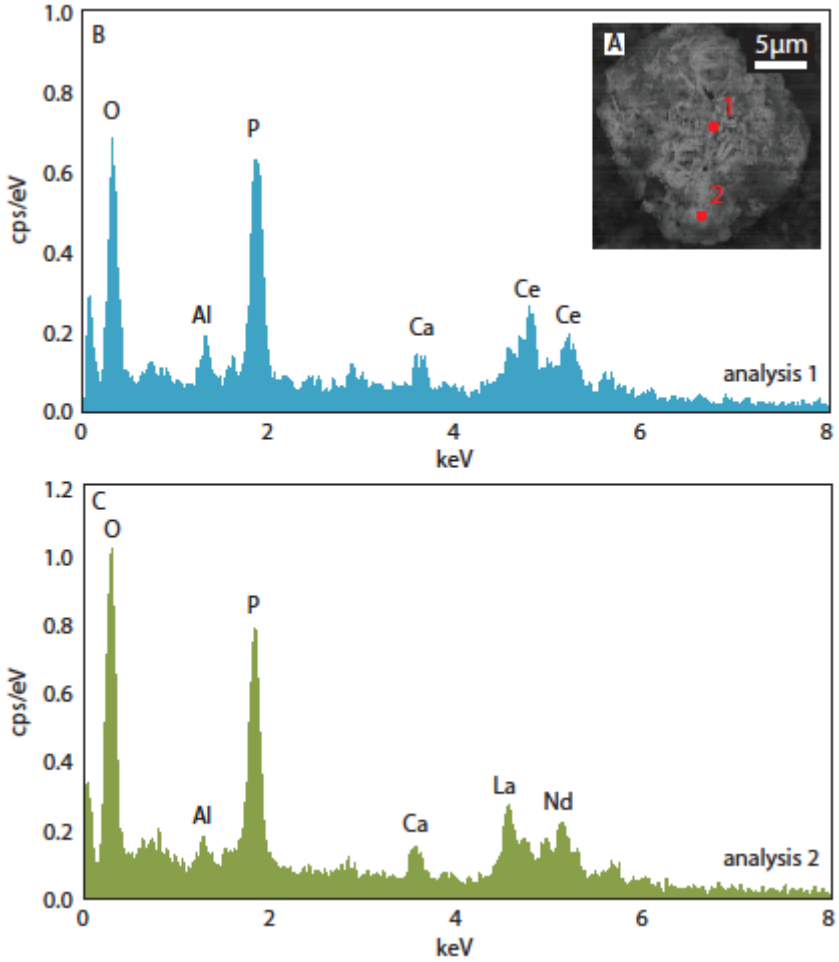

Figure 10. EDS analyses of authigenic florencite-(Ce) and florencite-(La) from the Esperança Basin. (A) Agglomerate of florencite crystals with location of two points analysed. (B) Analysis of florencite-(Ce). (C) Analysis of florencite-(La).

Table 4. Representative composition of rhabdophane-(Ce) from border siderite carbonatite (BSC) and monazite-(Ce) from the Esperança Basin.

	Rabdophane-(Ce)				Monazite		
	BSC				Esperança Basin		
P_2O_5	26.95	27.24	27.80	27.56	28.35	28.75	23.51
ThO_2	3.21	3.30	7.60	2.81	1.58	1.21	4.17
La_2O_3	2.28	2.31	2.58	3.87	18.74	16.06	12.95
Ce_2O_3	20.27	21.39	17.79	20.55	26.96	32.18	28.54
Pr_2O_3	3.76	3.73	3.05	3.42	3.67	3.22	3.23
Nd_2O_3	18.25	18.45	16.24	17.77	14.42	12.13	14.74
Sm_2O_3	2.70	2.82	3.48	3.23	2.32	2.20	2.84
Eu_2O_3	n.d.	n.d.	n.d.	n.d.	1.06	0.97	1.03
Gd_2O_3	1.65	1.83	1.82	2.00	n.d.	n.d.	n.d.
Dy_2O_3	1.20	1.30	0.89	1.42	n.d.	n.d.	n.d.
CaO	4.94	4.91	5.56	5.01	0.49	0.37	1.28
SrO	0.82	0.85	2.06	0.54	0.44	0.35	0.20
BaO	2.69	2.17	2.28	2.66	n.d.	n.d.	n.d.
H_2O	6.91	7.01	7.10	7.07	n.d.	n.d.	n.d.
Sum	95.63	97.31	98.25	97.91	98.03	97.42	92.49
Th	0.030	0.030	0.069	0.025	0.014	0.011	0.041
La	0.036	0.036	0.040	0.060	0.282	0.241	0.218
Ce	0.322	0.335	0.275	0.319	0.402	0.479	0.477
Pr	0.059	0.058	0.047	0.053	0.055	0.048	0.054
Nd	0.283	0.282	0.245	0.269	0.210	0.176	0.241
Sm	0.040	0.041	0.051	0.047	0.033	0.031	0.045
Gd	0.024	0.026	0.025	0.028	0.015	0.013	0.016
Eu							
Dy	0.017	0.018	0.012	0.019			
Ca	0.229	0.225	0.251	0.228	0.021	0.016	0.063
Sr	0.021	0.021	0.050	0.013	0.010	0.008	0.005
Ba	0.046	0.036	0.038	0.044			
Sum Cations	1.115	1.117	1.122	1.113	1.042	1.022	1.160
P	0.989	0.985	0.992	0.988	0.979	0.989	0.910

Calculated on the basis of 4 Oxygens

4.4.2 REE bearing minerals

Table 5 presents representative compositions of pyrochlores from border siderite carbonatite (BSC), from core siderite carbonatite (CSC) and from brown laterite. Many crystals present low total and are very poor in Na and Ca corroborating the petrographic evidences of weathering (Wall et al., 1996). The correlation between vacancy at A-site, loss of Ce and the vertical distribution of the samples is very prominent (Fig. 11). Fluorine was not detected.

The pyrochlore in the border siderite carbonatite is a Pb-Ba pyrochlore and is the poorest pyrochlore in REE with 1.8 wt% Ce_2O_3. CSC has higher concentrations of REE (Ce_2O_3 between 4.01 and 6.51 wt%). It is classified as Ce-Ba pyrochlore in most cases. The pyrochlore from the brown laterite is notably the richest in REE, with Ce_2O_3 concentrations in the order of 20 wt%. The Ce concentration increases with the decrease of depth and increase of weathering (Fig. 11). This Ce-pyrochlore also has significant concentrations of La (up to 6.13 wt% La_2O_3), Nd (up to 3.66 wt% Nd_2O_3) and Pr (up to 2.59 wt% Pr_2O_3). Y, Gd, Sm and Eu were detected in low concentrations in all pyrochlores. The other REE occur in very low concentrations or were not detected in most analyzes.

663 Table 5. Representative composition of pyrochlore from border siderite carbonatite (BSC), core siderite
664 carbonatite (CSC), and brown laterite.

	Carbonatite					Laterite				
	BSC	CSC				Brown Crust				
	54B	18-01	18-02	14-01	14-02	27-01	27-02	31-02	34-01	34-02
Na_2O	n.d.	n.d.	n.d.	n.d.	n.d.	0.02	0.02	0.68	1.67	1.01
K_2O	n.d.	n.d.	n.d.	n.d.	n.d.	0.02	n.d.	0.12	0.08	0.16
BaO	12.09	16.51	15.37	12.87	14.17	2.05	0.57	4.47	3.10	1.47
PbO	12.21	4.91	4.40	8.27	8.23	8.33	11.36	8.09	6.13	4.66
SrO	1.35	n.d.	0.03	0.15	0.31	0.03	n.d.	0.04	0.03	0.02
CaO	2.60	0.13	0.22	0.00	0.19	0.35	n.d.	0.14	n.d.	n.d.
MnO	n.d.	n.d.	n.d.	n.d.	n.d.	0.11	0.03	0.22	0.04	n.d.
La_2O_3	0.08	0.61	0.65	0.89	0.77	6.13	1.79	3.81	2.66	2.20
Ce_2O_3	1.48	4.01	4.48	6.51	6.38	18.92	24.13	15.66	21.48	23.36
Pr_2O_3	n.d.	0.10	n.d.	0.13	0.18	2.59	0.33	1.13	0.55	0.98
Nd_2O_3	0.70	1.72	1.72	0.94	0.99	3.66	0.34	1.40	1.37	2.35
Sm_2O_3	n.d.	0.80	0.79	n.d.	0.14	0.05	n.d.	0.13	0.07	0.07
Eu_2O_3	0.09	0.16	0.41	0.15	0.06	0.04	0.06	0.16	0.06	0.23
Gd_2O_3	n.d.	0.48	0.16	n.d.	0.02	0.25	0.35	0.32	0.27	0.42
Dy_2O_3	0.00	0.10	0.13	0.11	0.42	0.02	n.d.	0.02	n.d.	n.d.
Ho_2O_3	0.30	0.36	n.d.	n.d.	0.26	n.d.	n.d.	n.d.	n.d.	n.d.
Er_2O_3	0.03	0.13	0.05	0.02	n.d.	0.03	0.09	0.04	n.d.	n.d.
Y_2O_3	0.11	0.46	0.04	n.d.	0.03	0.12	0.02	0.32	1.56	0.22
ThO_2	1.00	3.15	1.16	1.02	1.09	0.38	0.40	1.05	0.90	2.55
Fe_2O_3	5.13	3.89	4.18	0.98	1.24	3.11	3.50	2.59	1.35	2.23
Al_2O_3	0.54	0.06	0.18	0.00	0.01	0.13	0.05	0.06	0.01	0.10
TiO_2	3.51	6.73	4.41	1.35	4.15	4.41	2.61	6.39	7.86	4.89
SiO_2	2.05	1.19	2.02	0.08	2.22	0.18	0.10	4.54	1.62	0.91
Nb_2O_5	36.16	41.42	45.85	50.72	44.77	49.04	51.46	44.27	43.25	39.66
Ta_2O_5	n.d.	0.08	n.d.	n.d.	n.d.	n.d.	0.01	0.16	n.d.	n.d.
WO_3	n.d.	0.11	0.12	0.17	0.82	n.d.	n.d.	n.d.	n.d.	n.d.
Sum	79.44	87.10	86.34	84.35	86.41	99.97	97.22	95.81	94.06	87.49
Na						0.003	0.003	0.084	0.230	0.161
K						0.002		0.010	0.007	0.017
Ba	0.371	0.462	0.409	0.407	0.415	0.057	0.016	0.111	0.086	0.047
Pb	0.257	0.094	0.080	0.180	0.166	0.159	0.218	0.139	0.117	0.103
Sr	0.061		0.001	0.007	0.013	0.001		0.001	0.001	0.001
Ca	0.218	0.010	0.016	0.000	0.015	0.027		0.010		
Mn						0.007	0.002	0.012	0.002	
La	0.002	0.016	0.016	0.026	0.021	0.161	0.047	0.089	0.070	0.067
Ce	0.042	0.105	0.111	0.192	0.175	0.492	0.630	0.365	0.559	0.703
Pr		0.003		0.004	0.005	0.067	0.009	0.026	0.014	0.029
Nd	0.020	0.044	0.042	0.027	0.026	0.093	0.009	0.032	0.035	0.069
Sm		0.020	0.018		0.004	0.001		0.003	0.002	0.002
Eu	0.002	0.004	0.009	0.004	0.002	0.001	0.001	0.003	0.001	0.006
Gd		0.011	0.003		0.001	0.006	0.008	0.007	0.006	0.011
Dy		0.002	0.003	0.003	0.010	0.000		0.000		
Ho	0.008	0.008			0.006					
Er	0.001	0.003	0.001	0.000		0.001	0.002	0.001		
Y	0.005	0.017	0.001		0.001	0.005	0.001	0.011	0.059	0.010
Th	0.018	0.051	0.018	0.019	0.019	0.006	0.006	0.015	0.015	0.048
ΣA	1.005	0.850	0.730	0.869	0.878	1.087	0.953	0.919	1.206	1.275
Fe	0.302	0.209	0.213	0.059	0.070	0.166	0.188	0.124	0.072	0.138
Al	0.052	0.006	0.015		0.001	0.011	0.004	0.005	0.001	0.010
Ti	0.206	0.361	0.225	0.082	0.234	0.236	0.140	0.306	0.421	0.303
Si	0.161	0.085	0.137	0.006	0.166	0.013	0.007	0.289	0.115	0.075
Nb	1.279	1.336	1.407	1.849	1.514	1.574	1.660	1.273	1.391	1.474
Ta		0.002					0.000	0.003		
W		0.002	0.002	0.004	0.016					
ΣB	2.000	2.000	2.000	2.000	2.000	2.000	2.000	2.000	2.000	2.000
Vacancy	0.995	1.150	1.270	1.131	1.122	0.913	1.047	1.081	0.794	0.725

Formula calculated on the basis of 2 cations

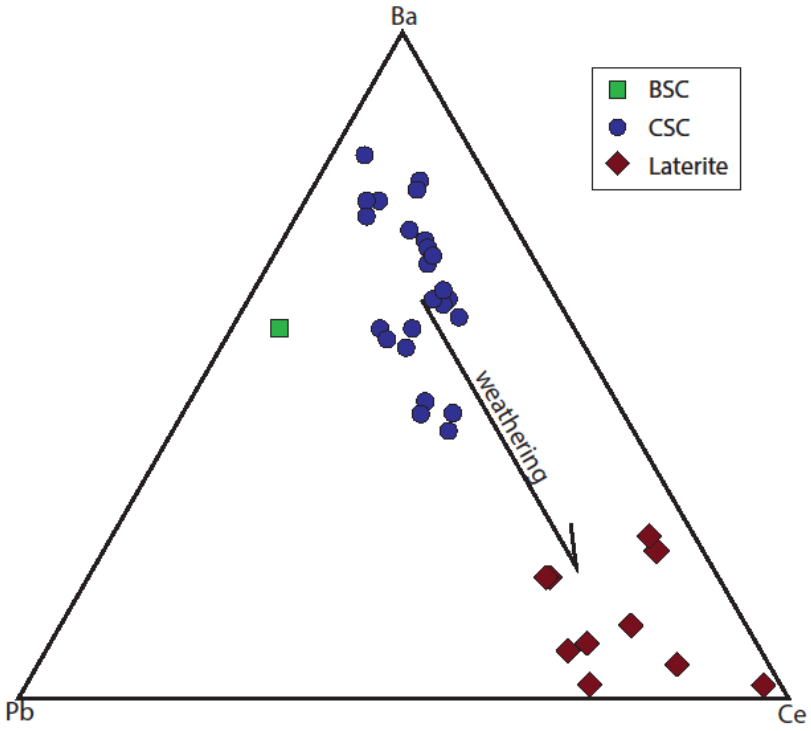

Figure 11. Pyrochlore from the Morro dos Seis Lagos deposit plotted in ternary diagram Ba–Ce–Pb. BSC= border siderite carbonatite; CSC= core siderite carbonatite.

Gorceixite is a mineral of the crandallite group, which is formed by hydrated aluminum phosphate with general formulae $AB_3(XO_4)_2(OH)_6$. The minerals of the group present a large variation of cations at site A (Ca^{2+}, Sr^{2+}, Ba^{2+}, Pb^{2+}, REE^{3+}, Na^{+}, K^{+}, Ag^{+}, NH^{4+}, H_3O^{+}). Depending on the A site, the main poles are gorceixite (Ba), crandallite (Ca), goyasite (Sr), plumbogummite (Pb), and florencite (REE). B site is more commonly Al^{3+} and Fe^{3+} (Zn^{2+} e Cu^{2+}) and X site is more commonly PO_4^{3-} (SO_4^{2-}, SiO_4^{4-}) (Toledo 1999). The mineral of the crandallite group in the siderite carbonatite of the MSLD is a Ce-rich gorceixite (Tab. 6). BaO values range from 19.77 to 24.74 wt%, which correspond to 0.613 and 0.786 Ba apfu. This gorceixite contains relatively high REE contents, notably Ce (2.53 - 6.36% Ce_2O_3) and Nd (0.80 - 3.97% Nd_2O_3). The REE_2O_3 values are between 4.25 and 12.05 wt%. The REE pattern in the gorceixite is almost identical to the REE pattern of rhabdophane-(Ce). Sr (SrO~ 1.7 wt%), Ca (CaO~ 0.5 wt%) and Mg (MgO~ 0.1 wt%) were detected in all analysis (Tab. 6, Fig. 12). The study mineral is a solid solution $Crandallite_{3\text{-}7}$ $Goyasite_{4\text{-}9}$ $Florencite_{13\text{-}30}$ $Gorceixite_{59\text{-}77}$.

685 Table 6. Representative compositions and respective structural formulae of gorceixite from the siderite
686 carbonatite from the Morro dos Seis Lagos deposit.

	Border Siderite Carbonatite								
	53C-01	53C-02	53C-03	54A-01	54A-02	54A-03	54B-01	54B-02	54B-03
BaO	22.29	24.24	24.70	22.08	22.81	23.98	19.77	22.59	22.11
SrO	1.67	1.97	1.55	1.99	1.90	1.39	1.78	1.71	1.00
CaO	0.61	0.46	0.56	0.55	0.35	0.40	0.77	0.50	0.48
MgO	0.04	0.15	0.07	0.12	0.05	0.17	0.08	0.16	0.11
La_2O_3	0.84	0.56	0.33	0.39	0.28	0.28	0.84	0.91	1.24
Ce_2O_3	6.36	4.06	3.21	3.09	2.53	2.63	4.32	4.99	5.86
Nd_2O_3	3.97	1.56	0.80	1.45	1.11	1.00	1.87	2.56	2.97
Sm_2O_3	0.59	0.02	n.d.	0.15	0.19	0.06	0.27	0.32	0.29
Eu_2O_3	n.d.	0.16	0.08	0.16	0.01	0.04	0.10	0.07	0.01
Dy_2O_3	0.55	0.01	0.08	0.24	0.22	0.12	n.d.	0.10	0.28
Er_2O_3	0.20	0.04	n.d.	0.01	0.07	0.12	0.06	0.02	0.00
Al_2O_3	31.21	28.73	29.47	30.43	30.76	30.44	30.65	30.33	29.51
Fe_2O_3	1.03	0.54	0.38	2.18	2.44	2.72	3.64	1.71	1.96
P_2O_5	23.47	22.96	22.93	21.30	22.24	21.60	21.99	22.25	22.29
Sum	92.81	85.48	84.16	84.13	84.93	84.96	86.14	88.21	88.09
Ba	0.666	0.769	0.786	0.709	0.716	0.762	0.613	0.701	0.683
Sr	0.073	0.092	0.073	0.094	0.088	0.065	0.081	0.078	0.045
Ca	0.049	0.040	0.049	0.048	0.030	0.035	0.065	0.042	0.041
Mg	0.005	0.018	0.009	0.014	0.006	0.021	0.010	0.018	0.013
La	0.024	0.017	0.010	0.012	0.008	0.008	0.025	0.027	0.036
Ce	0.177	0.120	0.095	0.093	0.074	0.078	0.125	0.145	0.169
Nd	0.108	0.045	0.023	0.042	0.032	0.029	0.053	0.072	0.084
Sm	0.015	0.001		0.004	0.005	0.002	0.007	0.009	0.008
Eu		0.005	0.002	0.004	0.000	0.001	0.003	0.002	0.000
Dy	0.013	0.000	0.002	0.006	0.006	0.003		0.003	0.007
Er	0.005	0.001		0.000	0.002	0.003	0.001	0.001	0.000
ΣA	1.136	1.109	1.050	1.027	0.967	1.007	0.983	1.097	1.085
Al	2.802	2.742	2.821	2.937	2.905	2.909	2.858	2.830	2.741
Fe	0.059	0.033	0.023	0.134	0.147	0.166	0.217	0.102	0.116
ΣB	2.861	2.775	2.844	3.071	3.052	3.076	3.075	2.931	2.857
P	1.955	2.032	2.036	1.907	1.948	1.914	1.902	1.925	1.920

Formula calculated on the basis of 10.5 Oxygens

687

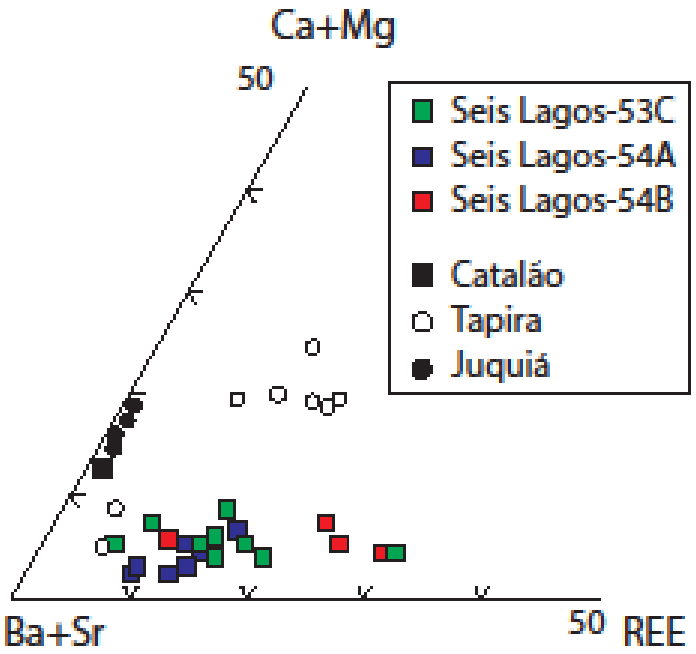

Figure 12. Gorceixites from the Morro dos Seis Lagos deposit (borde siderite carbonatite) and from the Catalão, Tapira and Juquiá carbonatites (data from Ferrari 2000 and Ferrari et al. 2007) plotted in the ternary diagram Ca+Mg – REE – Ba+Sr.

4.5 Geochemistry

Giovannini et al. (2017) present representative whole-rock composition of the carbonatite and laterites. Core and border siderite carbonatites have no Eu anomaly and are strongly enriched in LREE (Fig. 13), as typically occurs in carbonatites. However the border siderite carbonatite presents an unusual feature represented by a relative depletion of the La, Ce, and Pr (Fig. 13A). In the core siderite carbonatite there are two types of REE normalized patterns that directly reflect the REE mineralogy in the SG-04-AM drill cores. The REE pattern in the intervals 250-300m and 340-492m, where thorbastnäsite occurs, are richer in MREE (Fig. 13B). The patterns are richer in LREE (Fig. 13C) in the interval 290-340 m (REE rich zone, Fig. 5), where the REE minerals are monazite and bastnäsite. La/Yb average ratios of border siderite carbonatite, core siderite carbonatite and REE-rich core siderite carbonatite are, respectively, 12.2, 39.9, and 107 (Fig. 13 A, B and C).

The brown (Fig. 13I) and lower purple laterites (Fig. 13H) - the lowest laterites in the profile and, therefore, the least evolved - display similar REE distribution; they differ from the primary rock in being slightly poorer in REE (from Pr to Lu) and by the

presence of a positive Ce anomaly which is more pronounced in the brown laterite. The manganiferous (Fig. 13G) and upper purple laterites (Fig. 13F) have similar REE distribution patterns; with regard to the carbonatite, the laterites are depleted in REE (from Pr to Lu), have accentuated positive Ce anomaly and positive Gd anomaly. The pisolitic, fragmented and mottled laterites have similar REE patterns (Fig. 13D and E); with regard to the carbonatite they are poorer in REE from Pr to Lu; they have small positive Ce and Gd anomalies. The mottled laterite is richer in LREE than all the other laterites. In case of La and Ce, there is an enrichment compared to the primary rock and no positive Ce and Gd anomalies. All the laterites are poorer in HREE than the siderite carbonatite, especially the upper laterites (pisolitic, fragmented and mottled).

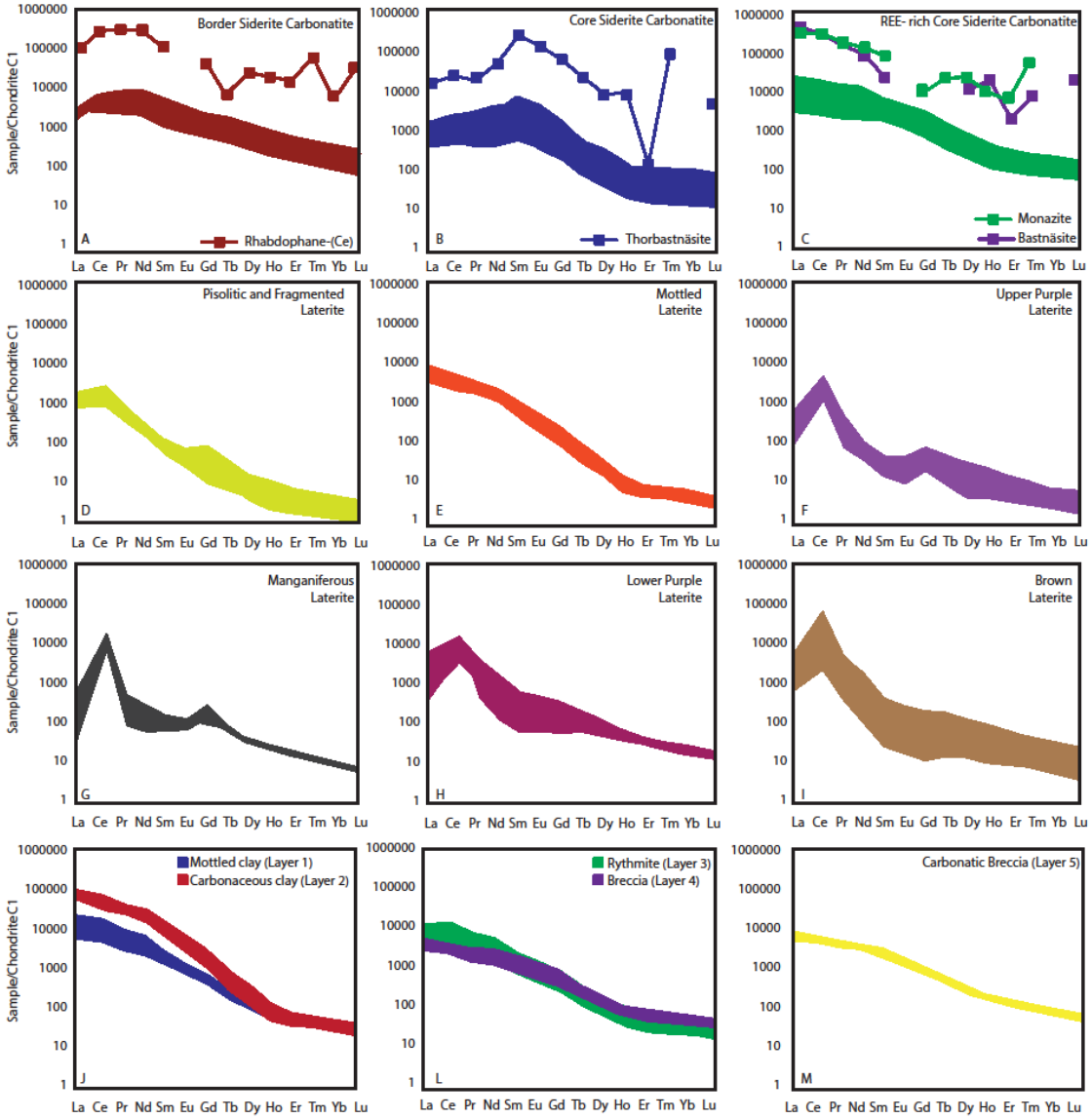

Figure 13. REE normalized patterns of siderite carbonatite (and respective REE minerals), laterites and sediments from the Esperança Basin.

The whole-rock composition of the sediments (Tab. 7) reflects directly the five-tiered division of the sediment column and the mineralogy (Tab. 2, Fig. 5). The ternary SiO_2-Al_2O_3-FeO diagram (Fig. 14) corroborates the evolution, from the base to the top, from Fe-rich sediments (closely related to the siderite carbonatite composition) into sediments essentially consisting of silica and alumina. The strong correlation REE vs P_2O_5 (Fig. 15) corroborates the REE are essentially in phosphates [florencite-(Ce), florencite-(La), and monazite] rather than adsorbed to clays surface as in ion adsorption clays REE deposit. As recognized by Bonow and Issler (1980), typical carbonatite related elements, such as Nb, Ba, Sr and Th, occur with anomalous concentrations in the sediments, as well as other elements such as Pb and Zn. With regard to layer 2, layer 1 is enriched in immobile elements (Nb, Zr) and impoverished in calcophile elements such as Pb, Zn, Ni, Co, As, Cd and in LOI, TOT/C and TOT/S, indicating it corresponds to the oxidation of the upper part of the sedimentary package. As for the REE normalized pattern, all the layers present a similar behavior (Fig. 13) with high levels of LREE and low levels of HREE, thus a high La/Yb values. The pattern of layers 3, 4, and 5 are quite similar to that of the core siderite carbonatite, layer 5 is richer in HREE compared to layer 3 and 4 (Fig. 5). The pattern of layers 2 (especially) and 1 are more similar to that of reworked laterites, especially to the mottled laterite.

755 Table 7. Whole-rock composition of sediments of the Esperança Basin.
756

Layer	1		2			3					4		5
Sample	04-2	04-28	04-29	04-32	04-34A	04-36	04-5	04-40	04-43	04-7	04-46	04-49	04-10
Depth (m)	9.3	14.5	16.4	50.0	70.0	78.0	93.0	99.8	119.0	133.0	148.5	165.0	227.5
%													
SiO_2	38.37	36.45	23.84	20.28	55.66	12.01	25.11	6.17	4.66	25.28	3.71	28.84	2.04
Al_2O_3	35.69	34.22	21.75	18.95	15.66	8.17	12.21	3.35	2.72	10.24	2.23	12.48	2.76
Fe_2O_3	3.93	4.24	3.20	3.12	5.42	40.17	28.36	71.12	73.30	21.62	71.42	31.48	55.73
MgO	0.03	0.04	0.05	0.03	1.67	0.22	0.17	0.24	0.51	0.21	0.82	0.13	0.42
CaO	0.05	0.06	0.04	0.04	3.08	0.77	0.44	0.49	0.57	0.35	0.85	0.27	0.63
Na_2O	0.04	n.d.	n.d.	n.d.	0.62	0.03	n.d.	n.d.	0.01	0.01	0.01	0.01	0.01
K_2O	0.03	0.02	0.02	0.03	1.74	0.19	0.16	0.04	0.04	0.22	0.02	0.18	0.03
TiO_2	3.72	2.23	1.71	1.38	0.78	0.58	1.12	0.25	0.21	0.81	0.69	1.17	0.40
P_2O_5	1.33	2.38	0.91	1.03	0.22	0.68	0.69	0.51	0.50	0.70	0.22	0.54	1.27
MnO	n.d.	n.d.	n.d.	n.d.	0.08	0.38	0.35	0.92	0.98	0.45	1.01	0.50	1.33
LOI	14.5	16.0	46.6	52.8	14.8	35.4	29.9	15.7	15.3	38.3	17.0	23.2	32.8
TOT/C	0.12	0.15	20.21	26.04	1.78	15.01	13.28	4.26	4.11	21.36	1.37	7.74	12.41
TOT/S	<0.02	0.02	2.03	1.82	0.12	1.09	0.76	0.30	0.35	0.82	1.80	0.92	1.98
Sum	97.67	95.68	98.16	97.70	99.75	98.63	98.55	98.81	98.81	98.25	98.01	98.75	97.50
ppm													
Ba	4920	6512	3064	2966	512	3704	2809	1836	1877	2116	3200	3001	4485
Sr	477	859	370	420	196	413	321	173	185	262	198	301	730
Pb	20	180	184	272	25	124	132	67	66	175	225	131	121
Th	2271	3328	1806	2841	88	1058	1478	491	474	1713	2702	807	2094
Zr	1056	374	288	295	237	132	191	51	46	228	119	400	140
Hf	29	11	8	9	6	4	5	1	1	6	7	11	3
Nb	3423	3596	1781	2226	111	989	1624	490	538	1923	6115	1249	2089
Ta	7	5	3	3	1	2	3	1	1	2	5	2	2
La	1362	4812	1457	2032	97	881	1043	1403	1517	1421	148	681	1850
Ce	2938	10736	3028	4079	182	1972	2172	3122	3040	2929	510	1472	4048
Pr	287	992	296	461	19	199	225	329	325	368	44	144	470
Nd	1084	3313	1058	1892	71	789	877	1234	1139	1646	275	593	2019
Sm	213	438	167	361	12	159	169	214	133	411	184	139	380
Eu	49	84	33	76	2	35	38	47	27	94	44	34	90
Gd	97	173	65	155	8	75	79	102	58	194	75	77	227
Tb	8	13	6	13	1	7	7	9	5	15	6	7	16
Dy	32	49	23	48	6	25	26	34	19	54	25	30	58
Ho	4	5	3	5	1	3	4	4	2	6	3	4	7
Er	9	9	7	10	3	7	8	9	5	14	7	10	15
Tm	1	1	1	1	1	1	1	1	1	2	1	1	2
Yb	7	8	5	8	3	6	7	7	4	10	7	9	11
Lu	1	1	1	1	1	1	1	1	1	1	1	1	1
Y	121	160	105	162	33	112	118	136	83	222	115	138	329
Sc	118	249	116	123	17	40	72	43	52	71	104	74	301
V	435	471	337	306	120	102	175	108	95	164	223	188	142
W	53	35	29	28	3	12	18	8	11	18	34	20	13
Zn	4	23	1083	409	115	359	353	102	126	350	785	375	998
Ni	n.d.	12	32	24	19	14	12	6	7	12	7	13	5
Co	1	2	51	43	13	33	31	17	18	42	39	30	47
As	4	15	26	26	4	13	15	2	6	15	48	14	20
Cd	n.d.	<0.1	8	2	1	3	1	1	1	1	1	1	3
F		433	200	248	360	342		182	185		231	133	

757

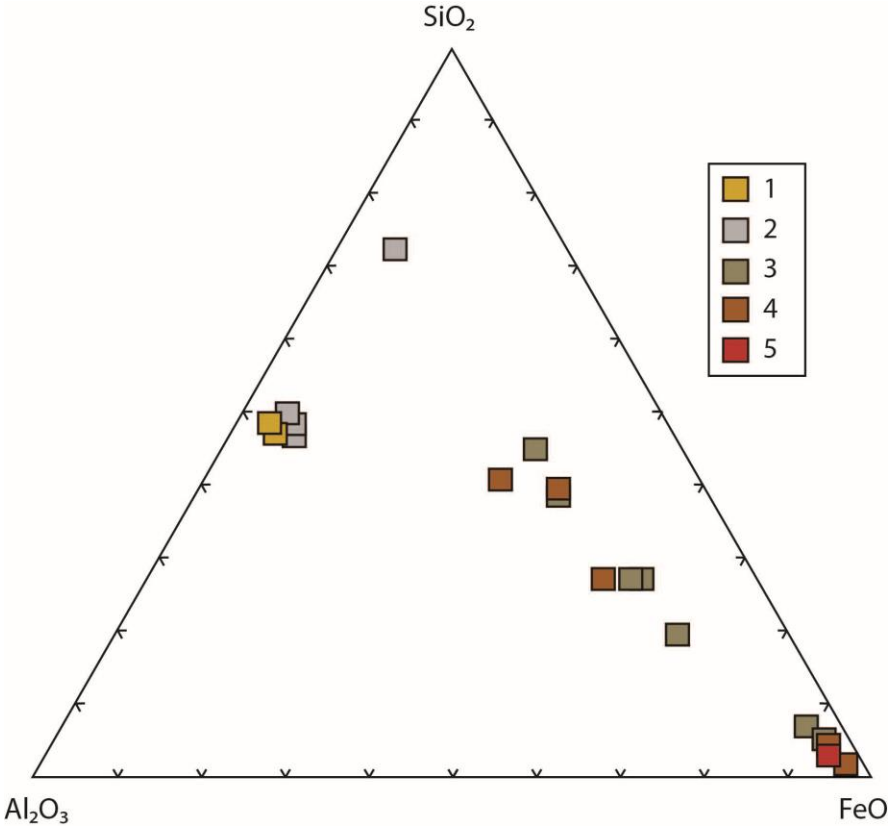

Figure 14. Ternary diagram SiO_2-Al_2O_3-FeO for the Esperança Basin sediments. (1) Mottled clay; (2) Carbonaceous clay; (3) Rythmite; (3) Brecia; (5) Carbonatic breccia.

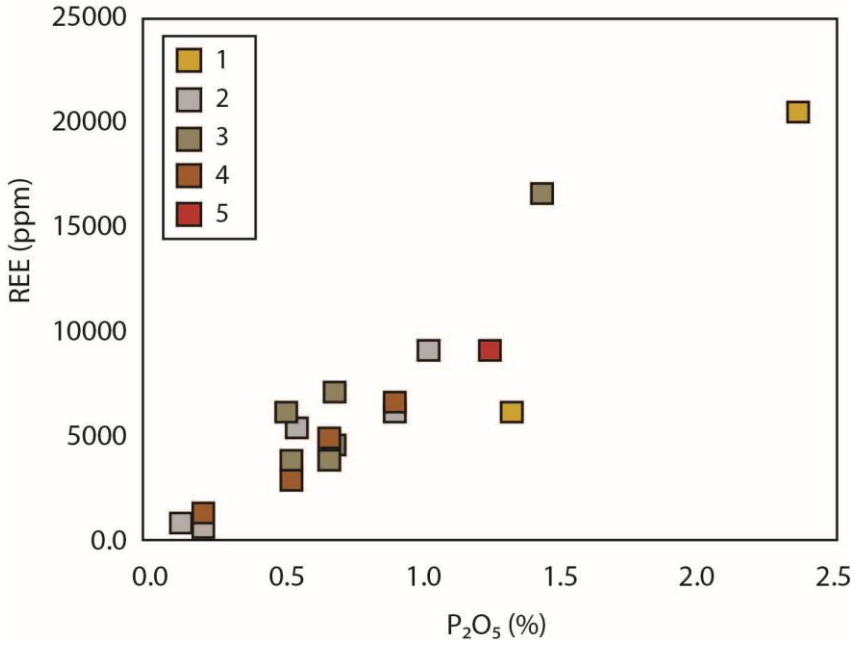

Figure 15. Binary diagram P_2O_5 vs REE for the Esperança Basin sediments. (1) Mottled clay; (2) Carbonaceous clay; (3) Rythmite; (3) Brecia; (5) Carbonatic breccia.

In order to calculate REE composite grades, we used the CPRM's data from the continuous core sampling of the boreholes SG-04-AM (0 to 492m) and SG-01-AM (0 to 59m) (Fig. 5). The REE content of brown laterite was calculated by the mean of punctual samples (analysis in Giovannini et al., 2017).

The intervals (Tab. 8) were based on the REE logs (Fig. 5) and geological criteria, as follows. The laterite profile was divided into 3 sets: upper set (reworked laterites); intermediate set (purple and manganiferous laterites); and brown laterite (the less evolved laterite). The REE concentration in the manganiferous laterite was also calculated because this laterite corresponds to a zone with the highest concentrations. In the case of the Esperança Basin, the depth of 73 m delimits two distinct packages as regards REE concentration, but also the mineralogy (Tab. 2) and coincides with the depth used by Bonow and Issler (1980) for the reserve calculation.

The following aspects can be highlighted (Tab. 8). LREE are much more abundant than HREE. Ce is the most abundant REE in all units and rocks. The reworked laterites have the lowest concentration of REE (avg. REE_2O_3= 0.649 wt%). The REE concentration in the laterite increases with depth toward the brown laterite (avg. REE_2O_3= 1.300 wt%). Within the laterite profile, the manganiferous laterite represents a particular zone characterized by a higher concentration (avg. REE_2O_3= 1.475 wt%). The upper package of the Esperança basin has the highest REE concentration in the MSLD (1.731 wt% REE_2O_3). This package represents a zone of accumulation of other LREE than Ce (avg. $LREE_2O_3$- Ce_2O_3= 0.900 wt%). The siderite carbonatite has an average content of 0.787 wt% REE_2O_3 and a richest zone (42m thick) with an average of 1.476 wt% REE_2O_3 associated with monazite and bastnäsite.

800 Table 8. Average REE concentrations in laterites, sediments of Esperança Basin and siderite carbonatite.
801

Unit / Rock		Depth (m)	wt%				Main REE-mineral
			$\sum REE_2O_3$	$LREE_2O_3$-Ce_2O_3	$HREE_2O_3$	Ce_2O_3	
Laterite	Reworked laterites	0 - 19.75	0.649	0.241	0.010	0.398	Florencite-(Ce)
	Intermediate laterites	19.75 - 58	1.033	0.097	0.017	0.919	Cerianite
	Brown laterite *	58 - 97	1.300	0.260	0.020	1.020	Cerianite
	Manganiferous laterite	31 - 40	1.544	0.108	0.020	1.416	Cerianite
Esperança Basin	Layers 1 + 2	0 - 73	1.721	0.900	0.034	0.787	Florencite-(Ce)
	Layers 3 + 4	73 - 212	0.676	0.342	0.02	0.314	Monazite
	Layer 5	212 - 233	1.065	0.558	0.039	0.468	Florencite-(Ce)
Siderite Carbonatite	Total section	233 - 492	0.787	0.456	0.054	0.277	Thorbastnäsite
	Richest zone	288 - 340	1.476	0.779	0.059	0.638	Monazite/ Bastnäsite

802
803
804
805 **5. DISCUSSION**
806
807 Primary REE mineralization and early secondary REE mineralization
808
809 The average REE concentration of the MSLD siderite carbonatite (0.7 wt.%
810 REE_2O_3) is considerably lower than the average grade of the main REE deposits in
811 carbonatite (6.57 wt% in Mountain Pass, 3.05 wt.% in Bear Lodge, 4.24 wt.% in
812 Kagankunde, see Tab. 1). However, at Seis Lagos there is a rich zone 42m thick, where
813 the concentration of 1.48 wt.% REE_2O_3 resembles that of the Songwe Hill (1.6 wt.%)
814 and Zandkopsdrift (1.89 wt.%) deposits. The REE minerals in the rich zone are
815 monazite and bastnäsite, which are high quality ore minerals due to their high REE
816 contents (respectively ~75 and ~65 wt.% REE_2O_3) and amenability for mineral
817 processing. In contrast, thorbastnäsite usually contains only ~10 wt.% REE_2O_3, but the

MSLD thorbastnäsite has an interesting feature that is the relative richness in Nd, the more valuable LREE.

The second world largest siderite carbonatite body (500m x 100m) occurs in the Sallanlatvi Complex (Zaitsev et al. 2004). It has a carbothermal origin, and REE_2O_3 concentrations up to 0.070 wt%, of which Ce_2O_3 are up to 0.022 wt.% The REE richest rock in the complex is the calcio carbonatite (up to 3.993 wt.% REE_2O_3 and up to 1.687 wt.% Ce_2O_3). The Morro dos Seis Lagos siderite carbonatite body, presumably the world largest siderite carbonatite body, is ~10 times richer in REE than the siderite carbonatite at Sallanlatvi. It is also much richer than the Swartbooisdrif ferrocarbonatite (up to 0.015 wt.% Ce_2O_3 and up to 0.035 wt.% REE_2O_3) which is supposed to be the only proven magmatic ferrocarbonatite (Thompson et al. 2002). According to Mitchell (2005), carbothermal fluids typically concentrate the REE, Sr, Ba, *etc*. and not Nb, whereas intrusive carbonatites associated with rocks of the melilitite clan are typically important sources of Nb, Ti and P, but not the REE. This highlights the ambiguity of the Seis Lagos siderite carbonatite, mineralized either in Nb and REE, whose origin is uncertain at this point and will be the subject of a separate contribution.

Weathering is the main cause of the release of REE from primary minerals. This leads to subsequent supergene REE enrichment, particularly in the humid tropics, and in areas where basin-type topography allows accumulation of residual minerals (Mariano, 1989b). The dissolution of primary carbonatite minerals allows the fractionation, mobilization and redistribution of REE and PO_4 in the weathering system (Nesbitt, 1979; Duddy, 1980; Humphris, 1984; Mariano, 1989a; Braun et al., 1993). These elements may be immobilized elsewhere in the profíle by mechanisms such as reprecipitation in stable authigenic secondary minerals, incorporation into recrystallized minerals, and adsorption by clays and hydrous Fe-Al oxides (Humphris, 1984; Braun et al, 1993). Lower pH (<5.7) favors the solution and transportation of REE, and higher pH (>5.7) favors the precipitation of REE (Humphris, 1984; Mgonde, 1994). HREE are more mobile than LREE. HREE are generally concentrated at the base of saprolite, whereas LREE are concentrated in the upper zones of the profile (Nesbitt, 1979; Lottermoser, 1990; Sholkvitz, 1992; Braun et al., 1993; Mgonde, 1994). At Mount Weld (Lottermoser 1990), crystallochemical controls and the absorption of REE by non-crystalline substances led to the incorporation of LREE into the minerals of the plumbogumite, rhabdofane and secondary monazite group in the upper part of the

851 weathering profile, whereas the HREE and Y were preferentially incorporated by
852 churchite at deeper levels. Lateral groundwater flow towards a central topographic low
853 of the laterite and associated decreasing pH of the solutions favored the mobilization of
854 large amounts of REE and the formation of a highly REE-enriched laterite center.
855 At the MSLD, the siderite carbonatite is much richer in HREE than all the
856 laterites, and among these, the upper ones (mottled, fragmented and pisolitic laterites)
857 are notably the poorest in HREE (Fig. 13). The HREE were remobilized from the upper
858 laterites, descended along the profile, and may have formed higher concentrations at the
859 base of the lateritic profile, at depths that could not be accessed in the present study.
860 Besides that, the higher phosphate concentration in the upper part of the lateritic profile
861 is also very pronounced. These laterites are rich in florencite-(Ce). These are evidences
862 that processes summarized above observed in other REE laterite deposit also acted on
863 MSLD. However, the processes we describe below prevailed and other features were
864 superimposed on the REE mineralization.
865
866 Cerianite-(Ce) mineralization
867
868 According to Braun et al. (1990) cerianite-(Ce) is stable under neutral to alkaline
869 conditions in oxidizing environment. This mineral is characterized by the systematic
870 presence of Th and always displays high contents of trivalent REE. Cerianite-(Ce) from
871 Sushina (India) has from 11.73 to 17.76 wt% of REE_2O_3 and from 6.03 to 11.69 wt%
872 Y_2O_3; this cerianite-(Ce) is also characterized by the presence of Nb (0.44-1.16 wt%
873 Nb_2O_5), Zr (0.99-1.89 wt% ZrO_2) and by traces of Ca, Mn, Ti, Na, and Si (Chakrabarty
874 et al., 2013). Cerianite-(Ce) from Kisete (Tanzania) (Zaitsev et al, 2011) has from 7.1 to
875 4.5 wt% Y_2O_3, from 7.9 to 15.5 $LREE_2O_3$ and from 4.9 to 9.7 wt% $HREE_2O_3$. This high
876 trivalent cations content is explained by the substitution: $2Ce^{4+} + O_2 = 2REE^{3+} +$
877 Vacancy. The vacancy in O-site is corroborated by Raman spectroscopy data. Cerianite-
878 (Ce) from Kisete is also characterized by high F contents (from 0.98 to 3.46 wt%).
879 The MSLD cerianite-(Ce) is particularly rich in Ce and poor in Th and REE
880 other than Ce. Many REE minerals from the siderite carbonatite weather to release Ce,
881 but other REE are also released, thus particular conditions are required to form such
882 pure cerianite-(Ce). The breakdown of the Ce-pyrochlore structure is the only
883 mechanism capable of releasing such amount of Ce. Although the original composition

884 of pyrochlore plays an important role in determining the variety of pyrochlore that
885 formed, secondary pyrochlores formed by weathering processes follow more or less
886 well-defined sequences at each locality as observed in Yenisei Ridge (Lapin and
887 Kulikova, 1989), Lueshe (Wall et al., 1996), Mount Weld (Lottermoser and England,
888 1988), Catalão (Rocha et al., 2001; Cordeiro et al. 2011), and Araxá (Silva, 1986).
889 Given these studies, Giovannini et al. (2017) interpreted the Pb-Ba-pyrochlore (border
890 siderite carbonatite) as an early product of primary pyrochlore weathering. This is
891 followed by Ce-Ba-pyrochlore (core siderite carbonatite, strongly weathered because of
892 the karstic process that formed the Esperança Basin) and then by Ce-pyrochlore (lower
893 part of the brown laterite) which was progressively weathered to become more and
894 more enriched in Ce^{4+} with loss of REE^{3+}, until disappearing in the upper part of the
895 brown laterite. Such process represented a pre-concentration of Ce and then a release of
896 this element under strongly oxidizing conditions. Thus, besides the weathering solutions
897 were enriched in Ce, they also had high Ce^{4+}/Ce^{3+}, which also favors cerianite-(Ce)
898 preferable incorporation of higher amounts of Ce^{4+} than any trivalent REE.
899 In the brown laterite, cerianite-(Ce) occurs as band intercalated with goethite
900 bands (Fig. 8), this association can be explained by variations in the pH of the solution
901 (Takeno 2005). In low pH (<5), both Fe^{3+} and Ce^{3+} are in solution, if the pH rises to ~6,
902 Fe^{3+} precipitates as hematite (or goethite), while the Ce^{3+} remains in the solution. A
903 slightly higher increase in pH (~7) implies the precipitation of CeO_2. According to
904 Krauskopf (1985), if the pH increases very slowly, Fe compounds reach the limit of
905 solubility before Mn compounds and so can precipitate while Mn is left in solution.
906 Consequently, the Mn remaining in solution may be deposited as an oxide if conditions
907 are oxidizing and the solution becomes still more alkaline. As the precipitation of Mn
908 oxides from solutions requires a higher oxidation potential than that for Fe oxides, the
909 Mn tends to precipitate closer to the water table (Krauskopf, 1985). Thus cerianite-(Ce)
910 from the manganiferous laterite formed later than that of the brown laterite, from a more
911 oxidizing or more alkaline solution. At Eh ~0.5, a high pH allows the simultaneous
912 deposition of CeO_2 and Mn oxide. Similarly, to a pH value of 7, the increase of Eh from
913 0.7 to 0.8 also allows the formation of this paragenesis (Takeno 2005).
914
915 Evolution of the Esperança Basin and associated REE mineralization
916

According to Lottermoser (1990), carbonatites are similar to limestones prone to weathering and there exist numerous carbonatites with overlying laterites, deep weathering profiles and weathering blankets. In response to different climatic conditions, weathering processes, and primary igneous carbonatite mineralogy and geochemistry, various weathering products have been produced above individual intrusions. In spite of these differences, carbonatite weathering products show striking similarities. Carbonatite laterites develop in small, locally confined karst systems and the overburden often ranges from zero thickness on ridges of fresh carbonatite material to over 200 m thick in troughs and sinks. The karstic process in MSLD was likely very intense as assigned by the large number (more than 15) of basins and lakes and their control by faults and fractures (Rossoni et al., 2016).

The first stage of the Esperança Basin evolution (layer 5) is characterized by the deposition of abundant carbonatite fragments, florencite-(Ce) is responsible for the phosphate contents of this layer (Fig. 5). Subsequently, during the deposition of layer 4, the influence of the carbonatite gradually decreased, and the influence of the gneiss wall rock gradually increased, represented by the deposition of quartz (Tab. 2) and feldspar (high K, Rb and Cs contents) (Tab. 7). The sedimentation of layer 3 in a typical lacustrine environment is marked by intercalations of variably ferruginized clay layers with clasts of ferruginous materials related to the early stages of siderite carbonatite alteration. The remarkable presence of quartz (Tab. 2) still registers the influence of the gneiss input into the basin; fragments of carbonatite do not occur. Layer 2 represents a remarkable change in environmental conditions assigned by the absence of quartz and hematite and by enrichment in phosphate, REE and organic matter (Tab. 2 and Fig. 5). We interpret that the passage from layer 3 to layer 2 represents the inversion of the relief and may be correlated to the reworking of the upper laterites, it is also in layer 2 that the layering of the sediments are no longer disturbed, meaning that the deformation response to karstification stopped. Layer 1 would correspond to the oxidation of the upper part of layer 2 with the consequent loss of organic matter, S and metals as Pb, Zn Ni, Co, As and Cd, and, consequently, residual concentration of phosphates and aluminum.

A major event regarding the REE mineralization is the formation of authigenic florencite-(Ce) and florencite-(La) in layer 2. The formation of diagenetic aluminum-phosphates by dissolving primary phosphates in low-pH environment and subsequent

precipitation of aluminum phosphates has already been described (Spötl, 1990), as well as the formation of aluminophosphates in clay-rich environment in a zone of sulfate reduction and microbial methanogenesis (Rasmussen, 1996). As the solubility of Al is extremely low in low-temperature aqueous fluids (Garrels and Christ, 1965), the site of Al release (the clay mineral substrate) was also the nucleation site for the formation of florencite-(Ce), as seen in Figure 9. The great increase in REE concentration in layers 2 and 1 (Fig. 5) requires input from the laterites. The similarity between the REE normalized pattern of layers 1 and 2 and the mottled laterites (Fig. 13) suggests that the upper laterites were the source of the REE and part of the phosphate carried by the groundwater flow towards the basin. This process formed the richest REE ore with 1.72 wt% REE_2O_3 (Tab. 8) which may also exist in ~15 other basins and lakes distributed throughout the MSLD.

The only case in the literature somewhat comparable to the Esperança Basin is that of the upper ore horizon of the Tomtor REE-Nb deposit (Siberia) associated to carbonatite. This horizon represents a buried placer deposit (up to 30 m thick), containing florencite-monazite-pyrocholore, deposited in lacustrine environment formed in local karst depression (Kravchenko and Pokrovsky, 1995). As reviewed by these authors, there are several hypotheses for the formation of REE mineralization associated to the placer: (i) enrichment due to removal of mobile components and to accumulation of inert constituents during oxidation and reduction (Lapin and Tolstov 1991, 1993); (ii) metasomatism (Entin et al., 1991); (iii) redeposition of weathered material and enrichment in heavy minerals during erosion of the ore-bearing sequence and deposition of heavy minerals in an aqueous environment (Kravchenco et al., 1990; Konoplev et al., 1992) and; (iv) development of REE phosphate minerals due to ground-water infiltration (Konoplev et al., 1992). Except for the metasomatism, all these proposed processes occurred in the Esperança Basin.

6. CONCLUSION

In the Morro dos Seis Lagos Nb (Ti, REE) deposit there are three types of REE mineralization: primary type associated to siderite carbonatite, supergene type associated to laterite, and sedimentary (detrital as well as of authigenic formation).

The main ore zone in the primary mineralization occurs in the core siderite carbonatite over a thickness of 42 m with 1.47 wt% REE_2O_3 mainly in monazite-(Ce) and bastnäsite. However, considering the entire section intersected in the core siderite carbonatite, the average grade drops to 0.7 wt% REE_2O_3, mainly in thorbastnasite. In the border siderite carbonatite the REE mineralization is hydrothermal [rhabdophane-(Ce) and REE-rich gorceixite (up to 12.50 wt% REE_2O_3)].

In a first stage of lateritization of the siderite carbonatite, the geochemical behavior of REE and phosphates was the same observed in other REE secondary deposits associated with carbonatite. The LREE and phosphates were concentrated at the reworked laterites relative to the HREE which are leached and may have formed higher concentrations at the base of the lateritic profile, at depths that could not be accessed in the present study. The pyrochlore has undergone successive transformations. The last pyrochlore was a Ce-pyrochlore, which itself was progressively weathered, with enrichment in Ce^{4+} and loss in REE^{3+}, until the breakdown of the mineral structure. Cerium was then released under strongly oxidizing conditions (high Ce^{4+}/Ce^{3+}) which favored the formation of cerianite-(Ce) extremely poor in Th and in trivalent REE. This cerianite-(Ce) occurs intercalated with goethite bands in the lower part of the profile (brown and lower purple laterites) and forms intergrowth with hollandite in the manganiferous laterite which was formed in a more alkaline environment closer to the water table. The brown laterite has 1.30 wt% REE_2O_3, the manganese laterite has 1.544 wt% REE_2O_3, of which 1.416 wt% is Ce_2O_3.

Tectonic and karstic processes over the siderite carbonatite formed ~15 sedimentary basins, among them the Esperança Basin, whose sedimentary record, in a column 233 m thick, shows the whole evolution of the MSLD. Layer 5, the lower layer, has abundant carbonatite fragments, florencite-(Ce) mineralization, and 1.07 wt% REE_2O_3. Layer 4 is formed by carbonatite fragments interbedded with clay rich layer. Layer 3 is a rhythmite deposited in lacustrine environment, with clasts of ferruginous materials related to the early stages of siderite carbonatite alteration, and detrital monazite. Layer 2 is made up by carbonaceous clay rich in organic matter, with autigenic florencite-(Ce), florencite-(La), and base metals. This layer marks the inversion of the relief and the input into the Esperança Basin of REE leached from the upper laterites, carried by the groundwater flow. Layer 1 was formed by the oxidation of the upper part of the layer 2, resulting in residual enrichment of REE by the loss of

organic matter, base metals and other mobile elements. Layers 1 + 2 have 73 m thick and average of 1.72 wt% REE_2O_3.

ACKNOWLEDGMENTS

The present work would not have been possible without the support given by the Companhia de Pesquisa de Recursos Minerais, through Roberto Ventura Santos, Eduardo Camozatto, and Renê Luzardo. Gert Rodolfo Woeltje (DNPM-Amazonas) is also thanked. The Conselho Nacional de Desenvolvimento Científico e Tecnológico CNPq is acknowledged for the financial support (projects 485415/2012-7 and 405839/2013-8).

REFERENCES

Almeida, M.E., Macambira, M.J.B., Santos, J.O.S., Nascimento, R.S.C., Paquette, J.-L., 2013. Evolução crustal do noroeste do cráton Amazonico (Amazonas, Brasil) baseada em dados de campo, geoquímicos e geocronologicos. In: Simpósio de Geologia da Amazonia, 13º, Belem, CD-ROM.

Andreoli, M.A.G., Smith, C.B., Watkeys, M., Moore, J.M., Ashwal, L.D., Hart, R.J., 1994. The geology of the Steenkampskraal monazite deposit, South Africa: implications for REE-Th-Cu mineralization in charnockite-granulite terranes. Econ. Geol. 89, 994–1016.

Arzamastsev, A., Yakovenchuk, V., Pakhomovsky, Y., Ivanyuk, G., 2008. The Khibina and Lovozero alkaline massifs: geology and unique mineralization. Guidebook for 33rd International Geological Congress Excursion 47 (58 pp.)

Bau, M., 1991. Rare-earth element mobility during hydrothermal and metamorphic fluid-rock interaction and the significance of the oxidation state of europium. Chem. Geol. 93(3–4), 219–230.

1045 Bonow, C.W., Issler R.S., 1980. Reavaliação e aspectos econômicos do jazimento de
1046 terras raras e ferro-ligas do Lago Esperança, Complexo carbonatítico de Seis Lagos
1047 - Amazonas, Brasil. In: Congresso Brasileiro de Geologia, 31, Camboriu, 3, 1431.

1048 Braun, J.J., Pagel, M., Muller, J.P., Bilong, P., Michard, A., Guillet, B., 1990. Cerium
1049 anomalies in lateritic profiles. Geochim. Cosmochim. Acta 54, 781–795.

1050 Braun, J.J, Pagel, M, Herbillon, A., Rosin, C., 1993. Mobilization and redistribution of
1051 REEs and thorium in a syenitic lateritic profile: A mass balance study. Geochim.
1052 Cosmochim. Acta 57: 4419-4434.

1053 Broom-Fendley, S., Styles, M.T., Appleton, J.D., Gunn, G., Wall, F., 2016. Evidence
1054 for dissolution-reprecipitation of apatite and preferential LREE mobility in
1055 carbonatite-derived late-stage hydrothermal processes. Am. Mineral. 101, 596–
1056 611.

1057 Carneiro, T., 2015. Reservas de terras raras, Companhia Brasileira de Metalurgia e
1058 Mineração (CBMM) in: III Seminário Brasileiro de Terras Raras, Rio de Janeiro,
1059 Brasil.

1060 Castor, S.B., 2008. The Mountain Pass rare-earth carbonatite and associated
1061 ultrapotassic rocks, California. Can. Mineral. 46, 779–806.

1062 Chakhmouradian, A.R., Reguir, E.P., Kressall, R.D., Crozier, J., Pisiak, L.K., Sidhu, R.,
1063 Yang, P., 2015. Carbonatite-hosted niobium deposit at Aley, northern British
1064 Columbia (Canada): Mineralogy, geochemistry and petrogenesis. Ore Geology
1065 Reviews 64, 642–666.

1066 Chakhmouradian, A.R., Wall, F., 2012. Rare earth elements: Minerals, mines, magnets
1067 (and more). Elements 8, 333–340.

1068 Chakhmouradian, A.R., Zaitsev, A.N., 2012. Rare earth mineralization in igneous rocks:
1069 Sources and processes. Elements 8, 347–353.

1070 Chakrabarty, A., Mitchell, R.H., Ren, M., Sen, A.K., Pruseth, K.L., 2013. Rinkite,
1071 cerianite-(Ce), and hingganite-(Ce) in syenite gneisses from the Sushina Hill

1072 Complex, India: occurrence, compositional data and petrogenetic significance.
1073 Mineral. Mag. 77, 3137–3153.

1074 Cordeiro, P.F. de O., Brod, J.A., Palmieri, M., de Oliveira, C.G., Barbosa, E.S.R.,
1075 Santos, R.V., Gaspar, J.C., Assis, L.C., 2011. The Catalão I niobium deposit,
1076 central Brazil: Resources, geology and pyrochlore chemistry. Ore Geol. Rev. 41,
1077 112–121.

1078 Corrêa, S.L.A. 1996. Evolução geoquímica das crostas lateríticas e dos sedimentos
1079 sobrepostos na estrutura de Seis Lagos (Amazonas). PhD. thesis, Universidade
1080 Federal do Pará (in Portuguese).

1081 Corrêa, S.L.A., Costa M.L., 1997. Mineralogia das crostas lateríticas ferruginosas de
1082 Seis Lagos (Amazonas). Geociências 16 (1), 141-156.

1083 CPRM, 2006. Geologia e recursos minerais do Estado do Amazonas. Map scale
1084 1:1.000.000. Companhia de Pesquisa de Recursos Minerais, Manaus. CD-ROM
1085 (abstract in English).

1086 Duddy, J.R., 1980. Redistribution and fractionation of rare earths and other elements in
1087 a weathering profile. Chem. Geol. 30, 363-381.

1088 Formoso M.L., Nardi, L.V.S., Hartmann, L.A., 1989. Geoquímica dos elementos terras
1089 raras no Brasil. Chapter 7: Fracionamento dos elementos terras raras e suas
1090 aplicações em metalogenese: Comportamento químico em sistemas diversos. 152p.

1091 Formoso M.L., Pereira, V.P., Menegotto, E., Nardi, L.V.S., Bastos Neto, A.C., Cunha,
1092 M.C.L., 2016. Os elementos terras raras e sua importância para o setor mineral do
1093 Brasil. In: Melfi, A.J., Misi, A., Campos D. A., Cordani, U.G. Recursos Minerais
1094 do Brasil: Problemas e Desafios. Edition 1, Chapter I, 68–83.

1095 Garcia, M., 2012. O depósito Nb-Ta de Pitinga – AM. In: V Simpósio brasileiro de
1096 exploração mineral. Ouro Preto, MG – Brazil.

1097 Giovannini, A.L., 2013. Contribuição à geologia e geoquímica do carbonatito e da
1098 jazida (Nb, ETR) de Seis Lagos. Msc thesis Universidade Federal do Rio Grande
1099 do Sul (in Portuguese).

1100 Giovannini, A.L., Bastos Neto, A.C., Porto, C.G., Pereira, V.P., Takehara, L.,
1101 Barbanson, L., Bastos, P.H.S., 2017. Mineralogy and geochemistry of laterites
1102 from the Morro dos Seis Lagos Nb (Ti, REE) deposit (Amazonas, Brazil). Ore
1103 Geol. Rev. 88, 461–480.

1104 Gittins, J., Harmer, R.E., 1997. What is ferrocarbonatite? A revised classification.
1105 Journal of African Earth Sciences 25, 159–168.

1106 Gomes, C.B., Ruberti, E., Morbidelli, L., 1990. Carbonatite complexes from Brazil: a
1107 review. J. S. Am. Earth Sci. (3/1), 51-63.

1108 Graham, A.R., 1955. Cerianite: a new rare-earth oxide mineral. Amer. Mineral., 40,
1109 560-564.

1110 Hatch, G. 2015. TMR Advanced Rare-Earth Projects Index,
1111 http://www.techmetalsresearch.com/metrics-indices/tmr-advanced-rare-earth-
1112 projects-index/

1113 Humphris, S.E., 1984. the mobility of the rare earth elements in the crust. In: P.
1114 Henderson (Ed). Rare Earth Element Geochemistry. Devel. in Geochem. 2, 317-
1115 373.

1116 Huston D.L., Maas R., Cross A., Hussey K.J., Mernagh T.P., Fraser G., Champion D.C.,
1117 2016. The Nolans Bore rare-earth element-phosphorus-uranium mineral system:
1118 geology, origin and post-depositional modifications. Mineralium Deposita 51,
1119 797–822.

1120 Issler, R.S., Silva, G.G. 1980. The seis lagos carbonatite complex. In: Congresso
1121 Brasileiro de Geologia 31, Camboriu, 3, 1564-1572.

1122 Jones, A.P., Genge, M., Carmody, L., 2013. Carbonate Melts and Carbonatites. Reviews
1123 in Mineralogy & Geochemistry. 75, 289-322.

1124 Justo, L.J.E.C., Souza, M.M., 1984. Jazida de nióbio do Morro dos Seis Lagos,
1125 Amazonas. In: Simpósio Amazonense 2, Manaus, 467-472.

1126 Justo, L.J.E.C., Souza, M.M., 1986. Jazida de nióbio do Morro dos Seis Lagos,
1127 Amazonas. In: Schobbenhaus, C. and Coelho, C.E.S. (Eds), Principais Depósitos
1128 Minerais do Brasil - Ferro e Metais da Indústria do Aço. Departamento Nacional
1129 da Produção Mineral, 2, 463-468.

1130 Konoplev, A. D., Kuzmin, V. I., Epshtein, E.M., 1992. Geological and geochemical
1131 peculiarities talus-lake placer above weathering crust of the rare-elements-bearing
1132 carbonatites, Mineralogy and geochemistry of placers: Moscow Nauka,111-123
1133 (in Russian).

1134 Krauskopf, K. B. 1985. Introduction to geochemistry. 2nd edition. Auckland, McGraw-
1135 Hill Book Company. 617p.

1136 Kravchenko S.M., Belyakov A.Y., Tolstov A.V., Kubishev A.I., 1990. Sc-REE-Y-Nb
1137 ores a new type of rare element economic resource. International Geology Reviews
1138 33, 280-284.

1139 Kravchenko, S.M., Pokrovsky, B.G., 1995. The Tomtor alkaline ultrabasic massif and
1140 related REE-Nb deposits, northern Siberia. Economic Geology 90, 676–689.

1141 Kynicky, J., Smith, M.P., Xu, C., 2012. Diversity of rare earth deposits: The key
1142 example of China. Elements 8, 361–367.

1143 Lapin, A.V. and Kulikova, I.M., 1989. Processes of pyrochlore alteration and their
1144 products in the carbonatite weathering crusts. Zap. Vses. Mineral. Obshch., 118,
1145 (in Russian), 419.

1146 Le Maitre, R.W., 2002. Igneous Rocks: A Classificarion and Glossary of Terms.
1147 Cambridge University Press. Cambridge UK.

1148 Lemos, R.L., Gaspar, J.C., 1998. Geologia do Complexo Ultramafico-alcalino-
1149 carbonatítico de Maicuru, noroeste do Estado do Para. In: Congresso Brasileiro de

1150 Geologia, 40, 1998, Belo Horizonte. Anais, vol. 1. SBG, Belo Horizonte, pp. 466-
1151 529.

1152 Lottermoser, B.G., 1990. Rare-earth element mineralisation within the Mt. Weld
1153 carbonatite laterite, Western Australia. Lithos 24, 151–167.

1154 Lottermoser, B.G., England, B.M., 1988. Compositional variation in pyrochlores from
1155 the Mount Weld carbonatite laterite, Western Australia. Mineralogy and Petrology
1156 38, 37–51.

1157 Mariano, A.N.; 1989a. Economic geology of rare earth minerals. In: B.R. Lipin and
1158 G.A. McKay (Eds). Geochemistry and mineralogy of rare earth elements. Rev.in
1159 Min. 21, 309-337.

1160 Mariano, A.N.; 1989b. Nature of economic mineralization in carbonatites and
1161 associated rocks. In: K. Bell (Ed). Carbonatites: Genesis and evolution,149-172.

1162 Mariano, A.N., Mariano, A. Jr., 2012a. Rare earth mining and exploration in North
1163 America. Elements 8, 369–376.

1164 Mariano, A.N., Mariano, A.Jr., 2012b. Overview of REE deposits and mines in the
1165 world and in Brazil. In: V Simpósio brasileiro de exploração mineral. Ouro Preto –
1166 MG, Brazil.

1167 Marini, O. J.; Botelho, N. F.; Rossi, P., 1992. Elementos terras raras em granitóides da
1168 Província Estanífera de Goiás. Revista Brasileira de Geociências 22, p. 61-72.

1169 Mgonde, F., 1994. Mobilization and redistribution of phosphate and rare earth elements
1170 in the weathering zone above Panda Hill carbonatite, SW Tanzania. Msc Thesis.
1171 Carleton University, 130p.

1172 Mitchell, R.H., 2005. Carbonatites and carbonatites and carbonatites. Can. Mineral. 43,
1173 2049–2068.

1174 Nesbitt, H.W.; 1979. Mobility and fractionation of rare earth elements during
1175 weathering of a granodiorite. Nature 279: 206-210.

1176 Pandur, K., Ansdell, K.M., Kontak, D.J., Halpin, K.M., Creighton, S., 2016.
1177 Petrographic and mineral chemical characteristics of the hoidas lake deposit,
1178 Northern Saskatchewan, Canada: Constraints on the origin of a distal magmatic-
1179 hydrothermal REE system. Econ. Geol. 111, 667–694.

1180 Pinheiro, S.S.; Fernandes, P. E. C. A.; Pereira, E. P.; Vasconcelos, E. G.; Pinto, A. C.;
1181 Montalvão, R. M. G.; Issler, R. S.; Dallagnoll, R.; Teixeira, W.; Fernandes, C. A.
1182 C. 1976. Folha NA.19 Pico da Neblina; geologia, geomorfologia, pedologia,
1183 vegetação e uso potencial da terra. Rio de Janeiro, Cap. 2, p.19-138.
1184 (Levantamento de Recursos Naturais).

1185 Ray, J. T., and Clark, J. G., 2015, Exploration for REE and Gold in the Bear Lodge
1186 Tertiary Alkaline Complex, Cook County, Wyoming, in: Pennell, W. M. and
1187 Garside, L. J., eds., New Concepts and Discoveries: Geological Society of Nevada
1188 Symposium Proceedings, May 2015, Sparks, Nevada, p. 905-920.

1189 Ribeiro, C.C., Brod, J.A., Junqueira-Brod, T.C., Gaspar, J.C., Palmieri, M., Cordeiro,
1190 P.F.O., Torres, M.G., Grasso, C.B., Barbosa, E.S.R., Barbosa, P.A.R., Ferrari,
1191 A.J.D., Gomide, C.S., 2014. Potencial e controles metalogenéticos de ETR, Ti e
1192 Nb em províncias alcalino-carbonatíticas brasileiras, Metalogenia das Províncias
1193 Tectônicas do Brasil. CPRM, Brasília, 559-589.

1194 Rocha, A., Schissel, D., Sprecher, A., Tarso, P., Goode, J.R., 2013. Process
1195 development for the Serra Verde weathered crust elution-deposited rare earth
1196 deposit in Brazil. In: London, I.M., Goode, J.R., Moldoveanu, G., Rayat, M.S,
1197 (eds), Rare Earth Elements. Eds: 277 - 288

1198 Rocha, E., Nasraoui, M., Soubiès, F., Bilal E., De Parseval, P., 2001. Évolution
1199 géochimique du pyrochlore au cours de l'altération météorique du gisement de
1200 Catalao II (Goiás, Brésil). Comptes Rendus l'Academie Sci. - Ser. IIa Sci. la Terre
1201 des Planetes 332, 91–98.

1202 Rossoni, M.B., Bastos Neto, A.C., Saldanha, D.L., Souza V.S., Giovannini, A.L., Porto,
1203 C.G., 2016. Aplicação de técnicas de sensoriamento remoto na investigação do
1204 controle do posicionamento do Complexo Carbonatítico Seis Lagos e no estudo do

depósito (Nb) laterítico associado (Amazonas, Brasil). Revista Pesquisas 43, 111-125.

Rossoni, M.B., Bastos Neto, A.C., Souza V.S., Marques, J.C., Dantas, E., Botelho, N.F., Giovannini, A.L., Pereira, V.P., 2017. U-Pb zircon geochronologycal investigation on the Morro dos Seis Lagos Carbonatite Complex and associated Nb deposit (Amazonas, Brazil). Journal of South American Earth Sciences 80, 1-17.

Santos, J.O.S., Faria, M.S.G., Riker, S.R., Souza, M.M., Hartmann, L.A., Almeida, M.E., McNaughton, N.J., Fletcher, I.R., 2006b. A faixa colisional K'Mudku (idade grenvilliana) no norte do cráton Amazonas: reflexo intracontinental do orógeno Sunsás na margem ocidental do craton. In: SBG-NO, 9º Simpósio de Geologia da Amazonia. CD-ROM, Belém

Santos, J.O.S., Hartmann, L.A., Faria, M.S., Riker, S.R., Souza, M.M., Almeida, M.E. & McNaughton, N.J. 2006. A compartimentação do cráton amazônico em províncias: avanços ocorridos no período de 2000-2006. In: SIMPÓSIO DE GEOLOGIA DA AMAZÔNIA, 9., 2006, Seção Temática 3, Belém, Pará. CD-ROOM.

Santos, J.O.S., Hartmann, L.A., Faria, M.S.G., Riker, S.R., Souza, M.M., Almeida, M.E., McNaughton, N.J., 2006a. A compartimentação do Cráton Amazonas em províncias: avanços ocorridos no período 2000-2006. In: SBG-NO, 9º Simposio de Geologia da Amazonia. CD-ROM, Belém.

Santos, J.O.S., McNaughton, N.J., Almeida, M.E., 2009. Magmatismo de idade Sunsás no centro-norte do cráton Amazonas. In: SBG-NO, 11º Simposio de Geologia da Amazonia. CD-ROM, Manaus.

Silva, A. B. da, 1986. Jazida de nióbio de Araxá, Minas Gerais. (in Principais depósitos minerais do Brasil. Vol. II, Shobbenhaus C., editor and Coelho C. E. da S., editor) DNPM, 435 – 453.

1231 Souza, V.S., Souza, A.G.H., Dantas, E.L., Valerio, C.S., 2015. K'Mudku A-type
1232 magmatism in the southernmost Guyana Shield, central-north Amazon Craton
1233 (Brazil): the case of Pedra do Gavião syenogranite. Braz. J. Geol. 45 (2), 293-306.

1234 Spötl, C., 1990. Authigenic aluminium phosphate-sulphates in sandstones of the
1235 Mitterberg Formation, Northern Calcareous Alps, Austria. Sedimentology, 37,
1236 837–845.

1237 Streckeisen, A., 1980. Classification and nomenclature of volcanic rocks, lamprophyres,
1238 carbonatites and melilitic rocks IUGS subcommission on the systematics of
1239 Igneous Rocks. Geol. Rundschau 69, 194-207.

1240 Takehara, L. C., Shintaku, I., Rabelo, D. M., Silveira, F. V., 2015. Avaliação do
1241 potencial de terras raras no Brasil. CPRM. Série minerais estratégicos n^{o} 2. 219.

1242 Tassinari, C. C. G. & Macambira M. J. B. 2004. A Evolução Tectônica do Cráton
1243 Amazônico. In: Manteso-Neto, V., Bartoreli, A., Carneiro, C.D.R. & Brito Neves,
1244 B.B. (Eds.). Geologia do Continente Sul Americano: Evolu- ção da Obra de
1245 Fernando Flávio Marques de Almeida. São Paulo. Ed. Beca, 471-486.

1246 Thompson, R.N., Smith, P.M., Gibson, S. a., Mattey, D.P., Dickin, a. P., 2002. Ankerite
1247 carbonatite from Swartbooisdrif, Namibia : the first evidence for magmatic
1248 ferrocarbonatite. Contrib. to Mineral. Petrol. 143, 377–395.

1249 Thrane, K., Kalvig, P., Keulen, N., 2014. REE deposits and occurrences in Greenland.
1250 In: 1st European Rare Earth Resources Conference

1251 Toledo, M.C.M., 1999. Os fosfatos aluminosos da série da crandallita: uma revisão.
1252 Rev. do Inst. Geológico 20, 49–63.

1253 Viegas Filho, J.R., Bonow, C.W., 1976. Projeto Seis Lagos (Internal Report).
1254 Companhia de Pesquisa de Recursos Minerais, Manaus.

1255 Voncken, J.H.L., 2016. The Rare Earth Elements : an Introduction.

1256 Wall, F., Williams, C.T., Woolley, A.R., Nasraoui, M., 1996. Pyrochlore from
1257 weathered carbonatite at Lueshe, Zaire. Mineralogical Magazine 60, 731-750.

1258 Williams-Jones, A.E., Migdisov, A.A., Samson, I.M., 2012. Hydrothermal mobilisation
1259 of the rare earth elements-a tale of "ceria" and "yttria." Elements 8, 355–360.

1260 Zaitsev, A. N., Sitnikova, M. A., Subbotin, V. V., Fernandez-Suarez J., Jeffries T. E..
1261 2004. Sallanlatvi Complex; a rare example of magnesite and siderite carbonatites
1262 (in Phoscorites and carbonatites from mantle to mine; the key example of the Kola
1263 alkaline province , (eds) Wall F., Zaitsev A. N.) Mineralogical Society Series 10:
1264 201-246.
1265

5 CONCLUSÕES

O Depósito Morro dos Seis Lagos é formado a partir de um intenso intemperismo sobre um siderita carbonatito, esse intemperismo gerou diversos tipos diferentes de mineralizações.

A rocha primária do depósito é um siderita carbonatito, nenhum outro tipo de carbonatito ou rocha alcalina foram encontradas no complexo, tais rochas podem ocorrer nas partes mais profundas e inexploradas do complexo, sugerimos que o Complexo de Carbonatititico Morro dos Seis Lagos representa as porções superiores de um sistema magmático carbonatítico.

Ocorrem 3 tipos de siderita carbonatito de siderite: (1) siderita carbonatito de núcleo, é altamente oxidado e brechado, formado por: siderita (até 95% em volume), hematita; pirocloro; Nb-brookita; Ti-maghemita; e thorbastnäsite; (2) uma porção rica em ETR e P do siderita carbonatito de núcleo com siderita (até 95 vol.%), hematita, pirocloro, monazita e bastnäsita; (3) siderita carbonatito de borda, de origem carbo-hidrotermal formado por siderita (~ 70% vol.), barita (~ 15% vol.), gorceixita (~ 7% vol) além de rabdofano e pirocloro.

A paragênese de Nb-Ti-óxido é bastante simples em comparação com a ocorrência na maioria dos depósitos de Nb sendo: Pb-Ba-pirocloro ocorre no siderita carbonatito de borda; Ce-Ba- pirocloro, Nb-brookita e titanomaghemita ocorrem no siderita carbonatito de núcleo; e Ce-Ba- pirocloro no siderita carbonatito de núcleo rico em ETR é mais rico em ETR. O Ce-Ba- pirocloro vai sendo alterado progressivamente para Ce- pirocloro e é totalmente destruído nas porções inferiores do perfil laterítico. A Nb-brookita do carbonatito é mais rica em Nb qua a Nb-brookita da laterita. A substituição $3Ti^{4+} = Fe^{2+} + 2Nb^{5+}$ explica este maior enriquecimento em Nb e indica formação em um ambiente redutor.

As inclusões fluidas e os estudos de isótopos estáveis indicam que o siderita carbonatito de núcleo está relacionado a processos tardi-magmáticos a hidrotermais e o siderita carbonatito de borda está relacionado a um estágio hidrotermal.

O siderita carbonatito de núcleo do Morro dos Seis Lagos é o mais rico em Fe já descrito (até 70% de Fe_2O_3) e o mais pobre em Ca (0.8 % de CaO). O alto teor de Nb (até 7667 ppm) em todas as amostras é incomum em ferrocarbonatitos.

Os dados isotópicos de Sr e Nd sugerem que o Complexo Carbonatítico Morro dos Seis Lagos tem uma origem mantélica sem praticamente nenhuma contaminação crustal. Se isso for correto, a idade do carbonatito é considerada muito mais nova do que a idade máxima previamente proposta da carbonatito de 1328 ± 58 Ma.

O perfil laterítico formado sobre esse carbonatito apresenta mais de 100m de espessura e é formado por seis tipos texturais e composicionais de laterita (do topo para a base): (1) laterita pisolítica, (2) laterita fragmentada, (3) laterita mosqueada, (4) laterita roxa, (5) laterita manganesífera e (6) laterita marrom. Todas as lateritas são formadas principalmente por goethita (predominante nas laterites inferiores) e hematita (predominante nas laterites intermediárias). O goethita torna-se mais abundante novamente nas laterites superiores como resultado da retrabalhamento das lateritas superiores. Na laterita manganesífera (10 m de espessura), os óxidos de manganês (principalmente holanditas, com cerianita associada) ocorrem como veios formadas em um evento tardio durante o desenvolvimento do perfil laterítico, precipitado a partir de uma solução com maior Eh do que solução com óxidos de Fe, e ocorre próximo ao nível de água. A siderita primária é a fonte do Mn.

Os minerais de minério de Nb são essencialmente o Nb-rutilo e secundariamente a Nb-brookita. O Nb-rutilo ocorre como cristais isolados em todas as laterites, com uma composição de 57,84 a 80,92% em peso de TiO_2, 11,26 a 22,23% em peso de Nb_2O_5 e 8,96 a 14,95% em peso de Fe_2O_3. A Nb-brookita é formada a partir da alteração do Nb-rutilo e possui uma composição semelhante a esse mineral, a Nb-brookita ocorre como esférulas comumente quebradas pelo colapso dos laterites durante o retrabalhamento das laterites superiores e possui estrutura de faixas finas interpretada como anéis de Liesegang. O Nb-rutilo e a Nb-brookita acomodam Nb seguindo a substituição [$1Fe^{3+}$ + 1(Nb, Ta) = 2Ti]. O mineral mais tardio apresenta algum desvio da substituição ideal; o estágio anterior à sua formação é representado por uma quebra da estrutura em partes dos cristais de Nb-rutilo, com a formação de um gel, no qual a formação incipiente de esférulas pode ser vista.

A presença de Nb-rutilo em vez de outros minerais Nb comuns está relacionada à intensa lateritização. O pirocloro primário foi progressivamente alterado, formando pirocloros secundários, até a formação do Ce-pirocloro que desaparece na parte superior da laterite marrom. A formação Nb-rutilo, observada na laterita marrom, ocorreu, juntamente com Ce-pirocloro, Nb-goethita e cerianita partir da alteração de um mineral, presumivelmente, um pirocloro secundário.

As laterites têm um teor médio de Nb_2O_5 de 2,91% em peso. As concentrações de TiO_2 também são significantes, com uma média de 5,00% em peso nos lateritas superiores.

No depósito Morro dos Seis Lagos Nb (Ti, ETR) existem três tipos de mineralização de ETR: (1) primária - associado ao siderita carbonatito, (2) supergênica - associada a laterita e (3) sedimentar – minerais detríticos e autigênicos formados na bacia. A principal zona de minério na rocha primária primária ocorre no siderita carbonatito de núcleo rico em ETR, que possui uma espessura de 42 m com teor médio de 1,47% em peso de ETR_2O_3, principalmente na forma de monazita (Ce) e bastnäsita. No entanto, considerando toda a seção interceptada no siderita carbonatito de núcleo, o teor médio cai para 0,7% ETR_2O_3, principalmente como thorbastnäsite. No siderita carbonatito de borda, a mineralização de ETR é hidrotermal, rhabdophano- (Ce) e gorceixita rica em ETR (até 12,50% em peso de ETR_2O_3).

Numa primeira fase de lateritização do siderita carbonatito, o comportamento geoquímico de ETR e fosfatos foi o mesmo observado em outros depósitos secundários de ETR associados à carbonatito. Os ETRL e os fosfatos foram concentrados nas lateritas retrabalhadas e os ETRP foram lixiviados e podem ter formado concentrações mais altas na base do perfil laterítico, em profundidades que não foram acessadas no presente estudo. O pirocloro passou por sucessivas transformações. O último pirocloro (Ce-pyrochlore) foi degradado progressivamente, com enriquecimento em Ce^{4+} e a perda de ETR^{3+}, até a quebra da estrutura do mineral. O Ce foi liberado sob condições fortemente oxidantes (alta razão Ce^{4+}/Ce^{3+}), o que favoreceu a formação de uma cerianita-(Ce) extremamente rica em Ce^{4+} e pobre em Th e ETR^{3+}. Esta cerianita-(Ce) ocorre intercalada com bandas de goethita na parte inferior do perfil (laterita marrom e laterita roxa inferior) e intercrescida com hollandita na laterita manganesífera que foi formada em um ambiente mais alcalino e mais próximo ao nível de água. A laterita

marrom possui um teor médio de 1,30% de ETR_2O_3, a laterita manganesífera possui um teor médio de 1,544% de ETR_2O_3, dos quais 1,416% é Ce_2O_3.

Processos tectônicos e cársticos sobre o siderita carbonatito formaram ~15 bacias sedimentares, entre elas a Bacia Esperança, cujo registro sedimentar, em uma coluna de 233 m de espessura, mostra toda a evolução do depósito. A camada 5, a camada mais inferior, possui abundantes fragmentos de carbonatito, mineralização florencita-(Ce) e um teor médio de 1,07% de ETR_2O_3. A camada 4 é formada por fragmentos de carbonatito intercalados com camadas ricas em argila. A camada 3 é um ritmito depositada em ambiente lacustre, com clastos de materiais ferruginosos relacionados aos estágios iniciais da alteração do siderita carbonatito e possui monazita detrítica. A camada 2 é composta por argila carbonosa rica em matéria orgânica, com florencita-(Ce) autigênica, e metais base. Esta camada marca a inversão do relevo e a entrada na Bacia Esperança dos ETR lixiviados das lateritas superiores, transportadas pelo fluxo de águas subterrâneas. A camada 1 foi formada pela oxidação da porção superior da camada 2, resultando em enriquecimento residual de REE pela perda de matéria orgânica, metais base e outros elementos móveis. As camadas 1 + 2 têm 73 m de espessura e um teor médio de 1,72% de ETR_2O_3.

6 BIBLIOGRAFIA

Aleva G. J. J. (Compiler) 1994. Laterites—Concepts, Geology, Morphology and Chemistry. International Soil Reference and Information Centre (ISRIC), Wageningen.

Almeida, M.E., Macambira, M.J.B., Faria, M.S.G. de, 2002. A granitogênese paleoproterozoica do sul de Roraima. In: Congresso Brasileiro de Geologia, 41, João Pessoa, 434.

Almeida, M.E., Macambira, M.J.B., Oliveira, E.C., 2007. Geochemistry and zircon geochronology of the I-type high-K calc-alkaline and S-type granitoid rocks from southeastern Roraima, Brazil: Orosirian collisional magmatism evidence (1.97-1.96 Ga) in central portion of Guyana Shield. Precambrian Research 155, 69–97.

Anand R. R. & Gilkes R. J. 1984c. Mineralogical and chemical properties of weathered magnetite grains from lateritic saprolite. Journal of Soil Science 35, 559–567.

Anand R. R. & Gilkes R. J. 1987a. Iron oxides in lateritic soils from Western Australia. Journal of Soil Science 35, 607–622.

Anand R. R. 1998. Distribution, classification and evolution of ferruginous materials over greenstones on the Yilgarn Craton— implications for mineral exploration. In: Eggleton R. A. ed. The State of the Regolith. Proceedings of the 2nd Australian Conference on Landscape Evolution and Mineral Exploration, pp. 175–193. Geological Society of Australia Special Publication 20.

Anand R. R., Gilkes R. J., Armitage T. M. & Hillyer J.W. 1985. Feldspar weathering in lateritic saprolite. Clays and Clay Minerals 33, 31–43.

Anand, R. R. & Gilkes, R. J. 1984. Mineralogical and chemical properties of weathered magnetite grains from lateritic saprolite. Journal of Soil Science 35, 559–567.

Anand, R.R., Butt, C.R.M, 1988. The terminology and classification of a deeply weathered regolith. CSIRO Division of Exploration Geoscience Discussion Paper.

Anand, R.R., Paine, M., 2002. Regolith geology of the Yilgarn Craton, Western Australia: implications for exploration. Australian Journal of Earth Sciences 49, 3–162.

Bell K., 1989. Carbonatites: Genesis and Evolution. Unwin Hyman, London.

Bonow, C.W., Issler R.S., 1980. Reavaliação e aspectos económicos do jazimento de terras raras e ferro-ligas do Lago Esperança, Complexo carbonatítico de Seis Lagos - Amazonas, Brasil. In: Congresso Brasileiro de Geologia, 31, Camboriu, 3, 1431.

Buchanan, F. 1807. A Journey from Madras through the countries of Mysore, Canara and Malabar. East India Company, London, pp. 436–461.

Castor S.B. & Hedrick J.B. Rare Earth Elements. In: Kogel J.E. Trivedi N.C. Barker J.M and Krukowski S.T. Industrial Minerals and Rocks: Commodities, Markets and Uses, ed. 7. SME. 2006. 1568p.

Chakhmouradian, A.R., 2006. High-field-strength elements in carbonatitic rocks: Geochemistry, crystal chemistry and significance for constraining the sources of carbonatites. Chemical Geology 235, 138–160.

Churchman G. 1990. J: Relevance of different intercalation tests for distinguishing halloysite from kaolinite in soils. Clays and Clay Minerals 38, 591–599.

Cornell R. M. & Schwertmann U. 1996. The Iron Oxides. VCH, Weinheim.

Corrêa, S.L.A. 1996. Evolução geoquímica das crostas lateríticas e dos sedimentos sobrepostos na estrutura de Seis Lagos (Amazonas). PhD. thesis, Universidade Federal do Pará (in Portuguese).

Corrêa, S.L.A., Costa M.L., 1997. Mineralogia das crostas lateríticas ferruginosas de Seis Lagos (Amazonas). Geociências 16 (1), 141-156.

CPRM, 2006. Geologia e recursos minerais do Estado do Amazonas. Map scale 1:1.000.000. Companhia de Pesquisa de Recursos Minerais, Manaus. CD-ROM (abstract in English).

Davy R. & Gozzard J. R. 1995. Lateritic duricrusts of the Leonora area, Eastern Goldfields,Western Australia: a contribution to the study of transported laterites. Geological Survey of Western Australia Record 1994/8.

Dawson J.B., 2008. The Gregory Rift Valley and Neogene-Recent Volcanoes of Northern Tanzania. Geological Society London, London.

Fitzpatrick R.W. & Schwertmann U. 1982. Al-substituted goethite—an indicator of pedogenic and other weathering environments in South Africa. Geoderma 27, 335–347

Fontes M. P. F. & Weed S. B. 1991. Iron oxides in selected Brazilian Oxisols. I. Mineralogy. Soil Science Society of America Journal 55, 1143–1149.

Garson M.S., Coats J.S., Rock N.M.S., Deans T., 1984. Fenites, breccia dykes, albitites, and carbonatitic veins near the Great Glen Fault, Inverness, Scotland. J Geol Soc 141(4):711-732.

Gittins, J., Harmer, R.E., 1997. What is ferrocarbonatite? A revised classification. Journal of African Earth Sciences 25, 159–168.

Hornig-Kjarsgaard I., 1998. Rare earth elements in sovitic carbonatites and their mineral phases. J Petrol 39(11- 12):2105-2121.

Issler, R.S., Silva, G.G. 1980. The seis lagos carbonatite complex. In: Congresso Brasileiro de Geologia 31, Camboriu, 3, 1564-1572.

Jones, A.P., Genge, M., Carmody, L., 2013. Carbonate Melts and Carbonatites. Reviews in Mineralogy & Geochemistry. 75, 289-322.

Justo, L.J.E.C., Souza, M.M., 1984. Jazida de nióbio do Morro dos Seis Lagos, Amazonas. In: Simpósio Amazonense 2, Manaus, 467-472.

Justo, L.J.E.C., Souza, M.M., 1986. Jazida de nióbio do Morro dos Seis Lagos, Amazonas. In. Schobbenhaus, C. and Coelho, C.E.S. (Eds), Principais Depósitos Minerais do Brasil - Ferro e Metais da Indústria do Aço. Departamento Nacional da Produção Mineral, 2, 463-468.

Lawrance L. M. 1991. Distribution of gold and ore-associated elements within lateritic weathering profiles of the Yilgarn Block,Western Australia. PhD thesis, University of Western Australia, Perth (unpubl.).

Le Bas M.J., 1987. Nephelinites and carbonatites. Geol Soc London Special Pub 30(1):53.

Le Bas M.J., SYang XM., Taylor R.N., Spiro B., Milton J.A., Peishan Z., 2007. New evidence from a calcite-dolomite carbonatite dyke for the magmatic origin of the massive Bayan Obo ore-bearing dolomite marble, inner Mongolia, China. Mineral Petrol 91:281-307.

Le Maitre, R.W., 2002. Igneous Rocks: A Classificarion and Glossary of Terms. Cambridge University Press. Cambridge UK.

Mariano, A.N.; 1989. Economic geology of rare earth minerals. In: B.R. Lipin and G.A. McKay (Eds). Geochemistry and mineralogy of rare earth elements. Rev.in Min. 21: 309-337.

Millot G. 1964. Geologie Des Argiles. Masson, Paris.

Mitchell, R.H., 2005. Carbonatites and carbonatites and carbonatites. Can. Mineral. 43, 2049–2068.

Nahon, D., Tardy, Y., 1992. The ferruginous laterites. In: Butt, C.R.M. and Zeegers, H. (Eds.), Regolith exploration geochemistry in tropical and sub-tropical terrains. Handbook of Exploration Geochemistry 4, Elsevier, 41–55.

Nelson D.R., Chivas A.R., Chappell B.W., McCulloch M.T., 1988. Geochemical and isotopic systematics in carbonatites and implications for the evolution of ocean-island sources. Geochim Cosmochim Acta 52:1- 17

Ollier, C. D.; Galloway R., 1990. The laterite profile, ferricrete an unconformity. Catena, 17, 97-109.

Pineau F., Javoy M., Allegre C.J., 1973. Etude systématique des isotopes de l'oxygène, du carbone et du strontium dans les carbonatites. Geochim Cosmochim Acta 37:2363-2377.

Pinheiro, S.S.; Fernandes, P. E. C. A.; Pereira, E. P.; Vasconcelos, E. G.; Pinto, A. C.; Montalvão, R. M. G.; Issler, R. S.; Dallagnoll, R.; Teixeira, W.; Fernandes, C. A. C. 1976. Folha NA.19 Pico da Neblina; geologia, geomorfologia, pedologia, vegetação e uso potencial da terra. Rio de Janeiro, Cap. 2, p.19-138. (Levantamento de Recursos Naturais)

Richardson D.G., Birkett T.C., 1996. Carbonatite-associated deposits. In: Geology of Canadian Mineral Deposit Types. Eckstrand OR, Sinclair WD, Thorpe RI (eds) Geological Survey of Canada, Ottawa, p 541-558.

Ridley W.I., Dawson J.B., 1975. Lithophile trace element data bearing on the origin of peridotite xenoliths, ankaramite and carbonatite from Lashaine volcano, N. Tanzania. Phys Chem Earth 9:559-569.

Rossoni, M.B., Bastos Neto, A.C., Saldanha, D.L., Souza V.S., Giovannini, A.L., Porto, C.G., 2016. Aplicação de técnicas de sensoriamento remoto na investigação do controle do posicionamento do Complexo Carbonatítico Seis Lagos e no estudo do depósito (Nb) laterítico associado (Amazonas, Brasil). Revista Pesquisas 43, 111-125.

Rossoni, M.B., Bastos Neto, A.C., Souza V.S., Marques J.C., Dantas, E.L., Botelho N.F., Giovannini, A.L., Pereira V.P., 2017. U-Pb zircon geochronologycal investigation on the Seis Lagos Carbonatite Complex and associated Nb-deposit (Amazonas, Brazil). Journal of South American Earth Sciences in press

Santos, J.O.S., Faria, M.S.G., Riker, S.R., Souza, M.M., Hartmann, L.A., Almeida, M.E., McNaughton, N.J., Fletcher, I.R., 2006b. A faixa colisional K'Mudku (idade grenvilliana) no norte do cráton Amazonas: reflexo intracontinental do orógeno Sunsás na margem ocidental do craton. In: SBG-NO, 9o Simpósio de Geologia da Amazonia. CD-ROM, Belém

Santos, J.O.S., Hartmann, L.A., Gaudette, H.E., Groves, D.I., Mcnaughton, N.J., Fletcher, I.R., 2000. A New Understanding of the Provinces of the Amazon Craton Based on Integration of Field Mapping and U-Pb and Sm-Nd Geochronology. Gondwana Research 3, 453–488.

Santos, J.O.S., Potter, P.E., Reis, N.J., Hartmann, L.A, Fletcher, I.R., McNaughton, N.J., 2003. Age, source and Regional Stratigraphy of the Roraima Supergroup and Roraima-like Sequences in Northern South America, based on U-Pb Geochronology. Geological Society of America Bulletin 115 (3), 331-348.

Schwertmann U. 1985. The effect of pedogenic environments on iron oxide minerals. Advances in Soil Science 1, 171–200. Springer- Verlag, New York.

Schwertmann U. 1988. Occurrence and formation of iron oxides in various pedoenvironments. In: Stucki J. W., Goodman B. A. & Schwertmann U. eds. Iron in Soils and Clay Minerals, pp. 267–308. D. Reidel Publishing Co., Dordrecht.

Silva, A. B. da, 1986. Jazida de nióbio de Araxá, Minas Gerais. (in Principais depósitos minerais do Brasil. Vol. II, Shobbenhaus C., editor and Coelho C. E. da S., editor) DNPM, 435 – 453.

Singh B. & Gilkes R. J., 1992. Properties and distribution of Fe oxides and their association with minor elements in the soils of southwestern Australia. Journal of Soil Science 43, 77–98.

Tardy, Y., Nahon, D., 1985. Geochemistry of laterites, stability of Al-goethite, Al-hematite, and Fe^{3+} kaolinites in bauxites and ferricretes: an approach to the mechanism of concretion formation. American Journal of Sciences 285, 865– 903.

Taylor H.P. Jr, Frechen J., Degens E.T., 1967. Oxygen and carbon isotope studies of carbonatites from the Laacher See District, West Germany and the Alnö District, Sweden. Geochim Cosmochim Acta 31(3):407-430.

Taylor R.M., 1987. Non-silicate oxides and hydroxides. In: Newman A. C. D. ed. Chemistry of clays amd Clay minerals, Mineralogical Society, London, 129 – 201.

Tomkeieff S.I., 1928. The volcanic complex of Calton Hill, Derbyshire. J. Geol. Soc. London 84, 703-718

Viegas Filho, J.R., Bonow, C.W., 1976. Projeto Seis Lagos (Internal Report). Companhia de Pesquisa de Recursos Minerais, Manaus.

Wall F., Mariano A.N., 1996. Rare earth minerals in carbonatites: A discussion centred on the Kangankunde carbonatite, Malawi. In: Rare Earth Minerals: Chemistry Origin and Ore Deposits. Jones AP, Wall F, Williams CT (eds) Chapman and Hall, London, p 193-225.

Walte,r J., 1915. Laterit in West Australien. Zeitschrift de Deutshens Geologischen Gesellchaft, 67B, 113-140.

Walther J., 1915. Laterit in West Australien. Zeitschrift de Deutschens Geologischen Gesellschaft 67B, 113–140.

Wells M. A., Gilkes R. J. & Anand R. R., 1989. The formation of corundum and aluminous hematite by the thermal dehydroxylation of aluminous goethite. Clay Minerals 24, 513–530.

Wells, M. A., Gilkes, R. J., Anand, R. R., 1989. The formation of corundum and aluminous hematite by the thermal dehydroxylation of aluminous goethite. Clay Minerals 24, 513–530.

Woolley A.R., 1982. A discussion of carbonatite evolution and nomenclature, and the generation of sodic and potassic fenites. Mineral Mag 46:7-13.

Woolley A.R., Bailey D.K., 2012. The crucial role of lithospheric structure in the generation and release of carbonatites: geological evidence. Mineral Mag 76:259-270.

Woolley A.R., Kempe D.RC., 1989. Carbonatites: Nomenclature, average chemical compositions and element distribution. In Carbonatites: Genesis and Evolution. Bell K (ed) Unwin Hyman, London, p 1-14-83.

Yang K-F., Fan H-R., Santosh F., Hu F.F., Wang K-Y., 2011. Mesoproterozoic carbonatitic magmatism in the Bayan Obo deposit, Inner Mongolia, North China: constraints for the mechanism of super accumulation of rare earth elements. Ore Geol Rev 40(1):122-131.

7 ANEXOS

7.1 *Aplicação de técnicas de sensoriamento remoto na investigação do controle do posicionamento do Complexo Carbonatítico Seis Lagos e no estudo do depósito (Nb) laterítico associado (Amazonas, Brasil)*

Pesquisas em Geociências, 43 (2): 111-125, maio./ago. 2016
Instituto de Geociências, Universidade Federal do Rio Grande do Sul, Porto Alegre, RS, Brasil
ISSN 1518-2398
E-ISSN 1807-9806

Aplicação de técnicas de sensoriamento remoto na investigação do controle do posicionamento do Complexo Carbonatítico Seis Lagos e no estudo do depósito (Nb) laterítico associado (Amazonas, Brasil)

Marco B. ROSSONI[1], Artur C. BASTOS NETO[2], Dejanira L. SALDANHA[2], Valmir S. SOUZA[3], Arthur L. GIOVANNINI[1] & Claudio G. PORTO [4,5]

(1) Programa de Pós-graduação em Geociências, Instituto de Geociências, Universidade Federal do Rio Grande do Sul. Av. Bento Gonçalves, 9500, Porto Alegre, CEP 91.540-000, RS, Brasil. E-mail: marco_rossoni@hotmail.com, arthur_giovannini@hotmail.com.
(2) Instituto de Geociências, Universidade Federal do Rio Grande do Sul. Av. Bento Gonçalves 9500, CEP 91.540-000, Porto Alegre, RS, Brasil. E-mail: artur.bastos@ufrgs.br, dejanira.saldanha@ufrgs.br.
(3) Instituto de Geociências, Universidade de Brasília. Campus Darcy Ribeiro, Asa Norte, CEP 70910-900, Brasília, DF, Brasil. E-mail: vsouza@unb.br.
(4) Divisão de Geoquímica, Companhia de Pesquisa de Recursos Minerais. Av. Pasteur, 404, CEP 22.290-240, Rio de Janeiro, RJ, Brasil. E-mail: claudio.porto@cprm.gov.br.
(5) Instituto de Geociências, Universidade Federal do Rio de Janeiro. Cidade Universitária, Ilha do Fundão, Av. Athos da Silveira Ramos, s/n, CEP 21949-900, Rio de Janeiro, RJ, Brasil. E-mail: porto@geologia.ufrj.br.

Recebido em 09/2014. Aceito para publicação em 04/2016.
Versão *online* publicada em 31/05/2016 (*www.pesquisasemgeociencias.ufrgs.br*)

Resumo - Este estudo teve como objetivos principais identificar as estruturas geológicas que controlaram o posicionamento do Complexo Carbonatítico Seis Lagos, localizado no noroeste do Estado do Amazonas, e contribuir para o conhecimento da geologia do depósito associado, através da delimitação da crosta laterítica e identificação de estruturas internas e de zonas de alteração hidrotermal onde maiores concentrações de Nb e ETR podem ocorrer. Foram utilizados os métodos geofísicos aeromagnetometria, aerogamaespectometria e mapas de anomalia Bouger, análise de modelo digital de elevação e técnicas de processamento de dados orbitais. A principal estrutura regional tem direção geral E-W, extensão de cerca de 400 km. O posicionamento do CCSL ocorreu onde ela é intersectada por estruturas de direção NE-SW e NW-SE. Os limites da crosta laterítica são em grande parte retilíneos, sugerindo estruturas rúpteis, sejam estas as paredes do conduto magmático, aberto seguindo falhas e fraturas, ou falhas que afetaram o corpo após sua cristalização. As principais estruturas afetando o depósito têm direção E-W ou NNW-SSE, controlaram a formação de vales e cristas, a atuação de processos cársticos com formação de bacias; exerceram, portanto, papel relevante durante o processo de lateritização. Zonas ricas em argilas indicativas de alteração hidrotermal foram identificadas em quatro estruturas.
Palavras-chave: nióbio, elementos terras raras, laterita.

Abstract - Remote sensing applied to investigate the emplacement of the Seis Lagos Carbonatitic Complex and the lateritic Nb-deposit associated (Amazonas State, Brazil). The main goals of this study were to identify geological structures that controlled the emplacement of the Seis Lagos Carbonatite Complex and contribute to the knowledge of the associated deposit, through the delimitation of the lateritic crust, the identification of internal structures and hydrothermal zones, where higher concentrations of Nb and REE may occur. Geophysical techniques, analysis of digital terrain elevation and processing techniques of orbital data were employed. The main regional structure has E-W direction and length of about 400 km. The positioning of the SLCC occurred where it is intersected by structures trending NE-SW and NW-SE. The boundaries of the lateritic crust are largely rectilinear, suggesting brittle structures, that may be the walls of the magma conduct, following open faults and fractures, or faults that affect the body after its crystallization. The main structures affecting the deposit have EW or NNW-SSE direction, controlled the formation of valleys and ridges, and karst processes with basin formation; therefore exerted role during laterization. Clayey zones likely related to hydrothermal processes were identified in four structures.
Keywords: Niobium, rare earth elements, laterite.

1 Introdução

A aplicação da técnica de imageamento por radar, auxiliando a cartografia geológica e geomorfológica do Brasil, realizada pelo projeto RADAM-BRASIL na década de 1970, permitiu identificar diversas estruturas circulares na Amazônia, entre elas as três estruturas que constituem o Complexo Carbonatítico Seis Lagos, localizado no município de São Gabriel da Cachoeira, Estado do Amazonas. O nome "Seis Lagos" já foi utilizado em combinação com muitos outros termos, tais como morro, intrusão, carbonatito, complexo carbonatítico, complexo vulcânico e complexo alcalino. Neste trabalho, utiliza-se o termo Complexo Carbonatítico Seis Lagos (CCSL) para designar esse conjunto de três corpos circulares e o termo Morro dos Seis Lagos (MSL) para designar o corpo circular principal.

As sondagens efetuadas pela Companhia de Pesquisa de Recursos Minerais (CPRM) no MSL revelaram o maior depósito de Nb até hoje encontrado, com reserva estimada de $2.898.10^6$ t, com teor médio de 2,81% de Nb_2O_5 (Justo & Souza, 1984, 1986). O depósito apresenta também concentrações anômalas de elementos terras raras (ETR) (Bonow & Issler, 1980; Issler, 1980a, 1980b), que, na época, não apresentavam o extraordinário interesse tecnológico que possuem atualmente.

Recentemente, a China, que abastece 95% do mercado mundial de ETR, anunciou que vai dirigir toda a sua produção para o mercado interno, gerando uma corrida na pesquisa por novos depósitos de ETR e na investigação dos potenciais de outros depósitos para explotação destes elementos como subprodutos (Stone, 2009; Service, 2010). Desta forma, houve um maior interesse pelo detalhamento do depósito de Seis Lagos, cujos testemunhos estão sendo reestudados por uma equipe de pesquisadores da UFRGS e da CPRM, o que, por sua vez, motivou a realização deste estudo utilizando técnicas de sensoriamento remoto. Este trabalho tem como objetivos: (i) identificar a(s) estrutura(s) que controlam o posicionamento do corpo carbonatítico; (ii) identificar contextos estruturais semelhantes em áreas vizinhas, que possam representar zonas com potencial para outros corpos mineralizados de mesma natureza; (iii) precisar a delimitação do corpo carbonatítico e do depósito laterítico associado; e (iv) identificar estruturas e zonas de alteração hidrotermal no interior do corpo que possam representar zonas de enriquecimento do minério.

2 Área, materiais e métodos

2.1 Geologia Regional

O CCSL situa-se na porção oeste do Escudo das Guianas, norte do Cráton Amazonas (Figs. 1 e 2). Conforme Souza (2009), o avanço do conhecimento da geologia e geocronologia da Amazônia tem corroborado os modelos evolutivos do cráton, que se baseiam em conceitos de orogenias modernas e consideram que, durante o Arqueano e do Paleo ao Mesoproterozoico, ocorreram sucessivos arcos magmáticos com a formação de material juvenil derivado do manto, assim como processos subordinados de retrabalhamento crustal (Tassinari, 1981; Cordani & Brito Neves, 1982; Tassinari & Macambira, 1999, 2004; Santos *et al*., 2000, 2006). Entretanto, ainda existem divergências científicas quanto aos limites geográficos, nomes e idades dos eventos geotectônicos que consolidaram o Cráton Amazonas. Nesse sentido, o CCSL estaria inserido no contexto geotectônico do domínio Ventuari, proposto por Tassinari & Macambira (1999), que seria aproximadamente equivalente ao domínio da província Rio Negro proposta por Santos *et al*. (2006).

A Província Rio Negro (Santos *et al*., 2000) comporta dois domínios tectono-estratigráficos principais (CPRM, 2006) (Fig. 3), Alto Rio Negro, a oeste (na região da "cabeça do cachorro"), e Imeri, a leste, o qual hospeda o CCSL (CPRM, 2006). O embasamento do domínio Imeri é representado pelo Complexo Cauaburi, o qual agrupa metagranitóides porfiríticos, ortognaises tonalíticos a monzoníticos, augen gnaisses, anfibolitos e migmatitos localizados, foliados na direção NE-SW (CPRM, 2002, 2006). Os poucos dados geocronológicos sobre essas rochas indicam idades em torno de 1,8 Ga (Santos *et al*., 2000; Santos, 2003; CPRM, 2006).

O domínio Imeri, particularmente, possui direção estrutural preferencial NE-SW assinalada pelo alinhamento de algumas serras, além de faixas internas com deformação heterogênea desenvolvida no seu embasamento, evidenciada por extensos lineamentos associados a expressivas zonas de cisalhamento; a direção NW-SE tem ocorrência mais restrita, mas é marcante em alguns casos (CPRM, 2006).

Segundo CPRM (2006), o Complexo Cauaburi é cortado por intrusões graníticas das suítes intrusivas Igarapé Reilau (tipo S), Marauiá e Marié-Mirim (ambas do tipo A) e Rio Uaupés. Souza (2009) divide os corpos graníticos da Província Rio Negro (Fig. 3) em granito tipo A, granitoide tipo S e gra-

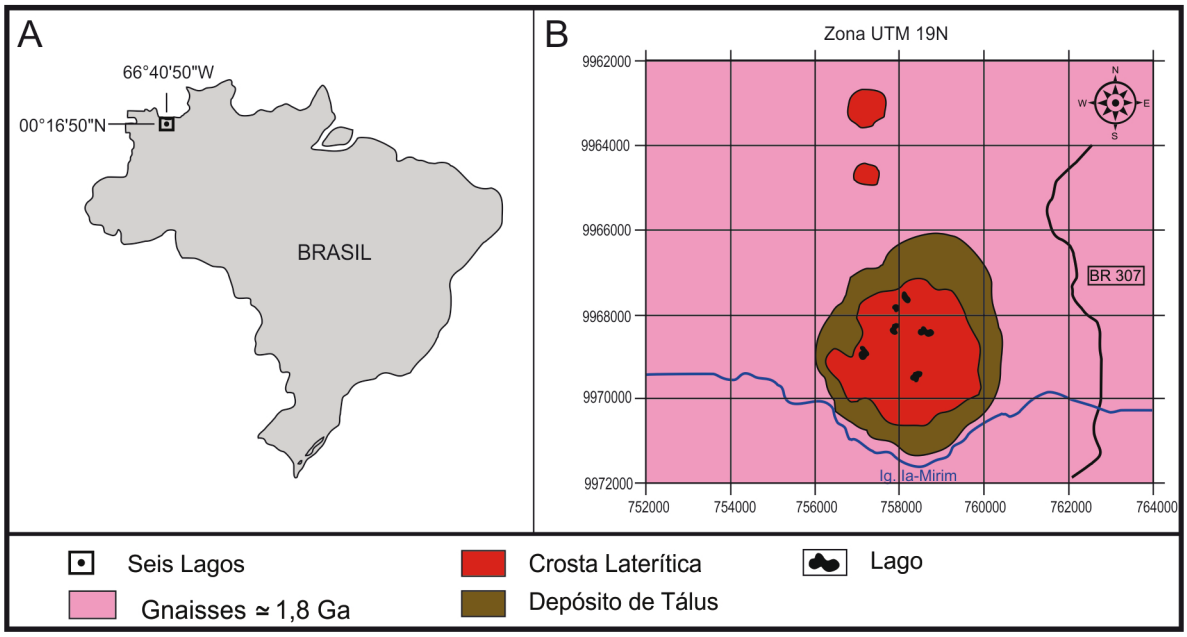

Figura 1. Localização da área de estudo. A) Localização do Complexo Carbonatítico Seis Lagos no mapa do Brasil; B) Mapa geológico simplificado do Complexo Carbonatítico Seis Lagos.

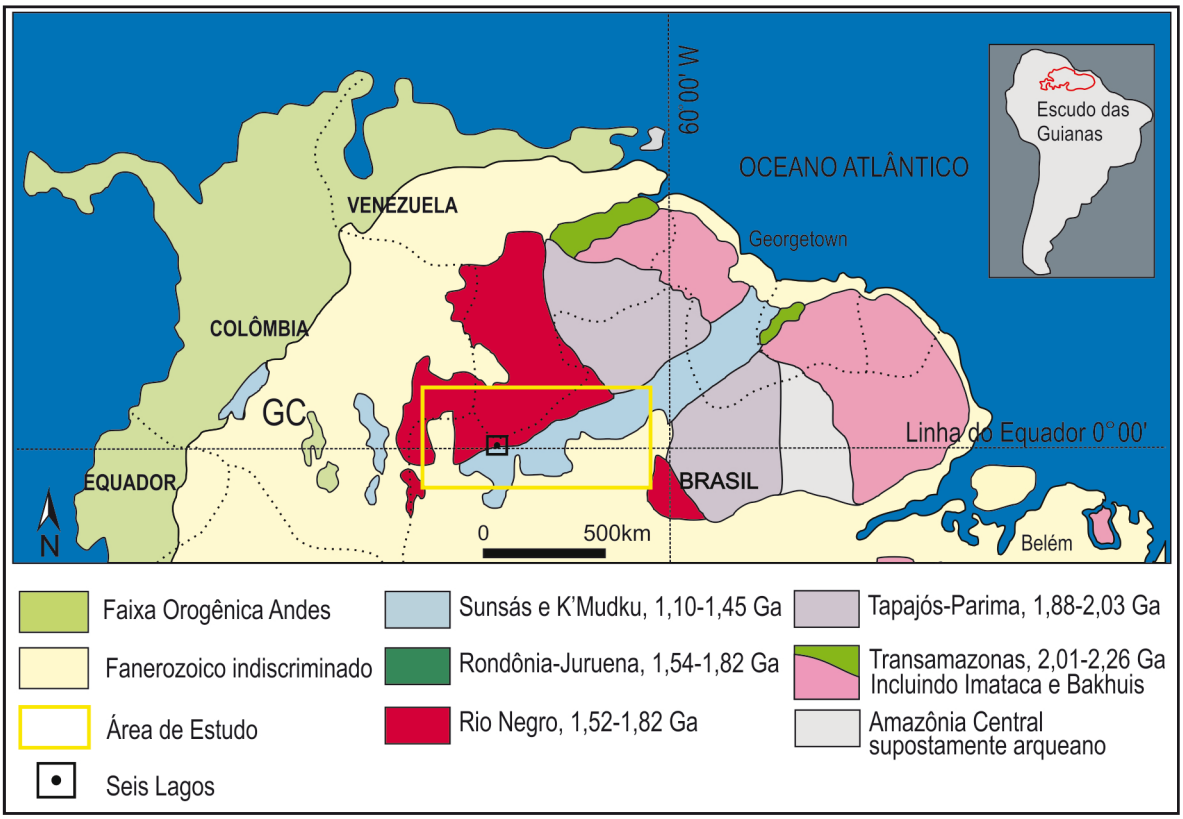

Figura 2. Localização da área estudada neste trabalho dentro do Escudo das Guianas, segundo a proposta de Santos *et al.* (2006).

nitoides proterozoicos. Estes últimos são os mais numerosos, sendo representados por monzogranitos, sienogranitos, granodioritos e granitoides deformados. Os granitos situados ao sul e a sudoeste do CCSL (Fig. 3) pertencem à Suíte Intrusiva Rio Uaupés. O termo granito Rio Uaupés (Dall'Agnol & Macambira, 1992) designa titanita-biotita monzogranitos (tipo predominante) com idade Rb-Sr de 1.459 ± 32 Ma e razão isotópica $^{87}Sr/Sr^{86}$ inicial de 0,070631, formados diretamente a partir de rochas crustais (ou derivado de fonte mantélica, mas fortemente afetado por contaminação crustal) durante evento colisional continental. Santos & Silva (1994, *apud* Souza, 2009), consideram tratar-se de uma suíte metaluminosa, cálcio-alcalina expandida (tipo-I cordilheirano), com evidências de acresção mantélica direta. Santos *et al.* (2000) relatam a dificuldade em distinguir esta suíte do

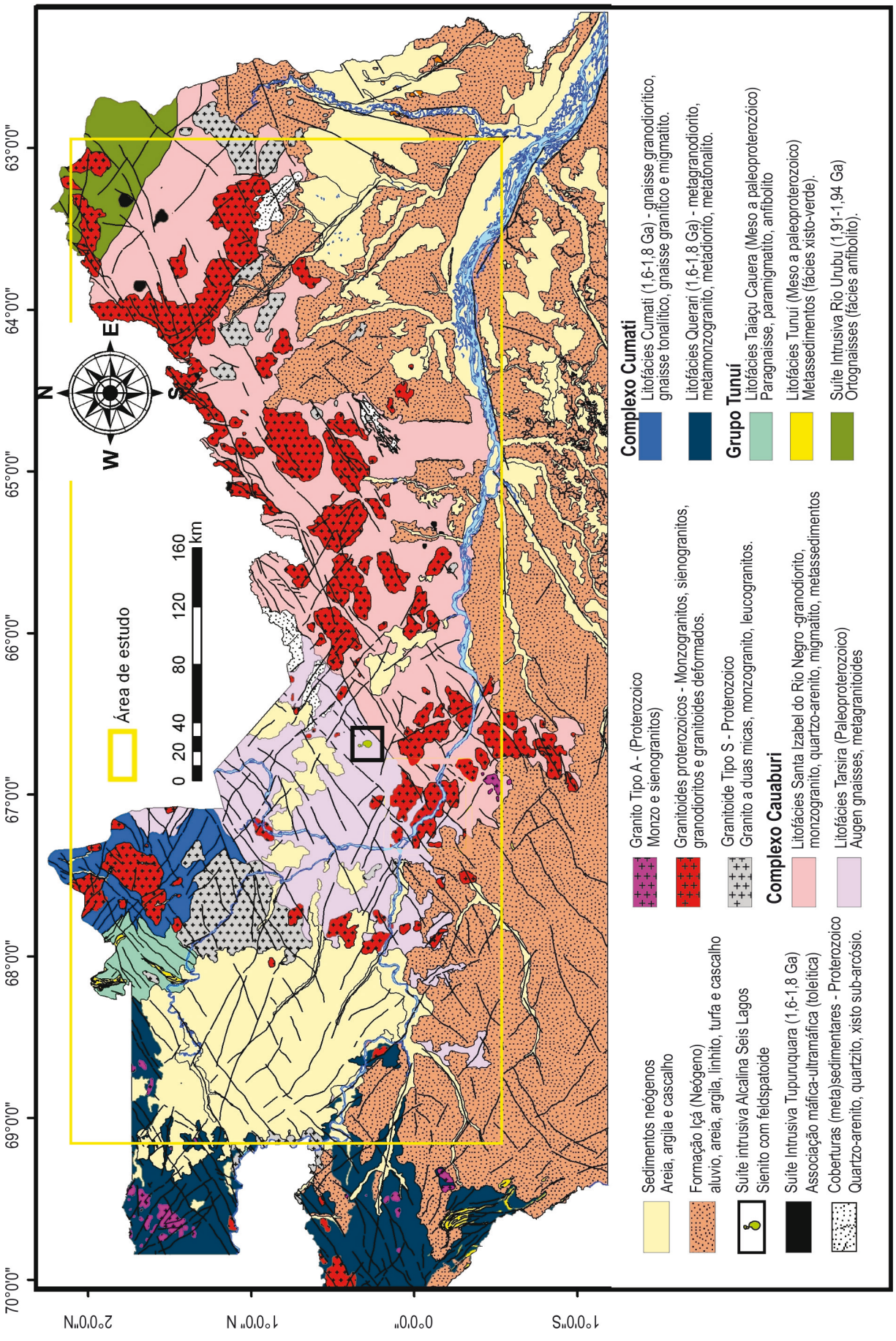

Figura 3. Mapa geológico da Província Rio Negro (modificado de Souza, 2009).

embasamento devido às similaridades químicas e mineralógicas e aos granitos serem sintectônicos e terem sido posteriormente cisalhados localmente pelo evento K'Mudku (1,2 Ga). Por outro lado, Souza (2009) caracterizou o Granito São Gabriel da Cachoeira, pertencente a esta suíte, como gerado por fusão parcial de uma fonte transamazônica dominantemente crustal, em ambiente de colisão em 1,5 Ga, e afetado por evento deformacional responsável pelas foliações (S_0 e S_1) com direção NE e por cisalhamentos transcorrentes de mesma orientação, com idade próxima à idade de cristalização do granito, uma vez que se trata de um granito sintectônico à deformação regional. Quanto à atuação de eventos posteriores à colocação do granito, o referido autor admite que possam ter ocorrido, mas destaca a necessidade de mais estudos, inclusive no que tange ao evento K'Mudku, do qual pouco se conhece e não há consenso sobre sua idade, temperatura e estruturação.

2.2 Complexo Carbonatítico Seis Lagos

O complexo é composto por três estruturas aproximadamente circulares. A feição morfológica do MSL possui comprimento de 5 km (na direção N-S) e largura de 4,50 km (na direção E-W), enquanto que as estruturas menores apresentam diâmetros de 0,75 km e 0,50 km, respectivamente. No MSL, o relevo é pseudo-cárstico, com diversas depressões por colapso, algumas das quais originaram lagos.

Segundo Pinheiro *et al.* (1976), o posicionamento do complexo deve-se à reativação de antigas fraturas que obedecem a um controle estrutural dado pela interseção de dois lineamentos segundo as direções NW-SE e NE-SW, respectivamente. O depósito está associado a uma crosta laterítica formada pela alteração do carbonatito. Duas campanhas de sondagens foram realizadas (CPRM, 1976; CPRM, 1983), mas não se conhece a espessura total da crosta, já que os furos não a atravessaram totalmente; o mais profundo dos furos na crosta (SG-01-AM) foi interrompido na profundidade de 255m. O furo mais profundo no CCSL (SG-04-AM, com 492 m) foi realizado numa bacia de origem cárstica, onde não ocorreu a formação de crosta laterítica.

Corrêa (1996) e Corrêa & Costa (1997) efetuaram as primeiras investigações científicas no MSL, focando na mineralogia da crosta laterítica, na qual identificaram hematita e ghoetita, como os minerais mais abundantes, e hollandita, romanechita, pirolusita, lithioforita, florencita, cerianita, gibbsita, ilmeno-rutilo, brookita niobífera e rutilo niobífero, além de monazita, zircão e quartzo. A origem da crosta foi interpretada como produto de alteração de rocha carbonatítica, corroborando a proposta original da CPRM (1976). Giovannini (2013) subdivide a crosta em 6 tipos texturais/composicionais, identificou como siderita carbonatito a rocha carbonática encontrada, que havia sido tentativamente classificada como beforsito (Pinheiro *et al*., 1976) e descreve, nesta rocha, os minerais siderita, barita, gorceixita, monazita e pirocloro. Não há dados de datação do carbonatito, de modo que a idade mesozoica proposta (Pinheiro *et al*., 1976; CPRM, 2006) baseia-se em correlações com diques de diabásio da região ou com corpos alcalinos situados mais a leste.

2.3 Métodos

O estudo foi iniciado numa área de 650 km (E-W) por 300 km (N-S), indicada na figura 3. Subsequentemente, o estudo focou o CCSL e suas proximidades.

Para elaboração do modelo digital de elevação (MDE) foram utilizadas nove imagens do projeto Topodata, de 1° de latitude por 1,5° de longitude, cada, obtidas através do site do INPE (INPE, 2012). O Projeto Topodata oferece o Modelo Digital de Elevação (MDE) e suas derivações locais básicas em cobertura nacional, ora elaborados a partir dos dados SRTM (*Shuttle Radar Topography Mission*) disponibilizados pelo USGS na rede mundial de computadores (para mais detalhes ver Valeriano & Rossetti, 2012). Através do *software* ENVI 4.5, foi gerado o mosaico das nove imagens que foram processadas com o *software Global Mapper*, utilizando a variável ZN, que corresponde aos valores de elevação do Topodata e sombreamento com aplicação de luz com azimute 45° e inclinação de 45°, gerando um amplo mosaico, no qual, a cada intervalo altimétrico, foi atribuída uma cor, conforme a paleta de cores que acompanha as respectivas figuras do trabalho. O propósito deste MDE foi salientar as morfoestruturas da área de estudo, principalmente no embasamento cristalino, e realçar outros corpos passíveis de serem interpretados como análogos ao MSL. O mapa de morfoestruturas (lineamentos) foi gerado com base no mapa estrutural da CPRM e adensado em informações pela definição de lineamentos visualizados sobre o mosaico. Este processo foi realizado com auxilio do software ArcGis. Os mapas geológicos foram confeccionados a partir do mapa geológico da CPRM (2006), na escala 1:1.000.000 georreferenciado pelo datum WGS 84. Utilizando o software ArcGis, o mapa e o modelo digital de elevação

foram sobrepostos e recortados de acordo com a área proposta para o trabalho, definida a partir do mosaico de imagens Topodata.

Os mapas geofísicos (aeromagnetométrico, aerogamaespectométrico e de anomalia Bouger) constam no mapa do Estado do Amazonas na escala 1:1.000.000 (CPRM, 2006). Eles foram sobrepostos, por transparência, aos mapas geológico, estrutural e ao mosaico gerado através dos arquivos Topodata. A região estudada se enquadra no domínio da Anomalia Magnética do Atlântico Sul, onde o campo magnético apresenta a menor intensidade de todo o globo e próxima do equador magnético, onde o campo magnético é aproximadamente horizontal.

Uma imagem de alta resolução do satélite SPOT 4, com pixel de 10 m foi utilizada para fins de detalhamento morfoestrutural da área do CCSL e análise de feições espectrais anômalas, cujo contraste permite a identificação de regiões de concentração de argilominerais, indicativos de possíveis zonas de alteração hidrotermal e também passíveis de concentrarem elementos terras raras. A área de estudo corresponde a um quarto da imagem original obtida pelo satélite, totalizando 225 km^2, em composições coloridas falsa cor, cujas bandas espectrais correspondem aos comprimentos de onda do verde, vermelho, infravermelho próximo (IVP) e infravermelho de ondas curtas (IVOC). Os comprimentos de onda (λ) são, respectivamente: 0,540; 0,650; 0,835; e 1,630 μm. O pré-processamento foi efetuado pelo método de ortorreferenciamento que gerou uma acuidade visual da ordem de 10 m em seu georreferenciamento e na projeção UTM, DATUM WGS84.

A sequência de processamentos foi efetuada pelo software ENVI 4.5, constando de: (a) recorte da imagem; (b) ajuste do "*stretch*" com redistribuição dos níveis de cinza da imagem nos 256 níveis possíveis, respeitando a proporcionalidade entre os níveis da imagem original (o *stretch* da imagem foi definido em 3%); (c) tratamentos através de filtros diversos (passa alta, passa baixa, laplaciano, gausiano, mediano, Sobel e Roberts). O melhor resultado foi obtido com o filtro de convolução direcional utilizando máscaras 3x3 em intervalos de 15°, partindo de 0° até 180°. Os diversos filtros foram empregados separadamente para cada banda da imagem e os melhores resultados foram alcançados nas bandas 3 (IVP) e 4 (IVOC); (d) combinações e análise de diferentes bandas espectrais gerando composições coloridas.

Entre as diversas combinações de bandas espectrais testadas, o melhor resultado foi alcançado através de combinação falsa cor, RGB, 234, na qual a banda 2 (banda do vermelho) é bastante destacada pela presença de ferro, a banda 3 (banda do infra vermelho próximo), bastante reflexiva pela vegetação, apresenta a cor verde, e a banda 4 (banda do infra vermelho de ondas curtas), na qual as argilas apresentam alta reflectância e aparecem na imagem em tons de azul. Tendo em vista a influência da posição do sol e a possibilidade da sobreposição de cores primárias gerando diferentes colorações no pixel, pode-se interpretar as cores da imagem colorida RGB como: verde representando a vegetação; vermelho, a crosta laterítica e áreas com concentração de ferro; e azul, as argilas.

3 Resultados

A maior parte da área de estudo é ocupada por uma planície de baixa altimetria, com pouca variação, não ultrapassando os 150 m em média (Fig. 4). Os terrenos de cota mais elevada (em vermelho) formam uma faixa fortemente orientada na direção NE-SW, sugerindo que esta pode tratar-se de um "bloco", limitado por estruturas com esta direção. Nesta faixa, ocorrem rochas do embasamento, granitos e metassedimentos (áreas mais altas, frequentemente acima de 2.000 m), de modo que a sua estruturação é bem mais complexa. Como observado por CPRM (2006), a direção NW-SE é menos frequente, mas onde ocorre é muito marcante, como no alinhamento da Serra Curupira. A extremidade sudoeste da faixa de direção NE-SW parece ser delimitada por um lineamento de direção NW-SE e outro de direção E-W (Fig. 4). O CCSL situa-se no prolongamento da faixa para SW e no prolongamento, para oeste, do alinhamento E-W que marca o seu limite sul. Observa-se na figura 4 que o sistema de drenagem da área, tanto pelo rio Negro, como pelos rios de 2ª e 3ª ordens, é fortemente orientado, havendo grande predomínio da direção E-W. A borda da bacia sedimentar do rio Solimões também tem forte orientação segundo a direção E-W.

O mapa gravimétrico (CPRM, 2006) não se mostrou eficiente para identificação de estruturas na área de estudo. Na área onde se situa o CCSL ocorre uma ausência de dados, claramente omitidos do mapa aerogamaespectométrico do Estado do Amazonas (CPRM, 2006). Não foi encontrada nas demais partes da área de estudo nenhuma anomalia positiva com a intensidade esperada (5.000 a 15.000 cps, conforme Pinheiro *et al*., 1976) para corpos semelhantes aos do CCSL.

O mapa aeromagnetométrico (relevo sombreado) (Fig. 5) mostrou-se altamente eficaz, com grande capacidade de separação de terrenos com

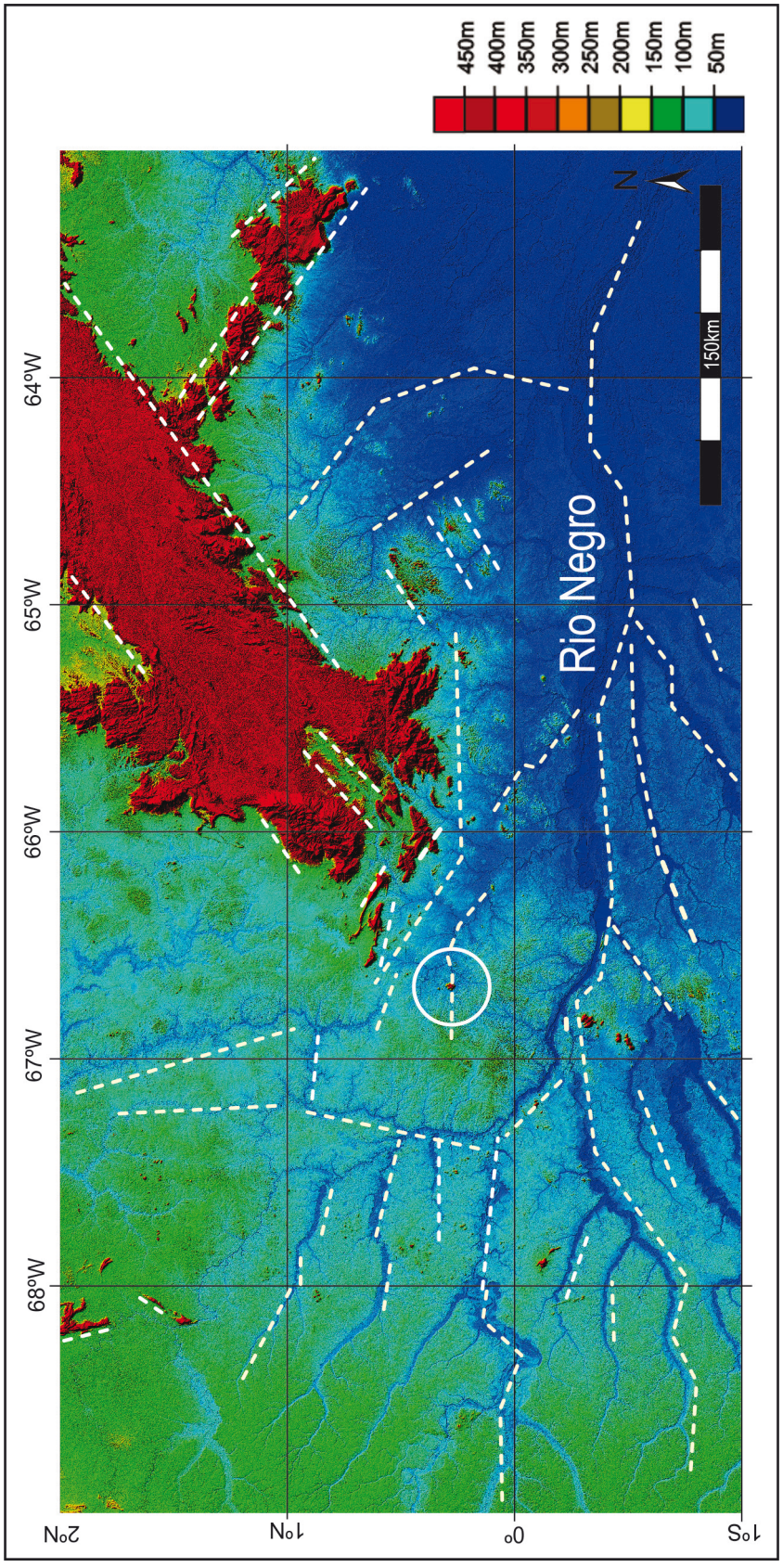

Figura 4. Modelo digital de elevação da área de estudo (localização na figura 3). Observa-se: a faixa de orientação NE-SW, onde ocorrem os terrenos de maior altitude; o possível alinhamento E-W no limite sul da faixa e; o forte controle das drenagens de 1ª, 2ª e 3ª ordens segundo a direção E-W. O círculo marca o Complexo Carbonatítico Seis Lagos.

respostas distintas. O CCSL situa-se exatamente no limite entre um domínio de alta intensidade magnética, a norte, e um domínio de baixa intensidade, a sul. Este limite tem uma direção geral E-W e pode ser seguido continuamente por mais de 400 km (Fig. 5A). No trecho onde se situa o CCSL e mais a oeste deste (Fig. 5B), o contato entre os dois domínios é muito abrupto e faz inflexões alternadas para ENE-WSW e ESE-WNW, sugerindo um contato por falhamento. Na litofácies Santa Izabel do Rio Negro, o domínio de alta intensidade magnética poderia corresponder a uma série de corpos graníticos que em superfície (Fig. 3) ocorrem muito próximos uns dos outros e, em subsuperfície, podem ter continuidade e fazer parte de um batólito alongado segundo a direção E-W. O domínio de baixa intensidade magnética corresponderia às rochas gnáissicas. Além disso, a posição da interface coincide com o alinhamento E-W que marca a extremidade sul da faixa de terrenos de maior altitude. É interessante notar que a faixa K'Mukdu faz uma inflexão para E-W na área próxima ao CCSL (Fig. 2). Não se observa nenhuma indicação no mapa geológico (Fig. 3) do que poderia corresponder a esta interface geofísica na litofácies Tarsira.

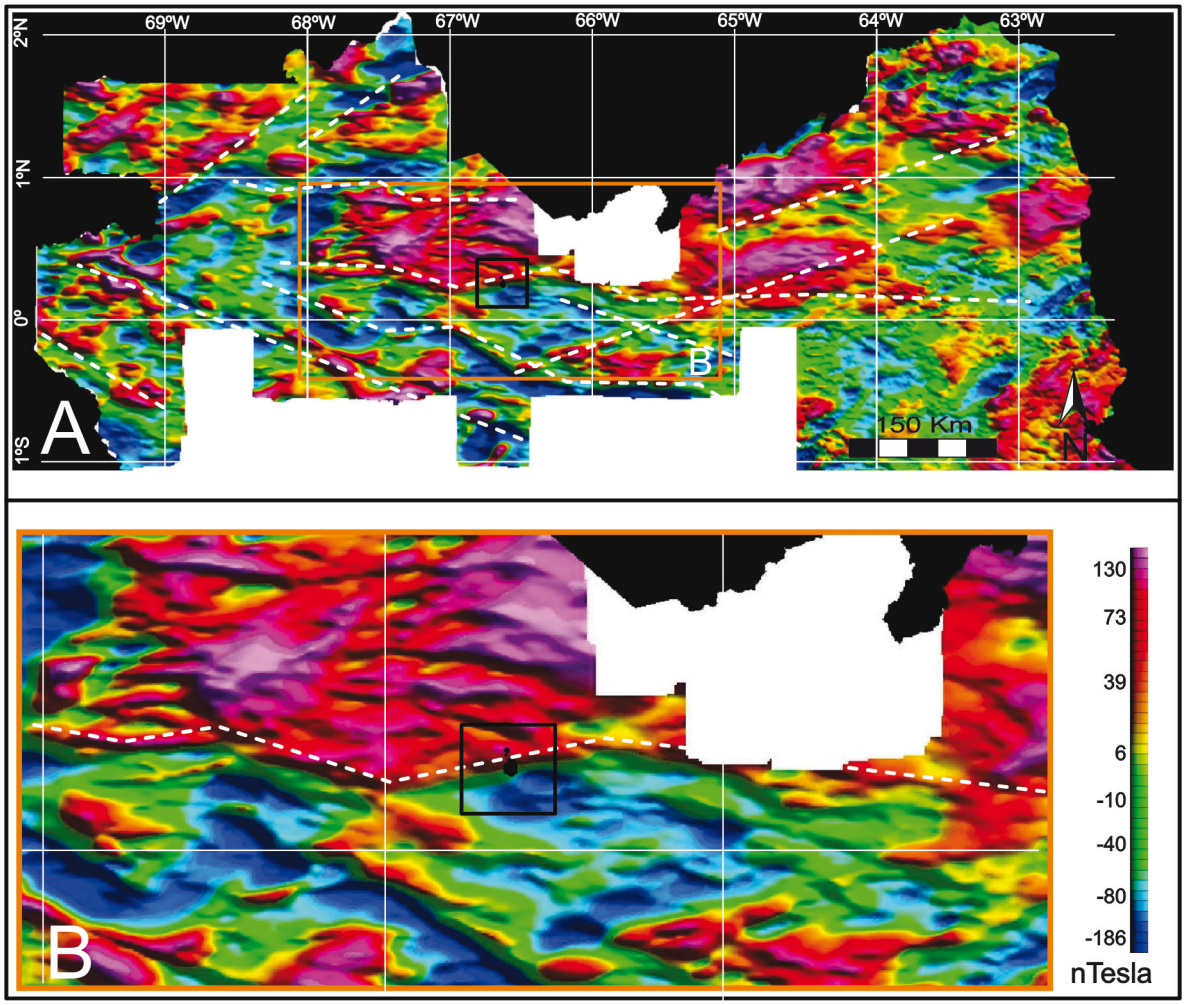

Figura 5. Mapa aeromagnetométrico (relevo sombreado), extraído de CPRM (2006). A) Área de estudo, observando-se a localização do CCSL (quadrado preto) sobre um lineamento de direção geral E-W que delimita dois domínios de intensidades magnéticas muito contrastantes; B) Área no entorno do complexo, observando-se as inflexões do lineamento alternadas para ENE-WSW e ESE-WNW, e o caráter muito abrupto da interface magnética.

As direções de morfoestruturas mais frequentes na área maior são NE-SW e NW-SE, e, subordinadamente, NNW-SSE e E-W (Fig. 6). Nesta figura, se observa duas faixas (destacadas pelo tracejado) nas quais as morfoestruturas de direções NW-SE e NE-SW ocorrem com maior densidade. A faixa de direção NE-SW coincide aproximadamente com o limite entre as litofácies do Complexo Cauaburi, Santa Izabel do Rio Negro (a SE da faixa) e Tarsira (a NW da faixa), observado no mapa geológico (Fig. 3). Nota-se uma menor densidade de morfoestruturas na porção da área a SE desta faixa, em relação à região a NW da mesma. Não é possível atribuir com certeza esta distinção a diferenças estruturais, pois a porção da área onde a densidade de morfoestruturas é menor tem cotas mais baixas

(Fig. 4), sendo, portanto, mais suscetível a inundações do rio Negro e seus afluentes, o que pode implicar o maior mascaramento dos lineamentos por sedimentos fluviais.

No entorno do CCSL (Fig. 7A), as morfoestruturas mais destacadas têm direção E-W; também ocorrem morfoestruturas NE-SW e WNW-ESE. Todas são marcadas principalmente pelos rios, cujos traçados altamente lineares indicam seus controles por falhas e fraturas. O corpo do morro dos Seis Lagos e um dos corpos menores situam-se, respectivamente, sobre os traços das duas principais estruturas da área, ambas de direção E-W (Fig. 7A). A estrutura mais ao sul controla um rio que, ao se aproximar do Morro dos Seis Lagos, circunda a parte sul do morro e, após contorná-lo, retoma a sua direção original, exatamente no prolongamento da mesma estrutura (Fig. 7). Na imagem de maior detalhe (Fig. 7B) observa-se que esta estrutura tem uma expressão muito clara dentro do corpo, controlando feições topográficas internas ao mesmo. Estas estruturas de direção E-W devem corresponder à expressão superficial do lineamento E-W identificado no mapa aeromagnetométrico (Fig. 5). As estruturas de direção NE-SW e NW-SE se enquadram nas duas faixas mostradas na figura 6 e devem ter exercido controle local no posicionamento dos corpos do complexo.

Na figura 7 observa-se que o formato circular/ovalado do MSL é conferido pelo contorno do seu sopé (verde brilhante no modelo digital de elevação). Em cotas mais elevadas (cores amarelo e vermelho), entretanto, o contorno é mais irregular e, no detalhe (Fig. 7B), observa-se uma forma mais semelhante a um polígono. O morro tem bordas abruptas e lineares em todos os lados do polígono, com exceção da borda NW, a qual também teve, presumivelmente, um caráter abrupto e linear na direção NE-SW, mas apresenta-se atualmente irregular, devido à existência de vales controlados por estruturas de direção NNW-SSE. A imagem SPOT (Fig. 8) confirma que o relevo no interior do morro é principalmente controlado por estruturas de direção NNW-SSE. Uma das raras exceções é dada pela estrutura de direção E-W que atravessa a parte sul do corpo. Na figura 8 - na qual a imagem SPOT foi tratada através de filtro linear, salientando estruturas de direção azimutal próximas a 150° e utilizando a banda 3 (IVP) – observa-se a grande frequência de estruturas NNW-SSE sobre o morro e também nas suas cercanias.

A composição de bandas espectrais RGB 234 (Fig. 9) possibilitou definir com precisão os limites da crosta laterítica ferruginosa. O corpo principal de laterita ferruginosa cobre uma área de cerca de 8 km^2. Alguns limites coincidem com aqueles inferidos a partir do modelo digital de elevação (Fig. 7B), como ocorre na borda SW, fortemente orientada na direção NW-SE, e na borda SE, orientada na direção NE-SW. Na borda E, ocorre um "corpo" alongado, aparentemente separado do corpo principal, que também é rico em Fe, mas com tom mais fraco do que o observado no-interior do corpo principal, podendo corresponder, portanto, a uma zona de laterita desenvolvida sobre a encaixante gnáissica. Configuração semelhante ocorre na borda norte, onde o "corpo" isolado tem uma orientação aproximadamente E-W. A reentrância

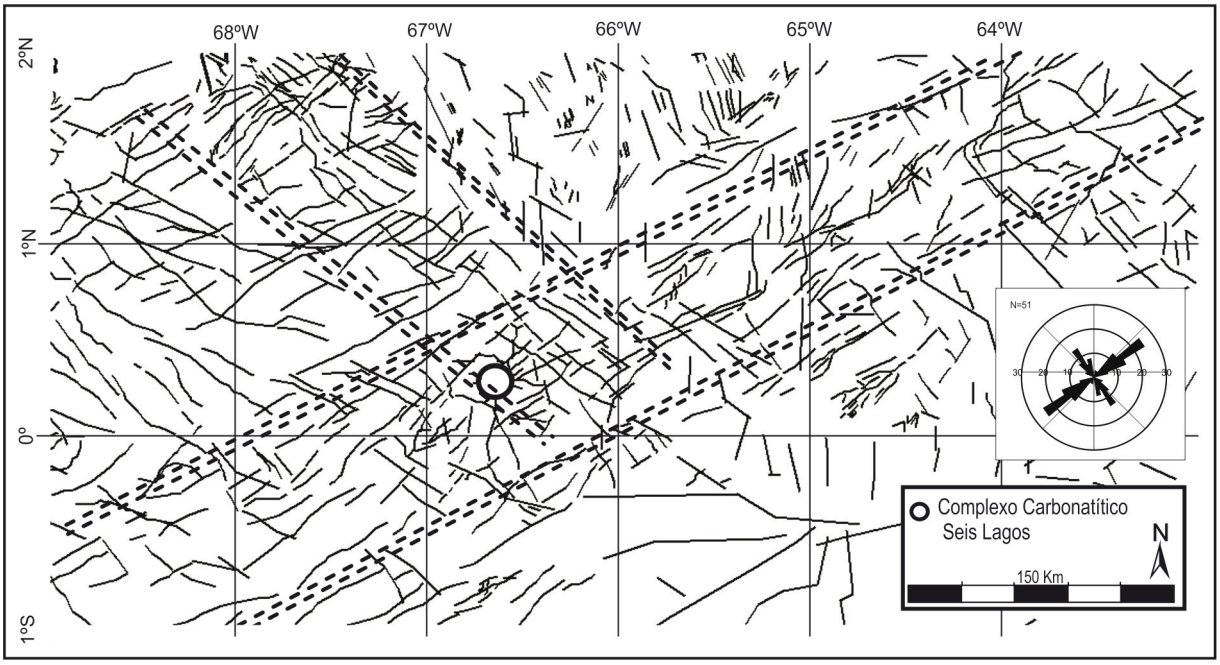

Figura 6. Principais morfoestruturas da área de estudo (retângulo amarelo da figura 3).

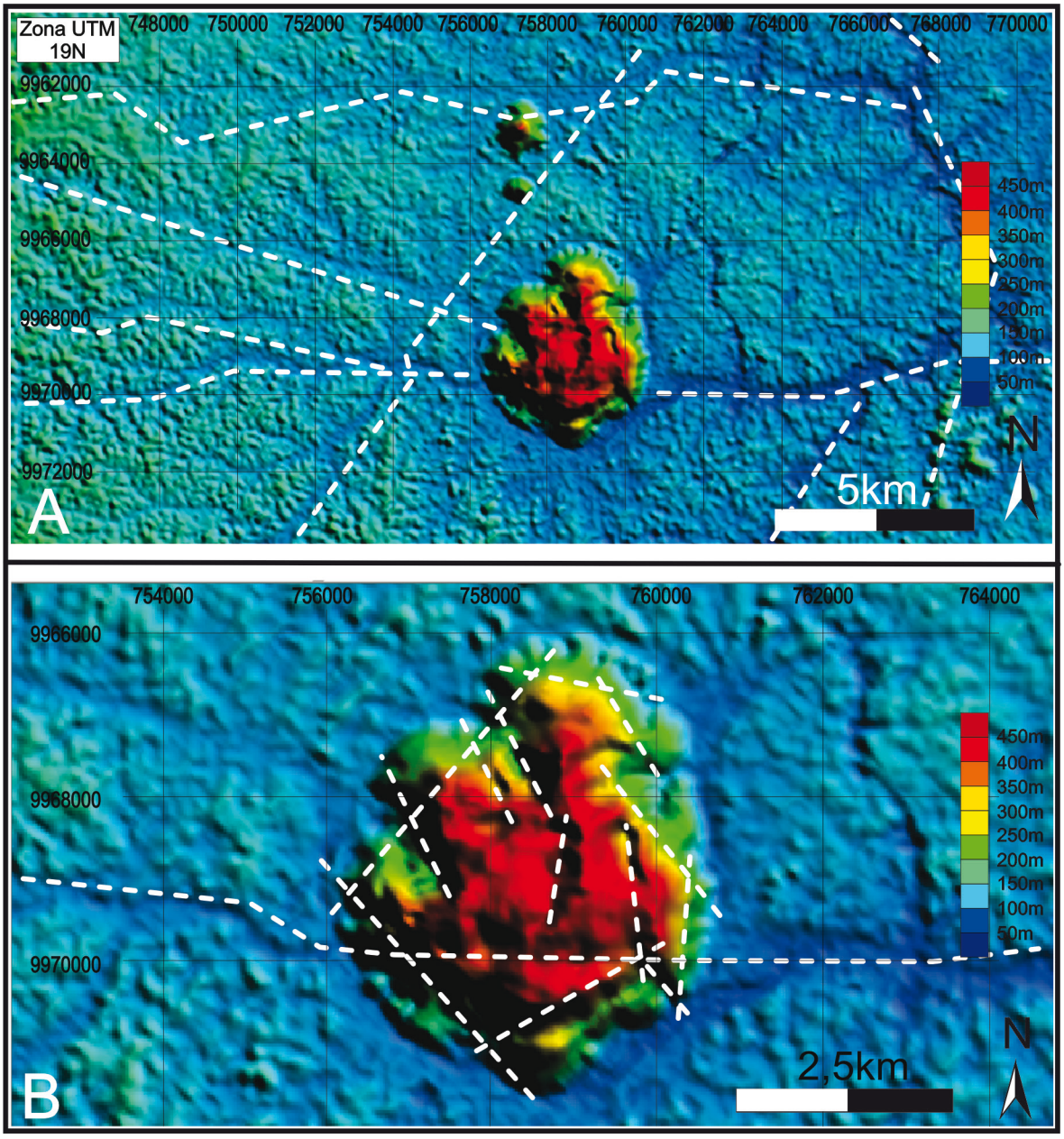

Figura 7. Principais morfoestruturas no entorno do Complexo Carbonatítico Seis Lagos (A) e no Morro dos Seis Lagos (B).

existente na borda NW está associada à erosão da laterita com a formação de um vale controlado por estrutura de direção NNE-SSW.

As áreas onde a resposta espectral é característica de argilas não ocorrem de forma destacada e apenas com uma análise cuidadosa é possível identificá-las (Fig. 9). Porém, a associação destas áreas com as estruturas é bem evidenciada pelas suas localizações e pelas suas formas alongadas (com exceção daquela marcada por um círculo) na mesma direção NNW-SSE ou N-S das estruturas (comparar com Fig. 7B). Adicionalmente, observa-se que pelo menos três dos lagos e algumas das depressões existentes sobre o morro parecem fazer parte destes alinhamentos, indicando que os processos cársticos, formadores dos lagos foram, pelo menos em parte, controlados pelas estruturas NNE-SSE a N-S. A figura 9 foi gerada através do tratamento da imagem do satélite SPOT, utilizando apenas a banda do IVOC. As elipses marcam as áreas cuja resposta espectral (áreas brancas, representando alta reflectância) indicam a presença de argilas. Quando comparada à figura 10, observa-se que cinco das zonas com argilas se repetem, confirmando, assim, a eficácia das técnicas utilizadas.

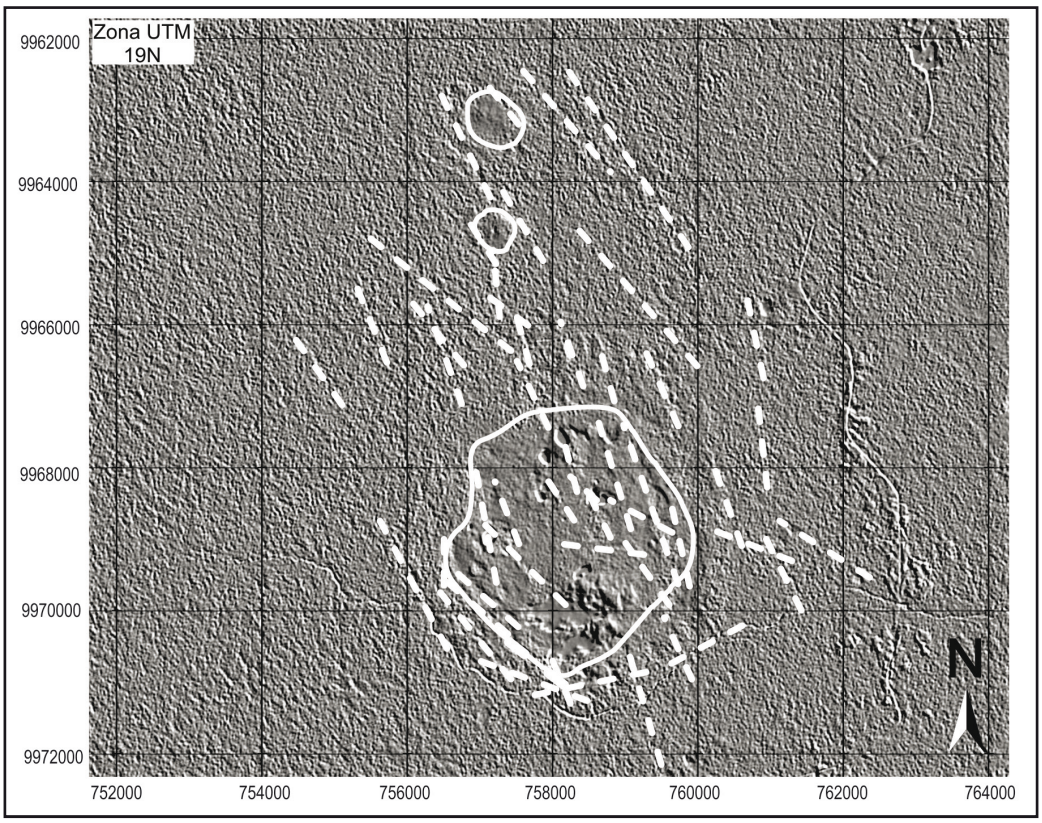

Figura 8. Imagem SPOT da área do Complexo Carbonatítico Seis Lagos tratada através de filtro linear, salientando estruturas de direção azimutal próximas a 150° utilizando a banda 3 (IVP).

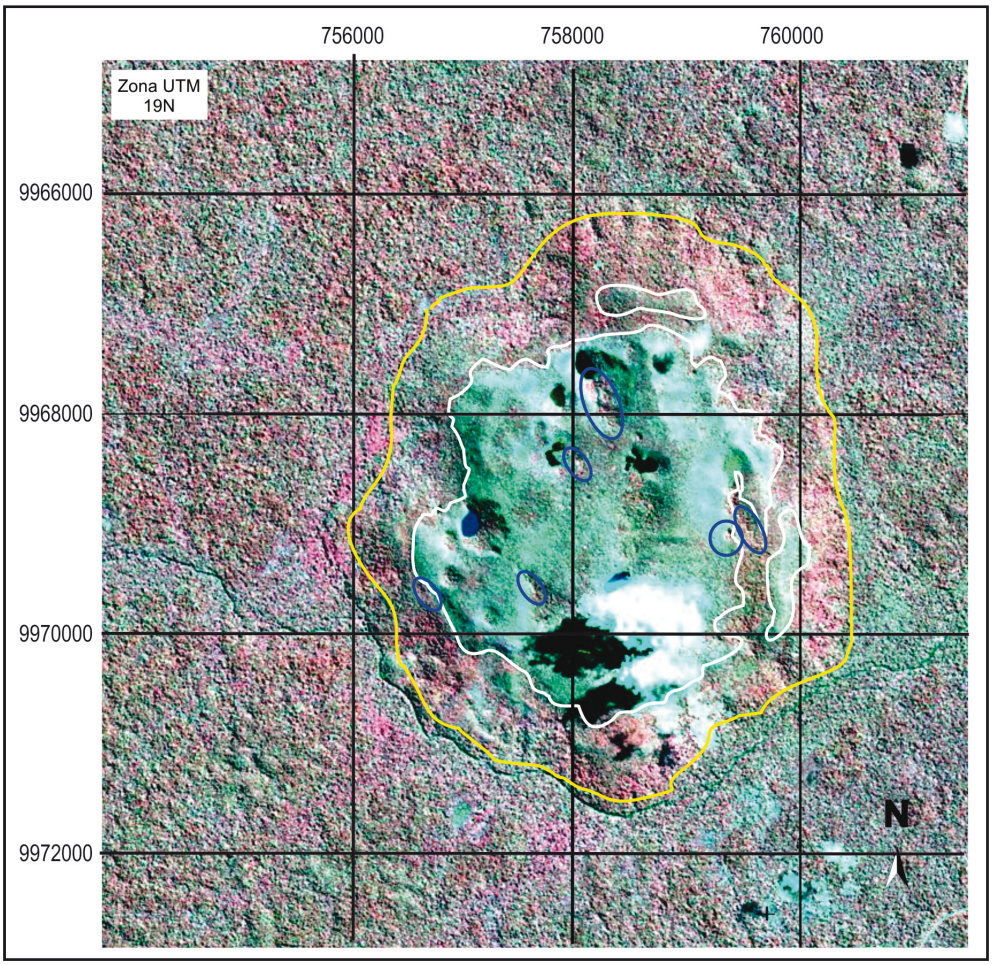

Figura 9. Morro dos Seis Lagos em composição colorida falsa cor sobre a imagem SPOT. A linha amarela delimita o sopé do morro; a linha branca delimita a crosta laterítica; as elipses azuis identificam zonas com resposta espectral característica de argila.

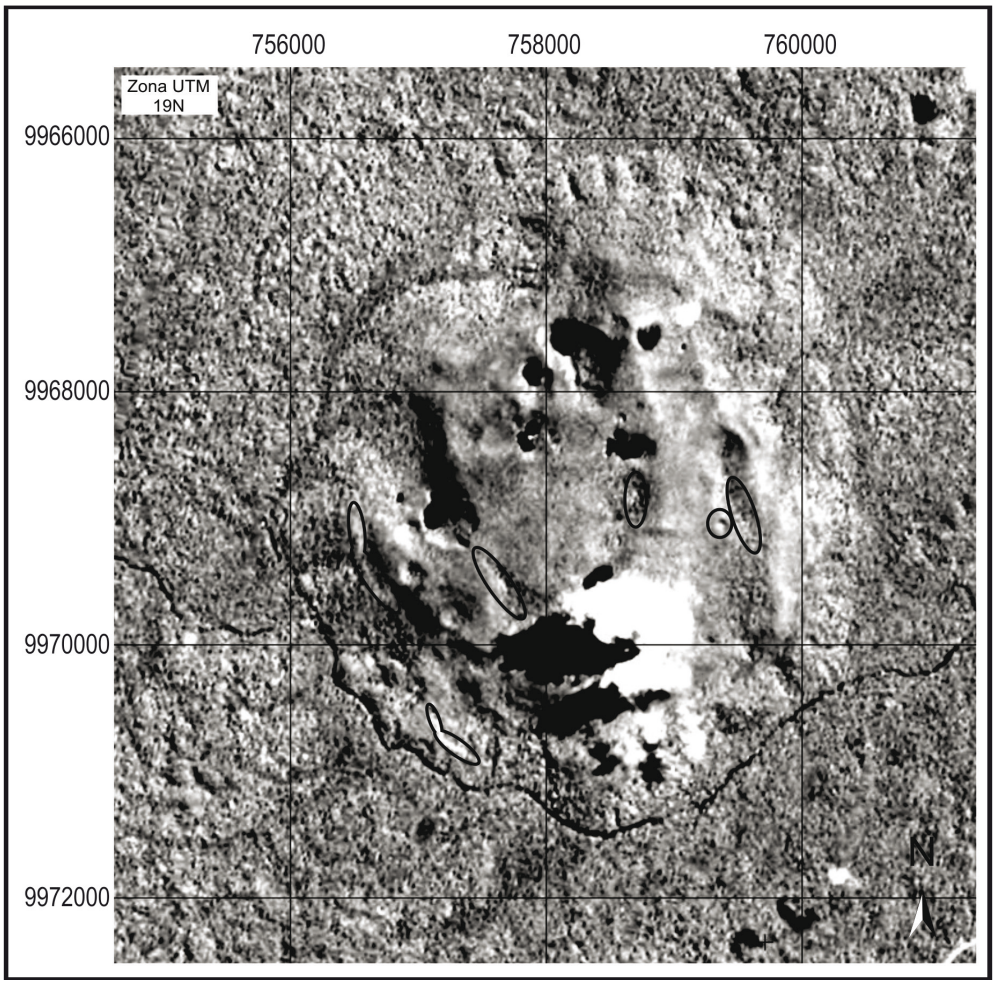

Figura 10. Resposta da imagem SPOT na área do Morro dos Seis Lagos utilizando apenas a banda do infravermelho de ondas curtas. As elipses pretas marcam áreas com resposta espectral indicativa da presença de argila.

4 Discussão dos resultados

4.1 Controle do posicionamento do carbonatito

Segundo os modelos petrogenéticos mais recentes, apoiados por grande número de dados isotópicos, os magmas parentais dos carbonatitos derivam de fontes mantélicas, sejam elas astenosféricas ou litosféricas. O controle principal sobre o posicionamento destes corpos é relacionado a megaestruturas que, muitas vezes, correspondem a descontinuidades crustais associadas a ambiente de rifte. Frequentemente, os corpos carbonatíticos distribuem-se ao longo de alinhamentos, como, por exemplo, aqueles encontrados no sudoeste da África e no oeste dos EUA e Canadá (Chakhmouradian & Zaitsev, 2012). Neste sentido, é muito pertinente a proposta da CPRM (2006), que considera que o CCSL e diques de diabásio do Domínio Alto Rio Negro (correlacionados ao Diabásio Uaraná do Eojurássico ao Neotriássico) podem registrar correspondência com o evento magmático Taiano que antecedeu a instalação do Rifte Tacutu (Reis *et al.,* 2006) no Domínio Guiana Central em Roraima, no prolongamento estrutural NE-SW do Domínio Imeri. Entretanto, não se conhece a idade do CCSL. Alternativamente, poder-se-ia aventar uma ligação do CCSL com os corpos carbonatíticos Maicuru e Mutum que estão aproximadamente alinhados na direção E-W com o CCSL, porém estes possuem idades muito distintas entre si, respectivamente: 586 ± 18 Ma (Lemos & Gaspar, 1998) e 1.0 Ga (Gomes *et al.*, 1990). Assim, enquanto a idade do CCSL não for conhecida, seu enquadramento em qualquer contexto geotectônico e/ou sua ligação com outro corpo carbonatítico são conjecturais.

Desde os trabalhos pioneiros do RADAM e CPRM, o controle do posicionamento do CCSL tem sido atribuído a estruturas de direção NE-SW e/ou NW-SE. De fato, o CCSL situa-se na intersecção de duas grandes estruturas com essas respectivas direções. Entretanto, a maior estrutura da região do CCSL é aquela de direção E-W e extensão de, pelo menos, 400 km, interpretada a partir dos mapas aeromagnetométrico e cuja existência é sustentada pelas evidências aqui apresentadas. A forte orientação do sistema de drenagem segundo a di-

reção E-W (tanto pelo rio Negro, como pelas drenagens de 2ª e 3ª ordens) e a orientação E-W da borda da bacia sedimentar do Solimões sugerem a existência na região de grandes estruturas com esta direção. Trata-se provavelmente de estruturas de idade proterozoica que podem ter sido diversas vezes reativadas (inclusive após o posicionamento do CCSL). É possível que esta estrutura seja relacionada ao evento K'Mudku, cuja faixa de ocorrência faz uma inflexão na direção E-W na região de estudo (Fig. 2). Sugere-se que o controle principal do posicionamento do CCSL foi exercido pela estrutura E-W e que, ao longo desta, a intrusão alojou-se onde ela é intersectada, no mesmo local, pelas faixas de estruturas de direção NE-SW e NW-SE.

O processo de laterização implica a remoção de elementos e, consequentemente, uma importante redução de volume. Nos casos de Mount Weld (Lottermoser, 1990) e Mrima Hill (Coetzee & Edwards, 1960) estimou-se que de cinco a dez volumes de carbonatito foram intemperizados para produzir um volume de laterita. No MSL, pode-se inferir uma redução da ordem de dez vezes, levando-se em conta os enriquecimentos médios de Nb e de Ti em relação ao carbonatito (Giovannini, 2013). Assim, a espessura mínima de 250m para a crosta de Seis Lagos implica a lateritização de uma "coluna" de carbonatito da ordem de 2,5km de altura.

4.2 Forma e estrutura interna do carbonatito e implicações metalogenéticas

Os limites da crosta laterítica delineados neste trabalho devem representar, de forma mais precisa, o formato original da intrusão, o qual contrasta com a forma circular do Morro dos Seis Lagos, cujo perímetro é hoje definido pelos depósitos de tálus. Os limites marcantemente retilíneos de boa parte da crosta sugerem que a forma do corpo carbonatítico seja controlada por estruturas rúpteis (falhas ou fraturas). Estas estruturas podem representar as paredes do conduto magmático, aberto, seguindo falhas e fraturas, ou podem ser falhas que afetaram o corpo após sua cristalização. Ao nível atual do conhecimento, não é possível discernir onde se aplica cada tipo.

A principal estrutura identificada no MSL situa-se na sua parte sul e coincide com o prolongamento, para dentro do corpo, da estrutura E-W que foi interpretada como a principal controladora da intrusão. A reativação desta estrutura formou internamente ao corpo uma crista acompanhada de um vale, ambos paralelos à direção E-W (Fig. 7B). As demais estruturas identificadas têm direção NNW-SSE e, subordinadamente, N-S, e a elas estão associados vales e cristas com estas direções. Portanto, estas falhas controlaram processos erosivos que contribuíram para o modelamento do relevo. Entretanto, num carbonatito, outros fatores condicionam a evolução do relevo. Durante a lateritização, ocorre a remoção de elementos mais móveis e o consequente enriquecimento relativo em elementos menos móveis. O processo gera espaços vazios e o material pode perder a sustentação e colapsar. Além disto, em um carbonatito, pode ocorrer processos cársticos e consequente formação de relevo deste tipo. Os carsts aumentam muito a porosidade e a permeabilidade da rocha, fazendo com que a frente de lateritização atinja profundidades muito maiores do que em outras rochas. Assim, a formação dos carsts no carbonatito também pode ser guiada por falhas e fraturas. Consequentemente, a lateritização e o colapso também podem ser fortemente influenciados por estruturas. Isto significa que as estruturas que afetam o corpo de Seis Lagos possivelmente balizam zonas onde a laterita é mais espessa e/ou mais rica em Nb e ETR.

Outro interesse da identificação de estruturas relaciona-se com o hidrotermalismo, o qual pode ser muito acentuado em carbonatitos, originando o carbohidrotermalismo (Chakhmouradian & Zaitsev, 2012), através do qual elementos e compostos químicos de interesse econômico podem formar acumulações anômalas. Em corpos carbonatíticos é relativamente comum a formação de fluorcarbonatos de ETR, como a synchysita e a parisita, em zonas mais fortemente hidrotermalizadas (Ruberti *et al.*, 2008). Nestas zonas, os silicatos podem ter sido alterados para minerais de argila, razão pela qual foram utilizadas técnicas de sensoriamento remoto, capazes de separar os alvos terrestres através das diferentes respostas de absorção e reflectância das ondas detectadas pelos satélites e radares orbitais, identificando assim as regiões com concentrações de argilominerais. Neste trabalho foram identificadas oito zonas com reflectâncias típicas de argilas. A associação destas zonas com estruturas é muito evidente: as quatro zonas de argilas situadas internamente ao corpo estão associadas a quatro estruturas NNW-SSE, cada uma destas, por sua vez, perfeitamente alinhada com um lago ou depressão; duas zonas localizam-se na borda SW, justamente a borda mais retilínea e supostamente controlada por falha. Estas quatro estruturas representam, portanto, locais a serem investigados detalhadamente em futuros trabalhos no MSL.

5 Conclusões

O posicionamento dos corpos do CCSL teve como controle principal uma estrutura de direção geral E-W, com uma extensão de cerca de 400 km, ao longo do Domínio Imeri. Na litofácies Tarsira, a estrutura se expressa em superfície na forma de falhas de direção E-W, com traços bem definidos, sobre os quais se localizam os dois maiores corpos do complexo. Ao longo desta estrutura E-W, o posicionamento dos corpos ocorreu onde ela é intersectada, no mesmo local, por duas faixas de estruturas de direção NE-SW e NW-SE.

Os limites da crosta laterítica aqui definidos devem representar o formato original do corpo no nível estrutural atualmente exposto, o qual corresponde a uma profundidade mínima de 2,5 km. Estes limites são em grande parte retilíneos, sugerindo estruturas rúpteis, sejam estas as paredes do conduto magmático, aberto seguindo falhas e fraturas, ou falhas que afetaram o corpo após sua cristalização. A principal estrutura interna ao corpo relaciona-se diretamente à própria falha E-W que controlou seu posicionamento, a qual foi reativada e formou uma crista acompanhada de um vale, ambos paralelos à direção E-W. O corpo foi também afetado por diversas falhas de orientação NNW-SSE, que também controlaram a formação de vales e cristas paralelos às mesmas, assim como os processos cársticos que formaram alguns dos lagos. Consequentemente, essas estruturas exerceram um papel relevante durante o processo de lateritização que formou o depósito de Nb a partir do carbonatito. Portanto, estas estruturas representam zonas onde pode ter ocorrido a formação de laterita mais espessa e mais enriquecida em Nb (e ETR). Em quatro destas estruturas foram identificadas zonas ricas em argilas, cuja formação pode ter sido relacionada a processos hidrotermais os quais, por sua vez, também podem contribuir para um enriquecimento do minério ao longo das estruturas NNE-SSW. Estas representam, portanto, zonas que devem ser investigadas mais detalhadamente em trabalhos futuros no MSL.

Agradecimentos- Os autores agradecem ao CNPq (proc. 483191/2010-8 e proc. 485415/2012-7) pelo apoio ao projeto, ao geólogo Antonio Gilmar de Souza (CPRM) pela colaboração e aos revisores pelas valiosas contribuições. Este trabalho é dedicado ao geólogo da CPRM Mateus Marcili dos Santos Silva (*in memoriam*).

Referências

Almeida, M.E., Macambira, M.J.B., Reis, N.J., Luzardo, R. & Pinheiro, S.S. 2007. Geologia, geoquímica multielementar e isotópica (Sm-Nd) das rochas do embasamento do extremo oeste da Província Rio Negro, NW do Amazonas, Brasil. *In:* SIMPÓSIO DE GEOLOGIA DA AMAZÔNIA, 10., 2007, Porto Velho. *Anais*... Porto Velho, SBG, v. 1, p. 26-29.

Bonow, W.C. & Issler, R.S. 1980. Reavaliação e aspectos econômicos do jazimento de terras raras e ferro-ligas do lago esperança, Complexo Carbonatítico dos Seis Lagos – Amazonas, Brasil. *In:* CONGRESSO BRASILEIRO DE GEOLOGIA, 31., 1980, Balneário Camboriú. *Anais*... Balneário Camboriú, SBG, v. 3, p. 1431-1443.

Chakhmouradian, A.R. & Zaitsev, A.N. 2012. Rare Earth Mineralization in Igneous Rocks: Sources and Processes. *Elements*, 8: 347-353.

Coetzee, G.L. & Edwards, C.B. 1960. The Mrima Hill carbonatite, Cost Province, Kenya. *Transactions of the Geological Society of South Africa,* 62: 373-397.

CPRM. Serviço Geológico Brasileiro. 1976. Projeto Seis Lagos*,* v. 1. Manaus, CPRM, 136p. Relatório Final

CPRM. Serviço Geológico Brasileiro. 1983. *Projeto Uaupés*. Manaus, CPRM, 214p. Relatório Final.

CPRM. Serviço Geológico Brasileiro. 2002. *Reconhecimento geológico ao longo dos rios Negro, Xié e Içana (Missão Tunuí), Noroeste do Estado do Amazonas*. Superintendência Regional de Manaus, CPRM, 16 p. (Relatório interno).

CPRM. Serviço Geológico Brasileiro. 2006. Geologia e Recursos Minerais do Estado do Amazonas. Manaus. CPRM, 144p.

Cordani, U.G. & Brito Neves, B.B. 1982. The Geologic Evolution of South America during the Archean and Early Proterozoic. *Revista Brasileira de Geociências*, 12(1-3): 78-88

Corrêa, A.S. 1996. *Evolução geoquímica da crosta laterítica e dos sedimentos sobrepostos na estrutura de Seis Lagos (Amazonas)*. Manaus, 212p. Tese de doutorado, Programa de Pós Graduação em Geociências, Instituto de Geociências, Universidade Federal do Pará.

Corrêa, A.S. & Costa, M.L. 1997. Mineralogia das crostas laterítica ferruginosas de Seis Lagos (Amazonas). *Revista Brasileira de Geociências*, 16: 141-156.

Dall' Agnol, R. & Macambira, M.J.B. 1992. Titanita-biotita granitos do baixo rio Uaupés, Província Rio Negro, Amazonas. Parte I: geologia, petrografia e geocronologia. *Revista Brasileira de Geociências*, 22(1): 3-14.

Giovannini, A.L. 2013. *Contribuição à geologia e geoquímica do carbonatito e da jazida (Nb, ETR) de Seis Lagos (Amazonas).* Porto Alegre, 128p. Dissertação de Mestrado, Programa de Pós-graduação em Geociências, Instituto de Geociências, Universidade Federal do Rio Grande do Sul.

Gomes C.B., Ruberti, E. & Morbidelli, L. 1990. Carbonatite complexes from Brazil: a review. *Journal of South America Earth Science* (3/1): 51-63.

INPE. Instituto Nacional de Pesquisas Espaciais. 2012.

Disponível em: <http://www.dsr.inpe.br/topodata>. Acesso em: 05 jun. 2012

Issler, S.R. 1980a. The Seis Lagos Carbonatite Complex. *In:* CONGRESSO BRASILEIRO DE GEOLOGIA, 31, Balneário Camboriú. *Anais*... Balneário Camburiú, SBG, v. 3, p. 1564-1573.

Issler, S.R. 1980b. Rare Earth Elements in the Seis Lagos Carbonatite Complex. *Mineração e Metalurgia*, 417: 20-30.

Justo, L.J.C.L. & Souza, M.M. 1984. Jazida de Nióbio do Morro dos Seis Lagos. *In:* SIMPÓSIO DE GEOLOGIA DA AMAZÔNIA, 2, 1984, Manaus, *Anais*... Manaus, SBG, p. 467-672.

Justo, L.J.E.C. & Souza, M.M. 1986. Jazida de Nióbio do Morro dos Seis Lagos, Amazonas. *In*: Schobbenhaus, C., Coelho, C.E.S. (coords.). *Principais Depósitos Minerais do Brasil.* Departamento Nacional de Produção Mineral – Companhia Vale do Rio Doce, Brasília, II: p. 463-468.

Lemos, R.L. & Gaspar, J.C. 1998. Geologia do Complexo Ultramáfico-alcalino-carbonatítico de Maicuru, noroeste do estado do Pará. *In:* CONGRESSO BRASILEIRO DE GEOLOGIA, 40, 1998, Belo Horizonte. *Anais*... Belo Horizonte, SBG, v.1, p. 466-529

Lottermoser, B. G. 1990. Rare-earth element mineralization within the Mt. Weld carbonatite laterite, Western Australia . *Lithos*, 24(2): 151-167.

Pinheiro, S.S., Fernandes, P.E.C.A., Pereira, E.R., Vasconcelos, E.E., Pinto, A.C., Montalvão, R.M.G., Issler, R.S., Dall'Agnol, R., Teixera, W. & Fernandes, C.A.C. 1976. Geologia. *In:* RADAM BRASIL – LEVANTAMENTO DE RECURSOS NATURAIS. V. 11. Folha NA-19 Pico da Neblina. 369p.

Reis N.J., Szatmari P. & Wanderlei Filho J.R. 2006. Dois eventos de magmatismo máfico mesozóico na fronteira Brasil – Guiana, Escudo das Guianas: enfoque à região do rifte Tacutu – North Savannas. *In:* CONGRESSO BRASILEIRO DE GEOLOGIA, 43, 2006, Aracaju. Anais... Aracaju, SBG, v. 1, p. 459-464.

Ruberti, E., Enrich, G.E.R. & Gomes, C.B. 2008. Hidrotermal REE fluorcarbonate mineralization at Barra do Itapirapuã, a multiplistockworkcarbonatite, southern Brazil. *The Canadian Mineralogist*, 46: 901-914.

Santos, J.O.S., Hartmann, L. A., Gaudette, H. E., Groves, D.I., Mcnaugthon, N.J. & Fletcher, L.R.A.2000. New understanting of the Provinces of Amazon Craton based on Integration of Field Mapping and U-Pb and Sm-Nd geochronology. *Gondwana Research*, 3(4): 453-488.

Santos, J.O.S. 2003. Geotectônica dos Escudos das Guianas e Brasil Central. *In:* Bizzi, L.A., Schobbenhaus, C., Vidotti, R.M. & Gonçalves, J.H. (Eds.). *Geologia tectônica e recursos minerais do Brasil: texto, mapas e SIG*. Brasília, CPRM - Serviço Geológico do Brasil, p. 168-226.

Santos J.O.S., Van Breemen O.B., Groves D.I., Hartmann L. A., Almeida M.E., McNaughton N.J. & Fletcher, I.R. 2004. Timing and evolution of multiple Paleoproterozoic magmatic arcs in the Tapajós Domain, Amazon Craton: constraints from SHRIMP and TIMS zircon, baddeleyite and titanite U–Pb geochronology. *Precambrian Research*, 131(10): 73-109.

Santos, J.O.S., Hartmann, L.A., Faria, M.S., Riker, S.R., Souza, M.M., Almeida, M.E. & McNaughton, N.J. 2006. A compartimentação do cráton amazônico em províncias: avanços ocorridos no período de 2000-2006. *In:* SIMPÓSIO DE GEOLOGIA DA AMAZÔNIA, 9., 2006, *Seção Temática* 3, Belém, Pará. CD-ROOM.

Service, R.F. 2010. Nations move to head off shortages of rare earths. *Science* 26(327): 1596–1597.

Souza, A.G.H. 2009*. Petrologia e geoquímica do batólito granítico São Gabriel da Cachoeira, Província Rio Negro, AM*. Manaus, 89p. Dissertação de Mestrado, Programa de Pós-Graduação em Geociências, Instituto de Ciências Exatas, Universidade Federal do Amazonas.

Souza A.G.H., Nascimento R.S.C., Navarro, T.A., Almeida, M.E. & Souza, V.S. 2009. Geoquímica do granito São Gabriel da Cachoeira (AM), Suíte Intrusiva Rio Uaupés. *In:* SIMPÓSIO DE GEOLOGIA DA AMAZÔNIA, 11, 2009, Manaus, Anais..., Manaus. p. 80-85

Stone, R. 2009. As China's rare earth R&D becomes ever more rarefied, others tremble. *Science*, 325: 1336-1337.

Tassinari, C.C.G. 1981*, Evolução tectônica da Província Rio Negro-Juruena na Região Amazônica*. São Paulo, 99p. Dissertação de Mestrado, Instituto de Geociências, Universidade de São Paulo.

Tassinari, C.C.G. & Macambira, M.J.B. 1999. Geochronological Provinces of the Amazonian Cráton. *Episodes*, 22(3): 174-182.

Tassinari, C. C. G. & Macambira M. J. B. 2004. A Evolução Tectônica do Cráton Amazônico. *In:* Manteso-Neto, V., Bartoreli, A., Carneiro, C.D.R. & Brito Neves, B.B. (Eds.). *Geologia do Continente Sul Americano: Evolução da Obra de Fernando Flávio Marques de Almeida. São Paulo.* Ed. Beca, p. 471-486.

Valeriano, M.M. & Rossetti, D.F. 2012. Topodata: Brazilian full coverage refinement of SRTM data. *Applied Geography*, 32: 300-309.

Man. 555.
Editores: Tatiana Silva da Silva & Maria do Carmo Lima e Cunha.

7.2 *U-Pb zircon geochronologycal investigation on the Seis Lagos Carbonatite Complex and associated Nb-deposit (Amazonas, Brazil).*

Journal of South American Earth Sciences 80 (2017) 1–17

Contents lists available at ScienceDirect

Journal of South American Earth Sciences

journal homepage: www.elsevier.com/locate/jsames

U-Pb zircon geochronologycal investigation on the Morro dos Seis Lagos Carbonatite Complex and associated Nb deposit (Amazonas, Brazil)

Marco B. Rossoni [a], Artur C. Bastos Neto [b, *], Valmir S. Souza [c], Juliana C. Marques [b], Elton Dantas [c], Nilson F. Botelho [c], Arthur L. Giovannini [a], Vitor P. Pereira [b]

[a] Programa de Pós-graduação em Geociências, Universidade Federal do Rio Grande do Sul, Avenida Bento Gonçalves 9500, Porto Alegre, 91501-970, RS, Brazil
[b] Instituto de Geociências, Universidade Federal do Rio Grande do Sul; Avenida Bento Gonçalves 9500, Porto Alegre, 91501-970, Porto Alegre, RS, Brazil
[c] Instituto de Geociências, Universidade de Brasília, Campus Darcy Ribeiro, Asa Norte, 70910-900, Brasília, DF, Brazil

ARTICLE INFO

Article history:
Received 15 December 2016
Received in revised form
8 September 2017
Accepted 18 September 2017
Available online 21 September 2017

Keywords:
Seis Lagos
Carbonatite
U-Pb geochronology
Guyana shield
Amazonas

ABSTRACT

We present results of U-Pb dating (by MC-ICP-MS) of zircons from samples that cover all of the known lithotypes in the Seis Lagos Carbonatite Complex and associated lateritic mineralization (the Morro dos Seis Lagos Nb deposit). The host rock (gneiss) yielded an age of 1828 ± 09 Ma interpreted as the crystallization time of this unit. The altered feldspar vein in the same gneiss yielded an age of 1839 ± 29 Ma. Carbonatite samples provided 3 groups of ages. The first group comprises inherited zircons with ages compatible with the gneissic host rock: 1819 ± 10 Ma (superior intercept), 1826 ± 5 Ma (concordant age), and 1812 ± 27 Ma (superior intercept), all from the Orosirian. The second and the third group of ages are from the same carbonatite sample: the superior intercept age of 1525 ± 21 Ma (MSWD = 0.77) and the superior intercept age of 1328 ± 58 Ma (MSWD = 1.4). The mineralogical study indicates that the ~1.3 Ga zircons have affinity with carbonatite. It is, however, a tendence rather than a well-defined result. The data allow state that the age of 1328 ± 58 Ma represents the maximum age of the carbonatite. Without the same certainty, we consider that the data suggest that this age may be the carbonatite age, whose emplacement would have been related to the evolution of the K'Mudku belt. The best age obtained in laterite samples (a superior intercept age of 1828 ± 12 Ma) is considered the age of the main source for the inherited zircons related to the gneissic host rock.

1. Introduction

The Seis Lagos Carbonatite Complex (SLCC), located in the upper Negro River region (Amazonas State), was discovered in the 1970's by the RADAM Project (Pinheiro et al., 1976). Some months after the discovery, the Companhia de Pesquisa de Recursos Minerais (CPRM), still the holder of the mineral rights, conducted an exploration program (Viegas Filho and Bonow, 1976) in the major body, the Morro dos Seis Lagos (Six Lakes Hill), that evidenced this hill is capped by an iron rich laterite that corresponds to the Morro dos Seis Lagos Nb deposit, the world's largest Nb deposit (2,898 × 10^6 t with 2.81 wt% Nb_2O_5; Justo and Souza, 1986).

The SLCC has not been dated by geochronological methods, but a Mesozoic age and a possible relationship with the evolution of the Brazilian Equatorial Continental Margin have been assigned. This interpretation, initially based on a possible correlation with basic rocks located hundreds of kilometers away, dated between 200 and 250 Ma by the K-Ar method (Pinheiro et al., 1976), is accepted until recent studies (CPRM, 2006). However, other carbonatites - Maicurú (586 ± 18 Ma; Lemos and Gaspar, 1998) and Mutum (1.0 Ga; Gomes et al., 1990) - in the southern part of the Guyana Shield have ages that preclude being related to the continental margin. The host rock of the SLCC has also not been dated. It has been tentatively correlated with the Cauaburi Complex (~1.81 Ga to 1.78 Ga), which forms the geological framework of the region (CPRM, 2006; Santos et al., 2000; Almeida et al., 2013).

* Corresponding author.
E-mail addresses: marco_rossoni@hotmail.com (M.B. Rossoni), artur.bastos@ufrgs.br (A.C. Bastos Neto), vsouza@unb.br (V.S. Souza), juliana.marques@ufrgs.br (J.C. Marques), angicos63@gmail.com (E. Dantas), nilsonfb@unb.br (N.F. Botelho), arthur_giovannini@hotmail.com (A.L. Giovannini), vitor.pereira@ufrgs.br (V.P. Pereira).

http://dx.doi.org/10.1016/j.jsames.2017.09.021
0895-9811/

In this paper we present the results of the U-Pb zircon geochronologycal investigation procceded at the SLCC and associated Nb-deposit. We separate zircons from the gneissic host-rock, from the carbonatite and from the laterite that forms the deposit. A mineralogical study was conducted to distinguish carbonatite zircons from inherited zircons. Since there are no detailed descriptions of the mineralization and there is no information about the carbonatite in the literature, we also present some unpublished data on the laterites and on the siderite carbonatite raised by our team.

2. Previous studies

2.1. Regional geology

The SLCC is located in the SW region of the Guyana Shield (Fig. 1). This is a region with limited geological knowledge due to the forest cover and existence of restricted areas (e.g. indigenous territories). Nevertheless, over time different Meso to Paleoproterozoic terranes have been recognized mainly based on geochronological data. However, the names, geographic boundaries, and age intervals of these terranes are still controversial issues (e.g., Teixeira et al., 1989; Tassinari and Macambira, 1999, 2004, Santos et al., 2000). The two main current evolution models proposed for the Brazilian side of the Amazon craton include the SLCC into different geotectonic/geochronological terranes. In the model of Tassinari and Macambira (2004), the SLCC is located in the Ventuari-Tapajós Province (1.98–1.81 Ga), whereas the model of Santos et al. (2000) places it in the Rio Negro Province (1.82–1.53 Ga). In the model by Santos et al. (2006a), the SLCC is located approximately at the boundary between the Rio Negro Province and the K'Mudku Belt (Fig. 1).

The SLCC is embedded in the Tarsira lithofacies of the Cauaburi Complex (Fig. 2), which forms the basement of the Imeri Domain of the Rio Negro Province (CPRM, 2006). The Imeri Domain is characterized by NE-SW-trending regional structures related to dextral shear zones, and its basement comprises orthogneisses and calc-alkaline metagranitoids with compositions that range from monzogranite to granodiorite, locally tonalite (Santa Izabel lithofacies), and monzogranite augen gneiss (Tarsira lithofacies) with ages of 1810 to 1790 Ma (igneous protolith ages; Almeida et al., 2013).

A set of geochronological studies (Table 1) has significantly furthered the understanding of the geological evolution of the region. Almeida et al. (2013) interpret the calc-alkaline basement of the Imeri Domain (from 1.81 Ga to 1.78 Ga) as a continental magmatic arc that dives beneath the Tapajós-Parima Province and includes late-to post-collisional A-type granites (1.75 Ga); this set of units represents the Cauaburi Orogeny. To the north (Uaupés Domain), the basement is younger (from 1.74 Ga to 1.70 Ga) and is interpreted as a juvenile magmatic arc (island arc?) that is associated with the Tunuí meta-volcano-sedimentary succession (Fig. 2); these units represent the Querari Orogeny. S-Type (and hybrid) granites of the Içana Suite and transitional granites between I- and A- (ambiguous) of the Uaupés Suite, which were derived from predominantly crustal sources and were generated between 1.54 Ga and 1.48 Ga, represent a key collisional system in the area (Içana Orogeny). In summary, according to Almeida et al. (2013), the northwestern craton consists of two Staterian accretionary orogens, the Cauaburi Arc (1.81–1.78 Ga) and the Querari Arc (1.74–1.70 Ga), that amalgamated during a Calymmian-age collisional process and are embodied by S-type S and A-I granitoids (1.54–1.48 Ga).

The granites located south and southwest of the Seis Lagos Carbonatite Complex (Fig. 2) are part of the Rio Uaupés Intrusive Suite, which is formed mainly of titanite-biotite monzogranites, with Rb-Sr age of 1459 ± 32 Ma and $^{87}Sr/Sr^{86}$ ratio = 0.070631 (Dall'Agnol and Macambira, 1992). Santos et al. (2000) highlight the difficulty in distinguishing them from the basement because they

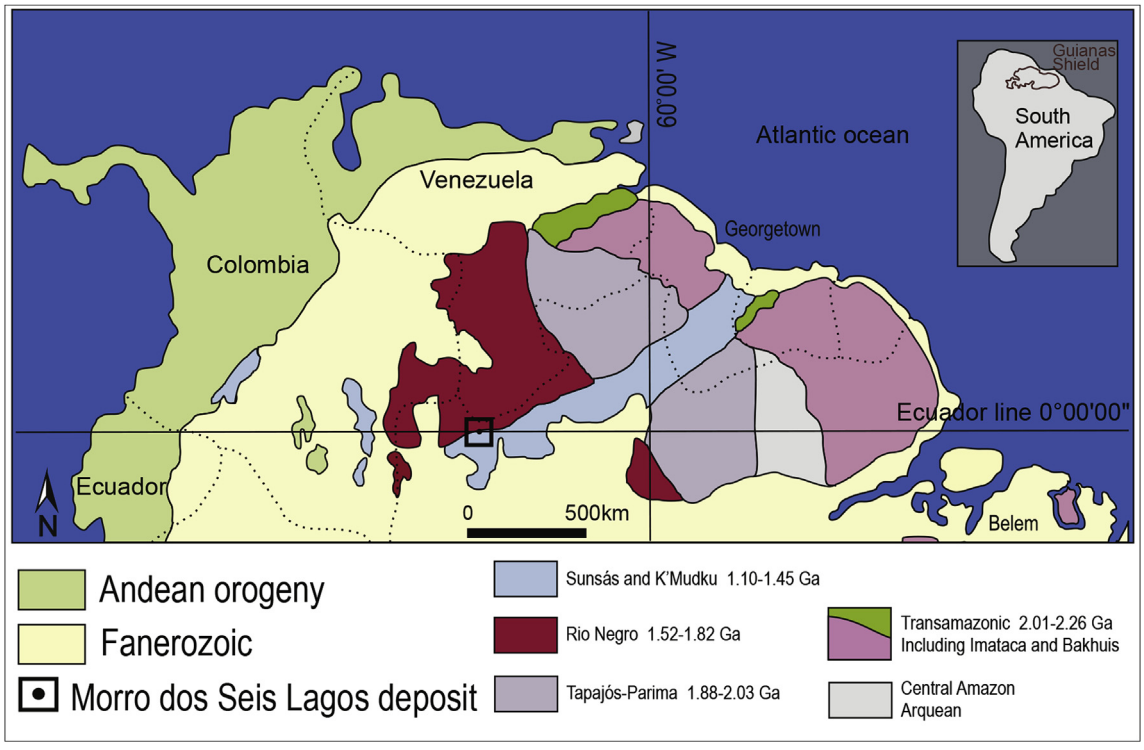

Fig. 1. Geochronological provinces of the Guyana Shield (modified from Santos et al., 2006a) showing the location of the Morro dos Seis Lagos deposit.

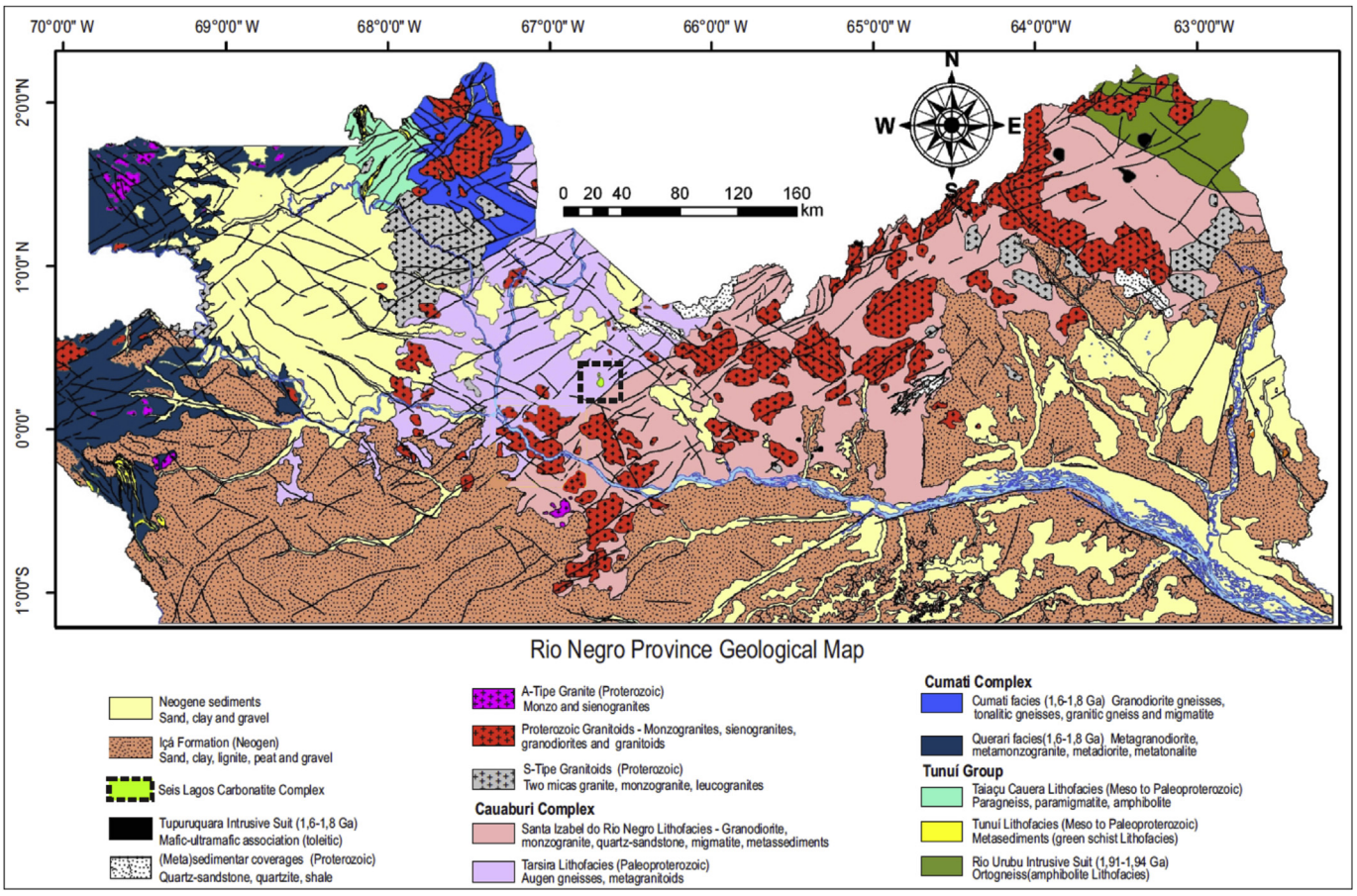

Fig. 2. Geological map of the Brazilian part of the Rio Negro Province showing the location of the Seis Lagos Carbonatite Complex. Adapted from CPRM (2006) by Souza (2009), simplified.

Table 1
Geochronological data from the Imeri Domain.

Unit	Lithology	Crystallization	Metamorphism	Reference
P. Gavião	Syenogranite	1218 (U-Pb)		Souza et al. (2015)
Rio Uapés	Granite	1459±32 (Rb-Sr)		Dall'Agnol and Macambira (1992)
Rio Uapés	Granite	1518±25 (U-Pb)		Santos et al. (2000)
Içana/Reilau	Granite	1521±32 (Pb-Pb)	1318±22	Almeida et al. (1997)
Igarapé Reilau	Muscovite leucogranite	1534 (Sm-Nd)		CPRM, 2006
Igarapé Reilau	Granite	1787±13 (U-Pb)	1423±14	Santos et al. (2006b)
Marauiá		1652±57 (Rb-Sr)		Basei (1975)
Marauia	Monzogranite	1746 (Sm-Nd)		CPRM, 2006
Marié-Mirim	Sienogranite	1756 (Sm-Nd)		CPRM, 2006
Cauaburi Complex	Monzogranite	1798 (Sm-Nd)		CPRM, 2006
LF Santa Isabel	Hnb. gneiss mzgranitic	1798 (Sm-Nd)		CPRM, 2006
	Gneiss	1798 (Sm-Nd)		CPRM, 2006
	Milonitic Monzogranite	1798 (Sm-Nd)		CPRM, 2006
	Gneiss	1796 (Sm-Nd)		CPRM, 2006
	Granodiorite	1798 (Sm-Nd)		CPRM, 2006
	Granite	1798 (Sm-Nd)		CPRM, 2006
	Gneiss	1807 ± 6 (U-Pb)		Almeida et al. (2013)
	Gneiss	1789 ±6 (U-Pb)		Santos et al. (2002)
	Gneiss	1796 ± 6 (U-Pb)		Santos (2003)
	Gneiss	1798 ±3 (U-Pb)	1468±8	Santos (2003)
	Gneiss		1490±3	Santos et al. (2006b)
LF Tarsira	Gneiss	1795 ± 2 (Pb-Pb)		Almeida et al. (2013)
Cauaburi Complex	MSLD laterite	1810±9 (U-Pb)		Santos et al. (2000)

are syntectonic, folded and sheared together with the host rock and were locally deformed and sheared during the K'Mudku event (1.2 Ga). One of these bodies, the São Gabriel da Cachoeira granite, was generated by partial melting of the dominantly crustal trans-Amazonian source in a collisional environment at 1.5 Ga (Souza, 2009).

The K'Mudku Belt (Fig. 1) is characterized by mylonite zones formed in amphibolite facies superior to granulite, between 1.15 and 1.47 Ga during three or four collisional periods that correspond to the Sunsás Province orogenies (Barron, 1966; Santos et al., 2006a, 2006b): the Santa Helena orogeny (dominantly juvenile, 1450-1320 Ma), the Candeias orogeny (combination of a continental arc with a collisional orogeny, 1320-1280 Ma), the San Javier orogen (1280-1230 Ma) and the Nova Brasilândia orogeny (collisional, 1230-1110 Ma).

Mesoproterozoic A-type magmatism (~1.2 Ga) is also present in the region, including the Samauma batholith (1179 Ma) and the Pedra do Gavião stock (1218 Ma). In general, this magmatism has alkaline high K_2O, metaluminous, reduced A-type and intraplate to post-collisional geochemical signature (Santos et al., 2009; Souza et al., 2015). The Pedra do Gavião stock presents inheritance between 1820 and 1720 Ma, suggesting partial melting from Cauaburi Complex rocks. Therefore, it is probable that the K'Mudku effect was not only milonitization on the previous rocks, but also contributed to magma generation.

2.2. Seis Lagos Carbonatite Complex and Morro dos Seis Lagos deposit

The Seis Lagos Carbonatite Complex (recognized as carbonatite and so called by Issler and Silva, 1980) consists of three approximately circular bodies (Fig. 3). The emplacement of the complex was controlled by an E-W lineament that can be followed in an aeromagnetic map for more than 400 km. Nearly the complex, the most prominent structures have an E-W direction, although NE-SW and WNW-ESE structures are also found (Rossoni et al., 2016).

The Nb deposit is associated to the main carbonatite body, where CPRM conducted two drilling campaigns. This study used samples from the boreholes of the first campaign (Viegas Filho and Bonow, 1976, Fig. 4). The main occurrence of carbonatite was recorded in borehole SG-04-AM, which was located in a karst basin and penetrated argillaceous sediments (0–166.55 m), a carbonate breccia (166.55 m–230.00 m) and carbonatite (230.00 m–483.00 m). Carbonatite was also present in borehole SG-02-AM, which penetrated non-mineralized laterite crust (0–33.90 m), gneiss (33.90–221.60 m), and carbonatite (221.60–227.70 m) and had no recovery from 227.70 to 230.85 m. Both boreholes encountered siderite carbonatite.

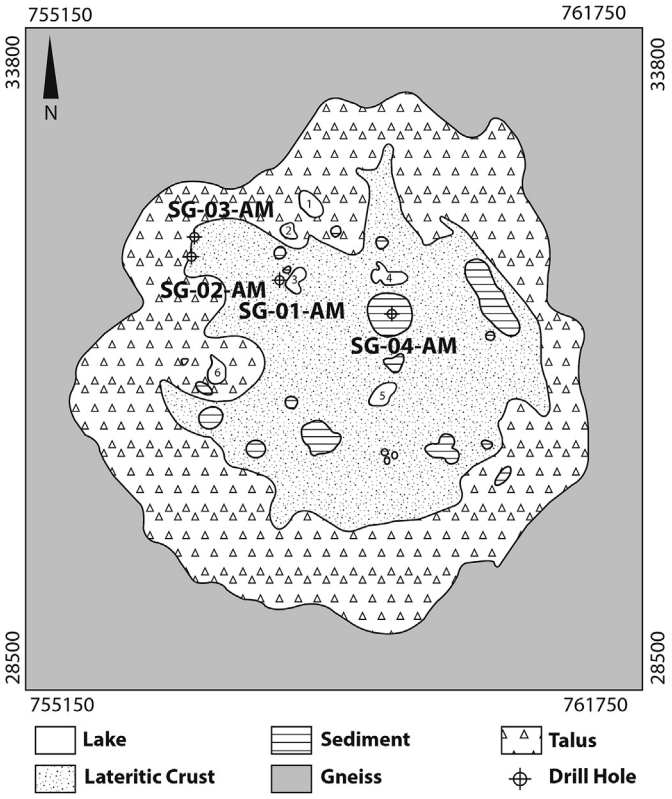

Fig. 4. Geological map of the Morro dos Seis Lagos carbonatite body (Viegas Filho and Bonow, 1976) with the locations of the boreholes used in this work. This is the main carbonatite body at the Seis Lagos Carbonatite Complex; the lateritic cover corresponds to the Morro dos Seis Lagos Nb deposit.

The siderite carbonatite in borehole SG-02-AM is light grey and highly friable. It is composed by siderite, barite and gorceixite, and minor monazite and pyrochlore. Siderite (~70 vol%) crystals are euhedral, brownish, with average size of 700 μm. Barite (~15 vol%) occurs as aggregates of fine crystals (up to 150 μm) that fill the

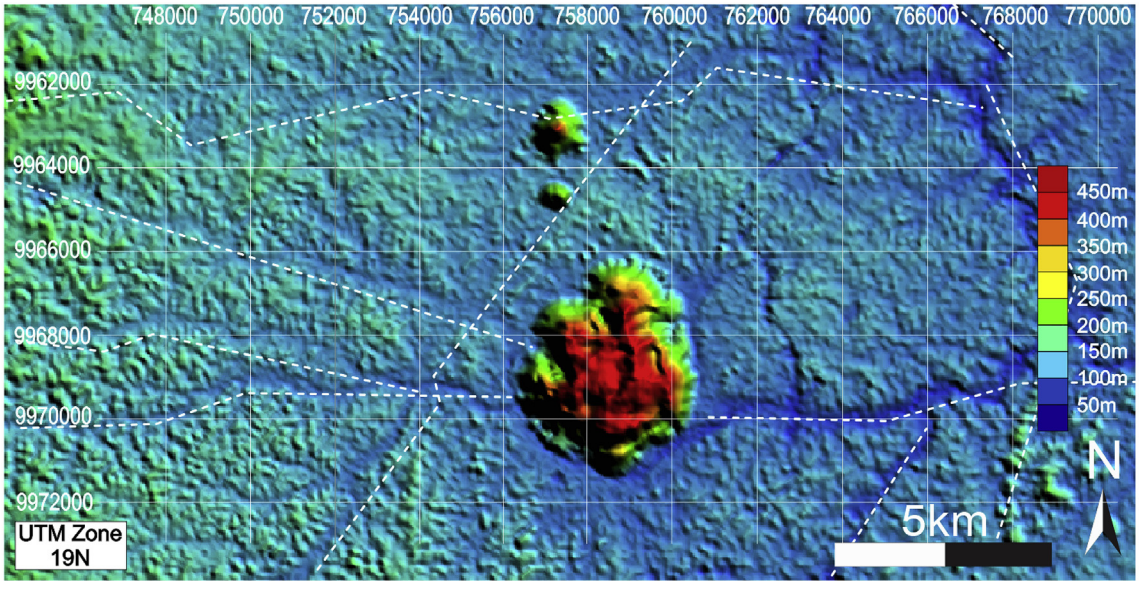

Fig. 3. Main morphostructures surrounding the Seis Lagos Carbonatite Complex. Modified from Rossoni et al. (2016).

interstices of siderite crystals or in veins in siderite crystals. Gorceixite (up to 7.5 vol%) occurs as the predominant mineral in aggregates with monazite and pyrochlore; the crystals are euhedral, with size up to 5 μm. Monazite (up to 1 vol%) occurs mainly as small crystals fibrorradiated with up to 5 μm. More rarely, monazite occurs filling gaps between siderite crystals. Pyrochlore (<1 vol%) occurs as euhedral crystal, with ~3 μm in the aggregates with monazite and gorceixite. In the siderite carbonatite from the borehole SG-04-AM, siderite grains are euhedral, brownish, with sizes up to 500 μm, and frequently present trails of fluid inclusions that can be very abundant. Hematite occurs at the edge of siderite crystals and in the rock matrix. Pyrochlore, monazite, bastnäsite, and thorbastnäsite were observed only in BSE images. Pyrochlore occurs as euhedral crystals of ~5 μm. Monazite occurs as agglomerate with 100 μm made by crystals with 5 μm. Bastnäsite occurs as rare single small (<5 μm) in the matrix. Thorbastnäsite occurs as acicular crystals fulfilling spaces between hematite crystals of the matrix. Gibbsite occurs as veinlets that cut siderite and hematite crystals. Quartz and gypsum were detected only by DRX in few samples (Giovannini et al., 2017).

Carbonatite weathering formed the Nb-mineralized laterite crust, whose total thickness is not known because the deepest borehole in the laterite (SG-01-AM) was interrupted within it at 225 m. Corrêa (1996) and Corrêa and Costa (1997) performed the first mineralogical and geochemical studies on the laterites. Giovannini et al. (2017) divided the lateritic profile in six textural and compositional types of laterite crusts (from the surface downwards): (1) pisolitic laterite, (2) fragmented laterite, (3) mottled laterite, (4) purple laterite, (5) manganiferous laterite, and (6) brown laterite. All the laterite crusts are mainly formed by goethite (predominant in the lower and upper laterite crusts) and hematite (predominant in the intermediary laterite crusts). In the manganiferous laterite crust, the manganese oxides (mainly hollandite, with associated cerianite) occur as veins or irregular masses. Manganese precipitation is a late event during the development of the lateritic profile. The main Nb ore mineral is secondary Nb-rich rutile (with 10.52–26.86 wt% Nb_2O_5), which occurs in all laterite crusts. Minor Nb-rich brookite formed from Nb-rich rutile occurs as broken spherules with oolitic structure (Liesegang rings). The laterite crusts in the SG-01-AM borehole have an average Nb_2O_5 content of 2.91 wt % and average TiO_2 content of 5.00 wt% in the upper crusts. Average Ce_2O_3 concentration in the crusts increases with increasing depth, from 0.34 wt% in the pisolitic laterite crust to 2.04 wt% in the brown laterite crust (Giovannini et al., 2017).

The host rock is present in boreholes SG-02-AM and SG-03-AM. It is a biotite-hornblende-gneiss with quartz-feldspathic bands interspersed with bands of mafic minerals with intense fractures filled by iron oxides and clay minerals. Plagioclase is the most abundant mineral, subhedral to anhedral, and sericitized. The K-feldspar is anhedral, fractured and contains argillic alteration. The quartz has wide variations in particle size and shape and always has ondulant extinction. The chloritized biotite and hornblende are associated with and commonly contain apatite inclusions. Leucoxene, zircon and opaque minerals occur as accessories.

The only geochronological data from the SLCC and the Morro dos Seis Lagos deposit area is a U-Pb age of 1810 ± 9 Ma, which was determined using a sensitive high-resolution ion microprobe (SHRIMP) on zircons from a sample from the laterite crust (Santos et al., 2000). According to the authors, the sample was collected to determine the age of the main clastic sources to the cover over the Seis Lagos Complex.

3. Materials and methods

The seven samples used in this study (Table 2) cover all of the known lithotypes in the Morro dos Seis Lagos deposit, including (a) host rock (gneiss), (b) feldspar/kaolin intercalation in the host rock, which was suspected of being an alkaline dike possible related to the carbonatite complex, (c) siderite carbonatite (3 samples) and (d) laterite crust (2 samples). The zircons were separated by manual scavenging under a binocular loupe using the following procedures: comminution in a porcelain crucible, ultrasound purification, magnetic separation with a Frantz device up to 1.8 Å and concentration of the dense minerals by panning. The minerals were then mounted on a circular epoxy mount with a diameter of 1 cm, which was polished until they appeared at the surface. Dating was performed at the Geochronology Laboratory of UNB in a Neptune Multicollector-Inductively Coupled Plasma Mass Spectrometer (MC-ICP-MS; Thermo Finnigan) coupled to a New Wave UP-213 laser. The following laser parameters were used: spot: 30 μm; energy: 85% (~4–5 J/cm^2); and frequency: 10 Hz. The MC-ICP-MS parameters were as follows: cooling gas: 15.00 L/min (argon); auxiliary gas: 0.70 L/min (argon); sample gas: 0.855 L/min (argon); added gas: 0.38 L/min (helium); and RF power: 1080 W. The GJ-1 and 91500 standards were used.

The chemical analyses of the grains were conducted in the Electron Microprobe Laboratory of UNB using a Jeol JXA-8230 electron probe microanalyzer equipped with 5 spectrometers. The correction of matrix effects was performed using the ZAF method. An accelerating voltage of 15 kV, a current of 10 nA and a counting time of 10 s were used for Si, Zr, Hf, Nb, Ta, Y, P, Fe, Mn, Ti, Al and Ca, and an accelerating voltage of 20 kV, a current of 50 nA, and a counting time of 10 s were used for the REEs, U and Th. The background counting time was half of that measured in the peak. The following spectral lines were used: SiKa, ZrLa, HfMa, NbLb, TaMa, PKa, FeKa, MnKa, TiKa, AlKa, CaKa, YLa, LaLa, CeLa, GdLa, TbLa, DyLa, EuLa, HoLa, ErLa, TmLa, YbLa, LuLa, PrLb, SmLb, NdLb, UMb, and ThMa. Synthetic oxide standards were used for the REEs, Y, U, Th, Hf, Nb, Ta, Mn, Ti, and mineral standards were used for the other elements. Corrections due to interference were performed using the device routine. The detection limits ranged from 50 to 200 ppm for all of the analyzed elements.

Table 2
Samples dated in his study.

Borehole/sample	Depth (m)	Rock	U-Pb AGE Zircon (Ma)
SG-01-AM/01	0.30	Pisolitic laterite crust	1828 ± 12
SG-01-AM/04	5.00	Fragmented laterite crust	1874 ± 56
SG-02-AM/35	62.00	Gneiss	1828 ± 09
SG-02-AM/22	34.00	Feldspar vein in gneiss	1839 ± 29
SG-02-AM/53	227.50	Siderite carbonatite (edge of the body)	1819 ± 10
SG-04-AM/70	315.50	Siderite carbonatite (center of the body)	1826 ± 05
SG-04-AM/73	335.00	Siderite carbonatite (center of the body)	1812 ± 27
			1521 ± 21
			1328 ± 58

4. Results

The results from the isotopic analyses are summarized in Tables 3–9. The ages shown in Table 2 were taken from the diagrams shown in Figs. 5–8. The probability density plots show only near-concordant ages (<10% discordance between $^{206}Pb/^{238}U$ and $^{207}Pb/^{206}Pb$ ages), except from sample SG-04-AM-73 (Fig. 8b) that shows only concordant ages (<2% discordance).

Table 3
Isotopic analysis of sample SG-02-AM-35.

	Isotopic Ratios									Ages (Ma)						
	ƒ(206)%	Th/U	$^{207}Pb/^{206}Pb$	1σ(%)	$^{207}Pb/^{235}U$	1σ (%)	$^{206}Pb/^{238}U$	1σ (%)	Rho	$^{207}Pb/^{206}Pb$	1σ (Ma)	^{207} P b/235U	1σ (Ma)	$^{206}Pb/^{238}U$	1σ (Ma)	Disc. (%)
Z4	0.005	2.26	0.111	0.518	4.742	0.951	0.309	0.797	0.84	1824	9	1775	8	1733	12	5
Z5	0.002	0.40	0.112	0.466	5.139	0.782	0.332	0.628	0.80	1839	8	1843	7	1846	10	0
Z6	0.053	0.44	0.113	0.528	4.602	0.961	0.295	0.803	0.84	1848	10	1750	8	1669	12	10
Z10	0.003	0.32	0.113	0.512	4.570	0.867	0.294	0.700	0.81	1846	9	1744	7	1660	10	10
Z11	0.011	0.58	0.112	0.625	5.150	1.089	0.333	0.892	0.82	1835	11	1844	9	1853	14	−1
Z12	0.003	0.37	0.113	0.550	4.501	0.923	0.290	0.741	0.80	1844	10	1731	8	1640	11	11
Z13	0.004	0.42	0.113	0.555	4.386	0.816	0.282	0.598	0.73	1847	10	1710	7	1600	8	13
Z16	0.004	0.34	0.113	0.625	4.422	0.929	0.283	0.688	0.74	1851	11	1716	8	1608	10	13
Z17	0.007	0.79	0.112	0.712	4.997	1.196	0.325	0.961	0.80	1824	13	1819	10	1814	15	1
Z18	0.003	0.34	0.113	0.515	4.429	0.942	0.284	0.788	0.84	1852	9	1718	8	1610	11	13
Z19	0.004	0.32	0.113	0.594	4.488	0.909	0.287	0.688	0.76	1852	11	1729	8	1629	10	12
Z20	0.005	0.36	0.113	0.867	4.677	1.092	0.300	0.664	0.61	1847	16	1763	9	1693	10	8
Z9	0.007	1.25	0.110	0.586	4.810	1.305	0.316	1.166	0.89	1807	11	1787	11	1769	18	2
Not used on age calculation																
Z7	0.648	0.64	0.110	0.749	4.554	0.996	0.300	0.657	0.68	1803	14	1741	8	1690	10	6
Z15	0.011	0.66	0.117	0.661	4.562	0.963	0.284	0.700	0.73	1906	12	1742	8	1609	10	16
Z23	0.021	3.52	0.114	1.282	5.240	2.206	0.333	1.796	0.81	1869	23	1859	19	1851	29	1
Z8	0.027	0.44	0.118	0.652	4.647	2.312	0.286	2.218	0.96	1921	12	1758	19	1624	32	15

ƒ(206)%- percentage of common ^{206}Pb.

Table 4
Isotopic analysis of sample SG-02-AM-22.

	Isotopic Ratios									Ages (Ma)						
	ƒ(206)%	Th/U	$^{207}Pb/^{206}Pb$	1σ(%)	$^{207}Pb/^{235}U$	1σ (%)	$^{206}Pb/^{238}U$	1σ (%)	Rho	$^{207}Pb/^{206}Pb$	1σ (Ma)	207 P b/235U	1σ (Ma)	$^{206}Pb/^{238}U$	1σ (Ma)	Disc. (%)
Z1	0.007	0.26	0.112	0.602	4.482	1.015	0.290	0.817	0.80	1832	11	1728	8	1643	12	90
Z3	0.007	0.50	0.113	0.905	4.496	1.158	0.290	0.721	0.62	1841	16	1730	10	1640	10	89
Z4	0.007	0.43	0.113	0.643	4.538	0.954	0.291	0.705	0.74	1849	12	1738	8	1647	10	89
Z5	0.011	0.38	0.113	0.610	4.227	1.231	0.272	1.069	0.87	1843	11	1679	10	1551	15	84
Z6	0.010	1.75	0.112	1.241	4.434	2.220	0.287	1.841	0.83	1830	22	1719	18	1629	26	89
Z7	0.007	0.48	0.113	0.708	4.318	1.138	0.276	0.891	0.78	1852	13	1697	9	1574	12	85
Z9	0.013	1.06	0.114	0.927	4.514	2.642	0.288	2.474	0.94	1859	17	1734	22	1631	36	88
Z10	0.004	0.32	0.113	0.677	4.839	0.909	0.310	0.607	0.67	1850	12	1792	8	1742	9	94
Z11	0.008	0.53	0.112	0.781	4.581	1.617	0.298	1.416	0.88	1825	14	1746	13	1681	21	92

ƒ(206)%- percentage of common ^{206}Pb.

Table 5
Isotopic analysis of sample SG-01-AM-04.

	Isotopic Ratios									Ages (Ma)						
	ƒ(206)%	Th/U	$^{207}Pb/^{206}Pb$	1σ(%)	$^{207}Pb/^{235}U$	1σ (%)	$^{206}Pb/^{238}U$	1σ (%)	Rho	$^{207}Pb/^{206}Pb$	1σ (Ma)	207 P b/235U	1σ (Ma)	$^{206}Pb/^{238}U$	1σ (Ma)	Disc. (%)
Z3	0.003	0.35	0.112	0.523	4.532	0.842	0.295	0.660	0.78	1826	9	1737	7	1664	10	9
Z5	0.005	0.46	0.110	0.483	4.343	0.793	0.287	0.628	0.79	1792	9	1702	7	1629	9	9
Z6	0.008	0.28	0.110	0.597	4.293	1.001	0.283	0.804	0.80	1797	11	1692	8	1608	11	11
Z7	0.006	0.27	0.113	0.790	4.669	1.151	0.299	0.837	0.73	1853	14	1762	10	1686	12	9
Z8	0.006	0.47	0.108	0.657	4.142	1.276	0.277	1.095	0.86	1771	12	1663	10	1578	15	11
Z9	0.007	0.35	0.109	0.642	4.190	1.108	0.280	0.903	0.81	1775	12	1672	9	1591	13	10
Z10	0.004	0.46	0.108	0.651	4.159	1.023	0.278	0.789	0.77	1771	12	1666	8	1584	11	11
Z11	0.002	0.18	0.112	0.603	4.399	1.019	0.285	0.822	0.81	1831	11	1712	8	1617	12	12
Z12	0.003	0.39	0.109	0.620	4.307	0.922	0.286	0.682	0.74	1787	11	1695	8	1621	10	9
Z13	0.004	0.52	0.110	0.687	4.326	1.014	0.286	0.745	0.73	1793	13	1698	8	1623	11	9
Z14	0.003	0.40	0.111	0.745	4.367	1.036	0.285	0.720	0.69	1821	14	1706	9	1615	10	11
Z16	0.007	0.28	0.111	0.938	4.195	1.337	0.275	0.952	0.71	1810	17	1673	11	1566	13	13
Z17	0.009	0.29	0.111	0.950	4.449	1.283	0.291	0.863	0.67	1817	17	1721	11	1644	13	10
Z19	0.002	0.26	0.112	0.659	4.452	0.937	0.289	0.666	0.71	1825	12	1722	8	1639	10	10
Z20	0.004	0.41	0.110	0.653	4.210	0.918	0.278	0.646	0.70	1798	12	1676	8	1580	9	12
Z22	0.008	0.25	0.112	0.634	4.590	0.993	0.297	0.765	0.77	1833	11	1747	8	1677	11	9
Z15	0.004	0.50	0.110	0.821	3.962	1.462	0.261	1.210	0.83	1798	15	1626	12	1497	16	17
Z18	0.007	0.26	0.110	0.754	3.952	1.329	0.261	1.095	0.82	1794	14	1624	11	1496	15	17

ƒ(206)%- percentage of common ^{206}Pb.

Table 6
Isotopic analysis of sample SG-01-AM-01.

Zircon	Isotopic Ratios									Ages (Ma)						
	$f(206)\%$	Th/U	$^{207}Pb/^{206}Pb$	1σ(%)	$^{207}Pb/^{235}U$	1σ (%)	$^{206}Pb/^{238}U$	1σ (%)	Rho	$^{207}Pb/^{206}Pb$	1σ (Ma)	207 P b/235U	1σ (Ma)	$^{206}Pb/^{238}U$	1σ (Ma)	Disc. (%)
Z3	0.007	0.32	0.112	0.531	4.967	0.782	0.322	0.573	0.73	1828	10	1814	7	1801	9	1
Z4	0.012	0.35	0.112	0.575	4.700	1.215	0.304	1.071	0.88	1836	10	1767	10	1709	16	7
Z5	0.004	0.33	0.111	0.581	4.956	1.083	0.323	0.914	0.84	1820	11	1812	9	1805	14	1
Z7	0.006	0.34	0.112	0.654	4.721	0.950	0.307	0.689	0.72	1827	12	1771	8	1724	10	6
Z10	0.007	0.38	0.110	0.593	4.263	0.868	0.281	0.633	0.73	1798	11	1686	7	1598	9	11
Z11	0.003	0.50	0.110	0.531	4.325	0.754	0.285	0.536	0.71	1797	10	1698	6	1619	8	10
Z12	0.006	0.69	0.110	0.554	4.198	1.133	0.278	0.988	0.87	1794	10	1674	9	1579	14	12
Z13	0.010	0.37	0.109	0.639	3.938	1.856	0.261	1.743	0.94	1790	12	1622	15	1495	23	17
Z19	0.007	0.28	0.111	0.530	4.775	1.328	0.311	1.218	0.92	1823	10	1781	11	1745	19	4
Z20	0.169	0.42	0.111	0.736	4.838	1.277	0.317	1.044	0.82	1812	13	1792	11	1774	16	2
Z23	0.033	0.37	0.111	1.002	4.824	1.649	0.315	1.310	0.79	1815	18	1789	14	1767	20	3
Z24	0.006	0.35	0.110	0.547	4.521	0.983	0.299	0.817	0.83	1794	10	1735	8	1687	12	6
Not used on age calculation																
Z1	0.010	0.27	0.115	0.586	5.275	1.107	0.333	0.939	0.85	1876	11	1865	9	1855	15	1
Z9	0.092	0.08	0.104	0.646	3.879	0.979	0.271	0.736	0.75	1696	12	1609	8	1544	10	9
Z15	0.016	0.39	0.114	0.877	4.409	1.419	0.280	1.116	0.79	1869	16	1714	12	1591	16	15
Z21	0.031	0.45	0.107	0.944	4.374	1.377	0.298	1.002	0.73	1742	17	1707	11	1679	15	4
Z16	0.006	0.41	0.111	0.548	5.097	1.047	0.334	0.892	0.85	1809	10	1836	9	1859	14	−3
Z22	0.005	0.30	0.109	0.631	4.616	1.013	0.308	0.793	0.78	1780	12	1752	8	1729	12	3

$f(206)\%$- percentage of common ^{206}Pb.

Table 7
Isotopic analysis of sample SG-02-AM-53.

Zircon	Isotopic Ratios									Ages (Ma)						
	$f(206)\%$	Th/U	$^{207}Pb/^{206}Pb$	1σ(%)	$^{207}Pb/^{235}U$	1σ (%)	$^{206}Pb/^{238}U$	1σ (%)	Rho	$^{207}Pb/^{206}Pb$	1σ (Ma)	207 P b/235U	1σ (Ma)	$^{206}Pb/^{238}U$	1σ (Ma)	Disc. (%)
Z1	0.010	0.366	0.11	0.793	4.721	1.073	0.298	0.724	0.67	1876	14	1771	9	1683	11	10
Z2	0.008	0.357	0.11	0.705	4.720	0.968	0.306	0.664	0.68	1828	13	1771	8	1722	10	6
Z3	0.019	0.342	0.11	0.833	4.810	1.111	0.304	0.734	0.66	1873	15	1787	9	1714	11	9
Z4	0.020	0.326	0.12	0.704	4.474	1.050	0.281	0.779	0.74	1888	13	1726	9	1596	11	15
Z5	0.006	0.117	0.11	0.625	4.553	0.972	0.288	0.744	0.77	1872	11	1741	8	1634	11	13
Z6	0.007	0.345	0.11	0.719	4.377	1.150	0.276	0.897	0.78	1879	13	1708	10	1573	13	16
Z8	0.014	0.353	0.11	0.985	4.321	1.439	0.277	1.049	0.73	1850	18	1697	12	1576	15	15
Z10	0.009	0.341	0.11	1.053	4.830	1.467	0.313	1.022	0.70	1832	19	1790	12	1755	16	4
Z11	0.010	0.355	0.11	0.925	5.025	1.332	0.329	0.959	0.72	1810	17	1824	11	1836	15	−1
Z12	0.009	0.325	0.11	0.761	4.851	1.791	0.312	1.621	0.91	1842	14	1794	15	1752	25	5
Z15	0.006	0.259	0.11	0.765	4.824	1.163	0.313	0.876	0.75	1829	14	1789	10	1755	13	4
Z16	0.012	0.236	0.11	0.947	4.785	1.312	0.308	0.907	0.69	1843	17	1782	11	1731	14	6
Z17	0.005	0.334	0.11	0.594	4.952	0.993	0.323	0.796	0.80	1817	11	1811	8	1806	13	1
Z18	0.010	0.363	0.11	0.727	4.893	1.238	0.318	1.002	0.81	1825	13	1801	10	1781	16	2
Z19	0.174	0.416	0.11	0.638	4.508	0.995	0.289	0.764	0.77	1850	12	1732	8	1636	11	12
Z20	0.012	0.486	0.11	0.660	4.684	1.097	0.301	0.876	0.80	1843	12	1764	9	1699	13	8
Z23	0.010	0.434	0.11	0.856	4.448	1.208	0.287	0.852	0.71	1838	16	1721	10	1627	12	11
Not used on age calculation																
Z7	0.014	0.326	0.12	0.885	4.513	1.534	0.276	1.253	0.82	1938	16	1733	13	1569	17	19
Z22	0.014	0.209	0.11	0.807	4.558	1.083	0.302	0.722	0.67	1791	15	1742	9	1701	11	5
Z26	0.029	0.408	0.12	0.927	4.905	1.121	0.299	0.630	0.56	1940	17	1803	9	1687	9	13
Z13	4.591	1.099	0.12	1.072	4.398	2.794	0.271	2.580	0.95	1924	19	1712	23	1544	35	20

$f(206)\%$- percentage of common ^{206}Pb.

Table 8
Isotopic analysis of sample SG-04-AM-70.

Zircon	Isotopic Ratios									Ages (Ma)						
	$f(206)\%$	Th/U	$^{207}Pb/^{206}Pb$	1σ(%)	$^{207}Pb/^{235}U$	1σ (%)	$^{206}Pb/^{238}U$	1σ (%)	Rho	$^{207}Pb/^{206}Pb$	1σ (Ma)	207 P b/235U	1σ (Ma)	$^{206}Pb/^{238}U$	1σ (Ma)	Disc. (%)
Concordant																
Z02	0.019	0.42	0.112	0.487	5.042	0.891	0.327	0.746	0.81	1832	9	1826	8	1822	12	99
Z05	0.001	0.37	0.111	0.626	5.037	0.982	0.328	0.757	0.74	1822	11	1826	8	1828	12	100
Z06	0.032	0.53	0.112	0.859	5.040	1.240	0.325	0.894	0.70	1838	16	1826	11	1816	14	99
Z08	0.026	0.32	0.113	0.836	5.030	1.238	0.324	0.913	0.72	1843	15	1824	10	1808	14	98
Discordant																
Z07	0.022	0.58	0.112	0.659	4.963	1.000	0.320	0.752	0.72	1838	12	1813	8	1792	12	98
Z10	0.004	0.84	0.113	0.579	5.008	0.952	0.322	0.756	0.77	1847	10	1821	8	1798	12	97
Z01	0.132	7.81	0.111	1.062	3.003	3.341	0.196	3.167	0.95	1819	19	1408	25	1153	33	63
Z11	0.022	0.74	0.113	0.544	4.601	1.057	0.295	0.906	0.84	1850	10	1750	9	1667	13	90
Not used on age calculation																
Z03	0.031	0.35	0.111	0.689	5.214	1.111	0.341	0.872	0.76	1814	13	1855	9	1892	14	104
Z09	0.013	0.20	0.110	0.630	4.756	1.003	0.315	0.780	0.75	1793	11	1777	8	1764	12	98

$f(206)\%$- percentage of common ^{206}Pb.

Table 9
Isotopic analysis of sample SG-04-AM-73.

Zircon	Isotopic Ratios									Ages (Ma)						
	$f(206)$%	Th/U	$^{207}Pb/^{206}Pb$	1σ(%)	$^{207}Pb/^{235}U$	1σ (%)	$^{206}Pb/238U$	1σ (%)	Rho	$^{207}Pb/^{206}Pb$	1σ (Ma)	$^{207}Pb/235U$	1σ (Ma)	$^{206}Pb/238U$	1σ (Ma)	Disc. (%)
Inherited Orosirian zircons																
Zir01	0.002	0.47	0.109	1.075	4.915	1.663	0.328	1.214	0.73	1775	19	1805	14	1830	19	−3
Zir02	0.004	0.47	0.112	0.577	5.164	1.156	0.333	0.931	0.81	1840	10	1847	10	1852	15	−1
Zir03	0.002	0.50	0.114	1.031	5.525	1.666	0.351	1.256	0.75	1866	18	1904	14	1940	21	−4
Zir06	0.001	0.46	0.109	1.441	4.716	2.177	0.315	1.589	0.73	1777	26	1770	18	1764	24	1
Zir13	0.008	0.41	0.109	1.730	4.583	1.909	0.306	0.718	0.38	1776	31	1746	16	1721	11	3
Zir14	0.007	0.48	0.113	0.530	5.256	0.889	0.336	0.610	0.69	1853	10	1862	8	1869	10	−1
Zir15	0.008	0.28	0.113	0.630	5.044	1.074	0.323	0.787	0.73	1855	11	1827	9	1802	12	3
Zir18	0.012	0.52	0.112	0.734	5.161	2.085	0.334	1.916	0.92	1834	13	1846	18	1857	31	−1
Zir24	0.005	0.33	0.111	0.549	5.362	1.003	0.351	0.753	0.75	1812	10	1879	9	1940	13	−7
Zir25	0.008	0.49	0.111	0.522	5.129	0.927	0.336	0.671	0.72	1813	9	1841	8	1866	11	−3
Zir27	0.007	0.46	0.112	0.740	5.288	1.067	0.344	0.674	0.63	1824	13	1867	9	1905	11	−4
ZirR38	0.007	0.38	0.115	0.500	5.416	0.934	0.341	0.697	0.75	1884	9	1887	8	1890	11	0
ZirR40	0.009	0.44	0.116	0.411	5.298	0.770	0.331	0.535	0.70	1896	7	1869	7	1844	9	3
ZirR41	0.005	0.36	0.112	0.433	5.374	0.826	0.348	0.598	0.72	1830	8	1881	7	1927	10	−5
ZirR43	0.017	0.31	0.112	0.336	5.254	0.765	0.339	0.579	0.76	1838	6	1861	7	1882	9	−2
ZirR44	0.013	0.25	0.113	0.401	5.409	0.935	0.348	0.760	0.81	1846	7	1886	8	1923	13	−4
ZirR46	0.005	0.34	0.112	0.509	5.463	0.961	0.353	0.726	0.76	1834	9	1895	8	1951	12	−6
ZirR47	0.012	0.40	0.113	0.386	5.368	0.858	0.346	0.671	0.78	1842	7	1880	7	1914	11	−4
ZirR49	0.015	0.43	0.108	0.411	4.814	0.782	0.323	0.552	0.71	1766	7	1787	7	1805	9	−2
ZirR51	0.005	0.39	0.110	0.424	5.012	0.897	0.330	0.698	0.78	1803	8	1821	8	1838	11	−2
ZirR52	0.006	0.42	0.112	0.431	5.276	0.787	0.341	0.545	0.69	1838	8	1865	7	1889	9	−3
ZirR55	0.018	0.26	0.110	0.355	4.889	0.709	0.322	0.490	0.69	1804	6	1800	6	1797	8	0
ZirR56	0.008	0.37	0.113	0.439	5.235	0.816	0.336	0.579	0.71	1849	8	1858	7	1866	9	−1
ZirR58	0.008	0.39	0.113	0.429	5.191	0.828	0.334	0.603	0.73	1845	8	1851	7	1857	10	−1
ZirR59	0.009	0.60	0.112	0.350	5.326	0.803	0.343	0.620	0.77	1840	6	1873	7	1903	10	−3
ZirR60	0.009	0.47	0.113	0.341	5.034	0.747	0.325	0.551	0.74	1840	6	1825	6	1812	9	2
Not used on Orosirian age calculation																
ZirR32	0.008	0.53	0.113	0.482	4.323	0.917	0.278	0.686	0.75	1847	9	1698	8	1579	10	15
Zir04	0.005	0.28	0.117	0.592	4.850	1.657	0.300	1.502	0.91	1914	11	1794	14	1692	22	12
ZirR48	0.019	1.64	0.113	0.636	4.476	1.322	0.289	1.098	0.83	1840	11	1727	11	1634	16	11
Zir28	0.004	0.50	0.117	0.723	4.987	1.270	0.309	0.977	0.77	1914	13	1817	11	1734	15	9
Zir16	0.005	0.20	0.107	0.671	4.108	1.248	0.279	0.985	0.79	1747	12	1656	10	1585	14	9
Zir08	0.003	0.63	0.112	0.780	4.076	1.465	0.263	1.184	0.81	1840	14	1649	12	1504	16	18
ZirR57	0.010	1.17	0.113	0.432	5.593	2.181	0.359	2.105	0.97	1850	8	1915	19	1975	36	−7
Younger zircons- tendency to 1.5 Ga																
ZirR34	0.006	0.34	0.095	0.475	3.581	0.831	0.273	0.573	0.69	1530	9	1545	7	1556	8	−2
Zir21	0.005	0.46	0.091	1.689	2.672	2.474	0.213	1.770	0.72	1443	32	1321	18	1247	20	14
Zir10	0.005	0.15	0.092	0.736	2.651	2.689	0.208	2.560	0.95	1477	14	1315	20	1218	28	18
Zir22	0.009	0.14	0.093	0.756	2.761	1.392	0.214	1.109	0.80	1497	14	1345	10	1251	13	16
Zir19	0.010	0.42	0.089	0.846	1.856	2.486	0.151	2.308	0.93	1409	16	1065	16	906	19	36
Younger zircons- tendency to 1.3 Ga																
ZirR45	0.004	0.40	0.086	0.934	2.832	1.792	0.239	1.484	0.83	1339	18	1364	13	1380	18	−3
ZirR50	0.001	1.52	0.086	1.729	2.403	3.636	0.202	3.177	0.87	1343	33	1243	26	1187	34	12
Zir26	0.002	0.14	0.082	1.408	2.209	2.584	0.196	2.135	0.83	1238	27	1184	18	1154	23	7
Zir09	0.001	0.46	0.071	1.592	1.371	2.611	0.140	2.036	0.78	965	32	877	15	842	16	13
Zir07	0.000	0.26	0.075	3.222	1.641	4.567	0.158	3.216	0.70	1076	63	986	28	946	28	12
ZirR36	0.009	0.14	0.076	0.401	1.768	1.371	0.168	1.258	0.92	1108	8	1034	9	999	12	10
ZirR61	0.003	0.23	0.076	0.945	1.720	1.554	0.165	1.176	0.76	1084	19	1016	10	984	11	9

$f(206)$%- percentage of common ^{206}Pb.

The host rocks of the carbonatite were dated and provide a general idea of the ages from the local basement. In sample SG-02-AM-35 (gneiss), 17 zircon grains were analyzed, but most of them experimented Pb-loss. A good alignment of 13 analysis yield a superior intercept age of 1828 ± 9 Ma, MSWD equal to 1.09 (Fig. 5A). The Th/U results range from 0.32 to 2.22 and suggest an igneous origin for the zircons. Consequently, the age is interpreted as the crystallization time of this unit. The sample SG-02-AM-22 is a feldspar/kaolin intercalation in the host rock. The results from nine zircon grains, all showing Pb-loss, provided a relatively imprecise age of 1839 ± 29 Ma, but with good MSWD (0.73) (Fig. 5B). The Th/U varies from 0.26 to 1.75, similar to the zircons from the gneiss. The obtained age is, within error, at the same interval of the gneiss and suggests that this intercalation either is part of the same body or, if considered as a late vein, intruded not far in age from the host rock.

All samples from Figs. 6 and 7 show similar intervals of ages yielded by inherited zircon grains, most of them exhibiting Pb-loss. The Pb-loss and the short range of ages, all within the Orosirian, make difficult to identify clearly if there is more than one source for the zircons.

Sample SG-01-AM-04, a fragmented laterite crust, reveals possible two different contribution (Fig. 6A and B), but it is only a suggestion considering all grains are near 10% discordant. The probability density plot of the $^{207}Pb/^{206}Pb$ ages (Fig. 6B) shows a significant peak at 1828 Ma and a possible slightly younger population. However, different combinations of analytical points in the Concordia diagram have not reproduced satisfactorily this two population tendency. When all data are plotted together, an imprecise age of 1874 ± 56 Ma, with relatively high MSWD (2.5) is produced (Fig. 6A) representing, possibly, a mixture between inherited zircons from more than one source.

Sample SG-01-AM-01, a pisolitic laterite crust, shows also some dispersion. However, this sample has a significant peak at 1824 Ma and only few grains either older or younger (Fig. 6D). When the

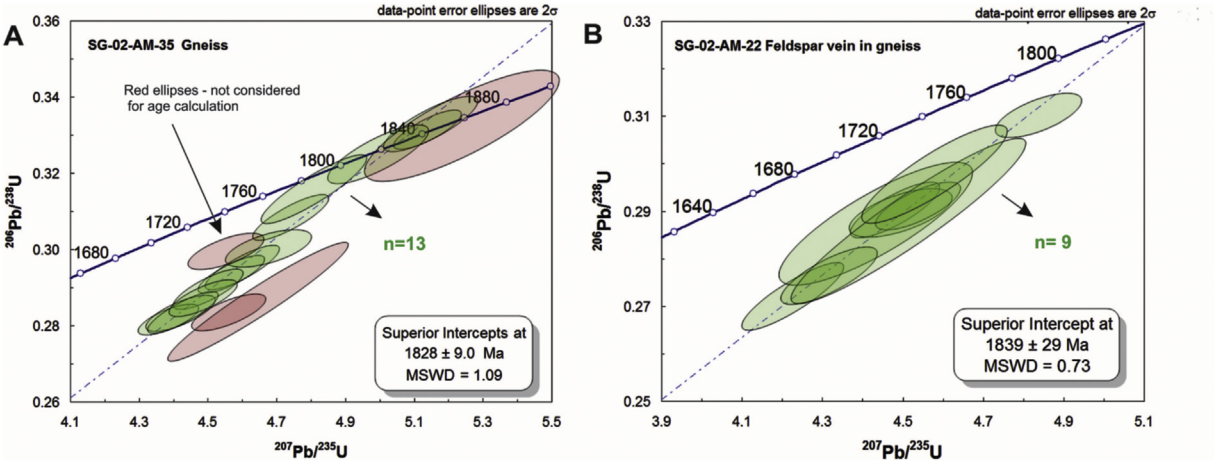

Fig. 5. Zircon U-Pb results from samples of the Morro dos Seis Lagos deposit. (A) Concordia diagram showing superior intercept age from sample SG-02-AM-35, a gneiss (host rock of the carbonatite); (B) Concordia diagram showing superior intercept age from sample SG-02-AM-22, a feldspar vein in the gneiss. Red ellipses represent analyses not used for age calculation. The number of analyses considered in the calculations are indicated as "n". (For interpretation of the references to colour in this figure legend, the reader is referred to the web version of this article.)

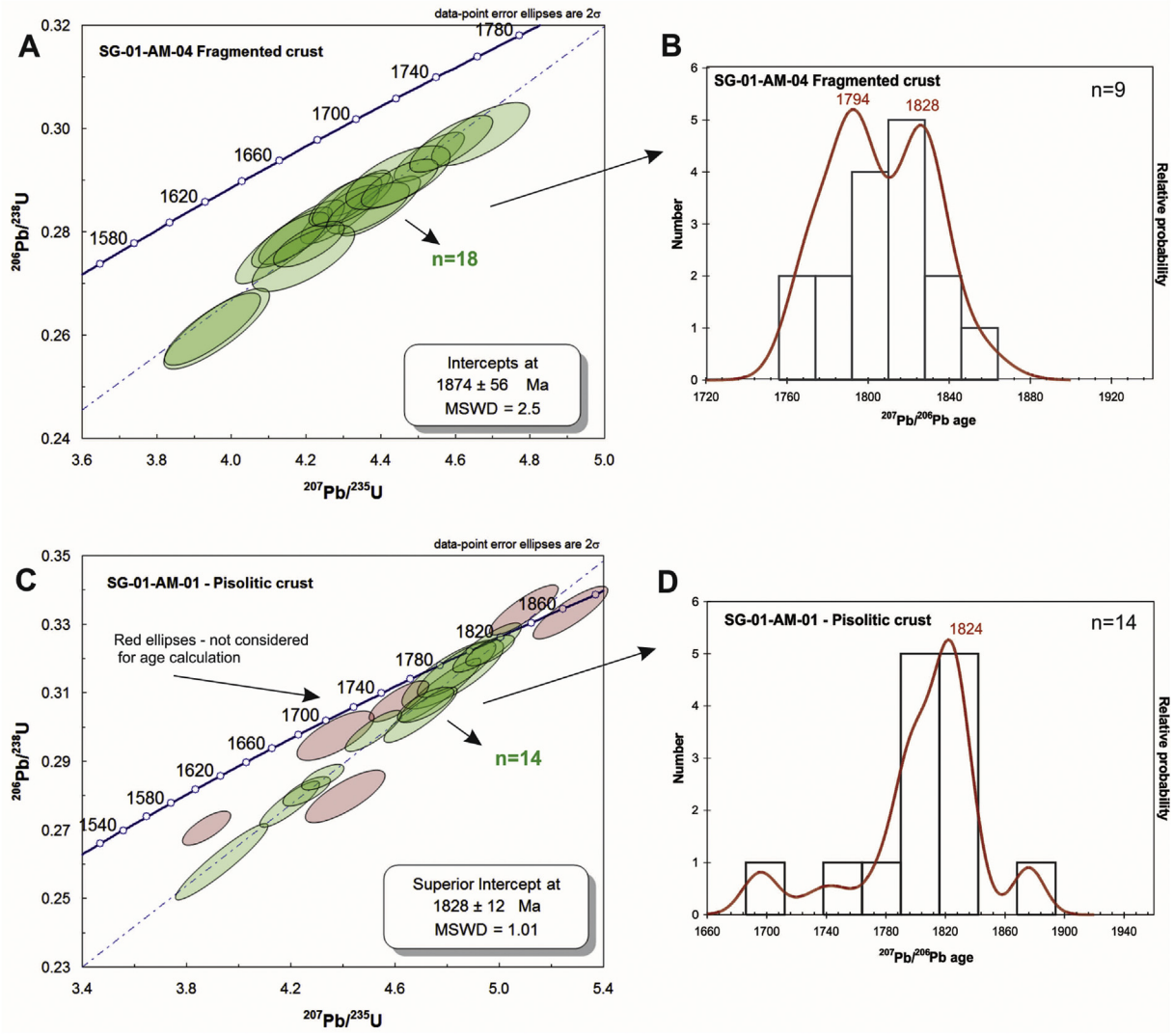

Fig. 6. Zircon U-Pb results from samples of the Morro dos Seis Lagos Deposit. (A) Concordia diagram showing superior intercept zircon age from a group of inherited grains found in a fragmented laterite crust, sample SG-01-AM-04; (B) Probability density plot of $^{206}Pb/^{207}Pb$ ages from near concordant analyses, sample SG-01-AM-04, illustrating a significant peak at 1828 Ma and a possible slightly younger population; (C) Concordia diagram showing superior intercept zircon age from a group of inherited grains found in a pisolitic laterite crust, sample SG-01-AM-01; (D) Probability density plot of $^{206}Pb/^{207}Pb$ ages from near concordant analyses, sample SG-01-AM-01, illustrating a significant peak at 1824 Ma. Red ellipses represent analyses not used for age calculation. The number of analyses considered either in the age calculation in the Concordia diagrams or in the probability density plots are indicated as "n". (For interpretation of the references to colour in this figure legend, the reader is referred to the web version of this article.)

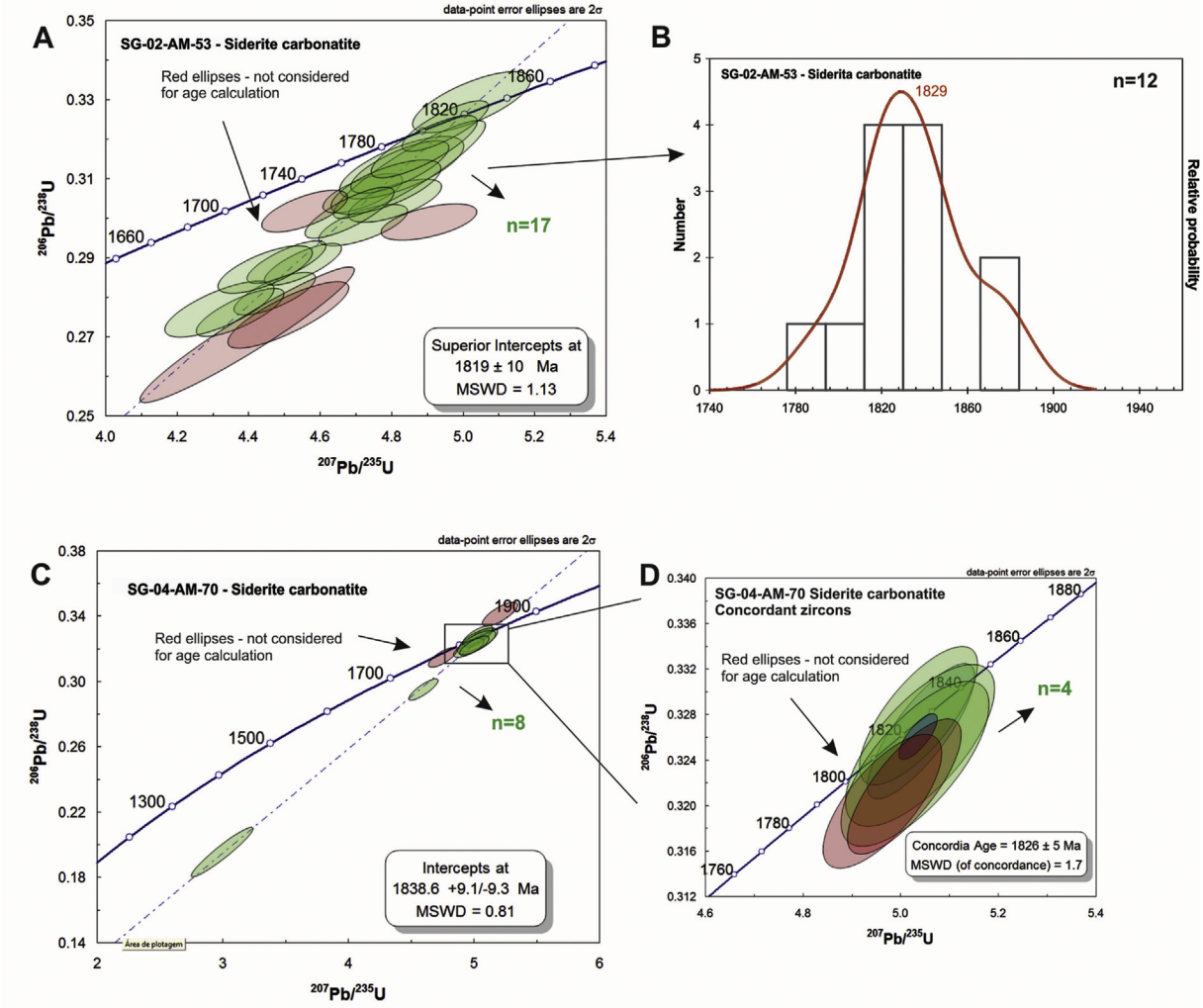

Fig. 7. Zircon U-Pb results from samples of the Morro dos Seis Lagos Deposit. (A) Concordia diagram showing superior intercept zircon age from a group of inherited grains found in a siderite carbonatite from the edge of the body, sample SG-02-AM-53; (B) Probability density plot of $^{206}Pb/^{207}Pb$ ages from near concordant analyses, sample SG-02-AM-53, illustrating a significant peak at 1829 Ma; (C) Concordia diagram showing superior intercept zircon age from a group of inherited grains found in a siderite carbonatite from the center of the body, sample SG-04-AM-70; (D) Concordia diagram showing a Concordia age of a small number of analyses from sample SG-04-AM-70. Red ellipses represent analyses not used for age calculation. The number of analyses considered either in the age calculation in the Concordia diagrams or in the probability density plots are indicated as "n". (For interpretation of the references to colour in this figure legend, the reader is referred to the web version of this article.)

most representative group is plotted in the Concordia diagram, a good superior intercept age of 1828 ± 12 Ma, with MSWD equal to 1.01, is produced (Fig. 6C). This age is considered the age of the main source for the inherited zircons and coincides with the age obtained for the gneiss, which strongly suggests the host rock as the source of the zircons. The Th/U ranges from 0.28 to 0.69, similar to other Orosirian grains.

Fig. 7 shows the results of siderite carbonatite samples. Sample SG-02-AM-53, collected at the edge of the body, produced in the probability density plot (Fig. 7B) a very distinctive peak around 1829 Ma, with few younger and older near concordant analysis. At the Concordia diagram, is possible to observe the Pb-loss in the majority of the analysis. However, seventeen grains are in relatively good alignment with superior intercept yielding an age of 1819 ± 10 Ma, with MSWD equal to 1.13 (Fig. 7A), possibly the interval of age of the main source of the zircons. Sample SG-04-AM-70, from the center of the body, produced just few grains (Fig. 7C), but with results similar to the former sample. The 1826 ± 5 Ma concordant age was obtained from a small group of grains (Fig. 7D), although with a not ideal MSWD (1.7). It is interpreted as the age of the main source for the inherited zircons. The Th/U for this group ranges from 0.32 to 0.53. The ages obtained for the main source of the zircons from both samples of the siderite carbonatite are, within error, at the same interval and also are coincident to the age of the host rock and with similar Th-U composition.

Sample SG-04-AM-73, a siderite carbonatite from the center of the body, provided a different signature (Fig. 8). Although, most of the inherited grains reveal Orosirian ages, two other peaks are possible to be identified in the probability density plot (Fig. 8B). The major population yields a peak at 1842 Ma. In the Concordia diagram, it was possible to obtain a relatively imprecise superior intercept age of 1812 ± 27 Ma, with high MSWD (5.7), suggesting a possible mixture of different sources, but all from the Orosirian. The images of the zircons reveal they are similar, small, fragmented and with no apparent zoning. All Th-U is relatively constant and ranges from 0.28 to 0.60. The two younger peaks, one at 1534 and another at 1360, are confirmed when analyses are plotted in the Concordia diagram. Despite the few grains (n = 5), many with Pb-loss, a superior intercept age of 1525 ± 21 Ma, with good MSWD (0.77) strongly suggests a source around 1.5 Ga (Fig. 8C). The Th-U from

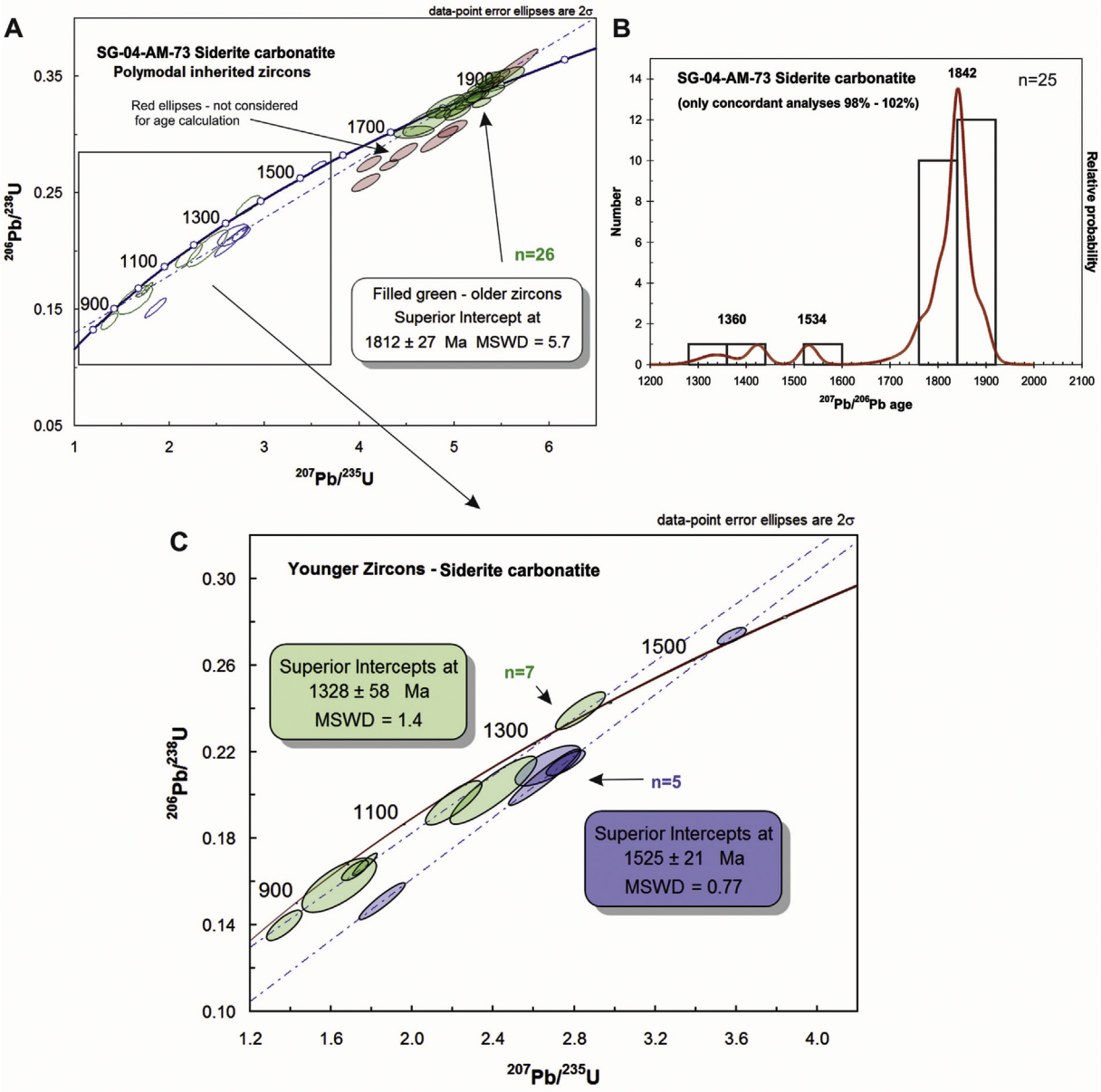

Fig. 8. Zircon U-Pb results from sample SG-04-AM-73, a siderite carbonatite from the center of the Morro dos Seis Lagos Deposit. (A) Concordia diagram showing superior intercept zircon age of the major group of inherited zircon grains; (B) Probability density plot of $^{206}Pb/^{207}Pb$ ages from near concordant analyses illustrating a major peak at 1842 Ma and two other minor peaks at 1534 Ma and 1360 Ma; (C) Concordia diagram showing superior intercept zircon ages of youger populations confirming the peaks identified in the probability density plot. Red ellipses represent analyses not used for age calculation. The number of analyses considered either in the age calculation in the Concordia diagrams or in the probability density plot are indicated as "n". (For interpretation of the references to colour in this figure legend, the reader is referred to the web version of this article.)

this group ranges from 0.14 to 0.46. The other group, with 7 results, provides a more imprecise superior intercept age, 1328 ± 58 Ma with MSWD equal to 1.4, but good enough to confirm the observed peak near 1.3 Ga. The Th/U is more variable and ranges from 1.52 to 0.14. The images of the grains from both younger groups (Fig. 9) show that they are variable in format and with no apparent zoning. It suggests a mixture of grains from different sources, but the results are significant considering it constrain a maximum age for the carbonatite at 1.3 Ga. The zircons from both younger groups (Fig. 9) tend to be larger (200 μm–300 μm) than the zircons with Orosirian ages (smaller than 100 μm, Fig. 10), fractures are rare or non-existent, the edges are smooth and well-defined, and fragments are rare.

Chemical analyses of the zircons from sample SG-04-AM-73 are presented in Tables 10 and 11. All diagrams used by Belousova et al. (2002) to identify the origin of zircon were tested, the best results are those that follow. In the Y vs Hf diagram, the younger zircons (both groups ~1.5 Ga and ~1.3 Ga) are concentrated in or relatively close to the carbonatite field (Fig. 11a), whereas the Orosirians zircons (Fig. 12a) are more dispersed. In the Th vs Y diagram (Fig. 11b), the ~1.3 Ga zircons plot in the carbonatite field or has affinity with lamproite (unfilled circles). In the REE + Y vs P diagram (Figs. 11c and 12c), the only zircon that plots in the carbonatite field is a ~1.3 Ga zircon. In the Nb/Ta vs Y diagram (Fig. 11d) all ~1.3 Ga zircons plot in or almost in the carbonatite field, whereas the Orosirians zircons are more quite dispersed. The results are not as decisive as expected but point out that younger zircons (~1.3 Ga) have more affinity with carbonatite than the two older zircon populations and this coherence has to be considered.

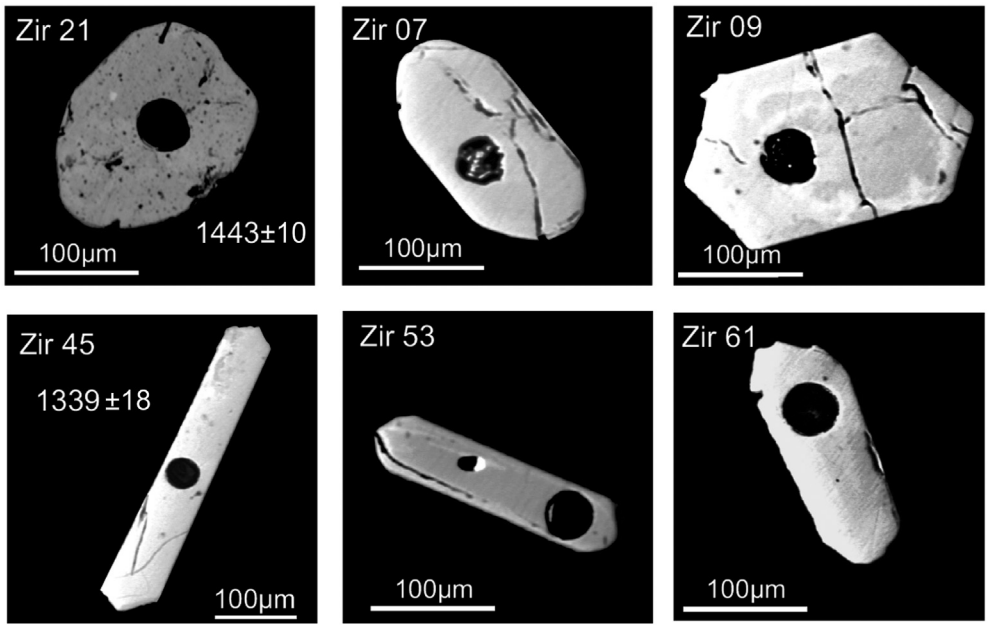

Fig. 9. SEM images of zircons from sample SG-04-AM-73 (carbonatite) representative of the population of Mesoproterozoic age.

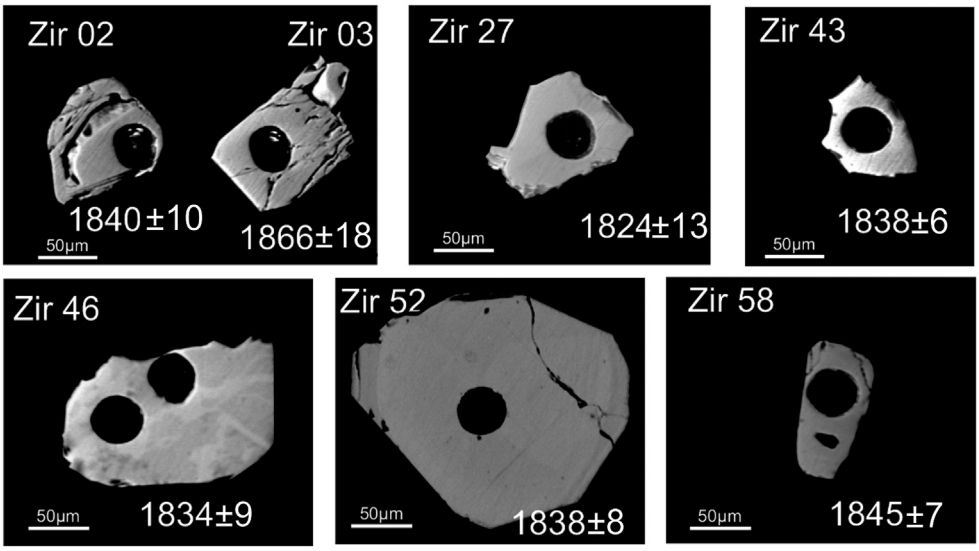

Fig. 10. SEM images of zircons from sample SG-04-AM-73 (carbonatite) representative of the population of Orosirian age.

5. Discussion

The gneiss sample yielded an age of 1828 ± 09 Ma and the altered feldspar vein that crosscuts the same gneiss yielded an age of 1839 ± 29 Ma. In the case of the gneiss, the age is interpreted as the crystallization time of this unit. The altered feldspar vein, despite the relatively imprecise age, is within error at the same interval of the gneiss and presents zircons with similar Th/U. Consequently, it is interpreted as either part of the same body or, if considered as a late vein, intruded not far in age from the host rock.

Three groups of ages were obtained in carbonatite samples. One group of ages are from the Orosirian and are the most abundant contribution occurring in all samples. The superior intercept age of 1819 ± 10 Ma obtained in the sample from the border of the carbonatite body and the 1826 ± 5 Ma concordant age obtained in the sample (SG-04-AM-70) from the central part of the body are interpreted as ages of the main source of the zircons. These ages are, within error, at the same interval of the host rock and samples show also similar Th-U zircon composition. The imprecise superior intercept age of 1812 ± 27 Ma, with high MSWD (5.7), obtained in the central part of the body (SG-04-AM-73) is a possible mixture of different sources, but all from the Orosirian.

The other two groups are younger, around 1.5 and 1.3 Ga, and only occur in one sample (SG-04-AM-73). The two peaks identified in the probability density plot are also confirmed in the Concordia diagram when discordant grains are added. The superior intercept age of 1525 ± 21 Ma, with good MSWD (0.77), strongly suggests a source around 1.5 Ga; Th-U range from 0.14 to 0.46. Although the other group produced a more imprecise superior intercept age of 1328 ± 58 Ma, with MSWD equal to 1.4, and zircons with Th/U more variable, ranging from 1.52 to 0.14, the result is considered suficient to confirm the observed peak near 1.3 Ga.

Table 10
Chemical analysis of the Orosirian zircons from sample SG-04-AM-73.

Oxide (%)	Zir 1 B	Zir 1 C	Zir 03 B	Zir 03 C	Zir 05 B	Zir 05 C	Zir 6 C	Zir 6 B	Zir 15 B	Zir 25 B	Zir 27 B	Zir 27 B	Zir 38 B	Zir 40 B	Zir 43 B	Zir 51 B	Zir 51 C	Zir 52 B	Zir 52 C	Zir 55 B	Zir 55 C
SiO_2	32.7	33.03	31.25	32.74	32.94	33.28	33.73	30.95	33.78	33.5	31.23	31.58	33.8	33.54	32.83	33.24	32.59	32.98	33.3	33.54	32.3
ZrO_2	64.94	65.2	63.79	65.56	65.45	64.84	64.29	63.74	64.6	65.1	63.51	63.27	64.34	64.57	64.82	65.25	65.68	66.37	65.46	64.68	65.01
HfO_2	0.94	1.06	0.91	0.95	0.68	0.58	1.11	0.64	0.74	0.84	1.12	1.01	1.01	0.58	0.92	0.96	0.82	0.63	0.45	0.1	0.63
Nb_2O_5	0.37	0.44	0.3	0.03	0.55	0.27	0.4	0.51	0.35	0.48	0.61	0.53	0.49	0.9	0.36	0.01	0.46	0.25	0.19	0.02	0.36
Ta_2O_5	0.14	0.15	0.03	0.24	0.12	0.28	n.d.	n.d.	0.37	0.05	n.d.	n.d.	0.02	0.19	n.d.	0.19	0.04	0.13	0.09	n.d.	n.d.
P_2O_5	0.17	0.11	n.d.	0.01	0.05	0.03	0.05	0.75	0.06	0.04	0.6	0.44	0.08	0.08	0.03	0.06	0.06	0.06	0.01	n.d.	0.14
TiO_2	n.d.	n.d.	n.d.	n.d.	0.02	0.08	n.d.	n.d.	n.d.	n.d.	0.13	0.09	0.1	0.1	n.d.	n.d.	0.02	0.07	n.d.	0.17	0.07
Al_2O_3	n.d.	0.04	n.d.	n.d.	n.d.	0.05	n.d.	0.62	n.d.	n.d.	0.31	0.3	0.05	n.d.	0.03	0.03	n.d.	0.02	0.02	0.09	0.02
FeO	0.09	0.4	0.03	n.d.	n.d.	0.02	0.01	0.44	0.08	0.03	0.3	0.36	n.d.	0.11	n.d.	n.d.	0.06	0.01	n.d.	0.1	0.03
MnO	0.11	0.04	n.d.	n.d.	0.03	0.2	n.d.	n.d.	n.d.	n.d.	0.03	0.01	n.d.	n.d.	0.05	n.d.	0.12	0.04	0.01	n.d.	0.03
CaO	0.28	0.2	n.d.	0.09	n.d.	0.19	0.32	0.36	0.2	0.04	n.d.	n.d.	n.d.	n.d.	0.05	0.03	0.07	n.d.	n.d.	0.38	n.d.
Y_2O_3	0.18	0.11	n.d.	0.13	0.25	0.35	0.19	0.68	n.d.	0.1	0.84	0.73	0.09	0.1	0.09	0.2	0.01	0.11	0.07	n.d.	0.23
La_2O_3	n.d.	0.04	0.01	n.d.	n.d.	n.d.	n.d.	n.d.	n.d.	n.d.	n.d.	n.d.	n.d.	n.d.	n.d.	n.d.	n.d.	n.d.	n.d.	0,05	0,05
Ce_2O_3	0.09	0.02	0.13	0.01	0.01	0.03	0.03	0.03	0.03	0.05	0.04	0.09	0.01	0.03	0.03	n.d.	0.08	0.05	0.03	n.d.	n.d.
Pr_2O_3	0.09	n.d.	n.d.	n.d.	n.d.	n.d.	n.d.	0.02	n.d.	n.d.	0.01	0.01	n.d.	n.d.	n.d.	n.d.	n.d.	n.d.	0.03	n.d.	n.d.
Nd_2O_3	0.03	0.03	0.05	0.03	n.d.	0.01	0.01	0.05	0.01	n.d.	0.03	0.02	n.d.	n.d.	0.02	n.d.	0.02	n.d.	0.03	n.d.	n.d.
Sm_2O_3	n.d.	0.03	0.09	n.d.	n.d.	n.d.	n.d.	n.d.	0.04	n.d.	0.09	0.05	n.d.	n.d.	n.d.	n.d.	n.d.	n.d.	n.d.	n.d.	n.d.
Eu_2O_3	0.03	0.01	0.12	0.03	0.06	0.08	0.01	0.02	0.08	0.02	n.d.	0.03	0.03	0.05	n.d.	n.d.	n.d.	0.04	n.d.	n.d.	n.d.
Gd_2O_3	n.d.	n.d.	0.15	n.d.	0.06	n.d.	n.d.	0.03	0.07	0.03	0.03	0.07	0.03	n.d.	0.02	n.d.	0.01	n.d.	n.d.	n.d.	n.d.
Tb_2O_3	n.d.	n.d.	n.d.	n.d.	n.d.	0.02	0.02	n.d.	n.d.	0.02	n.d.	n.d.	n.d.	n.d.	n.d.	0.09	n.d.	0.03	0.02	n.d.	n.d.
Dy_2O_3	n.d.	n.d.	0.41	n.d.	n.d.	n.d.	n.d.	n.d.	n.d.	n.d.	0.16	n.d.	0.03	n.d.	n.d.	n.d.	n.d.	n.d.	n.d.	n.d.	n.d.
Ho_2O_3	n.d.	0.09	0.15	n.d.	0.11	0.08	0.14	0.05	n.d.	n.d.	0.01	0.03	0.04	0.1	n.d.	n.d.	0.08	n.d.	0.01	0.05	0.06
Er_2O_3	0.08	0.04	0.43	0.08	0.03	0.08	0.01	0.05	0.03	0.11	0.28	0.14	0.05	0.03	0.06	0.01	0.02	n.d.	0.02	n.d.	n.d.
Tm_2O_3	n.d.	n.d.	0.04	n.d.	0.02	n.d.	0.03	0.01	n.d.	n.d.	n.d.	n.d.	n.d.	n.d.	0.03	n.d.	n.d.	n.d.	n.d.	n.d.	n.d.
Yb_2O_3	n.d.	0.02	0.59	0.08	n.d.	n.d.	0.01	0.04	n.d.	0.01	0.26	0.11	n.d.	0.07	n.d.	0.06	n.d.	n.d.	n.d.	n.d.	n.d.
Lu_2O_3	n.d.	0.02	0.12	0.03	0.01	0.04	n.d.	0.04	n.d.	0.01	n.d.	n.d.	n.d.	n.d.	0.02	0.03	n.d.	n.d.	0.06	n.d.	n.d.
Th (ppm)	n.d.	n.d.	2058	n.d.	346.12	205.8	177.74	299.35	n.d.	570.63	991.58	907.39	159.03	n.d.	187.09	n.d.	n.d.	205.8	336.76	9.35	9.35
U (ppm)	n.d.	n.d.	5015.38	n.d.	716.81	549.09	404.46	334.63	n.d.	1505.06	2592.94	1914.17	369.15	n.d.	444.71	n.d.	14.39	624.94	880.62	26.85	24.52
Total	100.23	101.07	99.37	100.01	100.43	100.5	100.36	99.22	100.45	100.48	100.16	99.25	100.17	100.45	99.37	100.15	100.13	100.8	99.81	99.18	98.93
Th/U	n.d.	n.d.	0.41	n.d.	0.48	0.37	0.44	0.89	n.d.	0.38	0.38	0.47	0.43	n.d.	0.42	n.d.	n.d.	0.33	0.38	0.35	0.38
Y_2O_3+REE_2O_3 (ppm)	4196.43	3129.09	18820.8	3027.01	4531.86	5273.54	3636.92	7922.86	2236.84	2831.04	14490.64	10495.99	2317.33	3217.55	2021.06	3013.15	1900.34	1876.08	1636.57	879.66	2836.15

Table 11
Chemical analysis of the Mesoproterozoic zircons from sample SG-04-AM-73.

Oxide (%)	Zir 07 B	Zir 07 C	Zir 09 B	Zir 09 B	Zir 09 C	Zir 09 C	Zir 10 B	Zir 19 B	Zir 21 B	Zir 21 C	Zir 22 B	Zir 26 B	Zir 34 B	Zir 45 B	Zir 45 C	Zir 50 B	Zir 53 B	Zir 53 C	Zir 61 B	Zirr 61 C
SiO_2	33.24	33.00	33.95	31.82	33.28	33.05	34.48	33.83	33.57	33.16	33.34	32.98	32.18	33.18	33.17	33.36	33.61	33.77	32.80	33.00
ZrO_2	65.34	65.38	64.47	65.13	64.98	64.53	64.35	64.70	64.21	64.82	64.59	65.86	66.19	65.18	64.70	64.81	64.98	64.39	65.38	65.53
HfO_2	0.94	0.95	0.96	0.98	1.07	0.65	1.10	1.21	1.11	1.20	0.80	0.87	0.67	0.86	1.28	0.42	0.99	0.82	0.97	0.87
Nb_2O_5	0.06	0.23	0.23	0.47	0.25	0.72	0.54	0.34	0.46	0.04	0.58	0.33	0.27	0.31	0.27	0.71	0.40	0.32	0.21	0.56
Ta_2O_5	n.d.	n.d.	0.12	0.23	0.05	0.10	0.05	n.d.	0.07	0.10	n.d.	0.14	n.d.	n.d.	0.33	0.07	0.40	0.02	0.11	n.d.
P_2O_5	0.04	0.06	0.01	n.d.	0.10	0.09	0.05	0.03	0.11	0.09	0.09	0.03	0.09	0.03	0.03	0.07	n.d.	0.09	0.05	0.02
TiO_2	n.d.	0.02	0.06	n.d.	0.16	n.d.	0.06	n.d.	n.d.	0.01	0.13	n.d.	0.04	n.d.	n.d.	n.d.	n.d.	0.20	n.d.	n.d.
Al_2O_3	0.02	n.d.	0.03	0.02	0.02	0.03	0.02	0.01	n.d.	0.01	n.d.	0.03	0.01	n.d.	n.d.	n.d.	0.02	n.d.	n.d.	n.d.
FeO	n.d.	0.01	n.d.	0.03	n.d.	n.d.	0.02	n.d.	0.11	0.04	n.d.	0.06	n.d.	n.d.	n.d.	0.04	n.d.	n.d.	n.d.	n.d.
MnO	0.01	n.d.	n.d.	0.12	n.d.	n.d.	0.03	0.03	0.01	0.03	n.d.	n.d.	0.09	n.d.	n.d.	0.12	n.d.	0.08	0.06	0.11
CaO	n.d.	0.26	n.d.	n.d.	n.d.	n.d.	0.01	n.d.	0.15	0.11	0.11	0.04	n.d.	0.07	0.08	0.21	0.17	n.d.	0.29	0.10
Y_2O_3	n.d.	0.07	0.09	n.d.	0.41	0.25	n.d.	0.11	0.11	n.d.	0.16	0.10	0.06	0.14	0.06	0.06	0.06	0.15	0.08	n.d.
La_2O_3	0.01	0.01	n.d.	0.02	n.d.	n.d.	n.d.	n.d.	n.d.	n.d.	0.01	n.d.	n.d.	0.03	0.01	n.d.	n.d.	n.d.	n.d.	n.d.
Ce_2O_3	0.06	0.04	0.03	0.06	0.04	n.d.	0.06	0.03	0.06	0.04	0.05	0.06	n.d.	0.08	0.07	0.07	0.07	0.01	0.04	n.d.
Pr_2O_3	0.02	0.02	n.d.	n.d.	0.02	0.01	0.05	0.01	n.d.	n.d.	0.01	n.d.	0.06	0.03	0.02	n.d.	0.02	0.03	n.d.	n.d.
Nd_2O_3	n.d.	n.d.	n.d.	n.d.	0.05	0.02	0.04	0.03	n.d.	0.02	n.d.	0.01	0.02	n.d.	0.03	n.d.	0.02	0.01	n.d.	n.d.
Sm_2O_3	n.d.	0.08	n.d.	0.02	0.02	0.01	0.13	n.d.	n.d.	0.01	n.d.	0.05	n.d.	n.d.	n.d.	n.d.	n.d.	0.10	0.04	n.d.
Eu_2O_3	n.d.	n.d.	n.d.	n.d.	0.03	n.d.	n.d.	0.03	0.04	n.d.	n.d.	0.04	0.01	n.d.	0.02	n.d.	0.04	0.01	n.d.	n.d.
Gd2O3	0.08	0.01	0.05	n.d.	n.d.	n.d.	n.d.	n.d.	n.d.	n.d.	0.02	0.01	n.d.	n.d.	n.d.	0.01	n.d.	0.00	0.01	n.d.
Tb2O3	0.06	0.07	0.01	n.d.	n.d.	0.06	n.d.	n.d.	n.d.	0.02	n.d.	n.d.	0.01	n.d.	n.d.	0.03	n.d.	0.02	0.04	0.02
Dy_2O_3	0.03	n.d.	n.d.	n.d.	0.05	n.d.	n.d.	n.d.	n.d.	n.d.	n.d.	n.d.	n.d.	n.d.	n.d.	n.d.	n.d.	0.05	n.d.	n.d.
Ho_2O_3	0.07	n.d.	0.08	0.01	0.01	n.d.	0.04	0.05	n.d.	n.d.	n.d.	0.05	n.d.	n.d.	0.17	n.d.	n.d.	n.d.	0.01	n.d.
Er_2O_3	0.11	n.d.	0.03	0.07	0.05	0.04	n.d.	0.02	0.03	0.03	0.06	0.04	n.d.	0.07	n.d.	n.d.	0.05	0.01	n.d.	0.06
Tm_2O_3	n.d.	n.d.	n.d.	n.d.	n.d.	0.02	n.d.	n.d.	0.01	n.d.	n.d.	n.d.	n.d.	n.d.	n.d.	n.d.	n.d.	0.02	n.d.	0.01
Yb_2O_3	n.d.	n.d.	n.d.	0.01	n.d.	0.01	n.d.	n.d.	0.02	0.02	n.d.	0.08	0.04	n.d.	n.d.	0.06	0.03	n.d.	n.d.	n.d.
Lu_2O_3	n.d.	n.d.	0.11	n.d.	n.d.	n.d.	n.d.	n.d.	n.d.	n.d.	0.01	n.d.	0.02	n.d.	n.d.	n.d.	n.d.	n.d.	0.02	0.02
Th (ppm)	n.d.	n.d.	439.66	n.d.	56.13	18.71	93.55	383.54	271.28	56.13	n.d.	196.45	486.44	420.95	n.d.	159.03	n.d.	18.71	215.15	n.d.
U (ppm)	19.03	n.d.	1162.57	46.68	133.58	94.53	244.30	906.04	609.72	138.82	n.d.	523.78	1275.25	1154.25	n.d.	442.79	n.d.	49.53	528.69	n.d.
Total	100.07	100.20	100.26	98.99	100.59	99.60	101.02	100.44	100.09	99.76	99.96	100.79	99.81	100.03	100.23	100.06	100.84	100.10	100.14	100.31
Th/U	n.d.	n.d.	0.38	n.d.	0.42	0.20	0.38	0.42	0.44	0.40	n.d.	0.38	0.38	0.36	n.d.	0.36	n.d.	0.38	0.41	n.d.
Y_2O_3+REE_2O_3 (ppm)	3715.75	2441,79	2371.25	1712.73	5554.21	3477.18	2624.59	2256.54	2252.25	1116.77	2514.06	3691.21	1681.79	2914.71	3259.75	2003.26	2382.45	3432.89	1912.84	785.82

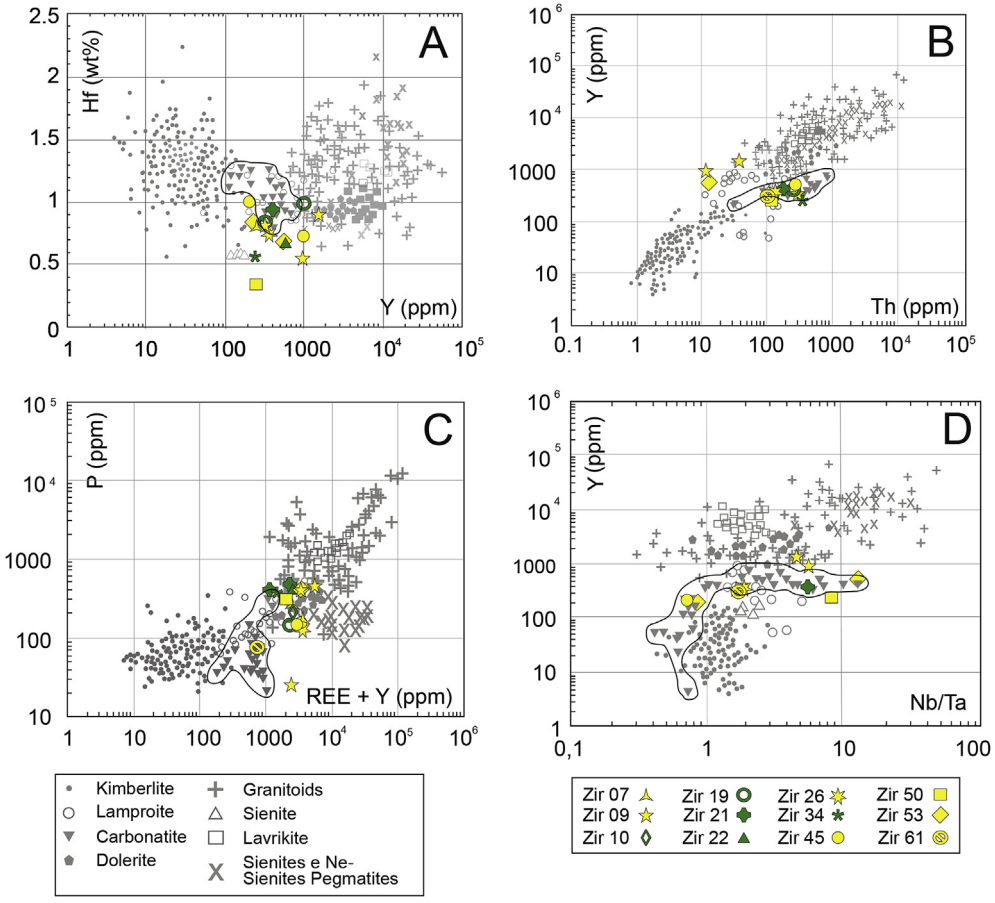

Fig. 11. Zircons of sample SG-04-AM-73 (carbonatite) with ages ~1.5Ga (green) and ~1.3 Ga (yellow) plotted in diagrams of Belousova et al. (2002) with carbonatite field delimited. (A) Y vs Hf diagram. (B) Th vs Y diagram. (C) REE + Y vs P diagram. (D) Nb/Ta vs Y diagram. (For interpretation of the references to colour in this figure legend, the reader is referred to the web version of this article.)

In Bayan Obo (Fan et al., 2014), zircons from a carbonatite dike yield a Paleoproterozic age, inherited from the host rock, and an age of 1418 ± 29 Ma (obtained in just three zircons) interpreted as the carbonatite age. This interpretation was supported by in situ Nd isotope measurements of monazite from the carbonatite dyke that yield an isochron age of 1275 ± 87 Ma, slightly younger than that of zircon U-Pb dating, but still consistent within errors. We tried to date the siderite carbonatite by Sm-Nd and Rb-Sr, but we did not get reliable isochrones.

The mineralogical study indicates that the ~1.3 Ga zircons have affinity with carbonatite. It is, however, a tendence rather than a well-defined result. The Th/U is also not capable to precisely determine the origin of the ~1.3 Ga zircons. Usually magmatic zircon is characterized by a typical Th/U of >0.5, although there are many exceptions to this observation. For example, kimberlitic zircons usually have Th/U in the range ~0.2–1.0, ranging to well below the typical magmatic Th/U (Kirkland et al., 2015). Data on Th/U on zircon from carbonatite are few and very contrasting. For instance, Amelin and Zaitsev (2002) reported zircons crystals from Kovdor carbonatite (Russia) with Th/U very high (6484–9506), while at Bayan Obo, Th/U of carbonatite zircons are ~2.2 (Fan et al., 2014). At Seis Lagos, Th/U in ~1.3 Ga zircons (from 0.14 to 1.52) are considerable lower than $Th/U_{(whole\ rock)}$ (500–1000, Giovannini, 2013). However, the Th/U reflects the distribution of Th and U between the various phases that are crystallizing at the same time as zircon, zircon may not be in equilibrium with the whole rock, and zircon easily accepts U rather than Th (Kirkland et al., 2015), thus the values of $Th/U_{(zircon)}$ and $Th/U_{(whole\ rock)}$ may be very different.

In summary, whether the ~1.3 Ga zircons are carbonatite zircons or inherited from other rock is a complex issue. The available data allow us to state that the age of 1328 ± 58 Ma represents, at least, the maximum carbonatite age. Without the same certainty, we can speculate this age may be the carbonatite crystallization time. So, the significance of this age within the regional geological context will be evaluated below.

The samples of the laterite crust may contain zircons of various origins, including (a) carbonatite zircons, (b) zircons inherited from deep rocks and carried by rising carbonatite magma, (c) zircons from the host rock, and (d) clastic zircons derived from distant sources and deposited, during formation of the laterite, in spaces generated by carstic processes. The age of 1874 ± 56 Ma obtained in the fragmented laterite crust is interpreted as a mixture between inherited zircons from more than one source. On the other hand, the sample from the pisolitic laterite provided a good superior intercept age of 1828 ± 12 Ma, considered the age of the main source for the inherited zircons, which coincides with the age obtained for the gneissic host-rock. Although the laterite is formed by carbonatite weathering, the absence of zircons with ~1.3 Ga age is not surprising as they are much more rare in the siderite carbonatite than the inherited zircons, similarly to Bayan Obbo carbonatite (Fan et al., 2014).

The gneissic host-rock of the Seis Lagos carbonatite was included by CPRM (2006) in the Tarsira lithofacies of the Cauaburi Complex. The age here obtained (1828 ± 09 Ma) is ~30 Ma older than the ages published for the lithofacies Tarsira and ~20 Ma older than the oldest age of the Cauaburi Complex (Table 1).

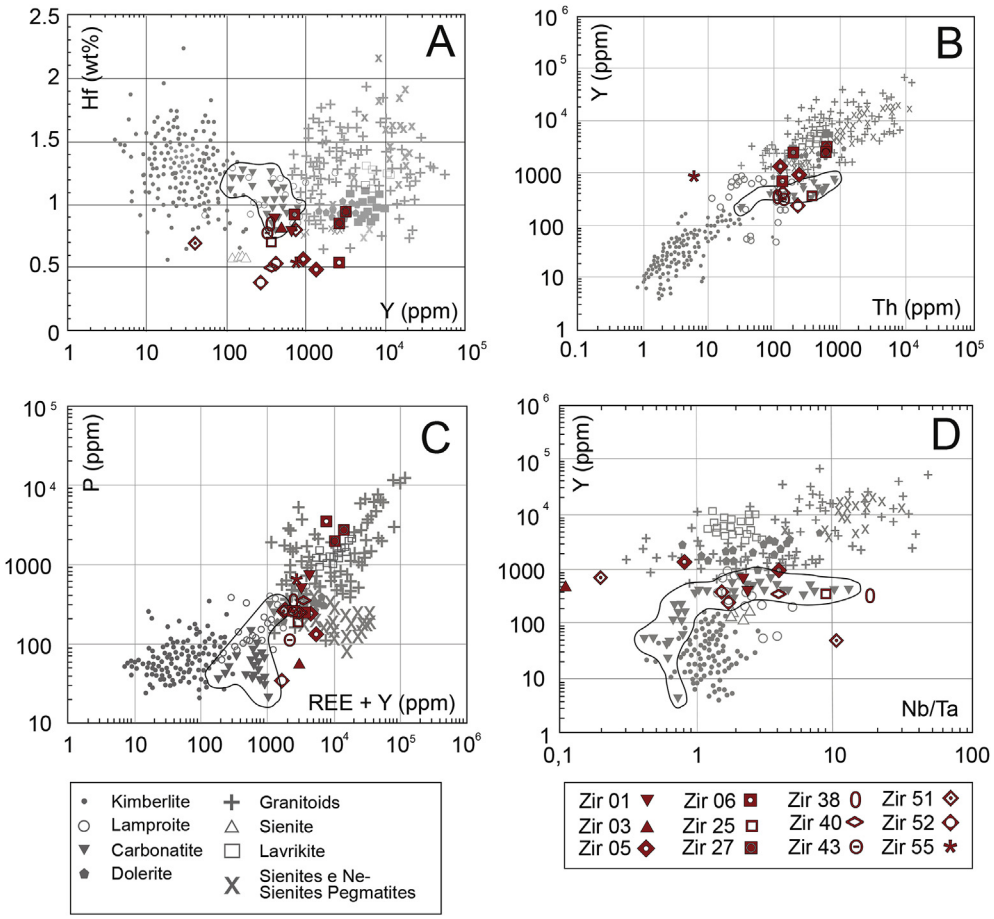

Fig. 12. Zircons of sample SG-04-AM-73 (carbonatite) with orosirian age plotted in diagrams of Belousova et al. (2002). (A) Y vs Hf diagram. (B) Th vs Y diagram. (C) REE + Y vs P diagram. (D) Nb/Ta vs Y diagram.

Consequently, the gneissic host-rock maybe is correlated to the rocks that constitute the basement of the Rio Negro Province in Venezuela, where Gaudette and Olszewski (1985) obtained ages of 1847 ± 65 Ma (U-Pb in zircon), 1823 ± 15 Ma (Rb-Sr whole-rock), 1859 ± 47 Ma (U-Pb in zircon) and 1783 ± 35 Ma (Rb-Sr whole-rock) in gneisses, and Tassinari et al. (1996) obtained a SHRIMP $^{207}Pb/^{206}Pb$ age of 1834 ± 24 Ma in tonalite.

During the mid-Proterozoic, the region was affected by the formation of the K'Mudku Belt, an intracontinental reflection of Sunsás collisions along the margin of the Amazon Craton. This latter event generated mylonitization and magmatism between 1.49 and 1.14 Ga in the previously coalesced domains (Santos et al., 2006a, 2006b, 2009; Almeida et al., 2013; Souza et al., 2015). Thus the Seis Lagos Carbonatite Complex could be related to final stage of the evolution of the successive orogenic belts or related to the K'Mudku Belt. The association between carbonatites and intracratonic shear zones related to continental collisional events has been reported in some locations. The alkaline carbonatite complex of South Purulia shear zone (Dwivedi et al., 2014) is related to the Grenvillian/Saptura orogeny (1.3–0.9 Ga), developed through the collision between the Bundelkhand Craton and the Singhbhum and Bastar Cratons. The Dharmapuri shear zone (India), linked to the formation of the Rodinia and Pangea supercontinents, is characterized by a large number of carbonatite alkaline intrusions with ages between 700 and 900 Ma (Chaturvedi and Parihar, 2014). According to Rossoni et al. (2016), the E-W mega-structure that controlled the emplacement of the Seis Lagos Carbonatite Complex is likely related to the K'Mudku Belt. In this sense, we interpret that the age of 1328 ± 58 Ma could be the carbonatite emplacement time impling a possible connection to the evolution of the K'Mudku Belt.

6. Conclusions

U-Pb dating of zircons associated with the different lithological types in the Morro dos Seis Lagos deposit led to the following conclusions.

The gneiss that hosts the carbonatite body yielded an age of 1828 ± 09 Ma interpreted as the crystallization time of this unit. The altered feldspar vein in the same gneiss yielded an age of 1839 ± 29 Ma; this vein is either part of the same body or, if considered as a late vein, intruded not far in age from the host rock. These rocks are ~30 Ma older than the lithofacies Tarsira of the Cauaburi Complex and are suggested to be correlated to rocks of the basement of the Rio Negro Province that occur in Venezuela.

Carbonatite samples provided 3 groups of ages. The first group comprises inherited zircons with ages compatible with the gneissic host rock. A superior intercept age of 1819 ± 10 Ma (sample from the border of the carbonatite body), the 1826 ± 5 Ma concordant age (sample from the central part of the body) and the imprecise superior intercept age of 1812 ± 27 Ma (high MSWD possible due to mixture of different sources) also obtained in the central part of the body (sample SG-04-AM-73) are all from the Orosirian.

The second and the third group of ages obtained in carbonatite samples are younger and both obtained in just one sample (SG-04-AM-73). The two peaks identified in the probability density plot are also confirmed in the Concordia diagram when discordant grains

are added. The superior intercept age of 1525 ± 21 Ma, with good MSWD (0.77), strongly suggests a source around 1.5 Ga; Th-U range from 0.14 to 0.46. Although the other group produced a more imprecise superior intercept age of 1328 ± 58 Ma, with MSWD equal to 1.4, and zircons with Th/U more variable, ranging from 1.52 to 0.14, the result is considered suficient to confirm the observed peak near 1.3 Ga.

The mineralogical study indicates that the ~1.3 Ga zircons have affinity with carbonatite. It is, however, a tendence rather than a well-defined result. The available data allow us to state that the age of 1328 ± 58 Ma represents the maximum age of the carbonatite. Without the same certainty, we consider that the data suggest that this age may be the carbonatite age, whose emplacement would have been related to the evolution of the K'Mudku belt.

The best age obtained in laterite samples (a superior intercept age of 1828 ± 12 Ma) is considered the age of the main source for the inherited zircons related to the gneissic host-rock.

Acknowledgments

The present work would not have been possible without the support given by the Companhia de Pesquisa de Recursos Minerais, through Roberto Ventura Santos, Eduardo Camozatto, and Renê Luzardo. Gert Rodolfo Woeltje (DNPM-Amazonas) is also thanked. The manuscript has benefitted from very constructive criticism from two anonymous reviewers. The Conselho Nacional de Desenvolvimento Científico e Tecnológico CNPq is acknowledged for the financial support (projects 485415/2012-7 and 405839/2013-8). Pedro Bastos and Mauricio Bidone are acknowledged for the collaboration in the separation of the zircons.

References

Almeida, M.E., Macambira, M.J.B., Scheller, T., 1997. Içana Intrusive Suite: age 207Pb/206Pb (zircon evaporation) of muscovite bearing granite, Amazonas State, Brazil. In: South-American Symposium on Isotope Geology, pp. 31–33, 1°, Campos do Jordão. Extended Abstracts.

Almeida, M.E., Macambira, M.J.B., Santos, J.O.S., Nascimento, R.S.C., Paquette, J.-L., 2013. Evolução crustal do noroeste do cráton Amazônico (Amazonas, Brasil) baseada em dados de campo, geoquímicos e geocronológicos. In: Simpósio de Geologia da Amazônia, 13°, Belém, CD-ROM.

Amelin, Y., Zaitsev, A.N., 2002. Precise geochronology of phoscorites and carbonatites: the critical role of U-series disequilibrium in age interpretations. Geochimica Cosmochimica Acta 66 (13), 2399–2419.

Barron, C.N., 1966. Notes on the stratigraphy of Guyana. In: Guyana Geological Conference, 7, Paramaribo, Proceedings, vol. 6, pp. 1–28.

Basei, M.A.S., 1975. Geocronologia de parte do Território Federal de Roraima e do norte do Estado do Amazonas. Belém, Projeto RADAM, Relatório interno, 19pp.

Belousova, E.A., Griffin, W.L., O'Reilly, S.Y., Fisher, N.I., 2002. Igneous zircon: trace element composition as an indicator of source rock type. Contrib. Mineral. Pet. 143, 602–622.

Chaturvedi, A.K., Parihar, P.S., 2014. Geophysical characterization of uranium-REE mineralization associated with alkaline-carbonatite complex along Singhbhum shear zone, Singhbhum craton, Jharkhand and West Bengal, India. In: Technical Meeting on Uranium from Uncoventional Resources, vol. 2014. International Atomic Energy Agency (IAEA), Viena, Austria, pp. 4–7.

Corrêa, A.S., 1996. Evolução geoquímica da crosta laterítica e dos sedimentos sobrepostos na estrutura de Seis Lagos (Amazonas). Doctoral thesis. Universidade Federal do Pará, Manaus, 112 pp.

Corrêa, A.S., Costa, M.L., 1997. Mineralogia das crostas laterítica ferruginosas de Seis Lagos (Amazonas). Rev. Bras. Geociências 16, 141–156.

CPRM. Serviço Geológico Brasileiro, 2006. Geologia e Recursos Minerais do Estado do Amazonas. CPRM, Manaus, 144pp.

Dall'Agnol, R., Macambira, M.J.B., 1992. Titanita-biotita granitos do baixo rio Uaupés, Província Rio Negro, Amazonas. Parte I: geologia, petrografia e geocronologia. Rev. Bras. Geociências 22 (1), 3–14.

Dwivedi, A.K., Joshi, M., Chaturvedi, A.K., 2014. Tectonic significance of alkali-granitoids from South Purulia shear zone, North Singhbhum fold belt, Easter India. In: 25th Indian Nuclear Society Annual Conference, Hyderabad, India, pp. 15–17.

Fan, H.R., Hu, F.F., Yang, K.F., Pirajno, F., Liu, X., Wang, K.Y., 2014. Integrated U–Pb and Sm–Nd geochronology for a REE-rich carbonatite dyke at the giant Bayan Obo REE deposit, Northern China. Ore Geol. Rev. 63, 510–519.

Gaudette, H.E., Olszewski, W.J., 1985. Geochronology of the basement rocks, Amazonas Territory, Venezuela and the tectonic evolution of the western Guiana Shield. Geol. Mijnb. 64, 131–144.

Giovannini, A.L., 2013. Contribuição à geologia e geoquímica do carbonatito e da jazida (Nb, ETR) de Seis Lagos (Amazonas). Masters dissertation. Universidade Federal do Rio Grande do Sul, Porto Alegre, 112 pp.

Giovannini, A.L., Bastos Neto, A.C., Porto, C.G., Pereira, V.P., Takehara, L., Barbanson, L., Bastos, P.H.S., 2017. Mineralogy and geochemistry of laterites from the Morro dos Seis Lagos Nb (Ti, REE) deposit (amazonas, Brazil). Ore Geol. Rev. 88, 461–480.

Gomes, C.B., Ruberti, E., Morbidelli, L., 1990. Carbonatite complexes from Brazil: a review. J. S. Am. Earth Sci. (3/1), 51–63.

Issler, R.S., Silva, G.G., 1980. The Seis Lagos carbonatite complex. In: Congresso Brasileiro de Geologia 31, Camboriu, vol. 3, pp. 1564–1572.

Justo, L.J.E.C., Souza, M.M., 1986. Jazida de Nióbio do Morro dos Seis Lagos, Amazonas. In: Schobbenhaus, C., Coelho, C.E.S. (Eds.), Principais Depósitos Minerais do Brasil. Departamento Nacional de Produção Mineral, Brasília, pp. 463–468.

Kirkland, C.L., Smithies, R.H., Taylor, R.J.M., Evans, N., McDonald, B., 2015. Zircon Th/U in magmatic environs. Lithos 212–215, 397–414.

Lemos, R.L., Gaspar, J.C., 1998. Geologia do Complexo Ultramáfico-alcalino-carbonatítico de Maicuru, noroeste do Estado do Pará. In: Congresso Brasileiro de Geologia, 40, 1998, Belo Horizonte. Anais, vol. 1. SBG, Belo Horizonte, pp. 466–529.

Pinheiro, S.S., Fernandes, P.E.C.A., Pereira, E.R., Vasconcelos, E.E., Pinto, A.C., Montalvão, R.M.G., Issler, R.S., Dall'Agnol, R., Teixera, W., Fernandes, C.A.C., 1976. Geologia. In: RADAM Brasil – Levantamento de Recursos Naturais, vol. 11. Folha NA-19 Pico da Neblina. 369pp.

Rossoni, M.R., Bastos Neto, A.C., Saldanha, D.L., Souza, V.S., Giovannini, A.L., Porto, C.G., 2016. Aplicação de técnicas de sensoriamento remoto na investigação do controle do posicionamento do Complexo Carbonatítico Seis Lagos e no estudo do depósito (Nb) laterítico associado (Amazonas, Brasil). Pesqui. em Geociências 43 (2), 111–125.

Santos, J.O.S., 2003. Geotectônica dos Escudos das Guianas e Brasil Central. In: Bizzi, L.A., Schobbenhaus, C., Vidotti, R.M., Gonçalves, J.H. (Eds.), Geologia, Tectônica e Recursos Minerais do Brasil (texto, mapas & SIG). Serviço Geológico do Brasil – CPRM/MME, Brasília, pp. 169–226.

Santos, J.O.S., Hartmann, L.A., Gaudette, H.E., Groves, D.I., Mcnaugthon, N.J., Fletcher, L.R.A., 2000. New understanting of the provinces of Amazon craton based on integration of field mapping and U-Pb and Sm-Nd geochronology. Gondwana Res. 3 (4), 453–488.

Santos J.O.S., Faria M.S.G. de Hartmann L.A., McNaughton N.J. 2002. Significant presence of the Tapajós – Parima orogenic belt in the Roraima Region, Amazon craton based on SHRIMP U-Pb zircon geochronology. In: SBG, Cong. Bras. Geol., 41, João Pessoa, Pb, Anais, p. 336.

Santos, J.O.S., Hartmann, L.A., Faria, M.S.G., Riker, S.R., Souza, M.M., Almeida, M.E., McNaughton, N.J., 2006a. A compartimentação do Cráton Amazonas em províncias: avanços ocorridos no período 2000-2006. In: SBG-NO, 9° Simpósio de Geologia da Amazônia. CD-ROM, Belém.

Santos, J.O.S., Faria, M.S.G., Riker, S.R., Souza, M.M., Hartmann, L.A., Almeida, M.E., McNaughton, N.J., Fletcher, I.R., 2006b. A faixa colisional K'Mudku (idade grenvilliana) no norte do cráton Amazonas: reflexo intracontinental do orógeno Sunsás na margem ocidental do cráton. In: SBG-NO, 9° Simpósio de Geologia da Amazônia. CD-ROM, Belém.

Santos, J.O.S., McNaughton, N.J., Almeida, M.E., 2009. Magmatismo de idade Sunsás no centro-norte do cráton Amazonas. In: SBG-NO, 11° Simpósio de Geologia da Amazônia. CD-ROM, Manaus.

Souza, A.J.H., 2009. Petrologia e geoquímica do batólito granítico São Gabriel da Cachoeira. Master dissertation. Universidade Federal do Amazonas, Província Rio Negro, AM, 89 pp.

Souza, V.S., Souza, A.G.H., Dantas, E.L., Valério, C.S., 2015. ḰMudku A-type magmatism in the southernmost Guyana Shield, central-north Amazon Craton (Brazil): the case of Pedra do Gavião syenogranite. Braz. J. Geol. 45 (2), 293–306.

Tassinari, C.C.G., Macambira, M.J.B., 1999. Geochronological provinces of the amazonian craton. Episodes 22 (3), 174–182.

Tassinari, C.G.C., Cordani, U.G., Nutman, A.P., Schmus, W.R.V., Bettencourt, J.S., Taylor, P.N., 1996. Geochronological systematics on basement rocks from the Rio Negro - Juruena province (amazonian craton) and tectonic implications. Int. Geol. Rev. 38, 161–175.

Tassinari, C.C.G., Macambira, M.J.B., 2004. A Evolução tectônica do cráton amazônico. In: Manteso-Neto, V., Bartoreli, A., Carneiro, C.D.R., Brito Neves, B.B. (Eds.), Geologia do Continente Sul Americano: Evolução da Obra de Fernando Flávio Marques de Almeida, pp. 471–486. São Paulo.

Teixeira, W., Tassinari, C.C.G., Cordani, G.U., Kawashita, K., 1989. A review of the geochronology of Amazonian Craton: tectonic implications. Precamb. Res. 42, 213–227.

Viegas Filho, J.R., Bonow, C.W., 1976. Projeto Seis Lagos. CPRM. Serviço Geológico Brasileiro, vol. 1. CPRM, Manaus, 136pp. Relatório Final.